Predicting Compression Failure of Fiber-reinforced Polymer Laminates during Fire

Patrick Timothy Summers

Thesis submitted to the faculty of the Virginia Polytechnic Institute and State University in partial fulfillment of the requirements for the degree of

Master of Science
In
Mechanical Engineering

Brian Y. Lattimer
Scott W. Case
Robert L. West

April 30, 2010
Blacksburg, VA

Keywords: Fire, Fiber-reinforced Polymer Laminate, Intermediate-Scale, Thermo-structural Modeling, Compressive Loading

Predicting Compression Failure of Fiber-reinforced Polymer Laminates during Fire

Patrick Timothy Summers

ABSTRACT

A thermo-structural model was developed to predict the failure of compressively loaded fiber-reinforced polymer (FRP) laminates during fire. The thermal model was developed as a one-dimensional heat and mass transfer model to predict the thermal response of a decomposing material. The thermal properties were defined as functions of temperature and material decomposition state. The thermal response was used to calculate mechanical properties. The structural model was developed with thermally induced bending caused by one-sided heating. The structural model predicts out-of-plane deflections and compressive failure of laminates in fire conditions. Laminate failure was determined using a local failure criterion comparing the maximum combined compressive stress with the compressive strength.

Intermediate-scale one-sided heating tests were performed on compressively loaded FRP laminates. The tests were designed to investigate the effect of varying the applied stress, applied heat, and laminate dimensions on the structural response. Three failure modes were observed in testing: kinking, localized kinking, and forced-response deflection, and were dependent on the applied stress level and independent of applied heating. The times-to-failure of the laminates followed an inverse relationship with the applied stress and heating levels. The test results were used to develop a relationship which relates a non-dimensionalized applied stress with a non-dimensionalized slenderness ratio. This relationship relates the applied stress, slenderness ratio, and temperature of the laminate at failure and can be used to determine failure in design of FRP laminate structures. The intermediate-scale tests were also used to validate the thermo-structural model with good agreement.

Dedication

This work is dedicated to my family, who has given me their full-fledged support throughout all my academic and personal endeavors. The influence of my father, mother, and brother, Michael, has given me the strength and desire to pursue all of my dreams in life.

Acknowledgements

I would like to acknowledge and thank the following persons who made the completion of this work possible.

Brian Y. Lattimer – Thank you for being my primary advisor, a mentor, and a friend. Thank you for your encouragement and honest desire to do whatever is possible to ensure that my motivation to pursue excellence in research never waned. Your ability to draw out the best in me motivates me to do the same with others. I sincerely look forward to continue working with you in pursuit of my doctorate.

Scott W. Case – Thank you for being an advisor to me and a mentor. The two classes I took with you were invaluable to advancing my knowledge in composites and the experience of having you as a teacher inspires me to one day share my knowledge with others through teaching. Thank you also for the many conversations we have had regarding various topics pertaining to this research.

Robert L. West – Thank you for introducing me to the field of finite element analysis. The two classes I have taken with you piqued my interest in the field and continue to inspire me to educate myself on it.

Emily Fogle – Thank you for your help in performing the testing for this research. Our work has been closely linked throughout graduate school and your help has been invaluable in finishing it. Also, your friendship is irreplaceable.

Stefanie Feih – Thank you for your assistance in developing the thermo-structural model. Your knowledge and willingness to educate me in the behaviors of composite materials has been invaluable.

Zhenyu Zhang – Thank you for assisting me in developing the thermo-structural model. Your inputs and our discussions made the development of the model and the finishing of it possible.

To the other members of the EXTREME Lab – Ryan Matulich, Jillian Chodak, and Tom Goodrich – your assistance in my research has been invaluable and your friendship means the world to me.

To the others who have assisted me – Jason Dress and Craig English – thank you for assisting me in my research and, most importantly, thank you for your friendship.

Table of Contents

List of Figures

List of Tables

Nomenclature

SYMBOL	DESCRIPTION	UNITS
A	pre-exponential factor	Hz
A_{cs}	cross-sectional area	m^2
c	distance from neutral axis to compressive laminate surface	m
C	specific heat capacity of solid material	J/kg-K
e	eccentricity	m
E	elastic modulus	Pa
E_a	activation energy	J/gmol
$(EI)_{eq}$	equivalent bending rigidity	$N\text{-}m^2$
$(EI)_{eq,av}$	bulk equivalent bending rigidity	$N\text{-}m^2$
F	fraction of decomposed mass remaining	--
h	enthalpy	J/kg
h_{conv}	convective heat transfer coefficient	$W/m^2\text{-}K$
$h^{(e)}$	elemental thickness	m
i	elemental/nodal index	--
I	moment of inertia	m^4
k	thermal conductivity	W/m-K
K	parabolic shape function fitting parameter	--
K_e	end condition constant to calculate effective bending length	--
l	thickness of material	m
L	bending length of axially compressed beam	m
m	solid material mass	kg
$\dot{m}_g$	mass flow rate of pyrolysis gases	kg/s
$\dot{m}_g''$	mass flux of pyrolysis gases	$kg/m^2\text{-}s$
M	kinetic rate expression function	--
M_e	moment due to eccentric loading	N-m
M_r	reaction moment	N-m
M_x^T	thermal moment	N-m
n	order of reaction	--
n_{elem}	number of elements in domain	--
N	shape function	--
P	compressive, axial load	N
P_{euler}	Euler buckling load	N
q	heat flow	W
q''	heat flux	W/m^2
Q	heat of decomposition	J/g
R	universal gas constant, 8.314	J/gmol-K
R_{rc}	scaling function for decomposition effects	--
t	time	s
T	absolute temperature	K

SYMBOL	DESCRIPTION	UNITS
T_∞	environmental temperature	K
T_{init}	initial material temperature	K
T_k	mechanically determined glass transition temperature	K
T_{ref}	reference temperature, 273	K
U	internal energy	J
v	out-of-plane deflection	m
V	volume	m^3
w	laminate width	m
W	weighting function	--
x	axial direction	m
y	through-thickness direction	m
y'	through-thickness integration variable	m

Greek

α	in-plane thermal expansion coefficient	1/K
β	empirical fitting parameter for decomposition	--
ε	total strain	m/m
ε_s	material emissivity	--
ε_{hfg}	water-cooled heat flux gauge emissivity	--
ε_m	mechanical strain	m/m
ε_T	thermal strain	m/m
κ	radius of curvature	m
η	relaxation parameter	--
ρ	solid material density	kg/m^3
Φ	material constant to represent temperature range	--
σ	Stefan-Boltzmann constant, 5.67×10^{-8}	$W/m^2\text{-}K^4$
σ_{app}	stress from applied load	Pa
σ_c	compressive strength	Pa
σ_{max}	maximum combined stress in laminate	Pa
ξ	natural coordinate system direction	--
λ	slenderness ratio	--
λ_c	constant of integration in elastic curve equation	1/m
θ	slope angle	rad
Δ	change in the following parameter	--

Subscripts

(*0*)	room temperature parameter value
(*R*)	residual parameter value
d	decomposed (char) material
g	pyrolysis gases
hfg	water-cooled heat flux gauge
i	elemental/nodal index
j	elemental/nodal index on '*i*+1' side of element
n	current time step
0	maximum value of parameter at mid-height of beam ($x=L/2$)
s	material surface
v	virgin material

CHAPTER 1 - Introduction

Background

Interest in using fiber-reinforced polymer (FRP) laminates for naval applications is increasing due to the extremely low weight and high corrosion resistance of such materials when compared to traditional construction materials such as steel. As a result of these properties, FRP laminates are being considered for construction of entire load-bearing structures. However, the laminates are combustible materials that will decompose and burn when exposed to a sufficiently strong heat source. In addition, their structural properties decrease significantly as the material temperature increases above the glass transition temperature (~120°C for the vinyl ester laminates being considered for naval applications). As a result, a major design challenge for the use of FRP laminates is fire performance.

Improving the fire performance of FRP laminate structures is critical to enabling their further use in naval applications. Fire performance includes a material's fire resistance, flammability, and smoke and toxic gas generation. Of primary interest in this research is fire resistance. Fire resistance is a measure of heat transmission from the fire-exposed surface of the laminate to the unexposed surface as well as the structural integrity. Heat transmission is the ability of a material to insulate the heat released by the heat source, thereby preventing fire spread through the material by conduction. Structural integrity is the ability of a material to maintain strength as it is heated. The FRP laminates examined in this thesis begin to lose their structural properties as low as 100°C, and degrade at temperatures as low as 200°C.

The fire performance of FRP laminate naval structures may be predicted either through large-scale testing or computational modeling. The more traditional method is to conduct large-scale testing. While large-scale tests will provide the most representative data that may be obtained for a given structure, they are expensive and time consuming. The high cost in terms of both money and time involved in running such tests renders parametric studies for design optimization highly impractical. In order to reduce the number of tests required, tests performed at a smaller scale and computational models can be used to conduct parametric studies and design optimizations, saving expensive large-scale tests for validation at the end of the design process. Performing modeling prior to testing saves both time and money, and allows for more design options to be explored.

The thermo-structural modeling of FRP laminates in fire conditions can be very complex in nature when considering the three-dimensional behaviour of naval structures. The thermal modeling of a laminate exposed to fire is inherently complex due to the decomposing nature of the material. Modeling the structural response of the laminate can also be complex due to the three-dimensional nature of the structure, potential failure modes, and load distribution. Modeling the three-dimensional thermo-structural response of an FRP laminate exposed to fire is similar to the costs and benefits of performing large-scale testing. A full three-dimensional model of the laminate will provide results most representative of the thermo-structural behavior;

however, the modelling will be expensive in terms of time required. Thermo-structural modeling of FRP laminates requires a special thermal model as well as a coupled structural model.

All aspects of fire performance require prediction of temperature and fuel production from the decomposing laminate. Predictions are generated using a heat and mass transfer model called a pyrolysis model. Figure 1 shows the layout of a typical one-dimensional pyrolysis model, in which one side of a laminate is heated. At any given time in these simulations, the laminate may be comprised of char (fully decomposed material), the pyrolysis region where virgin material is converted into gas and char, and virgin material that may be heated but has not yet lost mass. Gas produced from the pyrolysis process flows to the surface where it may ignite and burn. Ignoring char oxidation processes, the mass loss rate of the material is equal to the gas mass flow rate from the pyrolysis region. The mass flow rate of fuel (pyrolysis products) is directly related to the heat produced by burning the material as well as the toxic gases and smoke produced from the material. Temperature profiles from the model may be used to predict heat transmission through the laminate, which is useful in predicting fire spread to the unexposed surface of the material. In addition, the temperature profiles may be used to determine structural properties through the thickness of the material.

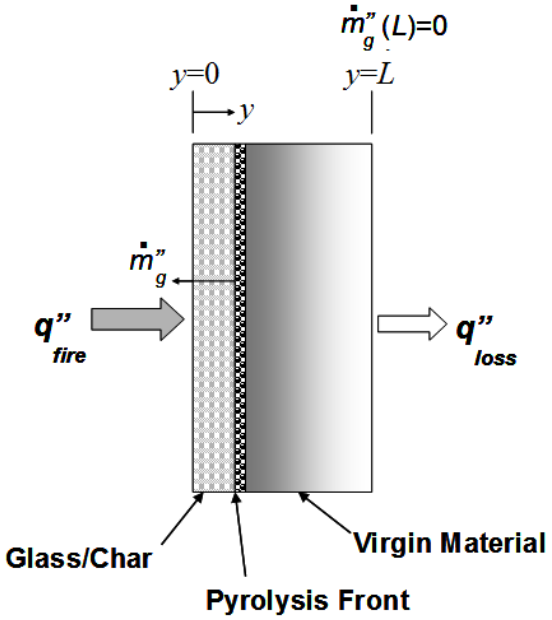

Figure 1. Pyrolysis model for a FRP laminate exposed to one-sided heating.

The thermal predictions from a pyrolysis model can be used to predict the structural response of a fire-exposed FRP laminate subjected to compressive loads. A compressively loaded laminate can experience one of several failure modes including global buckling, forced-response deflection, kinking, and delamination. The global buckling failure mode follows the Euler buckling formulation and occurs for a perfectly aligned laminate with no out-of-plane deflections. Forced-response deflection is failure due to excessive deflections of the laminate out of the plane of loading. Kinking, also referred to as local buckling, occurs when a localized portion of the laminate buckles, or kinks. Delamination occurs when the interlaminar forces are greater than the strength of the bond between the fiber plies causing the plies to separate, or

delaminate. The structural response and failure of FRP laminates may be predicted using structural properties calculated using the temperature profiles predicted by a pyrolysis model.

The predicted structural properties can be used in a variety of structural models to predict the response of a laminate to compressive loading conditions. These models range from simple compressively loaded column models to complex three-dimensional models created using commercially available finite element software. A complex three-dimensional model will provide the most accurate representation of laminate behavior; however, this scale of model has the greatest time requirement. A simple model, such as that based on a Euler buckling formulation for columns, will require the least amount of time but will also not be able to fully represent the behavior of the laminate. In a sense, a trade-off exists between the complexity and representative capabilities of a structural model and its time requirement. For the purposes of design, a compromise must be achieved between the complexity of a structural model and its ability to accurately represent the behavior of a compressively loaded laminate in fire conditions.

The focus of this research is the development of a simple thermo-structural model to predict the failure of fire-exposed FRP laminates under compressive load to aid in the design of naval structures. The model focuses on achieving a compromise between the complexity, and thereby time requirement, of the model and its ability to capture the behavior of intermediate and large-scale laminates at failure. The model is a thermal decomposition model coupled with a structural model. Intermediate-scale tests were performed and used to validate the model. In addition, test data was also used to develop design correlations for compressively loaded beams exposed to fire on one side.

Literature Review

This literature review provides an overview of work related to the thermo-structural modeling aspect of the research as well as the measurement of the structural response of composite laminates to one-sided heating. The modeling review includes previous work on related thermal pyrolysis models, structural models, as well as thermo-structural models.

There are numerous studies in the literature with the objective of developing pyrolysis models to predict the thermal response of FRP laminates in fire. A number of the pyrolysis models were integrated with mechanical models to predict the thermo-mechanical response of a compressively loaded FRP laminate in fire conditions. The thermo-mechanical models are generally divided into two distinct categories: micro-scale and macro-scale. The micro-scale models, referred to as thermo-mechanical models, are used to predict the laminate response for specific behaviors such as stresses due to pore formation or inter-ply delamination. The macro-scale models, referred to as thermo-structural models, are used to predict the global response of the laminate and predict the global structural failure of a compressively loaded FRP laminate in fire conditions. The focus of this research is to develop a coupled thermo-structural model for compressively loaded FRP laminates in fire conditions. The literature was reviewed for existing pyrolysis models, compressive strength models, and thermo-structural models for FRP laminates. The review highlights the implementation of the various models in predicting the thermal and thermo-structural response of compressively loaded FRP laminates in fire.

Pyrolysis models for predicting the thermal response of FRP laminates in fire originate in studies performed on the fire behavior of wood, most notably those by Kung [1], Kansa *et al.* [2], and Fredlund [3]. These models were developed to predict the thermal response of wood by analyzing the processes of transient conduction, pyrolysis, and internal convection of pyrolysis gases. Henderson, *et al.* [4] adapted the one-dimensional wood pyrolysis models for use with FRP laminates. Further developments by Henderson, *et al.* [5] expanded the capabilities of the model to include thermal expansion/contraction and material permeability and porosity. Henderson used the finite difference method to solve the set of simultaneous, coupled differential equations in both pyrolysis models. The measurement techniques used to obtain the necessary thermal properties for the pyrolysis models were described by Henderson *et al.* [6]. The measurement techniques used to obtain the thermal properties were investigated by Goodrich [7] and significant improvements were made in the measurement of the specific heat capacity, decomposition kinetics, permeability, and porosity. Chodak [8] further advanced the techniques used to determine the specific heat capacity and decomposition kinetics. Florio, *et al.* [9] found that the assumption of thermal equilibrium between solid material and pyrolysis gases in the models developed by Henderson causes lower predicted solid material temperatures. The pyrolysis models developed by Henderson are generally considered as the basis of a majority of subsequent pyrolysis models developed to predict the thermal response of decomposing FRP laminates.

Numerous one-dimensional pyrolysis models for FRP laminates have been developed based upon the models developed by Henderson, *et al.* [4-5]. These models further developed the pyrolysis models by including additional behaviors and/or solution methods. McManus and Springer [10] developed a finite-difference pyrolysis model to predict the thermo-mechanical response of FRP laminates including effects due to pore pressure rise, thermal expansion/contraction, and ablation of the material. The model was validated by showing good agreement between thermal predictions and test data for carbon-phenolic laminates [11]. Dimitrienko [12-13] developed a pyrolysis model to predict the thermo-mechanical response of a cylindrical FRP laminate with inclusion of pore pressure rise and thermal expansion/contraction. Predictions of the mechanical properties and strength of the material were compared with adequate agreement to experimental data; however, the thermal predictions were not explicitly validated. Gibson, *et al.* [14] developed a finite-difference pyrolysis model to investigate the thickness of a laminate in relation to burn-through in fire. The study arrived at the significant realization of the importance of the heat of decomposition and its impact on thermal predictions. The model was validated with good agreement with tests performed using a furnace following the hydrocarbon fire curve. Looyeh, *et al.* [15] developed a finite-element pyrolysis model for FRP laminates based on the model developed by Henderson, *et al.* [4], and does not include pore pressure or thermal expansions effects. The model was validated against furnace tests with good agreement. Bai, *et al.* [16-17] developed a finite-difference pyrolysis model which utilized new methods in representing the thermal properties, specifically the specific heat capacity. The model predictions were compared against experimental data with good results. Krysl [18] developed a finite-element pyrolysis model for FRP sandwich laminates considering no decomposition in the core. The model predictions showed adequate agreement with experimental data obtained from the literature for a single FRP laminate with constant material properties. This demonstrates that temperature dependent thermal properties are necessary for accurately predicting the thermal response of FRP laminates.

The pyrolysis models developed by Henderson, *et al.* [4-5] were also enhanced in subsequent pyrolysis models by extending thermal predictions into multiple dimensions and adding additional material behaviors. Sullivan and Salamon [19] developed a two-dimensional finite-element pyrolysis model to predict thermally-induced stresses. The model included the effects of pore pressure rise and thermal expansion/contraction. Predictions of thermally-induced stresses were compared against experimental data [20]; however, the thermal predictions were not explicitly validated. Milke and Vizzini [21] developed a three-dimensional pyrolysis model with arbitrary definition of the thermal boundary conditions designed to replicate realistic scenarios. The model was validated with good agreement between model predictions and experimental data. Wu and Katsube [22] developed a three-dimensional thermo-mechanical pyrolysis model to investigate the micro-scale behavior of the pores within the laminate considering no pyrolysis gas flow and the relationship between material decomposition and mechanical deformation. Restrained thermal growth and free thermal expansions tests were performed and compared to model predictions showing that pyrolysis gas flow may not be important to thermal predictions and pre-decomposition shrinkage is insignificant. Wu and Katsube [23-24] also developed a two-dimensional thermo-mechanical pyrolysis model to investigate the effects of moisture vaporization on the thermal response of FRP laminates. The model was verified by comparing predictions against the results of two thermal free expansion tests. Lua, *et al.* [25] developed a three-dimensional pyrolysis model which calculates the temperature and mass-dependent thermal properties at the woven-glass level. Laminate-level properties were then calculated and used to predict the thermal response of the laminate. The model predictions were validated against experimental data with good agreement.

Modeling of the structural response of compressively loaded FRP laminates in fire conditions requires knowledge of the degradation of the mechanical properties as a function of temperature. In all cases, elevated temperature data was taken for the mechanical properties and can be modeled using one of several curve-fitting techniques in the literature. Bausano, Boyd, and colleagues [26-27] used a Prony series to calculate the shear modulus for use in the Budianksy-Fleck compressive strength model. Kulcarni and Gibson [28] and Liu, *et al.* [29] used a polynomial expression to relate the mechanical properties of FRP laminates with temperature. Gibson, *et al.* [30] and Feih, *et al.* [31-32] used a tanh-function to represent the degradation of the mechanical properties with temperature and decomposition state of the laminate. The tanh-function was selected for use in calculating mechanical property degradation in this research because of its simplicity and dependence on the temperature and decomposition state of the material.

Numerous models exist in the literature to predict the thermo-structural response of compressively loaded FRP laminates in fire conditions. The models range in complexity from simply implemented analytical solutions to finite element simulations. The models also differ in their approach in integrating the thermal response of laminates exposed to fire. The models generally integrate the effect of fire exposure through either a pyrolysis model to predict the thermal response or through an assumption of the thermal response of the laminate. Obvious trade-offs exist in the models in terms of their complexity, accuracy, and time requirement. A more complex model, such as those developed using finite element analysis, will require considerably more time; however, predictions more accurately depict the thermo-structural response of laminates. Analytical models are generally simpler in their implementation and are

solved quickly; however, assumptions used in model development will restrict the ability of the model to accurately predict the thermo-structural response of FRP laminates in fire.

There are several analytical models published in the literature. Dao and Asaro [33] developed a thermo-structural model using simple beam theory to predict the structural response of FRP laminates. A three-dimensional heat conduction model which did not include material decomposition was used to predict the thermal response of the laminate. Dao and Asaro noticed that the laminate strength was focused at the unexposed surface and simplified the thermal predictions to a linear form for structural modeling. Asaro and colleagues [34-37] further developed this model by assuming a parabolic temperature profile to calculate the reduction in mechanical properties. The model predicts the structural response of the compressively loaded laminate through use of the Euler buckling equation. The model predictions were validated with reasonable agreement using experimental data for compressively loaded FRP laminates heated in a furnace [38]. Liu, *et al.* [29] developed a thermo-structural model with an assumed linear temperature gradient based on steady-state heat conduction in the laminate. Thermal effects were included in calculation of the structural response using a "thermal" moment and shift in neutral axis induced by non-uniform through-thickness mechanical properties. The mechanical properties were calculated using bulk analysis by smearing the ply properties through the laminate thickness. Kardamateos and colleagues [39-40] advanced the model developed by Liu, *et al.* [29], by integrating a pyrolysis model to predict the thermal response of FRP laminates. Temperature predictions were calculated at eight points through the laminate thickness and used to calculate the mechanical properties using a two-layer approach. In this approach, the mechanical properties are assumed to reduce to zero when material decomposition is 80% complete; however, the mechanical properties are calculated by interpolating the predicted temperatures through the remainder of the laminate. The two-layer approach coarsely approximates material decomposition and does not capture the effects of material decomposition on mechanical properties until material decomposition is 80% complete. Feih, *et al.* [31-32] developed a thermo-structural model that evaluates the failure of compressively loaded FRP laminates by bulk analysis. Temperature and material decomposition predictions from a pyrolysis model were used to calculate the bulk compressive strength of the laminate. Failure was predicted when the compressive strength was reduced to the applied stress. The model predictions were compared against experimental data with good agreement.

There are also several models available in the literature that are more complex in their approach to modeling the thermo-structural response of FRP laminates in fire. Gibson, *et al.* [30] developed a thermo-structural model using classical lamination theory (CLT) for compressively loaded FRP laminates. Temperatures and material decomposition were determined using a pyrolysis model. The model used progressive failure theory to predict laminate failure and was compared against experimental data with good agreement. Bausano, *et al.* [26] developed a thermo-structural model to evaluate the influence of viscoelasticity on FRP laminate failure. Commercially available finite element software (ANSYS) was used to calculate the transient thermal response of the laminate. The compressive strength of the laminate was calculated using the Budiansky-Fleck kinking failure model [41] with a temperature-dependent shear modulus. The compressive strength was used as the failure criterion in finite element and CLT analyses performed to predict failure of small-scale tests with reasonable agreement. Case and colleagues [27, 42-43] advanced prior work by Bausano, *et al.* [26] by introducing the time-temperature superposition principle to calculate the shear relaxation

modulus. A one-dimensional heat conduction model was used to predict the through-thickness temperature profile using surface temperature measurements as boundary conditions. CLT analysis was then used to calculate the stress state in each ply and the shear creep compliance and shear relaxation modulus were calculated. The average compressive strength through the laminate thickness was then calculated and compared to the applied compressive stress to determine laminate failure. The model was used to predict the failure of one-sided heat flux and isothermal compression tests with good agreement. Zhang, *et al.* [44] further advanced prior work by Case and colleagues [26-27, 42-43] by advancing the thermal model to a pyrolysis model similar to that developed by Henderson, *et al.* [5]. The thermo-structural model was incorporated in a three-dimensional finite element model developed in the commercially available finite element package, ABAQUS. The thermal predictions in the model were used to calculate the structural response of the compressively loaded FRP laminate in fire conditions. Model predictions were compared against experimental data with good agreement. Lua and colleagues [45-47] have developed a thermo-structural model using the LS-DYNA 3D finite element software package. The model used a one-dimensional pyrolysis model to predict the thermal response of FRP laminates to fire conditions. A multi-scale hybrid progressive damage model was developed to predict the structural response at the constituent, ply, and laminate levels. The predictive capabilities of the model have been demonstrated for a sandwich beam exposed to fire and subjected to compressive loading and three-point bending.

The aforementioned thermo-structural models require extensive experimental data sets for compressively loaded FRP laminates in fire conditions for validation; however, few studies have been performed to develop adequate data. Experimental data may also be used to characterize the behavior of FRP laminates at different scales for design purposes. Boyd, *et al.* [27] performed one-sided and isothermal tests at moderately low heat fluxes (5 to 20kW/m^2) on small-scale (25mm width and 50mm height), compressively loaded FRP laminates with fixed-fixed end conditions. Mouritz, *et al.* [48] performed one-sided heating tests for a wide range of heat fluxes (25 to 75kW/m^2) on small-scale (50mm width and 100mm height), compressively loaded FRP laminates. Lattimer, *et al.* [49] performed heated tests on intermediate-scale (710mm width by 910mm height), compressively loaded FRP laminates with fixed-pinned end conditions. The tests were performed using a furnace with exposures determined by the IMO A.754(18) [50] and UL 1709 [51] standard fire exposure time-temperature curves. Eric Greene Associates [52] performed intermediate-scale tests on compressively loaded FRP laminates according to ASTM E119 [53]. The laminates were compressively loaded in a fixed-pinned multi-axis loading frame and a furnace was used to heat the laminate following the ASTM E119 standard fire exposure time-temperature curve. A limited number of heated tests have been performed using a furnace for large-scale, compressively loaded FRP laminates [54].

Research Objectives

The focus of this research is the development of a thermo-structural model for compressively loaded FRP laminates in fire conditions. The focus of model development is achieving a compromise between the complexity of the model and its ability to capture the behavior of intermediate and large-scale FRP laminates in fire. Intermediate-scale tests were performed to develop an in-depth understanding of the structural response of FRP laminates and validate the thermo-structural model.

This research builds on existing studies to develop a thermo-structural model that predicts the thermal and structural response of compressively loaded FRP laminates in fire conditions. The thermal model was based on the previously developed one-dimensional pyrolysis models by Henderson, *et al.* [4] and Lattimer, *et al.* [55]. The mechanical properties were calculated using the predicted temperatures and material decomposition state using the tanh-function developed by Gibson, *et al.* [30]. The structural portion of the model was an analytical model developed based on the those by Liu, *et al.* [29] and Feih, *et al.* [31-32]. Liu, *et al.* [29] developed a methodology to predict the structural response of FRP laminates in fire by including thermal effects in the development of the governing equation. Feih, *et al.* [31-32] employed a compressive strength based failure criterion to determine the failure of compressively loaded FRP laminates in fire. The methodology to predict the structural response developed by Liu, *et al.*, was combined with the compressive strength failure criterion used by Feih, *et al.*, to develop the structural model in this research. The thermo-structural model used the thermal model to predict the temperatures and decomposition state through the laminate thickness and the structural model was used to predict the out-of-plane deflections and failure of FRP laminates in fire.

A series of intermediate-scale one-sided heating tests were performed on compressively loaded FRP laminates. An objective of these tests was to study the effect of scale on the failure mode a compressively loaded FRP laminate in fire conditions. The advantage of performing thermo-structural tests at an intermediate-scale is this scale gives an approximate representation of the mechanisms present in full-scale applications while reducing the complexity and time-requirement of performing large-scale tests. This makes it possible to use intermediate-scale tests to explore various parameters and their effects in full-scale applications of FRP laminates, such as naval structures. The intermediate-scale tests performed in this research included a parametric study to determine the effects of varying the laminate dimensions, loading conditions, and applied heating. The tests were analyzed to determine relationships between various parameters for use in design of structures using FRP laminates to withstand fire conditions. The tests were also used to validate the thermo-structural model.

CHAPTER 2 - Thermo-structural Model

Introduction

A thermo-structural model was developed to predict the structural failure of compressively loaded FRP laminates exposed to non-uniform, one-sided heating. The thermal portion of the model was developed as a one-dimensional heat and mass transfer model. The model predicts the temperature and decomposition response to one-sided heating for a decomposing material. The structural portion of the model analyzes the behavior of the compressively loaded laminate as a beam. The thermal model is integrated with the structural model to predict the change in mechanical properties of the laminate. An analytical solution is obtained for the case of non-uniform, one-sided heating of the laminate. Out-of-plane deflections and maximum combined stress due to axial compression and bending are calculated and compared to the compressive strength to determine laminate failure.

Thermal Model

A heat and mass transfer model was developed to predict the thermal response of fiber-reinforced polymer (FRP) laminates subjected to fire conditions. Of particular interest in this research is the thermal response of a decomposing FRP laminate subjected to one-sided heating. The physical behavior of a FRP laminate to one-sided heating is detailed in Figure 2. As heat is applied to the composite, the material will reach a temperature where the solid is converted into a gas. The decomposition of the virgin (solid) material occurs at the pyrolysis front and results in the formation of char and pyrolysis gases. After the decomposition is complete, the remaining material is a fiber/char matrix. The pyrolysis gases are transported toward the heated surface of the laminate through the fiber/char region. The pyrolysis gas transport within the laminate causes internal convection, cooling the material as it flows to the surface. This is an important effect that must be taken into account to accurately predict the thermal response of a decomposing material such as a FRP laminate. Numerous thermal models are available to predict the thermal response of a decomposing material including those by Henderson [4], Sullivan [19], McManus [10], Milke [21], and Gibson [14]. The heat and mass transfer model developed in this research was based on the one-dimensional pyrolysis model by Henderson [4] with further developments incorporated by Lattimer [55].

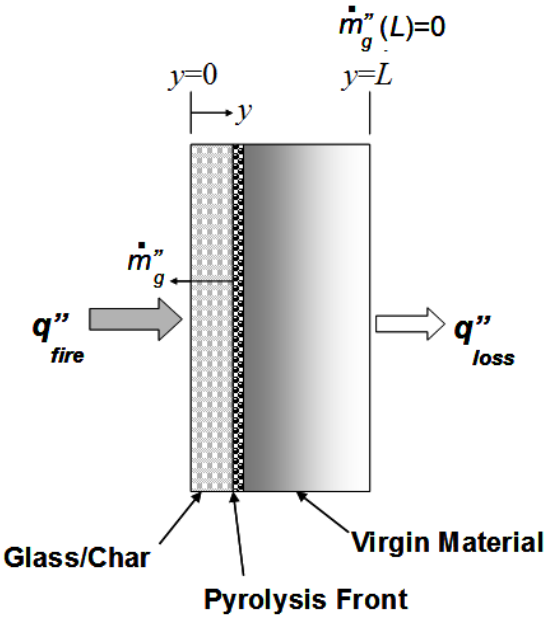

Figure 2. Decomposition of FRP laminate exposed to one-sided heating.

Key Assumptions

Several key assumptions were made to simplify the behavior of a decomposing material in the development of the heat and mass transfer model. These key assumptions are shown in Table 1. The combination of the first two assumptions, constant, uniform heating and insulated edges, reduces the thermal analysis of a decomposing material in fire conditions from three-dimensions to one-dimension. These assumptions also limit the temperature and mechanical property gradients solely to the through-thickness direction. The thermal analysis is further simplified by the third assumption which allows treatment of the material as a constant volume and, therefore, reduces the mass term to density. The fourth assumption infers no accumulation of pyrolysis gases in the solid material. As a result, no internal pressure accumulation occurs, allowing the permeability and porosity of the material to be ignored in the model development. The final assumption allows the pyrolysis gases and solid material to be treated as having the same temperature. This simplifies the thermal analysis in that no distinction must be made between the heating of the solid material and pyrolysis gases.

Table 1. Key assumptions for thermal model.

Number	Assumption
1	Constant, uniform heating over exposed surface
2	Insulated edges
3	No out-of-plane thermal expansion
4	Instantaneous, unidirectional flow of pyrolysis gases
5	Thermal equilibrium between pyrolysis gases and solid material

Governing Equations

Three governing equations were used to develop the thermal model. The governing equations are the energy equation, the model for the solid material decomposition, and the conservation of mass equation. To develop the governing energy and conservation of mass equations, first consider an infinitesimal control volume. A planar view of the control volume in the through-thickness direction is shown in Figure 3.

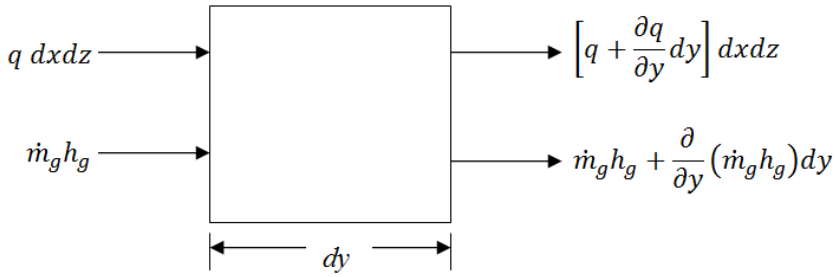

Figure 3. Control volume of a decomposing material.

The one-dimensional form of the energy equation is developed by considering the energy interactions at the boundaries of the given control volume. These include the energy transfer due to heat and mass flow. When considering these effects and performing an energy balance

$$\frac{\partial U}{\partial t} = -\frac{\partial q}{\partial y} dxdydz - \frac{\partial(\dot{m}_g h_g)}{\partial y} dy \qquad \text{Equation 1}$$

Applying Fourier's law for the heat flow in Equation 1 and rearranging

$$\frac{\partial U}{\partial t} + \frac{\partial(\dot{m}_g h_g)}{\partial y} dy = \frac{\partial}{\partial y}\left(k \frac{\partial T}{\partial y}\right) V \qquad \text{Equation 2}$$

where the thermal conductivity, k, is assumed to be dependent on temperature and therefore cannot be further simplified. For the solid material, the pressure does not change; therefore, the internal energy and enthalpy are equivalent. Applying this assumption, the one-dimensional form of the energy equation to be used for model development is obtained

$$\frac{\partial(mh + m_g h_g)}{\partial t} + \frac{\partial(\dot{m}_g h_g)}{\partial y} dy = \frac{\partial}{\partial y}\left(k \frac{\partial T}{\partial y}\right) V \qquad \text{Equation 3}$$

To account for the conservation of mass in the control volume, mass conversion from the solid material to the pyrolysis gases and mass flow due to internal convection must be considered. Performing a mass balance on the control volume shown in Figure 3

$$\frac{\partial(m + m_g)}{\partial t} = -\frac{\partial \dot{m}_g}{\partial y} dy \qquad \text{Equation 4}$$

Simplifying, this yields the general form of conservation of mass equation to be used for model development

$$\frac{\partial m_g}{\partial t} + \frac{\partial \dot{m}_g}{\partial y} dy = -\frac{\partial m}{\partial t} \qquad \text{Equation 5}$$

Energy Equation

The energy equation given in Equation 3 must be transposed into a useable form through application of some key assumptions and simplification through algebraic manipulation. Expanding the terms on the left hand side of the equation and applying the chain rule

$$m\frac{\partial h}{\partial t} + h\frac{\partial m}{\partial t} + m_g \frac{\partial h_g}{\partial t} + h_g \frac{\partial m_g}{\partial t} + \dot{m}_g \frac{\partial h_g}{\partial y} dy + h_g \frac{\partial \dot{m}_g}{\partial y} dy = \frac{\partial}{\partial y}\left(k \frac{\partial T}{\partial y} \right) V \qquad \text{Equation 6}$$

Noting the relationship between the enthalpy and temperature

$$\partial h = C \partial T \qquad \text{Equation 7}$$

Equation 6 may be simplified and rearranged into the following form

$$\left(mC + m_g C_g\right)\frac{\partial T}{\partial t} + h\frac{\partial m}{\partial t} + h_g\left(\frac{\partial m_g}{\partial t} + \frac{\partial \dot{m}_g}{\partial y} dy \right) + \dot{m}_g C_g \frac{\partial T}{\partial y} dy = \frac{\partial}{\partial y}\left(k \frac{\partial T}{\partial y} \right) V \qquad \text{Equation 8}$$

Applying mass conservation in the form of Equation 5 to the third term on the left hand side of Equation 8 reduces the equation to

$$\left(mC + m_g C_g\right)\frac{\partial T}{\partial t} + \left(h - h_g\right)\frac{\partial m}{\partial t} + \dot{m}_g C_g \frac{\partial T}{\partial y} dy = \frac{\partial}{\partial y}\left(k \frac{\partial T}{\partial y} \right) V \qquad \text{Equation 9}$$

The above equation is the mass form of the energy equation used in the thermal model. When considering a non-constant volume problem, such as that with out-of-plane thermal expansion, this form of the energy equation would be used. However, out-of-plane thermal expansion is not considered in this research; therefore, the mass form of the energy equation may be further reduced by assuming a constant volume during heating.

Applying the no out-of-plane thermal expansion assumption (constant volume) to reduce the mass form of the energy equation by dividing through by the volume results in

$$\rho\left(C + \frac{\left(m_g / V\right)}{\rho} C_g \right)\frac{\partial T}{\partial t} + \left(h - h_g\right)\frac{\partial \rho}{\partial t} + \dot{m}''_g C_g \frac{\partial T}{\partial y} = \frac{\partial}{\partial y}\left(k \frac{\partial T}{\partial y} \right) \qquad \text{Equation 10}$$

The specific heat capacity term in parentheses in the first term on the left hand side represents the specific heat capacity of the solid material and the pyrolysis gases in the volume of the voids within the solid material. The mass of pyrolysis gas in this term represents the mass of pyrolysis gases contained in the voids of the solid. The volume term, V, contained within the parentheses is the volume of the solid material being considered and is not equivalent to the void volume. Therefore, the mass of pyrolysis gases cannot be reduced to a density and (m_g/V) is not equal to the density of the pyrolysis gases.

To understand the first term in Equation 10, we must consider the measurement technique used for the specific heat capacity of the solid material to be investigated via the thermal model. When measuring the specific heat capacity of the degraded material, the voids are present within the solid material and are filled with a gas. The type of gas in the voids depends on the state of the material and the measurement technique. Therefore, the measured specific heat capacity for the degraded material includes the volume voids filled with a gas and may be represented as follows

$$C \approx \left(C + \frac{\left(m_g / V\right)}{\rho} C_g \right) \qquad \text{Equation 11}$$

This is not an exact representation of the specific heat capacity because the air/nitrogen contained in the voids during measurement does not have the same mass or specific heat capacity of the pyrolysis gases. However, in this research, they are considered to be equal for simplification purposes.

Inserting Equation 11 into the form of the energy equation in Equation 10, results in the final form of the energy equation to be used in development of the thermal model

$$\rho C \frac{\partial T}{\partial t} + \left(h - h_g\right) \frac{\partial \rho}{\partial t} + \dot{m}_g'' C_g \frac{\partial T}{\partial y} = \frac{\partial}{\partial y} \left(k \frac{\partial T}{\partial y} \right) \qquad \text{Equation 12}$$

In the above equation, the enthalpies are defined as

$$h = Q + \int_{T_{ref}}^{T} C dT \qquad \text{Equation 13}$$

$$h_g = \int_{T_{ref}}^{T} C_g dT \qquad \text{Equation 14}$$

where the heat of decomposition, Q, is defined as negative for an endothermic process. The thermal properties, k, C, and C_g, are defined as dependent on both material temperature and decomposition state. The first term in the energy equation in the form of Equation 12, represents the time-temperature response of the material, the second term represents the energy required to decompose the solid material, the third term represents the internal convection due to the flow of pyrolysis gases, and the term on the right hand side of the energy equation represents heat conduction through the thickness of the material.

Model for Solid Material Decomposition

The model for solid material decomposition calculates the change in mass with time of the solid material. However, in application to the thermal model the mass may be reduced to a density due to the assumption of no out-of-plane thermal expansion, as shown previously. Therefore, in the case considered in this research, the model for solid material decomposition calculates the change in density with time. This term appears in the second term of the energy equation in Equation 12.

The approach chosen for calculating the change in density with time is an *n*th order Arrhenius decomposition kinetics equation. This expression may be used to correlate the mass loss rate data for degrading materials at different heating rates [56]. The chosen *n*th order Arrhenius decomposition kinetics equation is

$$\frac{\partial M}{\partial t} = \left[1 - M\right]^n A \exp\left(\frac{-E_a}{RT}\right) \qquad \text{Equation 15}$$

where M is a function selected to best fit the decomposition behavior of the data to be analyzed. The function selected for application of Equation 15 is that selected previously by Flynn and Wall [57] and Cunningham and McManus [58].

$$\left(1 - M\right) = \left[\frac{m - m_d}{m_v - m_d}\right] \qquad \text{Equation 16}$$

Applying the assumption of no out-of-plane thermal expansion and, therefore, assuming a constant volume, the above equation is reduced to

$$F = \left(1 - M\right) = \left[\frac{\rho - \rho_d}{\rho_v - \rho_d}\right] \qquad \text{Equation 17}$$

Applying the function from Equation 17 to Equation 15 results in the following Arrhenius rate expression, which is used to model the solid material decomposition,

$$\frac{\partial \rho}{\partial t} = -\left(\rho_v - \rho_d\right)\left[\frac{\rho - \rho_d}{\rho_v - \rho_d}\right]^n A \exp\left(\frac{-E_a}{RT}\right) \qquad \text{Equation 18}$$

The function in Equation 17 is advantageous for use in modeling the solid material decomposition because it scales the results of the rate equation based on the fraction of material involved in the decomposition process (active material). Therefore, results of the function are scaled from zero to unity based on the relative decomposed state of the material. The function in Equation 17, also known as the instantaneous mass fraction, or F, is also used to calculate bulk thermal properties.

Conservation of Mass Equation

The conservation of mass equation derived in Equation 5 is used to determine the mass flux of pyrolysis gases through the thickness of the material. The mass flux of pyrolysis gases is of particular interest at the heated surface when considering one-sided heating of the material. At the heated surface, the mass flux of pyrolysis gases is equivalent to the mass loss rate of the material. First, the conservation of mass equation, Equation 5, was rearranged as follows

$$\frac{\partial \dot{m}_g}{\partial y}\delta y = -\frac{\partial\left(m + m_g\right)}{\partial t} \qquad \text{Equation 19}$$

Assuming the mass of the solid material is much larger than that of the pyrolysis gases and the volume remains constant due to no out-of-plane thermal expansion, the equation is further reduced

$$\frac{\partial \dot{m}''_g}{\partial y}\delta y = -\frac{\partial \rho}{\partial t} \qquad \text{Equation 20}$$

The mass loss rate may be determined at any point within the material by integrating the expression in Equation 20 from a location within the material (y') to the unheated surface (l)

$$\dot{m}''_g\left(l,t\right) - \dot{m}''_g\left(y',t\right) = -\int_{y'}^{l}\frac{\partial \rho}{\partial t} \qquad \text{Equation 21}$$

The pyrolysis gases are assumed to all instantaneously flow to the heated surface and the mass flux at the unheated surface (l) is assumed to be zero. Applying these assumptions, the above equation is reduced to

$$\dot{m}''_g\left(y',t\right) = \int_{y'}^{l}\frac{\partial \rho}{\partial t} \qquad \text{Equation 22}$$

where the density change with time term is solved directly as a function of time through the material thickness using Arrhenius kinetics. The combination of the model for solid material decomposition, Equation 18, and the conservation of mass equation, Equation 22, allows the calculation of the mass flux within the material. The mass flux of pyrolysis gases within the material is also needed in calculation of the energy equation, Equation 12, in the internal convection term.

Boundary Conditions

Particular attention was paid to one-sided heating of the material in this research. In this case, the material was exposed to a heat source at one surface and either insulated on the unheated surface or left exposed to environmental conditions. Due to this application, the

boundary conditions, although general in nature, were tailored to the one-sided heating case. The boundary conditions are defined at both the heated (y=0) and unheated surfaces (y=l).

The boundary conditions considered in the thermal model are listed in Table 2. The Dirchlet boundary condition simply allows definition of the surface temperature. The Neumann boundary condition defines an incident heat flux to the material at the surface with no other heating or thermal interactions with the environment. The Robin boundary condition defines a heat flux incident with the material surface with heat interactions in the forms of convective heat transfer and radiation.

Table 2. Boundary conditions for thermal model.

Name	Heat Interactions Considered
Dirchlet	Temperature
Neumann	Heat flux
Robin	Heat flux, convection, and radiation

Considering a one-sided heating case, specifically that involving fire conditions, the boundary condition is best defined using the Robin boundary condition. In this case, experimental efforts will likely employ a heat flux gauge to measure the total heat flux to the material. However, the measured heat flux from the water-cooled heat flux gauge will be different than that of the heat flux to the material. This is due to differences in the surface temperature of the heat flux gauge and material. To account for this difference, a relationship must be developed between the total heat flux as measured by a heat flux gauge and that experienced by the material.

The total heat flux for both the material and the water-cooled heat flux gauge are defined similarly

$$q_s'' = \varepsilon_s q_{rad}'' - \varepsilon_s \sigma T_s^4 + h_{conv}\left(T_\infty - T_s\right) \quad \text{Equation 23}$$

$$q_{hfg}'' = \varepsilon_{hfg} q_{rad}'' - \varepsilon_{hfg} \sigma T_{hfg}^4 + h_{conv}\left(T_\infty - T_{hfg}\right) \quad \text{Equation 24}$$

where Equation 23 is the total heat flux at the material surface and Equation 24 is the total heat flux measured by the water-cooled heat flux gauge. Solving Equation 24 for the radiation heat flux in the second term and inserting into Equation 23 results in

$$q_s'' = \frac{\varepsilon_s}{\varepsilon_{hfg}}\left[q_{rad}'' + \varepsilon_{hfg}\sigma T_{hfg}^4 - h_{conv}\left(T_\infty - T_{hfg}\right)\right] - \varepsilon_s \sigma T_s^4 + h_{conv}\left(T_\infty - T_s\right) \quad \text{Equation 25}$$

Simplifying the above expression and assuming that the emissivity of the material and heat flux gauge are identical results in

$$q_s'' = q_{hfg}'' + \varepsilon_s \sigma\left(T_{hfg}^4 - T_s^4\right) + h_{conv}\left(T_{hfg} - T_s\right) \quad \text{Equation 26}$$

This expression relates the total heat flux measured by the water-cooled heat flux gauge to the total heat flux at the heated surface of the material. Implementing the above expression, the total heat flux as measured by the heat flux gauge is inserted as the second term. The water-cooled heat flux gauge temperature, T_{hfg}, may be approximated as the temperature of the cooling water.

Thermal Properties

The thermal property definitions used in the thermal model define each respective property as a function of temperature and material decomposition state. This requires definition of the various thermal properties of the material in terms of temperature and decomposition state. Prior to the onset of material decomposition, the thermal properties will be solely a function of the virgin material. However, as the material decomposes fully the thermal property is that of the decomposed (char) material.

A given thermal property is determined in the thermal model by collecting data on the property as function of temperature for both the virgin and char material. The thermal properties are assumed to be a function of the fraction of virgin and decomposed material [4], defined as the instantaneous mass fraction in Equation 17. Using this function as a progress variable, the thermal conductivity and specific heat capacity are related to the decomposed state of the material

$$k = Fk_v + (1 - F)k_d \qquad \text{Equation 27}$$

$$C = FC_v + (1 - F)C_d \qquad \text{Equation 28}$$

The thermal conductivity and specific heat capacity of the virgin and decomposed material may also vary with temperature.

Thermal Model Implementation

The thermal model for a decomposing material was implemented using the mathematical toolbox, MATLAB. The finite element method was chosen to calculate the transient thermal response of a decomposing material using the governing equations. The energy equation is solved to determine the transient temperatures through the thickness of the material. The solid material decomposition model then uses the calculated temperatures to calculate the change in density of the material with time. Finally, the conservation of mass equation is used to calculate the mass flux of pyrolysis gases in the material. This solution sequence is performed iteratively for a given time step until the solution converges in temperature. This process is repeated for the defined duration of the thermal model.

The finite element method was chosen to solve the system of governing differential equations. Several finite element approaches were considered for representing the governing equations. These representations are the Rayleigh-Ritz method and Galerkin method. Both are methods of weighted residuals and each method has its advantages and disadvantages. The Rayleigh-Ritz method is desirable because it allows development of a full mathematical theory

for approximation and convergence. However, this method is difficult to implement for complex fluid flows and heat transfer. The Galerkin method provides a platform which essentially guarantees a procedure to integrate the differential equations and is simple to implement. For these reasons, the Galerkin method of weight residuals was chosen in this research.

The Galerkin method of weighted residuals was implemented using Pepper and Heinrich as a reference [59]. The weak formulation of the method of weighted residuals was used. This limits the weighted expression to first derivatives of the solution. The objective of the Galerkin method is to reduce the residuals of the differential equations to zero. To accomplish this, a function is chosen to approximate the solution, in this case temperature, and satisfy the boundary conditions, such as

$$T(y) = \sum_{i=1}^{n+1} a_i W_i(y) \qquad \text{Equation 29}$$

where a_i represents the unknown parameters. In general, the exact solution of the differential equation cannot be obtained using this function. Therefore, the approximate solution must be placed in the equation. To accomplish this, a residual function is defined as the error associated with the approximate solution

$$R(T, y) \equiv f(T, y) \qquad \text{Equation 30}$$

where, in this case, T is the unknown parameter and represents the approximation to the exact solution, T^*. If the exact solution, T^*, is considered, the result of the residual function is

$$R(T^*, y) \equiv 0 \qquad \text{Equation 31}$$

However, it is not possible to simply force the residual of the approximate solution to vanish to zero at all points. In the weighted residual method, the residual function is multiplied by a weighting function. The integral of the weighted expression is then forced to vanish

$$\int_0^l W(y) R(T, y) dy = 0 \qquad \text{Equation 32}$$

This generates a system of linear equations in temperature that will determine an approximate solution using Equation 29. The system of linear equations will satisfy the differential equation in an average sense.

The choice of weighting function depends on the finite element technique selected. In the case of the Galerkin form, the weighting functions are the finite element basis functions, or shape functions. The shape functions are defined over each element in the domain. For a one-dimensional domain, an element is defined over the region

$$element : \left\{ y \middle| y_i \le y \le y_{i+1} \right\} \qquad i = 1,2,\ldots,n_{elem} \qquad \text{Equation 33}$$

where n_{elem} is the total number of elements in the domain. In this research, linear shape functions are used. In this case, the end points of the element, y_i and y_{i+1}, are defined as the nodes. The linear shape functions are defined as

$$N_i^{(e)}(y) = \frac{y_{i+1} - y}{h^{(e)}} \quad \text{Equation 34}$$

$$N_{i+1}^{(e)}(y) = \frac{y - y_i}{h^{(e)}} \quad \text{Equation 35}$$

and are shown in Figure 4. Placing the above shape functions in the form of Equation 29, the approximate solution for temperature in a single element may be calculated in the following manner

$$T^{(e)}(y) = N_i^{(e)}(y)T_i^{(e)} + N_{i+1}^{(e)}(y)T_{i+1}^{(e)} \quad \text{Equation 36}$$

where the temperatures T_i and T_{i+1} are calculated at the nodes of the element. The temperature at any point through the element is calculated using the shape functions and the nodal temperatures.

To simplify the implementation of the linear shape functions in discretizing the governing differential equations, the shape functions were transformed from the local coordinate system to a natural coordinate system. The elemental natural coordinate system, shown in Figure 4, is defined on the interval $-1 \le \xi \le 1$. The local coordinate system is transformed to the natural coordinate system using the following transformation

$$y = \frac{1}{2}(1-\xi)y_i + \frac{1}{2}(1+\xi)y_{i+1} \quad \text{Equation 37}$$

which maps the interval $-1 \le \xi \le 1$ into the interval $y_i \le y \le y_{i+1}$ in the local coordinate system of the element. The linear shape functions for the natural coordinate system are defined as

$$N_i^{(e)}(\xi) = \frac{1}{2}(1-\xi) \quad \text{Equation 38}$$

$$N_{i+1}^{(e)}(\xi) = \frac{1}{2}(1+\xi) \quad \text{Equation 39}$$

The natural coordinate system allows the products and derivatives of the shape functions to be easily evaluated. This is accomplished by transforming the local coordinate system integration terms to the natural coordinate system

$$\frac{d}{dy} = \frac{d}{d\xi}\frac{d\xi}{dy} = \frac{2}{h^{(e)}}\frac{d}{d\xi} \quad \text{Equation 40}$$

$$dy = \frac{h^{(e)}}{2}d\xi \quad \text{Equation 41}$$

This form of the integration terms simplifies the integration bounds for the integral form of the weighted residual in Equation 32 from y_i to y_{i+1} to -1 to 1. This simplifies the mathematical expression and provides an easier form of the integral for computation.

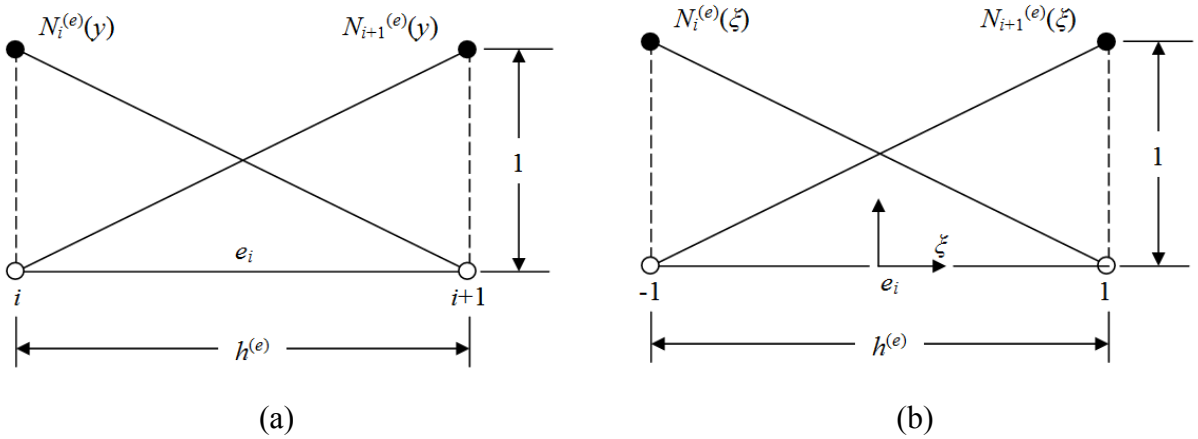

(a) (b)

Figure 4. Linear shape functions in (a) local coordinate system and (b) natural coordinate system.

Energy Equation Spatial Discretization

The energy equation, Equation 12, was spatially discretized using the Galerkin method of weighted residuals. The remaining governing equations, the model for solid material decomposition and conservation of mass equation, do not require spatial discretization. Density is the only parameter dependent on space in both equations. The spatial variation of density is directly a function of temperature and, due to the spatial discretization of temperature in the energy equation, both equations do not have to be spatially discretized. The energy equation is spatially discretized to generate an approximate solution for temperature using the integral form of the weighted residual expression.

In order to spatially discretize the energy equation, the parameters must be defined as either consistent or lumped. Consistent parameters are defined on a nodal basis and vary through the element according to the shape functions. Lumped parameters are defined on an elemental basis.

Table 3 provides a list of lumped and consistent parameters for the energy equation. The density was defined as a consistent parameter due to its use in the density change with time term in the energy equation. The mass flux of pyrolysis gases was defined as a consistent parameter because it is directly calculated from the density and, therefore, dependent on the density. The remainder of the parameters are defined as lumped.

Table 3. Lumped and consistent parameters in energy equation.

Symbol	Parameter	Lumped or Consistent?
ρ	Density	Consistent
$\dot{m}_g''$	Mass flux of pyrolysis gases	Consistent
C	Specific heat capacity of solid material	Lumped
h	Enthalpy of solid material	Lumped
h_g	Enthalpy of pyrolysis gases	Lumped
C_g	Specific heat capacity of pyrolysis gases	Lumped
k	Thermal conductivity	Lumped

To discretize the energy equation, we must first define the residual form of the energy equation in Equation 12. The residual form of the energy equation is defined as

$$R(T,y,t) = \rho C \frac{\partial T}{\partial t} + \left(h - h_g\right)\frac{\partial \rho}{\partial t} + \dot{m}_g'' C_g \frac{\partial T}{\partial y} - \frac{\partial}{\partial y}\left(k \frac{\partial T}{\partial y}\right) \qquad \text{Equation 42}$$

where the unknown parameter is temperature, T, and is a function of both time and space. The function then must be defined to approximate the solution for temperature. This is accomplished using the finite element expansion for the approximate solution

$$T(y,t) = \sum_{j=1}^{n_{elem}+1} N_j(y) T_j(t) \qquad \text{Equation 43}$$

where the temperature is reduced to be solely a function of time. The approximate solution in Equation 43 is also applied to the consistent parameters because of their variation through an element. In discretizing the residual form of the energy equation, each term in the expression is multiplied by the weighting function. In accordance with the Galerkin method, the weighting functions are the linear shape functions. Integrating the weighted residual expression over the domain

$$R(T,y,t) = \int_0^l W(y)\left(\rho C \frac{\partial T}{\partial t} + \left(h - h_g\right)\frac{\partial \rho}{\partial t} + \dot{m}_g'' C_g \frac{\partial T}{\partial y} - \frac{\partial}{\partial y}\left(k \frac{\partial T}{\partial y}\right)\right) dy \qquad \text{Equation 44}$$

The solution to Equation 44 over the entire domain, zero to l, nominally requires the use of many elements. In the following section, the spatial discretization of a single element is described for each individual term in the equation. To apply this discretization over the domain, one must consider many elements connected at their respective nodes, defined as the 'i' and 'j' nodes for an individual element. At these nodes, the approximate solution to the temperature is calculated. Therefore, over the domain, there will be many nodes and many temperatures that the integral of the weighted residual expression must be solved.

The first term in the energy equation is the material time-temperature response term. The density and specific heat capacity of the material are consistent and lumped parameters, respectively. The residual expression in the form of Equation 32 for the material time-temperature response term is

$$\{R^e\} = \int_{y_i}^{y_j} W(y)\left(\rho C \frac{\partial T}{\partial t}\right) dy \qquad \text{Equation 45}$$

Replacing the weighting functions by the shape functions, applying the approximate solution, and transforming to matrix notation

$$\{R^e\} = \int_{y_i}^{y_j} C\begin{bmatrix} N_i \\ N_j \end{bmatrix}\left(\begin{bmatrix} N_i & N_j \end{bmatrix}\begin{Bmatrix} \rho_i \\ \rho_j \end{Bmatrix}\begin{bmatrix} N_i & N_j \end{bmatrix}\begin{Bmatrix} \frac{\partial T_i}{\partial t} \\ \frac{\partial T_j}{\partial t} \end{Bmatrix}\right) dy \qquad \text{Equation 46}$$

The specific heat capacity is defined as a lumped parameter and is constant over the element and, therefore, can be removed from the integral. The integration is transformed from the local coordinate system to the natural coordinate system. Performing the coordinate system transformation and condensing the matrix notation

$$\{R^e\} = C\frac{h^{(e)}}{2}\int_{-1}^{1}[N]^T\left([N]\{\rho\}[N]\left\{\frac{\partial T}{\partial t}\right\}\right)d\xi \qquad \text{Equation 47}$$

Integrating the above expression we obtain the final residual expression for the time-temperature response term

$$\{R^e\} = \frac{h^{(e)}C}{12}\begin{bmatrix} 3\rho_i + \rho_j & \rho_i + \rho_j \\ \rho_i + \rho_j & \rho_i + 3\rho_j \end{bmatrix}\begin{Bmatrix} \frac{\partial T_i}{\partial t} \\ \frac{\partial T_j}{\partial t} \end{Bmatrix} \qquad \text{Equation 48}$$

The second term spatially discretized in the energy equation is the term representing the energy required to decompose the solid material. The density and enthalpies are consistent and lumped parameters, respectively. The residual expression in the form of Equation 32 for the second term is

$$\{R^e\} = \int_{y_i}^{y_j} W(y)\left((h - h_g)\frac{\partial \rho}{\partial t}\right) dy \qquad \text{Equation 49}$$

The above expression is simplified by transforming the integral to the natural coordinate system. Performing the transformation and replacing the weighting functions with the linear shape functions

$$\{R^e\} = (h - h_g)\frac{h^{(e)}}{2}\int_{-1}^{1}[N]^T[N]\left\{\frac{\partial \rho}{\partial t}\right\}d\xi \qquad \text{Equation 50}$$

Integrating the above expression we obtain the final residual expression for the second term in the energy equation

$$\{R^e\} = \frac{(h - h_g)h^{(e)}}{6}\begin{bmatrix} 2 & 1 \\ 1 & 2 \end{bmatrix}\begin{Bmatrix} \frac{\partial \rho_i}{\partial t} \\ \frac{\partial \rho_j}{\partial t} \end{Bmatrix} \qquad \text{Equation 51}$$

The third term spatially discretized in the energy equation is the term representing internal convection of the pyrolysis gases. The mass flux of pyrolysis gases and specific heat capacity of pyrolysis gases are consistent and lumped parameters, respectively. The residual expression in the form of Equation 32 for the internal convection term is

$$\{R^e\} = \int_{y_i}^{y_j} W(y)\left(\dot{m}_g'' C_g \frac{\partial T}{\partial y}\right)dy \qquad \text{Equation 52}$$

The temperature change term in the above expression is replaced by an equivalent group of terms where the temperature change with distance is represented by the derivative of the linear shape functions. Transforming the expression to the natural coordinate system

$$\{R^e\} = C_g \int_{-1}^{1} [N]^T \left([N]\{\dot{m}_g''\}\left[\frac{dN}{d\xi}\right]\{T\}\right)d\xi \qquad \text{Equation 53}$$

Integrating the above expression we obtain the final residual expression for the internal convection term in the energy equation

$$\{R^e\} = \frac{C_g}{6}\begin{bmatrix} -(2\dot{m}_{g,i}'' + \dot{m}_{g,j}'') & 2\dot{m}_{g,i}'' + \dot{m}_{g,j}'' \\ -(\dot{m}_{g,i}'' + 2\dot{m}_{g,j}'') & \dot{m}_{g,i}'' + 2\dot{m}_{g,j}'' \end{bmatrix}\begin{Bmatrix} T_i \\ T_j \end{Bmatrix} \qquad \text{Equation 54}$$

The fourth term spatially discretized in the energy equation is the heat conduction term. The residual expression in the form of Equation 32 for the heat conduction term is

$$\{R^e\} = -\int_{y_i}^{y_j} W(y)\left(\frac{\partial}{\partial y}\left(k\frac{\partial T}{\partial y}\right)\right)dy \qquad \text{Equation 55}$$

The weighted residual expression contains a second order derivative. However, the use of the weak form in the finite element approach forces use of only first order derivatives. Therefore, the above expression must be reduced using the chain rule

$$\{R^e\} = \int_{y_i}^{y_j}\left(\frac{\partial W(y)}{\partial y}k\frac{\partial T}{\partial y} + W(y)\frac{\partial}{\partial y}\left(k\frac{\partial T}{\partial y}\right)\right)dy \qquad \text{Equation 56}$$

Integrating the second term results in

$$\{R^e\} = \int_{y_i}^{y_j} \left(\frac{\partial W(y)}{\partial y} k \frac{\partial T}{\partial y} \right) dy + W(y) \left(k \frac{\partial T}{\partial y} \right)_{y_i}^{y_j} \qquad \text{Equation 57}$$

where the second term is related to the heat flux at boundaries (y=0 and y=l) of the domain via Fourier's law. Transforming the expression to the natural coordinate system and replacing the weighting functions by the shape functions

$$\{R^e\} = \int_{-1}^{1} [N]^T \left(\left[\frac{dN}{d\xi} \right]^T k \left[\frac{dN}{d\xi} \right] \{T\} \right) d\xi + [N]^T (-q'')_{y=0}^{y=L} \qquad \text{Equation 58}$$

Integrating the above expression we obtain the final residual expression for the conduction term in the energy equation

$$\{R^e\} = \frac{k}{h^{(e)}} \begin{bmatrix} 1 & -1 \\ -1 & 1 \end{bmatrix} \begin{Bmatrix} T_i \\ T_j \end{Bmatrix} + \begin{Bmatrix} q''_{y=0} \\ -q''_{y=L} \end{Bmatrix} \qquad \text{Equation 59}$$

where the heat fluxes are defined only at the boundaries of the domain.

Governing Equation Time Discretization

The governing equations are discretized with time to obtain the transient solution. The time discretization is performed for the temperature in the energy equation and the density in the solid material decomposition model. Time discretization for temperature and density using a linear approximation results in

$$\left\{ \frac{\partial T}{\partial t} \right\} = \frac{\{T_{n+1}\} - \{T_n\}}{\Delta t} \qquad \text{Equation 60}$$

$$\left\{ \frac{\partial \rho}{\partial t} \right\} = \frac{\{\rho_{n+1}\} - \{\rho_n\}}{\Delta t} \qquad \text{Equation 61}$$

A relaxation parameter is used to vary the solution technique in calculating the transient solution. The role of the relaxation parameter is to control the stability and accuracy of the solution algorithm. In the case of a general time-dependent function, the relaxation parameter is applied at the current, n, and next, n+1, time steps

$$f(y,t) = \eta f(y,t_{n+1}) + (1-\eta) f(y,t_n) \qquad \text{Equation 62}$$

The relaxation parameter can be varied between zero and unity. Three relaxation parameter definitions were considered in this research and are listed in Table 1. Defining the relaxation parameter as forward explicit provides the fastest solution technique; however, the explicit scheme is unstable and requires small time steps. The centered implicit technique is slightly less efficient than the explicit technique in terms of computation time but is more stable. The

backwards implicit solution technique was chosen as the relaxation parameter for the transient solution technique in this research. Despite being the slowest in terms of computation time, it is the most stable transient solution technique.

Table 4. List of relaxation parameter values.

Relaxation Parameter Value	Parameter Description
0	Backwards implicit
½	Centered implicit (Crank-Nicolson-Galerkin)
1	Forward explicit (Euler)

The time discretization of the energy equation treats temperature as the only time-varying parameter in the equation. However, the applied heat fluxes, also referred to as the thermal loads, have a direct impact on the transient temperature solution. This entails the treatment of these in a similar manner to temperature. It would be inappropriate to discretize the thermal loads with time because it is an input and not a solution. Applying a relaxation parameter to the thermal loads would appropriately represent the time-dependent behavior of the thermal loads. To discretize the energy equation, the temperature variables are first grouped in the spatially discretized energy equation

$$[M]\left\{\frac{\partial T}{\partial t}\right\}+\left([K_c]+[K_g]\right)\{T\}+[K_d]\left\{\frac{\partial \rho}{\partial t}\right\}-\{L\}=0 \qquad \text{Equation 63}$$

where $[M]$ is the capacitance matrix, $[K_c]$ the thermal conductivity matrix, $[K_g]$ the pyrolysis gas convection matrix, $[K_d]$ the decomposition energy matrix, and $\{L\}$ the thermal load vector. In components, these matrices are

$$M_{ij}=\frac{h^{(e)}C}{12}\begin{bmatrix}3\rho_i+\rho_j & \rho_i+\rho_j\\ \rho_i+\rho_j & \rho_i+3\rho_j\end{bmatrix} \qquad \text{Equation 64}$$

$$K_{c,ij}=\frac{k}{h^{(e)}}\begin{bmatrix}1 & -1\\ -1 & 1\end{bmatrix} \qquad \text{Equation 65}$$

$$K_{g,ij}=\frac{C_g}{6}\begin{bmatrix}-\left(2\dot{m}''_{g,i}+\dot{m}''_{g,j}\right) & 2\dot{m}''_{g,i}+\dot{m}''_{g,j}\\ -\left(\dot{m}''_{g,i}+2\dot{m}''_{g,j}\right) & \dot{m}''_{g,i}+2\dot{m}''_{g,j}\end{bmatrix} \qquad \text{Equation 66}$$

$$K_{d,ij}=\frac{\left(h-h_g\right)h^{(e)}}{6}\begin{bmatrix}2 & 1\\ 1 & 2\end{bmatrix} \qquad \text{Equation 67}$$

$$\{L\}=\begin{Bmatrix}q''_{y=0}\\ -q''_{y=L}\end{Bmatrix} \qquad \text{Equation 68}$$

Applying time discretization and relaxation parameters for the temperature and thermal load vectors to Equation 63 results in

$$[M]\frac{\{T_{n+1}\}-\{T_n\}}{\Delta t}+\left([K_c]+[K_g]\right)\left(\eta\{T_{n+1}\}+(1-\eta)\{T_n\}\right)+[K_d]\left\{\frac{\partial\rho}{\partial t}\right\} \qquad \text{Equation 69}$$
$$-\left(\eta\{L_{n+1}\}+(1-\eta)\{L_n\}\right)=0$$

Grouping terms in the equation to solve for the temperatures at the next time step, n+1, results in the final expression for the energy equation

$$\left([M]+\eta\Delta t\left([K_c]+[K_g]\right)\right)\{T_{n+1}\}=\left([M]-(1-\eta)\Delta t\left([K_c]+[K_g]\right)\right)\{T_n\} \qquad \text{Equation 70}$$
$$+\left(\eta\Delta t\{L_{n+1}\}+(1-\eta)\Delta t\{L_n\}-[K_d]\left\{\frac{\partial\rho}{\partial t}\right\}\right)$$

This is the form of the equation implemented in the thermal model to solve for the transient, spatial solution for temperature for a decomposing material. Specifically, the thermal model will solve at each time step for the temperatures at the next time step at all defined nodes through the thickness using the current temperatures and various elemental matrices and thermal loads.

The time discretization of the solid material decomposition model treats the density as the only time-varying parameter in the equation. The solid material mass is calculated as a function of temperature using Equation 18. The temperatures, $\{T_{n+1}\}$, are calculated at the next time step using the time and spatial discretization in Equation 70. These temperatures are then used to calculate the change in density with time using the solid material decomposition model. The next time step density, $\{\rho_{n+1}\}$, is then calculated in the following manner

$$\{\rho_{n+1}\}=\{\rho_n\}+\left\{\frac{\partial\rho}{\partial t}\right\}\Delta t \qquad \text{Equation 71}$$

where $\{\rho_n\}$ is the density from the current time step. This is the form of the equation implemented in the thermal model to calculate the density at the next time step using the solid material decomposition model and current time step density at all defined nodes through the material thickness.

Implementation of Conservation of Mass Equation

The conservation of mass equation, derived in the form of Equation 22, is used in the thermal model to calculate the mass flux of pyrolysis gases. This term is used in the energy equation to incorporate the internal convection of the pyrolysis gases into the thermal response of the decomposing material. The mass flux of pyrolysis gases is calculated using the change in density with time from the solid material decomposition model.

A trapezoidal integration scheme is used to integrate the change in density with time with respect to y through the thickness of the material. The assumption of instantaneous, unidirectional flow of the pyrolysis gases to the heated surface is used to simplify the calculation of the mass flux. The mass flux at an arbitrary point, y', is determined by integrating the change in density with time from that point through the thickness of the material. This is graphically

shown in Figure 5. The temperatures and densities are only calculated at the nodes through the material thickness; therefore, the mass flux of pyrolysis gases can only be calculated at the nodes. The mass flux of gases at each node will equal the integral of the change in density with time from that node to the unheated surface.

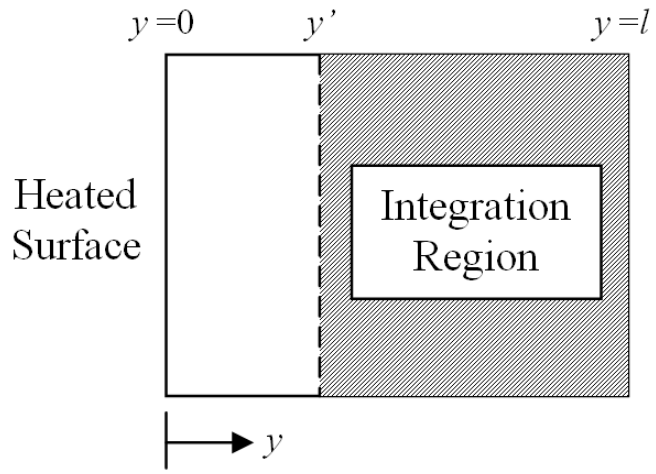

Figure 5. Conservaiton of mass equation integration region.

Boundary & Initial Conditions

The thermal model boundary conditions are enforced in the heat flux terms from the energy equation in the thermal load vector in Equation 68. The heat flux terms are the only relation between the domain boundaries and the environment in the system of equations. In enforcing the boundary conditions, the heat input to the material is represented as either an incident heat flux or a heat flux measured by a water-cooled heat flux gauge. The relationship between the surface heat flux and the measured heat flux from a water-cooled heat flux gauge is defined in Equation 26. This relationship adjusts for effects due to convection and radiation. However, the equation is a fourth order polynomial and requires excessive computational effort. To minimize the computational effort while maintaining approximately the same result, the equation was linearized in the following manner

$$q_s'' = q_{hfg}'' + \left[h_{conv} + \varepsilon_s \sigma \left(T_{hfg} - T_s\right)\left(T_{hfg}^2 - T_s^2\right)\right] T_{hfg} \qquad \text{Equation 72}$$

where the surface heat flux is defined for either the heated (y=0) or unheated (y=l) surface. Likewise, the surface temperatures, T_s, are defined at either the heated or unheated surface. This equation is implemented as the boundary conditions in the thermal load vector.

The thermal model initial conditions are defined for the temperature and density. The initial material temperature is defined through the thickness of the material. The initial material density is defined as the virgin density of the material.

Thermal Model Features

Several features were included in the thermal model to aid in defining the materials of interest and the elemental and transient definitions. The thermal model was designed as to not limit the number of materials that could be defined in the domain. Any number of materials may be defined in the one-dimensional geometry. Also, the material definitions include an option to inert the material so it will not decompose with heating. This capability is necessary to model materials such as insulation.

The elemental definitions included in the model include several features that may reduce the required computational time. The finite element method allows the user to define the number of elements to use to solve for temperature in the domain. This spatial discretization of the one-dimensional domain is referred to as the mesh. In the thermal model, the user has the option to define numerous mesh regions in the domain. Also, the number of elements in each mesh region may be specified by the user. An example of this is shown in Figure 6. The varying of the mesh size allows the user to reduce the time required to calculate the transient solution. This is done by reducing the number of elements by appropriately assigning mesh sizes to the defined regions. Mesh regions that experience large thermal gradients and high rates of solid material decomposition require more elements. This is called a fine mesh. However, a fewer number of elements may be used for regions containing low thermal gradients or materials such as insulation which experience no thermal decomposition. This is called a coarse mesh. An appropriate meshing scheme will reduce the computational time required by the thermal model. The transient definitions included in the model are fairly simple. The time at which to end the thermal model and the time step are defined. The time step definition is constant through the length of the simulation.

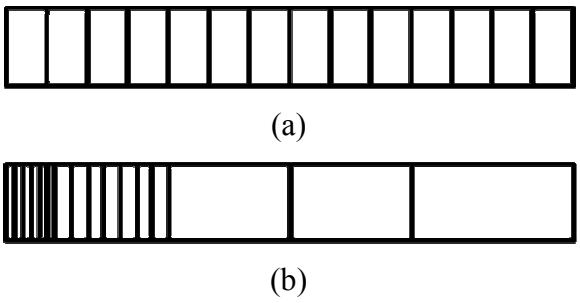

(a)

(b)

Figure 6. Mesh regions defined for a one-dimensional domain for a (a) uniform mesh and (b) non-uniform mesh.

Thermal Model Solution Algorithm

The following section will provide a general outline of the solution algorithm for the thermal model. Detailed will be the process to solve the system of governing equations and stepping of this process in time to obtain the transient solution.

1) Enter user inputs

a) Geometry and time definitions
b) Mesh regions and sizes
c) Materials and thermal properties
d) Thermal boundary conditions
e) Initial temperature and density

2) Apply boundary and initial conditions
   a) Apply boundary conditions to thermal loads in energy equation
   b) Calculate properties from initial temperature definition
   c) Calculate initial matrices for solving governing equations
3) Transient solution loop
   a) Advance time step for calculation of solution one increment (the n+1 time step)
   b) Temperature convergence loop
      i) Initialize all properties and matrices for energy equations
         (1) Determine temperatures to use in current convergence iteration
         (2) First iteration in convergence loop, use current time step temperatures, $\{T_n\}$
            (a) Calculate thermal properties
            (b) Calculate matrices for energy equation
         (3) Iterations other than first iteration, use previous iteration temperatures
            (a) Calculate thermal properties
            (b) Calculate matrices for energy equation
      ii) Pre-multiply the decomposition matrix, $[K_d]$, by $\{\partial\rho/\partial t\}$ from current time step
      iii) Calculate the temperatures, $\{T_{n+1}\}$, for the next time step
      iv) Compare current iteration temperatures against previous iteration
         (1) If maximum nodal temperature difference is less than convergence criteria, exit temperature convergence loop
         (2) Else, remain in temperature convergence loop until temperatures converge or reach the maximum number of iterations
   c) Calculate $\{\partial\rho/\partial t\}$ for next time step using the solid material decomposition model
      i) In the equation, calculate using
         (1) Temperatures calculate for the next time step, $\{T_{n+1}\}$
         (2) Densities from the current time step, $\{\rho_n\}$
   d) Calculate the mass flux of pyrolysis gases using $\{\partial\rho/\partial t\}$ from previous solution step
   e) Calculate next time step density, $\{\rho_{n+1}\}$, using next time step $\{\partial\rho/\partial t\}$ and current time step density, $\{\rho_n\}$
   f) Repeat steps a) through e) until the end of designated simulation run time
4) Post-process

Thermal Model Verification and Validation

Thermal model verification was performed using a standard heat conduction model, HEATING 7.3 [60]. The verification was performed solely to compare the prediction of the thermal response of the models due to a common set of heat inputs and thermal properties. The standard heat conduction model is incapable of modeling material decomposition; therefore, decomposition of the material was not considered. This aspect of the model will be investigated in the model validation.

The model verification was performed using an FRP material, specifically E-glass vinyl ester. This material was chosen because it is the material system of interest in this research. The material properties are listed in Appendix A. The thermal properties were considered to be functions of temperature but are not defined as functions of the decomposition state; however, this is inconsequential because the material is considered inert for verification. A Robin boundary condition was defined at both surfaces for verification. A list of the initial conditions and boundary conditions are given in Table 5.

Table 5. Boundary and initial conditions for thermal model verification.

Parameter	Parameter description	Defined Value
h_{conv}	convective heat transfer coefficient	10 W/m^2-K
$q''(y=0)$	heat flux at node 1	25 kW/m^2
$q''(y=l)$	heat flux at node n	0 kW/m^2
T_{init}	initial temperature	300 K

The results of the simulations using the developed thermal model and the standard heat conduction model, HEATING, are shown in Figure 7. Three temperatures are plotted with time from both the finite element model and HEATING. These temperatures are at the heated surface, (node 1 or $y=0$), the mid-depth ($y=l/2$), and the unheated surface (node n or $y=l$). No distinguishable difference can be seen between the thermal predictions through the thickness of the material. This verifies the heat conduction capabilities of the thermal model.

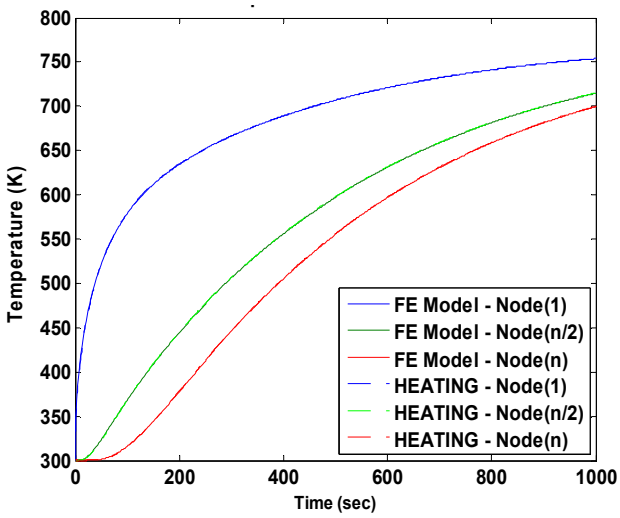

Figure 7. Results of thermal model verification against a standard heat conduction model.

Thermal model validation was performed using an E-glass vinyl ester FRP composite heated in a cylindrical ceramic heater, shown in Figure 8. A detailed description of the experimental apparatus, experiment, and material thermal properties may be found in Lattimer, *et al.* [55]. The validation was performed for both the thermal response and mass loss rate of the material. The material properties were defined as functions of both temperature and decomposition state. A Robin thermal boundary condition was used for the heating conditions.

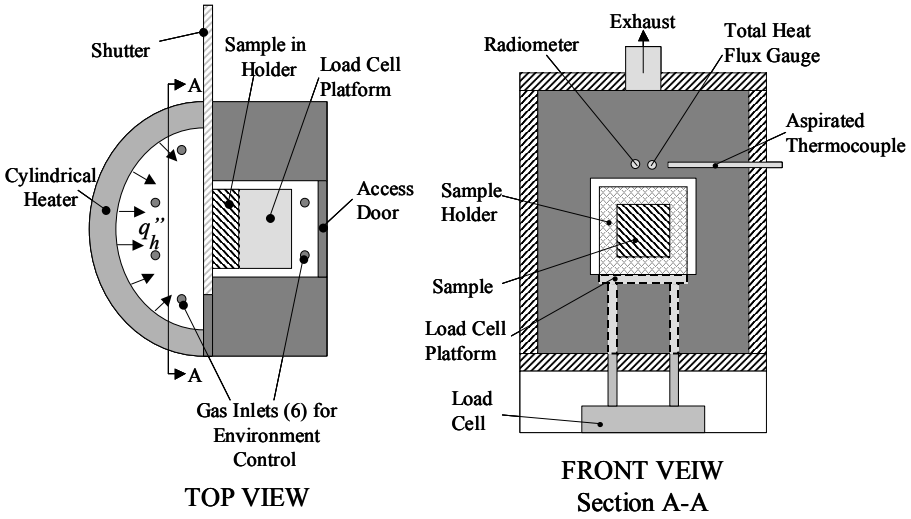

Figure 8. Cylindrical ceramic heater used to by Lattimer, *et al*. [55], to heat a FRP sample for validation of the thermal model.

The E-glass vinyl ester sample used in validation was manufactured using a quasi-isotropic layup with a brominated Derakane 510A resin. The volume fraction of resin was approximately 30%. The sample had a 12.7mm thickness and exposed dimensions of 100mm by 100mm, resulting in an exposed surface area of 100cm^2. A 38.1mm thick piece of ceramic insulation board, UNIFRAX Duraboard LD, was placed behind the sample. Material properties for the ceramic insulation were obtained from the manufacturer [61]. A shutter was used to protect the sample until the heater reached its operating temperature, at which point it was removed to initiate the test. The shutter system caused a slight ramping of the measured heat flux at test initiation. The average measured heat flux through the duration of the test, excluding the ramping portion, was approximately 60kW/m^2. The heat flux to the sample was measured using a 0-200kW/m^2 Schmidt-Boelter type total heat flux gauge. The mass loss rate of the FRP was measured using a load cell. The measured change in mass was divided by the cross-sectional area of the sample to determine mass loss rate per unit area, or mass flux. Temperatures were measured using thermocouples at the exposed surface (y=0mm), mid-depth (y=6.35mm), and interfacial surface between the sample and insulation board (y=12.7mm).

The results of the thermal model simulation for the validation test are shown in Figure 9. The temperatures from the model were compared at the points through the thickness where thermocouples were located. The predicted temperatures compare well against the experimental temperatures. It is notable that the predicted temperatures at the interfacial surface (y=12.7mm) follow the same dip in temperature that is measured experimentally at approximately 500 seconds. The predicted mass flux at the exposed surface compares well against the

experimentally measured mass flux. The predicted mass flux has a noticeable spike near the start of the test. This may be attributed to the kinetic parameters used in the solid material decomposition model. In the solid material decomposition model, the decomposition reaction was modeled using a single-step global reaction mechanism. In reality, the FRP laminate decomposition includes multiple steps and the failure to represent all of these reactions may explain the behavior at the outset of the simulation.

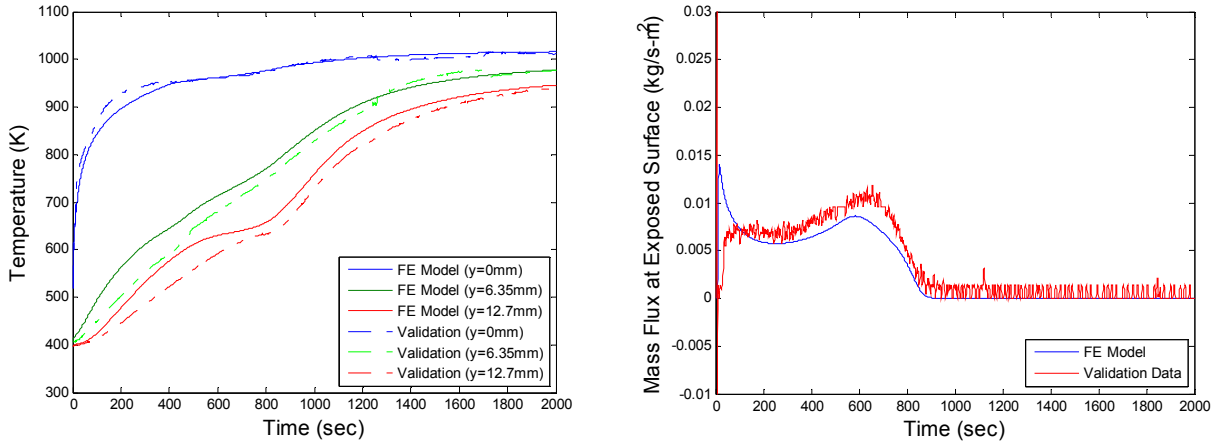

(a) (b)

Figure 9. Thermal validation with (a) temperatures and (b) mass flux at the exposed surface compared against experimental data.

Thermo-Structural Model

A thermo-structural model was developed to predict the structural response of a decomposing member subjected to an axial, compressive load in fire conditions. The fire conditions are represented by a one-sided heating assumption. The thermal response of the material, such as a FRP laminate, to one-sided heating is predicted using the developed thermal model. The structural response of the FRP laminate is closely linked to the thermal response of the compressively loaded member.

Consider a FRP laminate fixed at both ends and compressively loaded in the axial direction. The compressive load is applied at the centerline of the laminate which is initially coincident with neutral axis. The structural response of this loading case is governed by Euler buckling. Now consider a non-uniform heat source applied to one side of the laminate. The heat source is assumed to be centered and parabolic with height and, therefore, causes a parabolic vertical temperature profile. The one-sided heat source also causes a temperature gradient through the thickness which is appropriately scaled with height in relation to the centered heat source. The mechanical properties of the laminate, including the elastic modulus and compressive strength, are temperature dependent. Therefore, the temperature gradient degrades the mechanical properties in a non-uniform manner causing a mechanical property gradient. The mechanical property gradient will shift the neutral axis away from the centerline resulting in loading of the member away from the centerline. This is known as eccentric loading and will cause moments to develop at the fixed ends of the laminate. The equivalent moment loading of

the eccentric load is shown in Figure 10. Additionally, the temperature gradient will cause non-uniform in-plane thermal expansion through the thickness. The effect of this is a moment developing at the fixed ends due to the non-uniform reaction forces from the thermal expansion. This moment is referred to as the thermal moment.

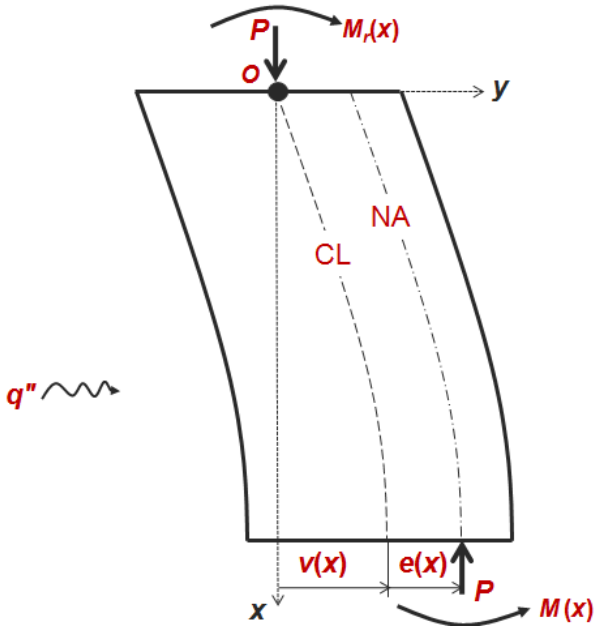

Figure 10. Free body diagram of laminate bending due to eccentric load and bending moment.

The out-of-plane bending of the laminate will change the governing mechanics of the problem from Euler buckling to bending. The laminate essentially behaves as an axially compressed beam experiencing bending due to moments at the fixed ends. In this research, the governing equation was developed from the stress-strain relationship applied to a FRP laminate fixed at both ends with vertically non-uniform, one-sided heating. A non-uniform heating condition was selected because a uniform heating condition will result in no out-of-plane bending due to the thermal moment counteracting the moment due to eccentric loading caused by temperature-dependent mechanical properties.

To model the structural response, the thermo-structural model is divided into two distinct parts. The thermal portion of the model, developed previously, predicts the temperature gradient and decomposition state of the laminate at the mid-height. The assumed parabolic vertical shape of the temperatures due to centered heating, which implies a similar shape for the applied heat flux, was then used to scale the predicted temperature gradient with height in a similar manner. The structural portion of the model calculates the mechanical properties as a function of temperature and decomposition state. The thermal moments and shifts in neutral axis (eccentricity) are then calculated and scaled with height in relation to the temperatures. The governing equation derived for a FRP laminate with fixed end conditions uses these mechanical properties to calculate the out-of-plane deflection and maximum combined stress in the laminate.

Structural Model Governing Equations

Key Assumptions

In developing the thermo-structural model, several key assumptions were made to simplify the behavior of the compressively loaded, heated laminate. These key assumptions are shown in Table 6. The first two assumptions develop the basis for the development of the model by stating that a non-linear temperature gradient exists through the thickness and that the mechanical properties are dependent upon these temperatures. As stated previously, the gradients cause a shift in the neutral axis leading to bending of the laminate. The third assumption is a consequence of the assumption of centered heating. However, a limitation was added such that the eccentricity and thermal moment are parabolic with height with a maximum at the mid-height and reduce to specified values at the ends. The final assumption allows the governing equation to be simplified by allowing the slopes to be solved directly. For this to be valid, the slope should be within $\theta \leq 15°$, allowing the approximation of $\sin\theta \approx \theta$.

Table 6. Key assumptions for structural model.

Number	Assumption
1	Non-uniform, centered, one-sided heating
2	Mechanical properties are temperature and decomposition state dependent
3	Thermal moment and eccentricity are parabolic with height of laminate
4	Axial movement of laminate is unrestrained
5	Laminate experiences only small deflections

Governing Equation

The governing equation was developed for the case of an axially compressed laminate with fixed end conditions and centered, non-uniform heating. The free body diagram of this is shown in Figure 10. Summing the moments about point "*O*" at the origin of the coordinate axes

$$\sum M_O = M(x) + Pe(x) + Pv(x) = 0 \qquad \text{Equation 73}$$

The moment, $M(x)$, in the above equation is a result of the curvature of the beam and non-uniform, in-plane thermal expansion. The stress-strain relationship for the bending, thermally exposed laminate is applied to calculate this moment. An unheated beam experiencing bending is considered to define the relation between the applied moment and the curvature of the beam for the defined coordinate system. The free body diagram for this member is shown in Figure 11.

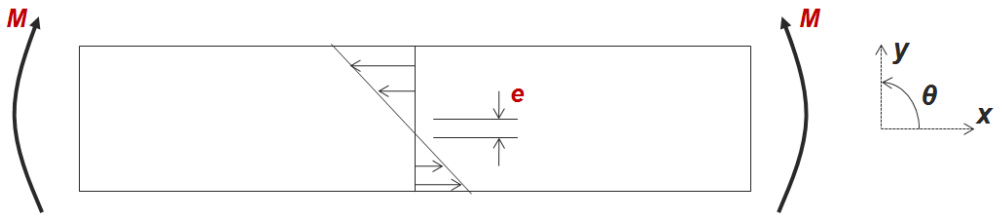

Figure 11. Free body diagram for a unheated, bending beam with eccentricity.

The applied moments cause compressive strains on the top surface of the beam and tensile strains on the bottom surface. The curvature of the beam caused by the applied moments is related to the strain and is defined as the reciprocal of the radius of curvature at the neutral surface. The curvature of a beam is also defined as the derivative of the slope for small slopes. Considering that the beam experiences a shift in the neutral axis, the strain for the shown beam is defined as

$$\varepsilon = \frac{-(y-e)}{\kappa} = -(y-e)\frac{d\theta}{dx} \qquad \text{Equation 74}$$

where the negative sign is placed in the equation to account for the direction of the defined coordinate system and enforce compressive strains on the top surface.

The definition of the mechanical strain is used in the stress-strain relationship for the axially compressed, heated laminate to determine the bending moment in the beam. The one-dimensional stress-strain relationship is

$$\sigma = E(\varepsilon - \varepsilon_T) \qquad \text{Equation 75}$$

where the thermal strain, ε_T, is subtracted from the total strain to calculate the mechanical strain. The bending moment is calculated in relation to the stress using

$$M = -\int \sigma(y-e)dA \qquad \text{Equation 76}$$

where the eccentricity is included to account for the shift in neutral axis. The stress-strain relationship from Equation 75 is substituted into the expression, resulting in

$$M = -\int E(\varepsilon - \varepsilon_T)(y-e)dA \qquad \text{Equation 77}$$

The total strain, ε, was previously defined in Equation 74 and the thermal strain, ε_T, is defined as the in-plane thermal expansion of the laminate. Substituting these relations into the equation

$$M = -\int E\left(-(y-e)\frac{d\theta}{dx} - \alpha\Delta T\right)(y-e)dA \qquad \text{Equation 78}$$

Simplifying the expression results in

$$M = \frac{d\theta}{dx}\int E(y-e)^2\,dA + \int E\alpha\Delta T(y-e)dA \qquad \text{Equation 79}$$

where the equivalent bending rigidity, $(EI)_{eq}$, is defined as the first integral term and the thermal moment is defined as the second integral term. Simplifying the expression with the definition of these terms results in the final form of the bending moment equation

$$M = (EI)_{eq}\frac{d\theta}{dx} + M_x^T \qquad \text{Equation 80}$$

The relation for the bending moment was then used with the moment balance from Equation 73 to form the governing equation. Substituting and rearranging the terms results in

$$(EI)_{eq}\frac{d\theta(x)}{dx} + Pv(x) = -M_x^T(x) - Pe(x) \qquad \text{Equation 81}$$

The small angle assumption simplifies the relationship for the beam slope, which is defined as the derivative of the out-of-plane deflection

$$\frac{dv}{dx} = \sin\theta \approx \theta \qquad \text{Equation 82}$$

Taking the derivative of Equation 81 with respect to the axial direction, x, and applying the slope simplification results in

$$(EI)_{eq}\frac{d^2\theta(x)}{dx^2} + P\theta(x) = -\frac{dM_x^T(x)}{dx} - P\frac{de(x)}{dx} \qquad \text{Equation 83}$$

A relationship for the eccentricity and thermal moment must be developed to relate their behavior to the height of the beam.

The relationships for the behavior of the eccentricity and thermal moment are developed from the assumption of a parabolic shape with beam height. Criteria are placed on the parabolic shape in that it must be at a maximum at the mid-height (x=L/2) and reduce to a percentage of the maximum value at the ends (x=0,L). The shape function is scaled between zero and unity where it is unity at the mid-height and a fitting parameter is defined as some fraction of unity at the ends. For example, in this research, the eccentricity and thermal moment at the ends are assumed to be 80% of the maximum value at the mid-height; therefore, the fitting parameter, K, was set to 0.8. This relationship was determined using vertical temperature measurements during testing. The symmetric parabolic shape function for the eccentricity and thermal moment are defined as

$$e(x) = e_0\left[-(4-4K)\left(\frac{x}{L}\right)^2 + (4-4K)\left(\frac{x}{L}\right) + K\right] \qquad \text{Equation 84}$$

$$M_x^T(x) = M_{x,0}^T\left[-(4-4K)\left(\frac{x}{L}\right)^2 + (4-4K)\left(\frac{x}{L}\right) + K\right] \quad \text{Equation 85}$$

Taking the derivative of the equations and substituting into the elastic curve equation

$$(EI)_{eq}\frac{d^2\theta(x)}{dx^2} + P\theta(x) = \left(M_{x,0}^T + Pe_0\right)\left(\frac{8-8K}{L^2}x - \frac{4-4K}{L}\right) \quad \text{Equation 86}$$

This is the final form of the governing equation used to develop the analytical solution for the slope. Forms for the homogeneous and particular solutions are assumed for the second order differential equation. The assumed solution forms for the homogeneous solution, $\theta(x)$, and particular solution, $f(x)$, are given as

$$\theta(x) = C_1\sin(\lambda_c x) + C_2\cos(\lambda_c x) + f(x) \quad \text{Equation 87}$$

$$f(x) = C_3 x + C_4 \quad \text{Equation 88}$$

The constants in the particular solution are solved by setting the particular solution equal to the right-hand side of Equation 86

$$C_3 x + C_4 = \left(M_{x,0}^T + Pe_0\right)\left(\frac{8-8K}{L^2}x - \frac{4-4K}{L}\right) \quad \text{Equation 89}$$

Solving for C_3 and C_4

$$C_3 = \frac{8-8K}{L^2}\left(\frac{M_{x,0}^T}{P} + e_0\right) \quad \text{Equation 90}$$

$$C_4 = -\frac{4-4K}{L}\left(\frac{M_{x,0}^T}{P} + e_0\right) \quad \text{Equation 91}$$

Substituting the constants into the particular solution and simplifying to obtain the final form

$$f(x) = \left(\frac{8-8K}{L^2}x - \frac{4-4K}{L}\right)\left(\frac{M_{x,0}^T}{P} + e_0\right) \quad \text{Equation 92}$$

This form of the particular solution is placed into the homogenous solution to solve for the remainder of the constants.

The homogeneous solution is solved for the slope by enforcing the end conditions given for the case of a fixed-fixed beam. These end conditions are the slope is equal to zero at both fixed ends, $\theta(x=0) = \theta(x=L) = 0$. The solution after substitution of the particular solution is

$$\theta(x) = C_1 \sin(\lambda_c x) + C_2 \cos(\lambda_c x) + \left(\frac{8-8K}{L^2} x - \frac{4-4K}{5L} \right) \left(\frac{M_{x,0}^T}{P} + e_0 \right) \quad \text{Equation 93}$$

Enforcing the boundary conditions at the fixed ends, the constants are solved

$$C_1 = -\frac{4-4K}{L} \left(\frac{M_{x,0}^T}{P} + e_0 \right) \left(\frac{\cos(\lambda L)+1}{\sin(\lambda L)} \right) \quad \text{Equation 94}$$

$$C_2 = \frac{4-4K}{L} \left(\frac{M_{x,0}^T}{P} + e_0 \right) \quad \text{Equation 95}$$

Substituting the constants into the homogenous solution and simplifying results in the solution for the slope as a function of position along the beam

$$\theta(x) = \frac{4-4K}{L} \left(\frac{M_{x,0}^T}{P} + e_0 \right) \left(\frac{-\cos(\lambda_c L)-1}{\sin(\lambda_c L)} \sin(\lambda_c x) + \cos(\lambda_c x) + \frac{2}{L} x - 1 \right) \quad \text{Equation 96}$$

The out-of-plane deflection as a function of beam height is also of interest in this research. The deflections are solved for by integrating the slope, which is valid by the small deflection assumption applied in Equation 82. The integration results in an integration constant which is solved for by enforcing the condition of no out-of-plane deflection at the ends of the beam, $v(x=0) = 0$. The final form of the solution for the out-of-plane deflections as a function of beam height is

$$v(x) = \frac{4-4K}{L} \left(\frac{M_{x,0}^T}{P} + e_0 \right) \left(\frac{\cos(\lambda_c L)+1}{\lambda \sin(\lambda_c L)} (\cos(\lambda_c x) - 1) + \frac{\sin(\lambda_c x)}{\lambda_c} + \frac{x^2}{L} - x \right) \quad \text{Equation 97}$$

where λ_c is developed from the form of the differential equation in Equation 83

$$\lambda_c = \sqrt{\frac{P}{(EI)_{eq,av}}} \quad \text{Equation 98}$$

where the equivalent bending rigidity of the laminate is calculated as a bulk value through the thickness.

Mechanical Property Relationships

The mechanical property relationships for the elastic modulus and compressive strength of a FRP laminate were originally developed by Gibson, *et al* [30]. A semi-empirical relationship was developed to fit the measured data as a function of temperature and decomposition state. Further development of the relationship was performed by Feih, *et al* [31-32]. The data for elastic modulus and compressive strength follows the general shape of the curve shown for compressive strength as a function of temperature in Figure 12.

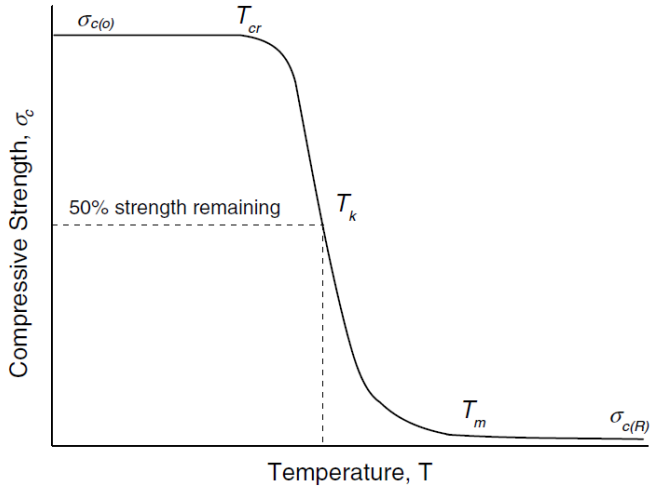

Figure 12. Effect of temperature on compressive strength of FRP laminates [32].

The semi-empirical relationship developed for the mechanical properties as a function of temperature and decomposition state of a FRP laminate is

$$P(T) = \left(\frac{P_{(0)} + P_{(R)}}{2} - \frac{P_{(0)} + P_{(R)}}{2} \tanh\left(\Phi\left(T - T_k\right)\right) \right) R_{rc}(T)^{\beta} \qquad \text{Equation 99}$$

where P represents either the compressive strength, σ_c, or the elastic modulus, E. The material constant, Φ, describes the temperature range over which the property is reduced during the thermal softening process. The residual property value is defined at the temperatures where the property is no longer degrading but decomposition has not yet started. The further reduction of mechanical properties due to decomposition is taken into account using the scaling function, R_{rc}. This function is the instantaneous mass fraction, F, as calculated by the thermal model. A fitting parameter, β, was used to fit the scaling function to measured data for the mechanical properties. Feih, *et al* [32], empirically determined the best value to be three for the fitting parameter.

Calculation of Eccentricity and Thermal Moment

The eccentricity, or neutral axis shift, is caused by the though-thickness thermal gradient. The non-uniform temperatures degrade the mechanical properties, specifically the elastic modulus. This creates a non-uniform elastic modulus gradient through the thickness, shifting the neutral axis from the mid-surface. The distance of the neutral axis shift is determined by calculating where a "zero" moment exists due to the non-uniform elastic modulus. This concept is implemented by dividing the first moment of the elastic modulus by the average elastic modulus

$$e = \frac{\int_A E(T) y dA}{\int_A E(T) dA} \qquad \text{Equation 100}$$

The thermal moment is also caused by the non-uniform thermal gradient. In addition to the elastic modulus gradient caused by the non-uniform temperature, the thermal moment is dependent on the in-plane thermal expansion. The non-uniform temperatures cause non-uniform in-plane thermal expansion. The thermal moment is developed due to this effect and is calculated using the thermal stress-strain relationship. Referring to Equation 79, the thermal moment was defined as the integral term representing the effects of the thermal expansion on the moment

$$M_x^T = \int_A E\alpha\left(T - T_{ref}\right)(y - e)dA \qquad \text{Equation 101}$$

where the (y-e) term calculates the location of the neutral axis using the eccentricity from Equation 100. The change in temperature term, ΔT, is expanded to represent the definition of the thermal expansion as the relation between the current temperature and the reference temperature.

Calculation of Combined Axial and Bending Stress

The maximum stress developed in the laminate due to axial compression and bending is calculated using superposition of strains. The strain for the axial compression portion of the total mechanical strain is proportional to the applied load and load-bearing area. The mechanical strain for the bending portion is defined as before using the total and thermal strains. Superimposing the axial and bending strains results in the expression for the mechanical strain

$$\varepsilon_m(x) = -\frac{P}{EA_{cs}} - (y - e)\frac{d\theta(x)}{dx} - \alpha\Delta T \qquad \text{Equation 102}$$

where $d\theta(x)/dx$ is the curvature of the beam and is solved for by taking the derivative of Equation 96 with respect to the axial direction

$$\frac{d\theta(x)}{dx} = \frac{4 - 4K}{L}\left(\frac{M_{x,0}^T}{P} + e_0\right)\left(\frac{-\cos(\lambda_c L) - 1}{\sin(\lambda_c L)}\lambda_c \cos(\lambda_c x) - \lambda_c \sin(\lambda_c x) + \frac{2}{L}\right) \qquad \text{Equation 103}$$

Applying the stress-strain relationship, $\sigma = E(\varepsilon - \varepsilon_T)$, to the expression results in the combined compressive stress

$$\sigma(x) = -\frac{P}{A_{cs}} - E(y - e)\frac{d\theta(x)}{dx} - E\alpha\Delta T \qquad \text{Equation 104}$$

where the maximum combined compressive stress for a laminate with fixed-fixed end conditions will occur at the mid-height, $x = L/2$. This is apparent in the development of the governing equation where the vertical temperature profile and, therefore, eccentricity and thermal moment, is at a maximum at the mid-height. Also, the maximum out-of-plane deflection occurs at the mid-height for a beam with symmetric end conditions.

Failure Determination using Thermo-Structural Model

The thermo-structural model uses a localized failure criterion to determine laminate failure. The model will predict the failure of a compressively loaded, heated laminate when the calculated maximum combined compressive stress is equal to the compressive strength at the same location. The failure criterion was chosen as the compressive strength because the compressive strength of an FRP laminate is significantly lower than the tensile strength. The time that has elapsed in the model before failure is predicted is called the time-to-failure. No progressive failure is taken into account in the structural model; therefore, when failure is predicted at a single point within the laminate, the laminate is assumed to fail. Also, the model does not take creep or viscoelastic effects into account when predicting laminate failure.

Thermo-Structural Model Implementation

The structural model developed using the governing equation for a compressively loaded, heated FRP laminate in Equation 81 was integrated with the thermal model developed in MATLAB. The linking of these two models forms the thermo-structural model. Essentially the structural model was integrated as a post-processing step to the thermal predictions. The structural model uses the thermal predictions as inputs to calculate the mechanical properties. The analytical equation is then solved for the out-of-plane deflection of the laminate as a function of height. The maximum combined compressive stress is used to determine if the laminate fails based on a comparison to the compressive strength. This is performed at each time step in the simulation.

The mechanical properties are needed for calculation of the analytical solution in the structural model. The thermal predictions for each time step are used to calculate the mechanical properties at the calculated temperature locations, the nodes, through the laminate thickness. The instantaneous mass fraction at the nodes is also used to further scale the properties with the material decomposition state. In some cases, a bulk, or average, mechanical property is needed. For instance, the bulk equivalent bending rigidity is needed for use in determining the slope and out-of-plane deflection of the laminate. To calculate the bulk value, the equivalent bending rigidity calculated at the nodes is integrated through the thickness. This is performed using Simpson's integration technique

$$\int_{y=0}^{y=l}(EI)_{eq}(y)dy = \frac{l}{3n_{elem}}\left[(EI)_{eq}(y_0)+4(EI)_{eq}(y_1)+2(EI)_{eq}(y_2)+\cdots+2(EI)_{eq}\left(y_{n_{elem}-2}\right)\right. \\ \left.+4(EI)_{eq}\left(y_{n_{elem}-1}\right)+(EI)_{eq}\left(y_{n_{elem}}\right)\right] \quad \text{Equation 105}$$

where the number of intervals is identical to number of elements from the thermal model. The bulk equivalent bending rigidity is calculated by dividing the integral by the laminate thickness

$$(EI)_{eq,av} = \frac{1}{l}\int_{y=0}^{y=l}(EI)_{eq}(y)dy \quad \text{Equation 106}$$

where l is the material thickness.

The eccentricity and thermal moment are calculated in a similar manner to the mechanical properties. The nodal temperatures are used to calculate the temperature and decomposition state dependent mechanical properties at the nodes. The properties are used to calculate the eccentricity and thermal moment at each node. Simpson's integration technique was then applied to the nodes to obtain the eccentricity and thermal moment for use in the analytical solution.

Thermo-Structural Model Solution Algorithm

The following section provides a general outline of the solution algorithm for the thermo-structural model. The integration of the structural model into the thermal model is listed in detail. Changes to the solution algorithm for the stand-alone thermal model are highlighted in bold text.

1) Enter user inputs
   a) Geometry and time definitions
   b) Mesh regions and sizes
   c) Materials and thermal properties
   d) Thermal boundary conditions
   e) Initial temperature and density
   f) Mechanical property relations
   g) Applied load and laminate dimensions for bending
2) Apply boundary and initial conditions
   a) Apply boundary conditions to thermal loads in energy equation
   b) Calculate properties from initial temperature definition
   c) Calculate initial matrices for solving governing equations
3) Transient solution loop
   a) Advance time step for calculation of solution one increment (the n+1 time step)
   b) Temperature convergence loop
      i) Initialize all properties and matrices for energy equations
         (1) Determine temperatures to use in current convergence iteration
         (2) First iteration in convergence loop, use current time step temperatures, $\{T_n\}$
            (a) Calculate thermal properties
            (b) Calculate matrices for energy equation
         (3) Iterations other than first iteration, use previous iteration temperatures
            (a) Calculate thermal properties
            (b) Calculate matrices for energy equation
      ii) Pre-multiply the decomposition matrix, $[K_d]$, by $\{\partial\rho/\partial t\}$ from current time step
      iii) Calculate the temperatures, $\{T_{n+1}\}$, for the next time step
      iv) Compare current iteration temperatures against previous iteration

(1) If maximum nodal temperature difference is less than convergence criteria, exit temperature convergence loop

(2) Else, remain in temperature convergence loop until temperatures converge or reach the maximum number of iterations

c) Calculate $\{\partial\rho/\partial t\}$ for next time step using the solid material decomposition model

i) In the equation, calculate using

(1) Temperatures calculate for the next time step, $\{T_{n+1}\}$

(2) Densities from the current time step, $\{\rho_n\}$

d) Calculate the mass flux of pyrolysis gases using $\{\partial\rho/\partial t\}$ from previous solution step

e) Calculate next time step density, $\{\rho_{n+1}\}$, using next time step $\{\partial\rho/\partial t\}$ and current time step density, $\{\rho_n\}$

f) **Calculate eccentricity, thermal moment, equivalent rigidity, and compressive strength**

g) **Calculate out-of-plane deflection**

h) **Calculate combined compressive stress due to axial loading and bending**

i) **Compare combined stress to local compressive strength to predict structural failure**

i) **If failure predicted, record temperature profile, decomposed state, and time**

j) Repeat steps a) through e) until the end of designated simulation run time

4) Post-process

Thermo-Structural Model Validation

The thermo-structural model was validated with the intermediate-scale tests performed as part of this research. The tests were performed using a FRP laminate with an applied compressive load and exposed to one-sided heating.

CHAPTER 3 - Experimental Methods

Introduction

A series of intermediate-scale thermo-structural tests were performed on FRP laminates. The purpose of these tests was to validate the thermo-structural model and determine design correlations for the chosen material. An intermediate-scale load frame was constructed to evaluate the thermo-structural response of material. The apparatus was designed to subject the materials to one-sided heating while simultaneously applying a compressive load. The load frame is capable of applying loads up to approximately 200kN. The thermo-structural response of the material is characterized with measurement of in-plane and out-of-plane deflections, temperatures, heat flux, and applied load during testing. Experiments were performed to evaluate the effects of applied heat flux, laminate dimensions (thickness, height, width), and applied stress on the time-to-failure and failure temperature.

Intermediate-Scale Compressive Load Frame

A load frame was designed to perform compressive load tests on heated intermediate-scale test articles. The experimental setup for evaluating the thermo-structural response of materials is shown in Figure 13. The setup includes a compressive load frame, including a box-beam frame, loading surfaces, and test article mounting clamps, hydraulic loading system, and data acquisition components.

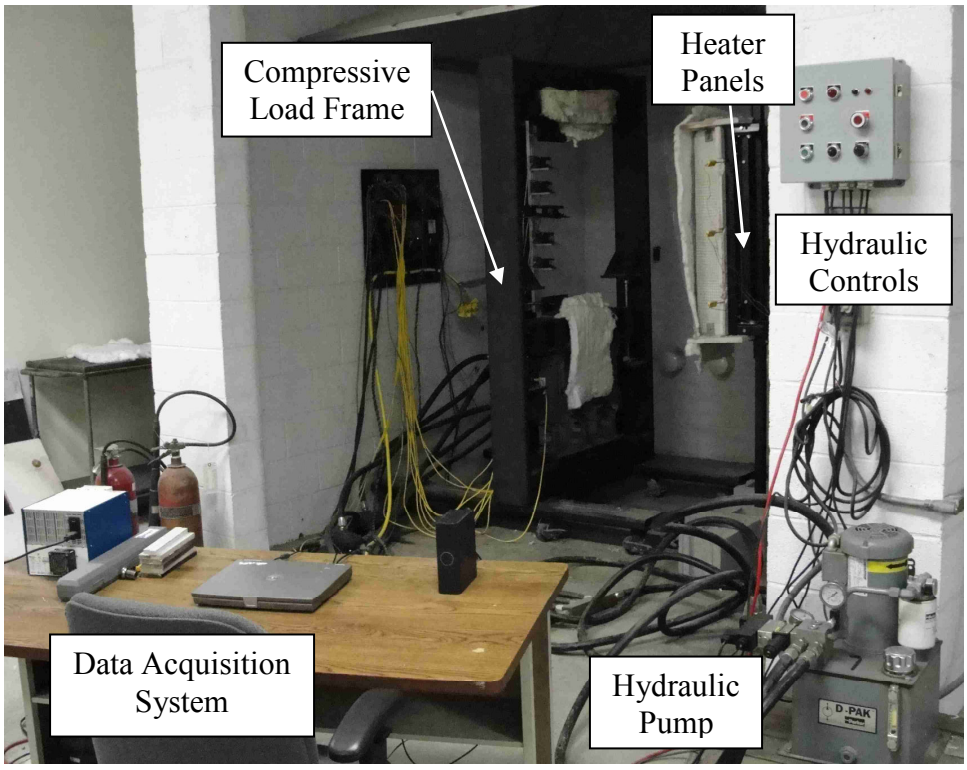

Figure 13. Intermediate-scale test setup for evaluating thermo-structural response of materials.

The steel box beam compressive load frame has overall dimensions of 2.24m high, 1.22m wide, and 510mm in depth. The load frame is shown in Figure 14. It can accommodate a maximum test article size of 880mm in height and 760mm in width. The sides and bottom of the load frame were constructed of 51mm high by 203mm wide box beams with a thickness of 9.5mm. The top of the load frame was constructed of a slightly narrower box beam with dimensions 51mm by 102mm with the same thickness. The loading surfaces consist of stainless steel I-beams with reinforcement between the flanges and capped ends. The I-beams have a 150mm flange, 140mm web, and are 950mm in length. The upper I-beam was welded to the top box beam support, whereas the bottom I-beam is mounted to the top ends of the hydraulic cylinders. The bottom I-beam is allowed to translate vertically via linear bearings mounted to the capped ends.

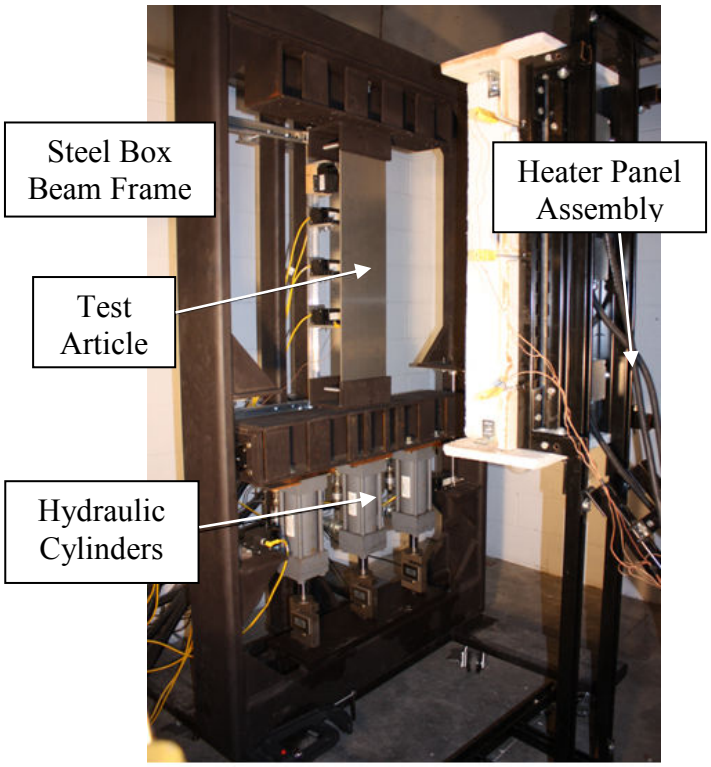

Figure 14. Compressive load frame.

The test article mounting clamps are attached to both I-beams. The mounting clamp is shown in Figure 15. The clamps were constructed of 12.7mm thick steel. The front face is 76.2mm in height and is 230mm in width. Threaded posts with 12.7mm thick steel plates attached are threaded through the back face to secure the test article. Gussets were added to the sides of the clamps to increase the strength of the front face in order to withstand the forces applied due to test article bending. Heat transfer through the clamps to the test article was also of concern. To thermally isolate the test article, Superwool 607 insulation blanket was placed over the face of the clamps. Further thermal insulation was provided by placing 12.7mm thick Pyrotek NAD-11 compressed insulation board between the test article and surfaces of the mounting clamp. The addition of the NAD-11 located the front of the test article 6.4mm from the center of the I-beam.

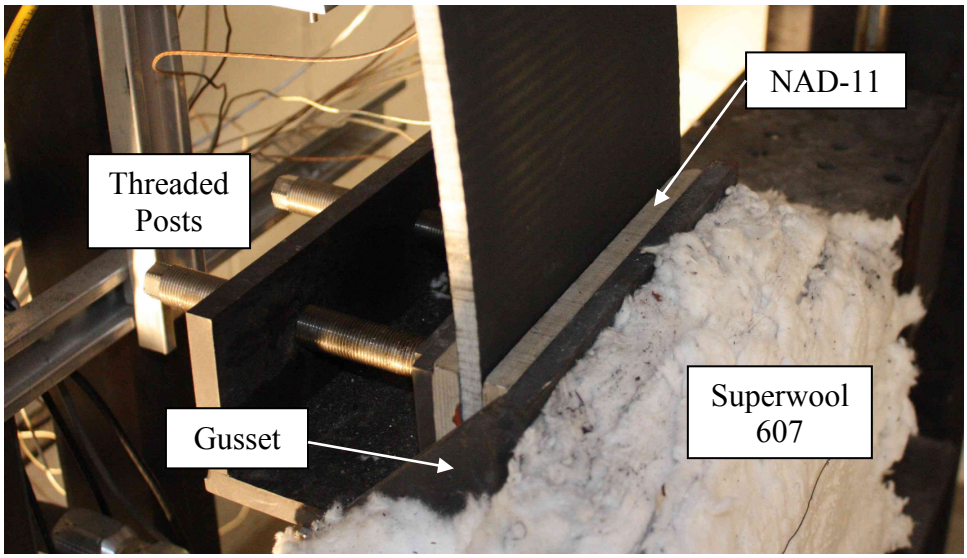

Figure 15. Test article mounting clamp mounted to bottom I-beam.

The hydraulic loading system uses three hydraulic cylinders to compressively load the test article. The hydraulic loading system is shown in Figure 16. Each cylinder has an 82.6mm bore with a 152mm rod extension. Hydraulic fluid supply and return lines were connected to the backside of the cylinders (as viewed in the figure). Each cylinder has an Omega PX302-3KGV pressure transducer attached to the hydraulic fluid lines. The pressure transducers are capable of measuring pressures in the range of 0 to 20.7 MPa. An electronic control unit controls the extension and retraction of the cylinders. The hydraulic pump is capable of outputting a maximum power of 1.49kW. The pump pressure to the cylinders was regulated via a manually adjustable, external pressure regulator. A bleed valve was placed in line with the pressure regulator to maintain a constant loading of the test article during testing. Load cells were mounted beneath the hydraulic cylinders to measure the load applied to the test article. Omega LCCA-15K load cells were used and are mounted to a single 25mm thick steel plate attached to the bottom box beam of the frame. Each load cell has a range of 0 to 66.7kN and an accuracy of 0.037% of the full-scale range. In the shown configuration, the load cells are capable of measuring loads up to 200.1kN. The pressure transducers attached to the hydraulic fluid lines were used to verify the load cell measurements.

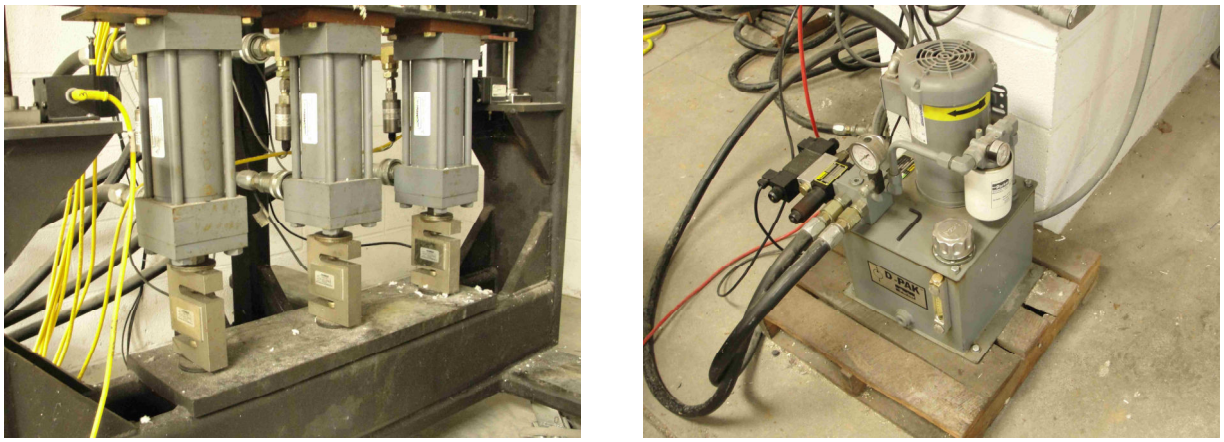

(a) (b)

Figure 16. Hydraulic loading system including (a) hydraulic cylinders and (b) pump.

The system used to heat the test articles in the compressive load frame is shown in Figure 17. The system consists of three temperature controlled quartz-faced heater panels with square dimensions of 300mm. The overall dimensions of the heater panel assembly were 910mm high by 300mm wide. The system was surrounded by 25.4mm thick compressed ceramic fiberboard insulation projecting 170mm perpendicular to the heating surface. The insulation board was placed flush to the sides of the heater panels. A steel frame was constructed and placed on casters to allow easy movement of the heater panel assembly. The bottom of the heater panels was located 960mm from the ground. This arranges the heater panel assembly so that, for the testing performed in this research, the top of the heater panels aligns with the bottom of the front face of the upper mounting clamp. The insulation projecting from the heater panels locates the assembly 280mm from the test article during testing.

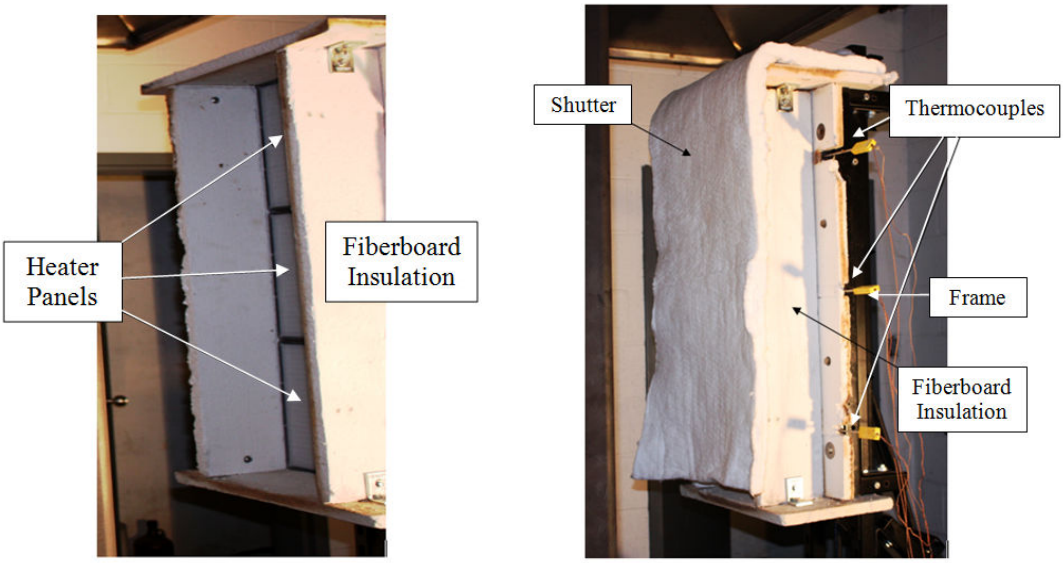

(a) (b)

Figure 17. Heater panel arrangement with (a) quartz-faced heater panels and (b) shutter system.

The quartz-faced heater panel temperatures were controlled independently for each panel via three WATLOW SD PID controllers. The temperature of the heater panels was measured using Inconel sheathed Type-K thermocouples placed in thermowells at the center of each heater panel. The heaters were measured to be capable of providing a 50kW/m^2 heat flux in the described setup.

A shutter was used with the heater panel assembly to allow preheating of the heater panels prior to testing. The shutter is shown in Figure 17. The shutter is comprised of a length of 25.4mm thick Superwool 607 insulation blanket and completely covers the heating surface of the assembly. The insulation is draped over the insulation board projecting from the assembly.

The data acquisition system was used to record the output signals from the load cells, pressure transducers, thermocouples, and deflection gauges. The data acquisition system is shown in Figure 18. The main component of the system was a National Instruments SCXI-1000 three slot chassis with a SCXI-1600 control module. The thermocouple signals were recorded via a SCXI-1102 module and SCXI-1303 accessory card. This card is specifically designed for use with thermocouple signals and includes a cold junction compensation circuit. The load cell and pressure transducer signals were also measured with a separate SCXI-1102 module and SCXI-1303 accessory card. The deflection gauge signals were measured via a SCXI-1100 module and SCXI-1300 accessory card. The signal processing program for data acquisition was created using National Instruments LabView 8.6.

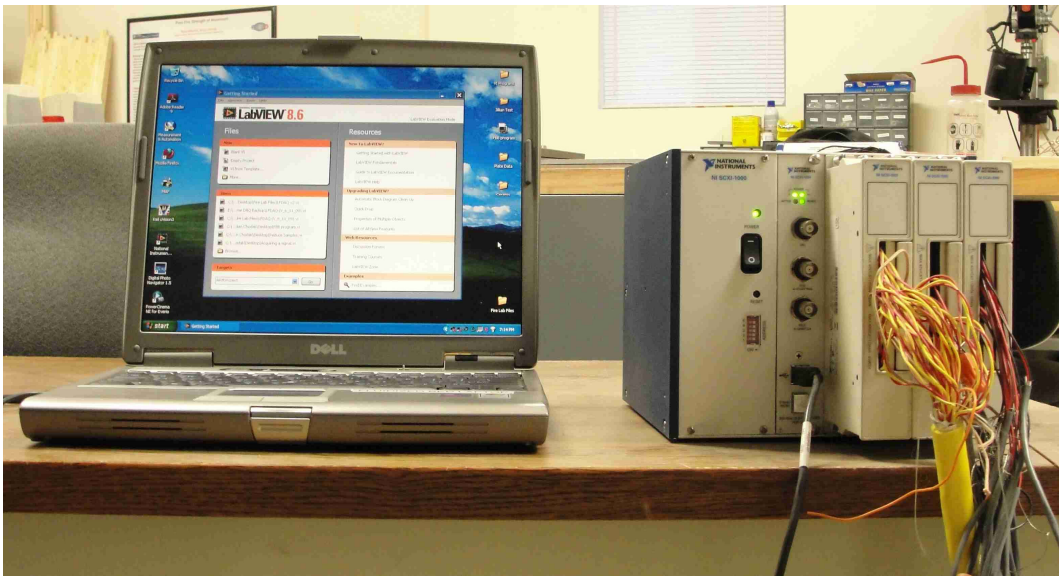

Figure 18. Data acquisition system.

Test Article Instrumentation

Instrumentation used to quantify the response of the test article to various heating and loading conditions includes thermocouples and deflection gauges. The temperatures and out-of-plane deflections were measured at the locations shown in Figure 19.

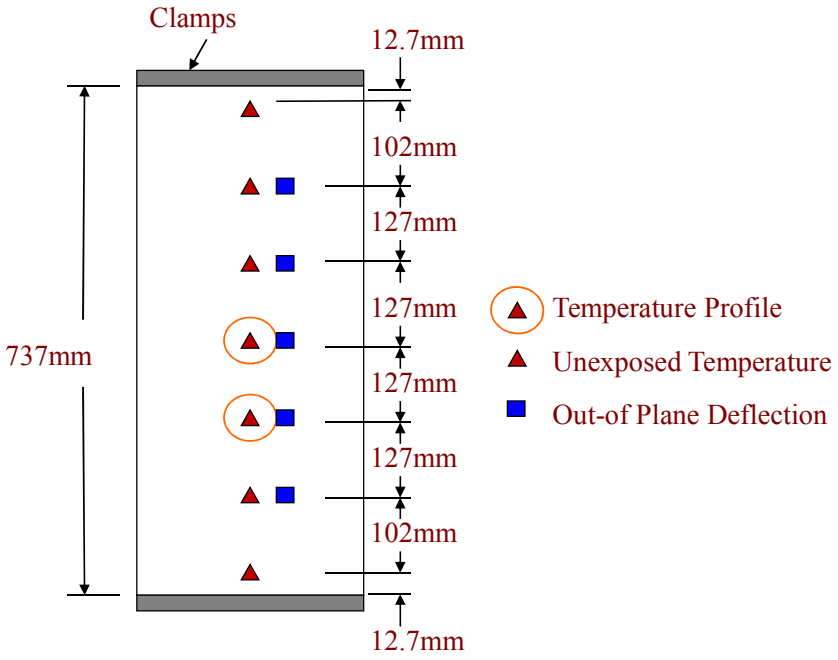

Figure 19. Test article instrumentation.

The structural response of the test article was quantified by measuring the in-plane and out-of-plane deflections. The in-plane deflections were measured using Celesco PT1DC-10-UP-Z10-MC4 string potentiometers with a range of 250mm and an accuracy of 0.05% of full-scale. The in-plane deflections were measured by attaching the string eyelet to the bottom of the I-beam while the gauge body was mounting on an L-bracket welded to the frame. Measurements were taken on both sides of the I-beam. The out-of-plane deflections were measured using Celesco PT1DC-15-FR-Z10-MC4 string potentiometers with a range of 380mm and an accuracy of 0.05% of full-scale. The out-of-plane deflections were measured by anchoring the gauge body to a brace on the rear of the load frame. The potentiometer line was attached to hooks secured to the unexposed surface of the test article. Refer to Figure 20 for a detailed view of the string potentiometers for in-plane and out-of-plane deflection measurements.

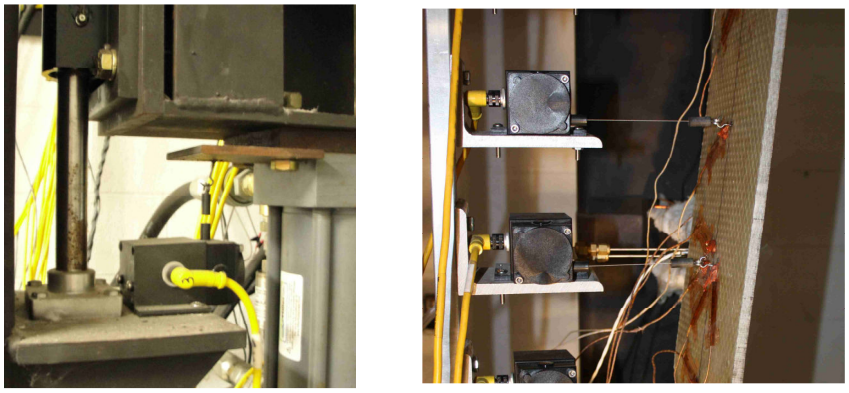

(a) (b)

Figure 20. String potentiometer mounting for measuring (a) in-plane and (b) out-of-plane deflections.

The thermal response was quantified using thermocouples to record the through-thickness temperatures and the vertical temperature profile on the unexposed surface of the test article. Temperature measurements were made using 24-gauge, bare bead, Type-K thermocouples with an accuracy of 2.2°C. The through-thickness temperatures were measured at two locations. The vertical locations of the through-thickness profile measurements are at approximately 242mm and 369mm from the bottom mounting clamp. The temperature profile was typically measured at the exposed surface, one-third of the thickness from the exposed surface, two-thirds of the thickness from the exposed surface, and at the unexposed surface. The through-thickness measurement profile is shown in Figure 21. The vertical temperature profile was also measured during testing on the unexposed surface of the test article. The vertical profile is shown in Figure 19.

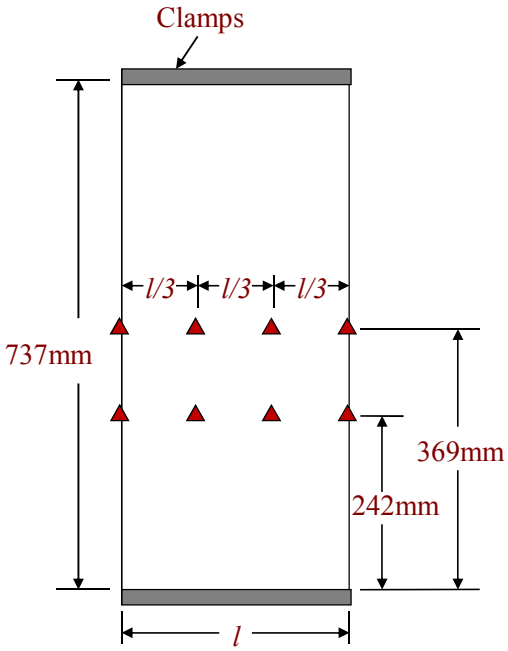

Figure 21. Through-thickness temperature profile locations.

The measurement of the through-thickness temperature profile requires several different thermocouple attachment techniques. For the exposed surface temperature measurement, a pilot hole was first drilled through the test article within 5mm of the desired measurement location. The thermocouple bead was then inserted through the pilot hole and bent 90 degrees at approximately 5mm from the bead. The wire was then pulled back through the hole until the bead came in contact with the surface of the test article, keeping the bent portion as close to the surface as possible. A light coating of DURASEAL +1530 GOLD Non-Sag Putty, a high-temperature silicone, was used to insulate the thermocouple bead. The wire was then bent against the unexposed surface and secured using high-temperature Kapton tape. The pilot hole was covered with the high-temperature silicone on the unexposed surface. Refer to Figure 22 for exposed surface thermocouple attachment details.

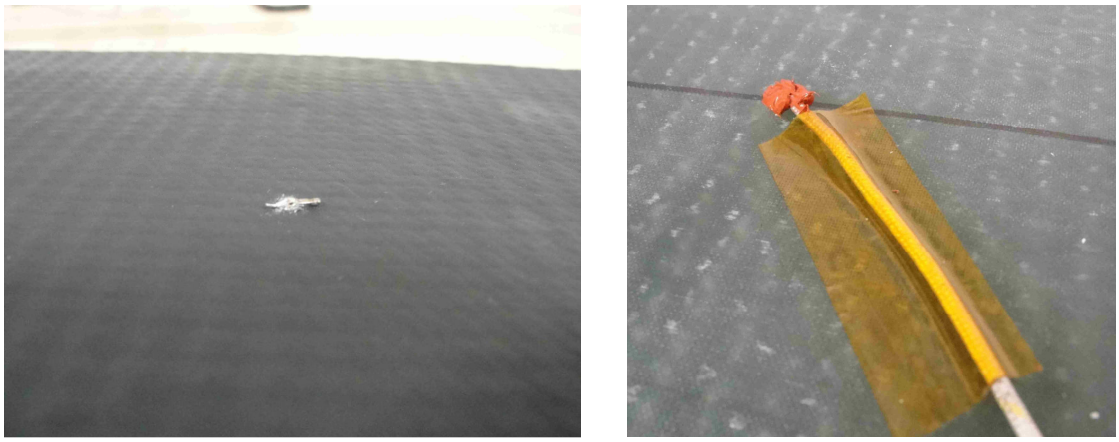

(a) (b)

Figure 22. Thermocouple attachment on the exposed surface with (a) bead on the exposed surface with sheathing pulled back and (b) wire secured with Kapton tape on the unexposed surface.

The thermocouples located at one-third and two-thirds of the thickness were installed into the test article by first drilling a pilot hole to the desired depth. The thermocouple was then inserted until the bead was in contact with the center of the drilled hole. The wire was bent over and secured to the unexposed surface to ensure the bead stayed in contact with the desired location in the hole. The hole was then covered with high-temperature silicone in a similar manner to that used for the exposed surface thermocouple.

The thermocouples located at the unexposed surface were attached by first slightly arching the thermocouple near the bead. The bead was then placed in contact with the unexposed surface and the wire was secured using Kapton tape. The slight arching before the bead creates pressure between the bead and the surface when the wire is secured. This helps maintain contact between the bead and unexposed surface during testing. As with the thermocouple at the exposed surface, the bead was insulated using a light coating of high-temperature silicone. Refer to Figure 23 for unexposed surface thermocouple attachment details.

Figure 23. Thermocouple attachment at the unexposed surface showing slight arching of thermocouple wire before bead prior to insulating with silicone.

Load Frame Characterization

The incident heat flux to the test article and velocity profiles on the test article surfaces were characterized. Heat flux mapping was performed to determine the uniformity of the incident heat flux. Also, a relationship was developed between the heater panel temperature set points and the incident heat flux at the center of the test article. The nominal test article size used in intermediate-scale thermo-structural testing with the compressive load frame had dimensions of 203mm in width and 737mm in exposed height; therefore, the heat flux and velocity mapping were performed over an identical area.

The heat flux mapping was performed using a water-cooled total heat flux gauge. The heat flux gauge was a Medtherm #64-20SB-19 (Serial #158431) Schmidt-Boelter type total heat flux gauge. It has a range of 0 to 200kW/m^2 with an accuracy of 3% of the full scale range. The heat flux mapping method used Type-X gypsum board mounted in the mounting clamps to support the heat flux gauge. The overall dimensions of the board were 860mm in height and 250m in width. One-inch holes were drilled in the board in the pattern shown in Figure 24. The heat flux was recorded at each hole location for 60 seconds. The average heat flux over the measurement time was recorded as the heat flux at that location. The heat flux recorded at the center hole location is referred to as the applied heat flux for that given heater panel temperature set point.

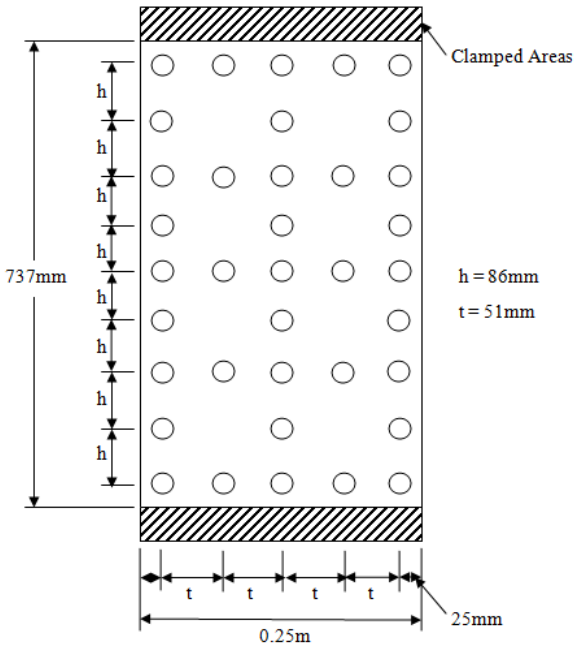

Figure 24. Heat flux gauge measurement locations for heat flux mapping.

Heat flux maps were taken at three different heater panel temperature set points. The first heat flux map was taken at a heater panel temperature set point of 529°C. This heater panel set point corresponds to a heat flux of approximately 10kW/m^2 at the center measurement location with the gypsum board in the loading frame. The heat flux map taken at this set point was normalized based on the approximation of 10kW/m^2. The normalized heat flux map is shown in Figure 25. For the 10 kW/m^2 set point, the integrated average heat flux across the test article is

9.12kW/m^2 with a maximum drop of 29% and 25% from the measured center value along the vertical centerline and horizontally at the mid-height, respectively.

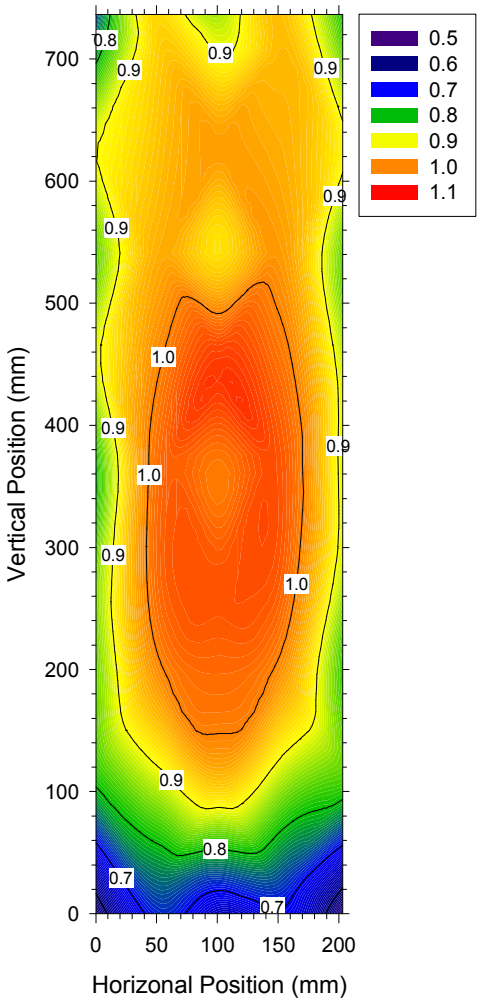

Figure 25. 10kW/m^2 normalized heat flux map.

The second heat flux map was taken at a heater panel temperature set point of 707°C. This heater panel set point corresponds to a heat flux of approximately 25kW/m^2 at the center measurement location. The normalized heat flux map is shown in Figure 26. For the 25kW/m^2 set point, the integrated average heat flux across the test article is 21.9kW/m^2 with a maximum drop of 24% and 17% from the measured center value along the vertical centerline and horizontally at the mid-height, respectively.

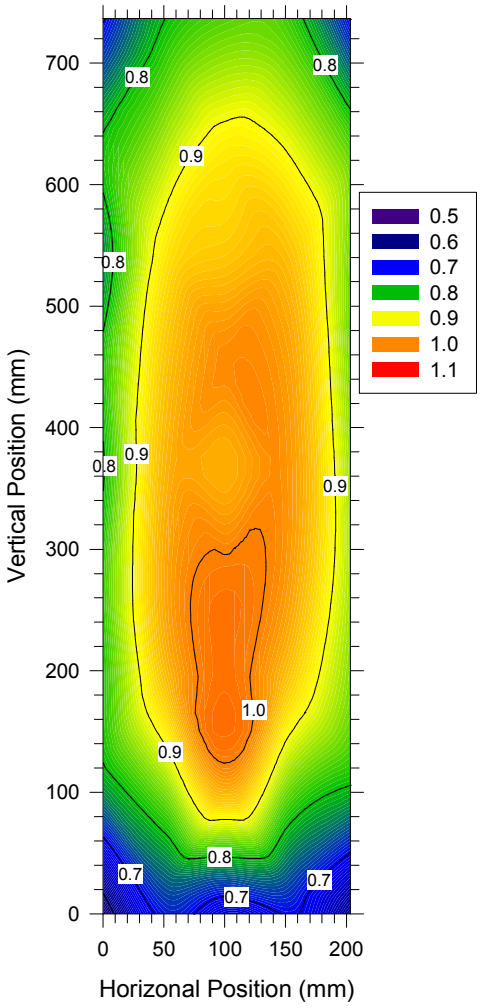

Figure 26. 25kW/m^2 normalized heat flux map.

The final heat flux map was taken at a heater panel temperature set point of 871°C. This heater panel set point corresponds to a heat flux of approximately 50kW/m^2 at the center measurement location. The normalized heat flux map is shown in Figure 27. For the 50 kW/m^2 set point, the integrated average heat flux across the test article is 43.1kW/m^2 with a maximum drop of 24% and 21% from the measured center value along the vertical centerline and horizontally at the mid-height, respectively.

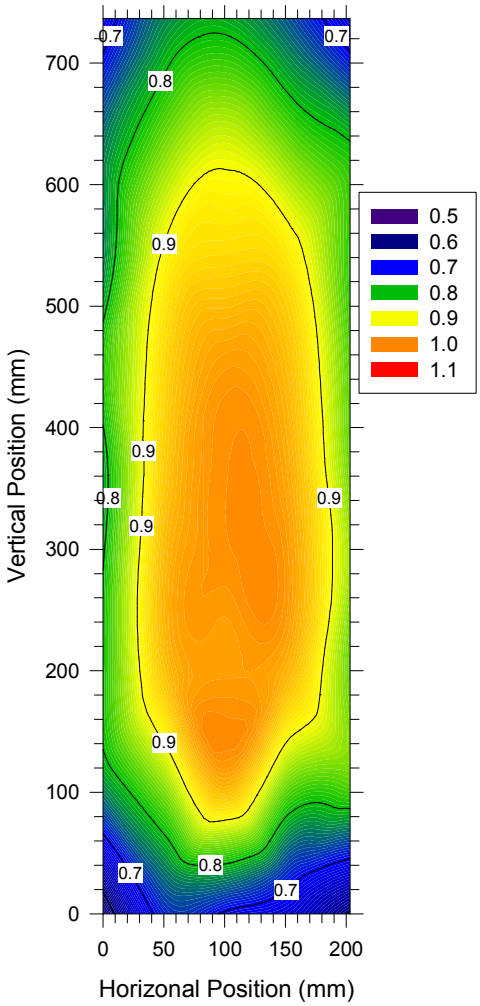

Figure 27. 50kW/m^2 normalized heat flux map.

The relationship between the incident heat flux at the center of the test article and the heater panel temperature set point was also characterized. This was accomplished by drilling a one-inch hole at the center of an FRP laminate test article of nominal size. The laminate was then mounted in the load frame using the same procedure used during testing. The heater panels were set to the temperature set points corresponding to the mapped heat fluxes of 10, 25, and 50kW/m^2. The water-cooled heat flux gauge was placed in the hole in the test article and the heater panel assembly was placed in front of the test article after removing the shutter. The heat flux measurement was recorded for 120 seconds. The measured heat flux was observed to reach steady-state after approximately 20 seconds in each measurement. The average heat flux was calculated for the duration of each measurement after the heat flux reached steady-state. The average value over this length of time was used as the incident heat flux to the test article at that respective temperature set point. The correlations generated using this method are shown in Table 7.

Table 7. Correlation between heater panel temperature and incident heat flux to test article.

Heater Panel Temperature (°C)	Measured Incident Heat Flux (kW/m^2)	Heat Flux Measured During Mapping (kW/m^2)
529	8.0	10
707	19.3	25
871	38.0	50

Vertical and horizontal velocity profiles on the exposed and unexposed surface of the test article were measured to determine the effect of forced convection. The velocity profile mapping was performed using an Omega FMA1002R-V2 hot wire anemometer. The velocity was measured in both the horizontal and vertical directions. From this an average speed was calculated across the surfaces of the test article. The speed maps are shown in Figure 28. The average speed measured for the exposed and unexposed surfaces of the test article are 0.12m/s and 0.34m/s, respectively.

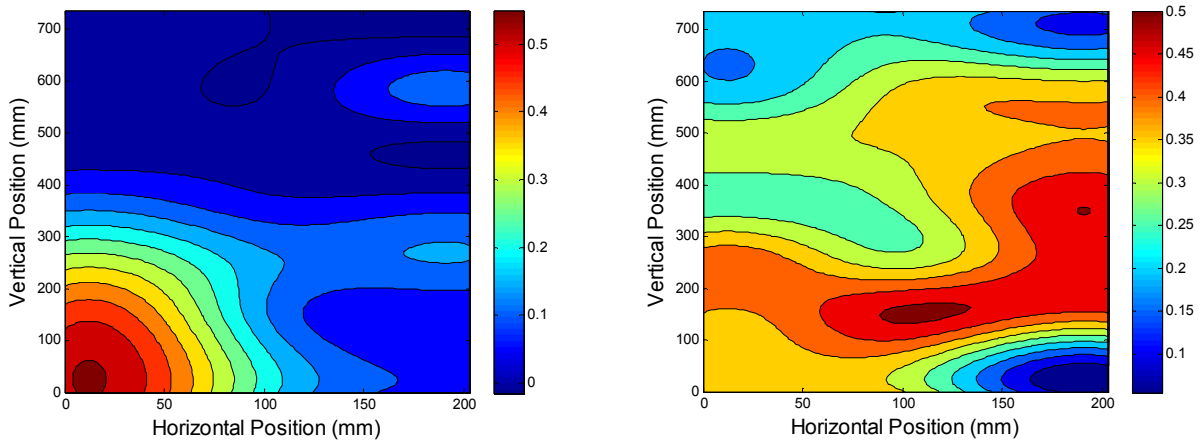

(a) (b)

Figure 28. Air speed profile maps in meters per second (m/s) for the (a) exposed surface and (b) unexposed surface of the test article.

Test Articles

E-glass vinyl ester FRP laminates were used in the intermediate-scale thermo-structural tests performed in this research. The nominal dimensions of the FRP laminate test articles were 203mm wide and 864mm high. Approximately 64mm of each end of the test article was inserted into the mounting clamps during testing. This resulted in an effective bending length approximately 127mm shorter than the overall length of the test article. This was 737mm for the nominal length of 864mm. The height and width of the test article was varied independently to evaluate the effect of slenderness ratio. The height was reduced to 787mm (effective bending length of 660mm) for three tests, and the width was reduced to 140mm for three tests. The test article sizes used in this research are listed in Table 8.

Table 8. Test articles sizes used in thermo-structural testing

Thickness (mm)	Overall Length (mm)	Bending Length (mm)	Width (mm)
12	864	737	203
9	864	737	203
9	787	660	203
9	864	737	140
6	864	737	203

The FRP laminates were manufactured in-house using the vacuum assisted resin transfer molding (VARTM) technique. The fiber used in the material was Colan AR105 0.83kg/m^2 Woven Roving plain weave E-glass fibers. A warp-aligned orientation was used for all test articles. The thicknesses of 12, 9, and 6mm used in testing were achieved using 20, 15, and 10 layers of the E-glass fabric, respectively. The resin used was Derakane 411-350 vinyl ester. The cure package for the resin used MEKP (1.5% by weight) to provide free radicals for curing, 2.4 Pentedione (0.06% by weight) as the retarder, and cobalt napthanate (0.2% by weight) as the catalyst. All E-glass vinyl ester test articles were post-cured in a humidity controlled environmental chamber at 80°C for two hours. Also, prior to testing, the exposed surface was painted with a high-temperature flat black paint to maintain constant boundary conditions and increase radiative heat transfer.

Figure 29. E-glass fabric layup in VARTM vacuum bag prior to resin infusion.

Test Procedure

The following section will provide a general outline of the procedure used for performing thermo-structural tests with the intermediate-scale compressive load frame.

1) Instrument the test article with thermocouples and hooks to attach deflection gauges. Let the silicone used for thermocouple installation cure overnight
2) Place the test article in load frame and secure
   a) Place Pyrotek NAD-11 between test article and mounting clamps

b) Secure test article by tightening down bolts to 12.54N-m

3) Apply initial load to test article using hydraulic loading system
4) Preheat heater panels to temperature set point corresponding to desired heat flux
   a) Preheat with shutter in front of heater panel assembly
5) Remove shutter and place heater panel assembly in front of test article
6) Stop test when test article fails and can no longer carry the applied load
   a) Normally this is accompanied by excessive out-of-plane deflections

Test Matrix

The test matrix was designed to evaluate the effects of heat exposure, stress level, and slenderness ratio on the thermo-structural response. The applied loads for the heated tests were determined as fractions of the calculated Euler buckling load of the individual test articles. The Euler buckling loads were calculated using the room-temperature properties for E-glass vinyl ester

$$P_{euler} = \frac{\pi^2 EI}{(K_e L)^2} \qquad \text{Equation 107}$$

where the elastic modulus, E, is 26.8GPa [62] and the end condition constant, K_e, is 0.5 for fixed-fixed end conditions. The moment of inertia, I, was calculated using

$$I = \frac{wl^3}{12} \qquad \text{Equation 108}$$

The calculated Euler buckling loads for the different panel sizes used in testing are listed in Table 9. The test matrix used for testing is listed in Table 10. Listed for each test is the test number, thickness, width, bending length, applied heat flux, applied load, applied stress, and the load as a percentage of the calculated Euler buckling load. Also, a buckling test was performed for each thickness to analyze the assumption of fixed-fixed end conditions. The test numbers corresponding to the room-temperature buckling tests are 18, 35, and 39 for thicknesses of 12, 9, and 6mm, respectively.

Table 9. Calculated Euler buckling loads for thicknesses used in testing.

Thickness (mm)	Bending Length (mm)	Width (mm)	Euler Buckling Load (kN)
12	737	203	59.8
9	737	203	25.2
9	660	203	31.4
9	737	140	18.9
6	737	203	7.5

Table 10. Test matrix.

Test Number	Thickness (mm)	Width (mm)	Bending Length (mm)	Heat Flux (kW/m^2)	Applied Load (kN)	Applied Stress (MPa)	$\%P_{euler}$
1	12	203.2	736.6	38	29.92	12.08	50
2	12	203.2	736.6	38	14.96	6.04	25
3	12	203.2	736.6	38	8.98	3.62	15
4	12	203.2	736.6	38	5.98	2.41	10
5	12	203.2	736.6	19.3	29.92	12.08	50
6	12	203.2	736.6	19.3	14.96	6.04	25
7	12	203.2	736.6	19.3	8.98	3.62	15
8	12	203.2	736.6	11.8	29.92	12.08	50
9	12	203.2	736.6	11.8	14.96	6.04	25
10	12	203.2	736.6	11.8	8.98	3.62	15
11	12	203.2	736.6	8.0	29.92	12.08	50
12	12	203.2	736.6	8.0	20.94	8.45	35
13	12	203.2	736.6	8.0	14.96	6.04	25
14	12	203.2	736.6	8.0	29.92	12.08	50
15	12	203.2	736.6	38	14.96	6.04	25
16	12	203.2	736.6	19.3	14.96	6.04	25
17	12	203.2	736.6	19.3	8.98	3.62	15
18	12	203.2	736.6	--	--	--	--
19	9	203.2	736.6	38	18.94	10.19	75
20	9	203.2	736.6	38	12.62	6.79	50
21	9	203.2	736.6	38	6.31	3.40	25
22	9	203.2	736.6	38	3.79	2.04	15
23	9	203.2	736.6	19.3	18.94	10.19	75
24	9	203.2	736.6	19.3	12.62	6.79	50
25	9	203.2	736.6	19.3	6.31	3.40	25
26	9	203.2	660.4	19.3	18.94	10.19	50
27	9	203.2	660.4	19.3	10.99	5.92	35
28	9	203.2	660.4	19.3	7.85	3.40	25
29	9	139.7	736.6	19.3	18.94	10.19	50
30	9	139.7	736.6	19.3	10.99	5.92	35
31	9	139.7	736.6	19.3	7.85	3.40	25
32	9	203.2	736.6	8.0	18.94	10.19	75
33	9	203.2	736.6	8.0	12.62	6.79	50
34	9	203.2	736.6	8.0	6.31	3.40	25
35	9	203.2	736.6	--	--	--	--
36	6	203.2	736.6	38	3.74	3.02	50
37	6	203.2	736.6	19.3	3.74	3.02	50
38	6	203.2	736.6	8.0	3.74	3.02	50
39	6	203.2	736.6	--	--	--	--

CHAPTER 4 - Intermediate-Scale Testing Results

Introduction

The thermo-structural intermediate-scale tests on E-glass vinyl ester FRP laminates were performed as listed in Table 10. The applied loads, in-plane deflections, out-of-plane deflections, and temperature gradients were plotted with time. Test article failure was determined during testing as the point at which the test article was no longer capable of supporting the applied load. The test was further characterized by reducing the through-thickness temperature measurements recorded at the time of failure to an average temperature. The recorded data was used to characterize the test performed with varying dimensions, loads, and heat fluxes.

Testing Results

Failure Determination

Test article failure was characterized for the intermediate-scale testing by analyzing the recorded data from the tests. Recorded video of the tests was aligned with the measured applied load as well as in-plane and out-of-plane deflections. Test article failure is evident in the video recording; therefore, by aligning the measured data with the video, the data aligns with the visual recognition of failure. After reviewing the results from the tests with video, the failure of the E-glass vinyl ester test articles was determined to coincide with 2mm of in-plane deflection. The 2mm of in-plane deflection was defined as the failure criterion for the tests. The failure criterion was used to determine the time-to-failure of the test article. The time-to-failure was defined as the time elapsed from when the heater panels were moved in front of the test article to the test article failure.

Example Test Result

Tests were performed as described in the test matrix in Table 10. These tests included 36 heated tests and three unheated tests. An example of the results obtained from the 12mm, 38kW/m^2, 25% Euler buckling load test is included in Figure 30. Four plots were generated for each test and error bars are plotted for select signals to demonstrate measurement error. Refer to Appendix B for the error analysis. The temperature profile recorded at the mid-height of the laminate is shown in the upper-left plot. The out-of-plane deflections are shown in the upper-right plot with positive deflection defined as towards the heater panels. Refer to Figure 19 for out-of-plane deflection measurement locations. The laminate deflects towards the heaters initially, peaking at a value of 2mm at approximately 50 seconds. The laminate then begins to deflect away from the heaters, crossing the zero-plane and failing away from the heaters at 193 seconds. The in-plane deflection and applied load are plotted simultaneously in the lower-left

plot. In-plane deflection is defined as positive when the laminate is being compressed. The in-plane deflection is negative throughout the test until failure, showing that the laminate thermally expanded due heating. The applied load remains nearly constant during the test. The unexposed surface temperatures are shown in the lower-right plot. The plot shows that the temperatures except for those near the clamps (13mm and 724mm) are close throughout the test. This demonstrates the laminate is being heated in a uniform fashion over the majority of the panel. The remainder of the test results are presented in a similar fashion in Appendix C.

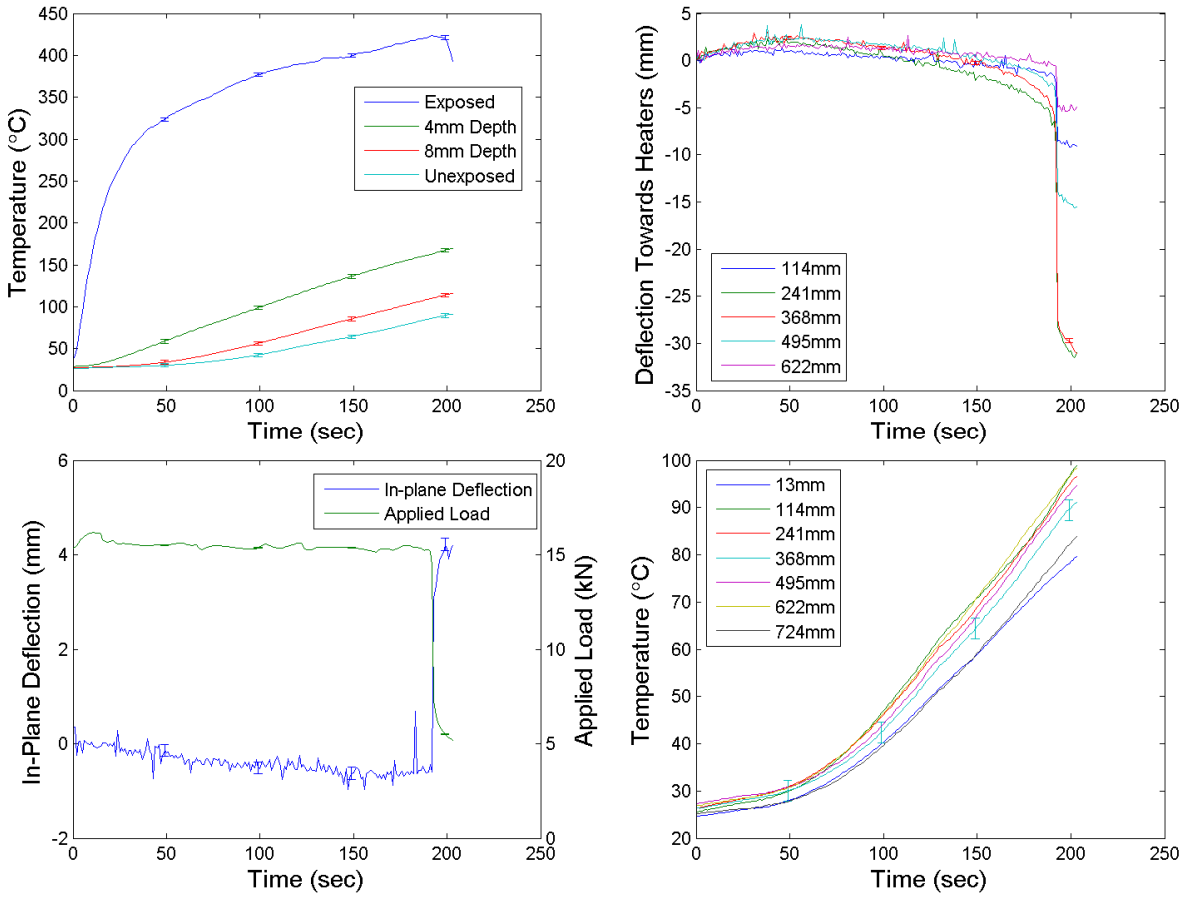

Figure 30. Example test result for 12mm, 38kW/m^2, 25% Euler buckling load test with plots of mid-height through-thickness temperature profile, out-of-plane deflections, in-plane deflection and applied load, and unexposed surface temperatures. Failure occurred at 193 seconds.

Temperature Profiles for Applied Heat Fluxes

The mid-height temperature profiles for the various applied heat fluxes are compared in Figure 31. The shown tests were selected on the basis of having the longest test run-time for the 12mm thick laminate. This corresponds to the tests at 25%, 15%, 15%, and 10% of the Euler buckling load for 8, 11.9, 19.3, and 38kW/m^2 heat fluxes, respectively. This provides a comparison of the relative scale of the through-thickness temperatures experienced by the laminate due to the varying heat fluxes. The highest heat flux, 38kW/m^2, has the largest

through-thickness temperature gradient with a measured exposed surface temperature above 500°C. As the heat flux is reduced, the temperature gradient through the thickness of the laminate also decreases. The steady-state exposed surface temperatures were measured to be approximately 240, 300, and 360°C for heat fluxes of 8, 11.8, and 19.3kW/m^2, respectively.

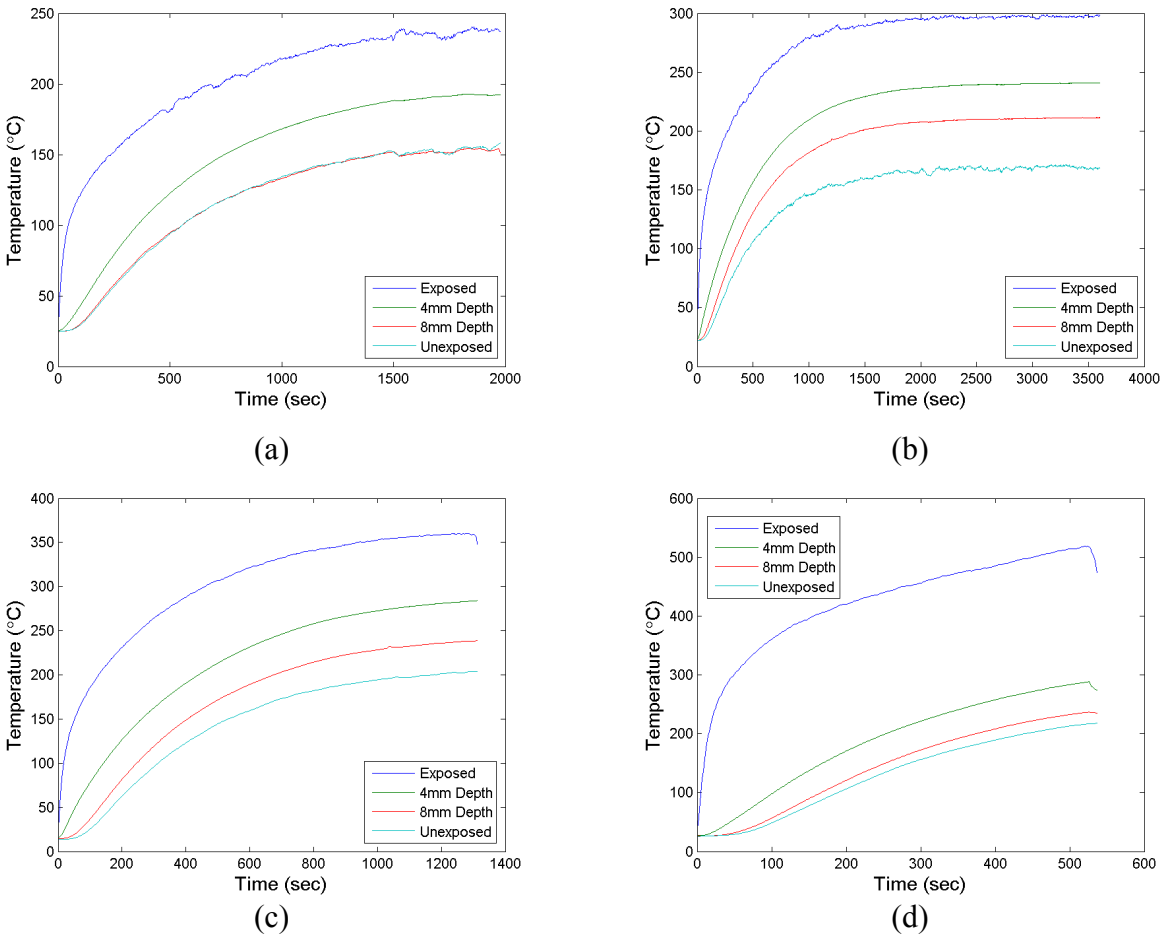

Figure 31. Mid-height through-thickness temperature profiles for 12mm thick laminate at (a) 8kW/m^2 (b) 11.8kW/m^2 (c) 19.3kW/m^2 and (d) 38kW/m^2 heat fluxes.

Observed Failure Modes

Several failure modes were observed during compressive testing of the thermally exposed laminates. Examples of the failure modes are shown in Figure 32. Three failure modes were visually observed during post-test inspection of the test articles. The observed failure modes were kinking, localized kinking, and forced-response deflection. The kinking failure mode was observed in tests with applied loads less than or equal to 15% of the Euler buckling load. The failure mode then transitioned to localized kinking with increasing applied load. In this failure mode, the laminate exhibited some out-of-plane deflection at failure with kinking through the thickness at the point of the largest deflection. At 50% of the Euler buckling load, the failure mode transitioned to forced-response deflection. The forced-response deflection failure mode is

characterized by significant out-of-plane deflection at failure with little to no kinking observed through the laminate thickness. The kinking visible in the example of forced-response deflection failure mode in Figure 32 was caused post-failure and was initiated by the significant out-of-plane deflections experienced during failure. The failure mode observed in post-test inspection showed no obvious dependence on heat flux or laminate thickness. The failure mode for the intermediate-scale tests performed in this research appears to solely depend on the applied load level. The failure mode transitions from kinking to localized kinking to forced-response deflection as the load level is increased as a percentage of the Euler buckling load.

(a) (b) (c)

Figure 32. Failure modes observed during testing include (a) kinking (b) localized kinking and (c) forced-response deflection.

Analysis of Test Results

Stress and Time-to-Failure Relationship

The 36 heated tests were analyzed to determine any relationships that exist between the various parameters investigated in testing. The first relationship examined was between the applied stress and the time-to-failure of the laminates. This relationship was plotted for all tests performed at each laminate thickness in Figure 33. The plots show that the time-to-failure for a given test is dependent on both the applied stress and the heat flux. This is evident in the plots for laminate thicknesses of 12mm and 9mm; however, there are not enough data points for the

6mm thickness to also draw this conclusion. The relationship between the applied stress and the time-to-failure is an inverse relationship. As the applied stress is increased, the time-to-failure decreases. The time-to-failure also decreases as the heat flux is increased; therefore, the relationship between the heat flux and the time-to-failure is also an inverse relationship. Also, a minimum applied stress for laminate failure can be inferred for each heat flux. Failure was not observed to occur for two tests: 9mm, 8kW/m^2, 25% buckling load and 12mm, 11.8kW/m^2, 15% buckling load. This is particularly evident in the plot for the 12mm laminates where the observed time-to-failure can be seen to asymptotically increase when decreasing the applied stress. If the applied stress is below this minimum stress level, the laminate will not fail at that given heat flux.

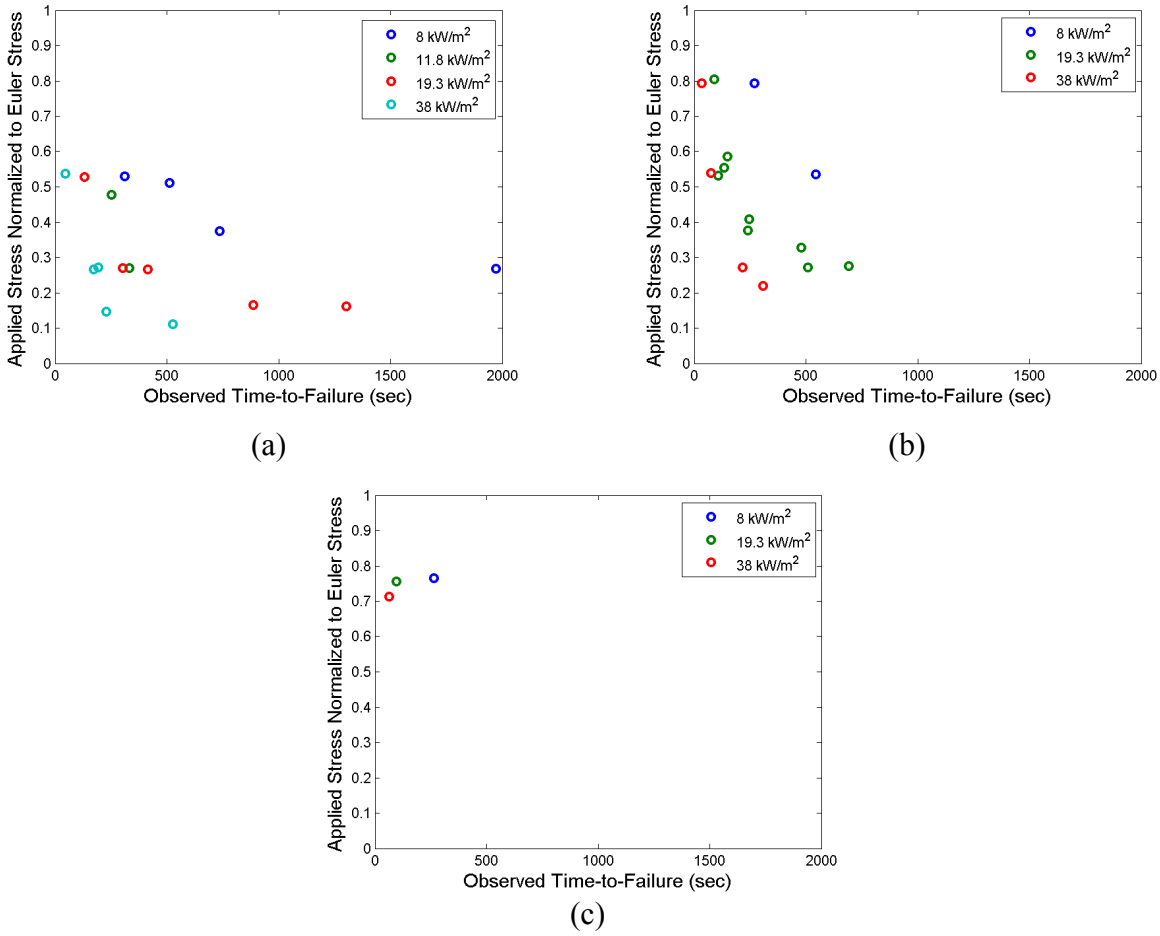

Figure 33. Stress normalized by critical Euler buckling stress against time-to-failure for laminate thicknesses of (a) 12mm (b) 9mm and (c) 6mm.

The tests performed also included a parametric study of the effect of the bending length and width of the laminate. These tests were isolated to the 9mm laminate thickness with an applied heat flux of 19.3kW/m^2. As with the previous plots, a relationship is evident between both the applied stress and the time-to-failure; however, there is no apparent relationship in regards to the length or width of the laminate. Therefore, the conclusion may be drawn that

varying the length or width to the degree done in the research for a given laminate thickness, applied stress, and heat flux will not significantly affect the time-to-failure of the laminate.

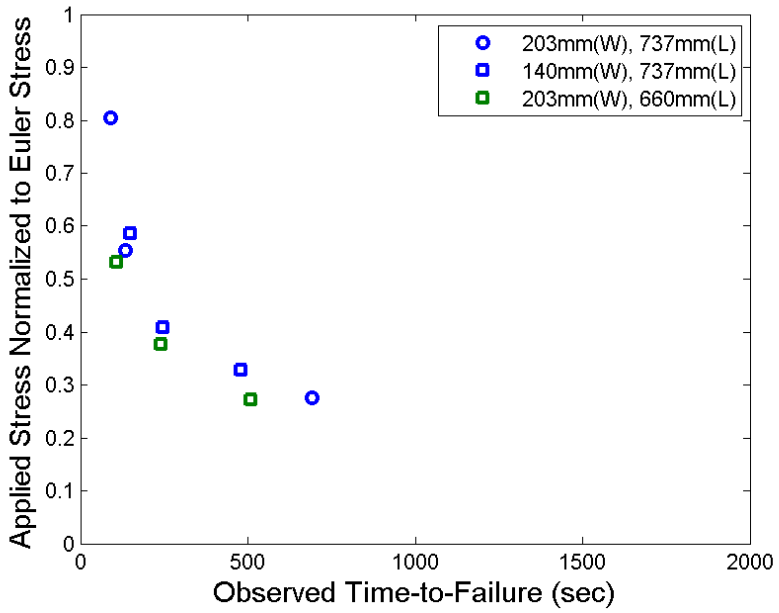

Figure 34. Applied stress normalized by Euler buckling stress against time-to-failure for parametric study performed for the 9mm thick laminate at 19.3kW/m^2.

All of the plots comparing normalized applied stress against time-to-failure for the different laminate thicknesses in Figure 33 were combined into a single plot in Figure 35. Error bars have been included to show the error associated with the time-to-failure as characterized by the repeatability test sets. The error associated with the observed time-to-failure is 24.12%, refer to Appendix B for calculation details. The error associated with the normalized applied stress is insignificant; therefore, the error bars are indistinguishable and have not been included in the plot. The relationship between both applied stress and heat flux with the time-to-failure of the laminate is again evident. A small dependency of the time-to-failure on the laminate thickness also exists causing the larger thicknesses to have shorter times-to-failure. This is most evident in the tests performed at a 19.3kW/m^2 heat flux. This may be caused by the relative levels of heat penetration into the laminate thickness. The heat will take longer to fully penetrate the larger thicknesses resulting in larger through-thickness temperature gradients. The in-plane thermal expansion is directly related to the temperatures through the laminate thickness; therefore, a larger thermal gradient results in a larger thermal expansion gradient. The thermal expansion gradient will cause a moment to be developed within the laminate, causing additional stresses. This additional stress will cause the laminate to fail in a shorter period of time.

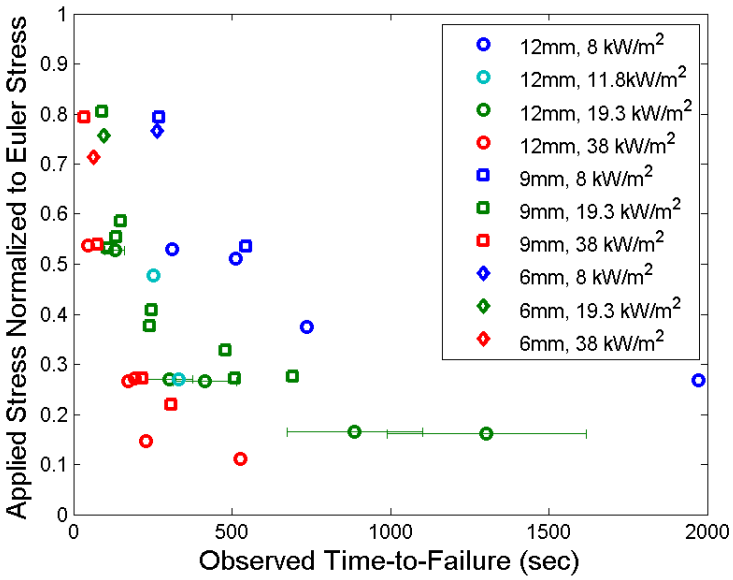

Figure 35. Applied stress normalized by Euler buckling stress against time-to-failure for all heated tests.

Stress and Surface Temperature at Failure Relationship

The heated tests were then analyzed to examine if a relationship exists between the applied stress and temperatures at failure on the exposed and unexposed surfaces. The tests performed for the parametric study were plotted for this relationship in Figure 36. There appears to be a linear relationship between the normalized applied stress and the exposed and unexposed surface temperature. The effect of length and width; however, is not evident in this relationship and a correlation between the time-to-failure and the length or width cannot be developed.

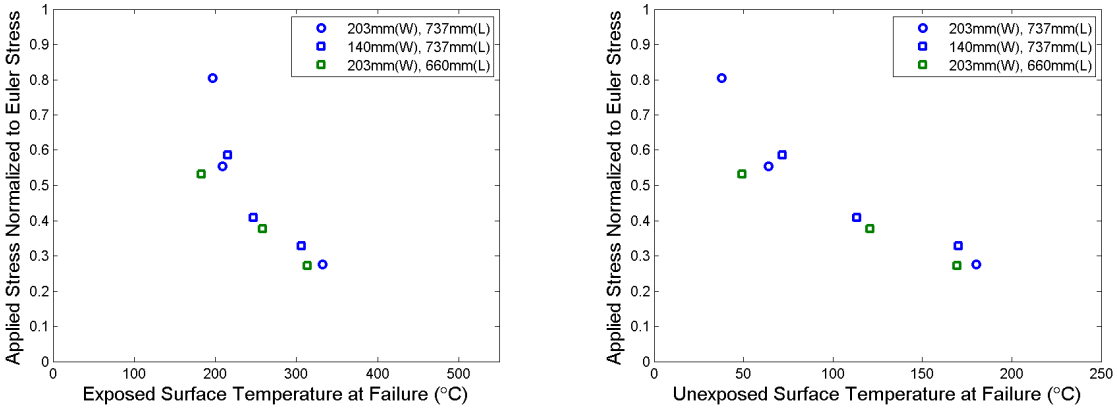

(a) (b)

Figure 36. Applied stress normalized by Euler buckling stress against (a) exposed surface temperature at failure and (b) unexposed surface temperature at failure for parametric study performed for the 9mm thick laminate at 19.3kW/m^2.

The heated tests were analyzed for the existence of a relationship between the normalized applied stress and surface temperatures at failure. A plot of this relationship is shown in Figure 37. As is expected, higher applied stress levels will result in the lower temperatures at failure at both the exposed and unexposed surfaces. A relationship between the applied heat flux and the exposed surface temperature at failure is also apparent. This is expected as the effect of the applied heat flux will be the greatest at the exposed surface; however, this does not reflect the heat penetration through the thickness of the laminate at failure. The unexposed surface temperature at failure should more accurately represent the heat penetration into the laminate at failure. This relationship, however, is not apparent in the plot as no clear relationship can be deduced.

The lack of a relationship between the unexposed surface temperature at failure and all parameters except the applied stress shows that these measurements alone cannot accurately represent the mechanics that cause failure of the laminate. This is in part due to the variation of the failure temperature due to the applied stress; however, it is evident that additional factors are involved in failure as the unexposed surface temperature at failure varies up to 100°C for a given stress level. Therefore, the selection of a single temperature measurement at either surface is not sufficient to evaluate the failure of the laminate.

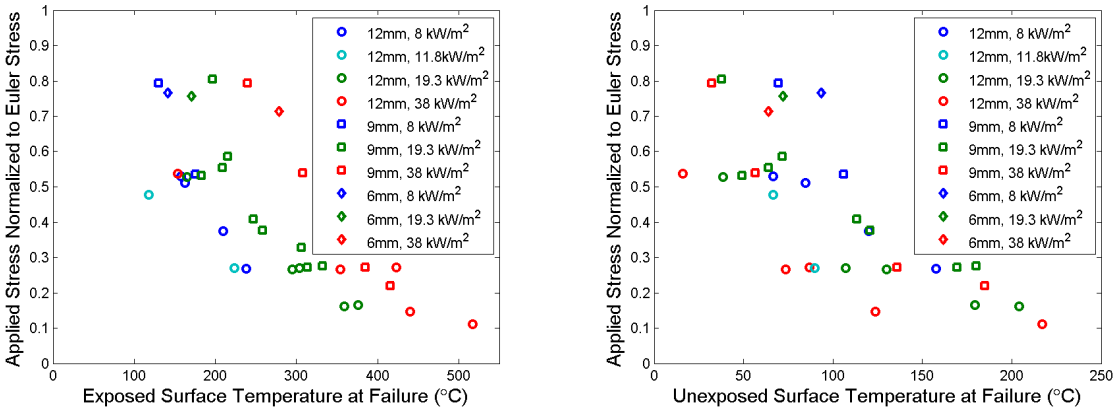

(a) (b)

Figure 37. Applied stress normalized by Euler buckling stress against (a) exposed surface temperature at failure and (b) unexposed surface temperature at failure.

Stress and Average Through-Thickness Temperature Relationship

The heated test laminate temperatures at failure were further analyzed by examining if a relationship exists between the applied stress and the average through-thickness temperature of the laminate at failure. The average temperature through the laminate thickness at failure gives a better representation of the heat penetration at failure. The average temperature captures the heat penetration through the laminate thickness through the use of multiple thermocouple measurements instead of selecting a single thermocouple measurement to represent the heat penetration. The average temperature of the laminate was calculated using the mid-height temperature profile. The temperature measurements were integrated through the thickness using

a trapezoidal integration scheme. The accuracy of this method is evaluated in Appendix B. The tests performed for the parametric study were first analyzed and are plotted in Figure 38. An inverse linear relationship exists between the applied stress and the average through-thickness laminate temperature at failure; however, no relationship exists between the length and width of the laminate and the average temperature at failure.

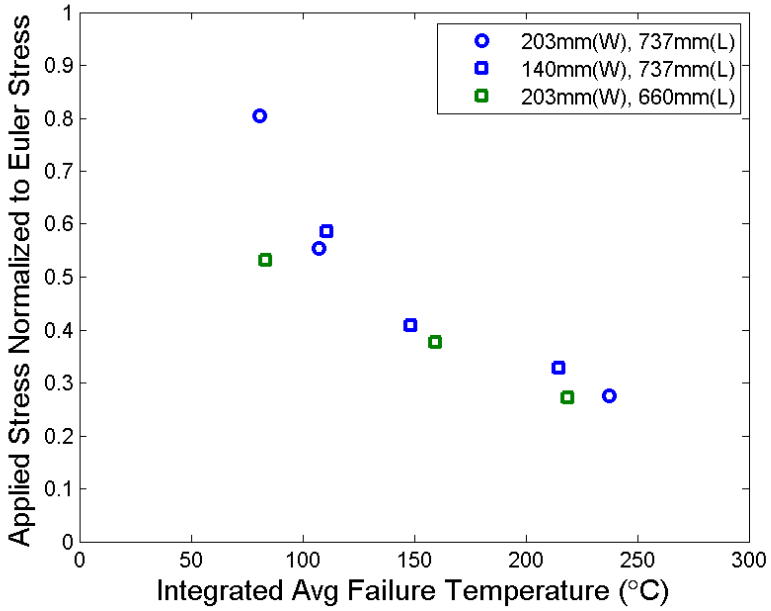

Figure 38. Applied stress normalized by Euler buckling stress against integrated average failure temperature for parametric study performed for the 9mm thick laminate at 19.3kW/m^2.

The heated tests were analyzed for a relationship between the normalized applied stress and the average temperature at failure. This relationship is plotted in Figure 39. The inverse relationship between the normalized applied stress and average failure temperature is again evident; however, the average temperature at failure is independent of the heat flux and laminate thickness. The average temperature is a good representation of the heat penetration in the laminate; therefore, the penetration of heat into the laminate at failure is highly dependent on the applied stress level. The average temperature at failure varies from approximately 75°C at high stress levels to nearly 300°C at lower stress levels with a wide variation at any given stress level. This exemplifies that there must be other factors involved causing the average temperatures at failure to vary in this manner.

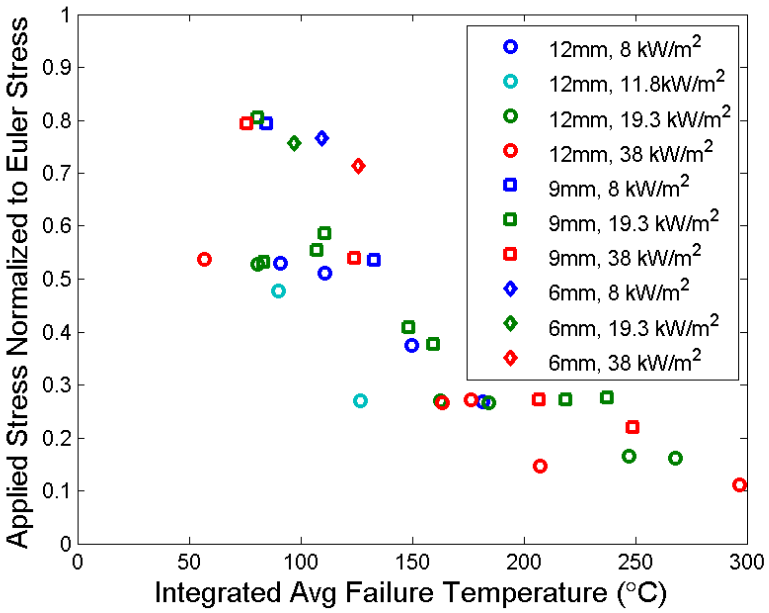

Figure 39. Applied stress normalized by Euler buckling stress against integrated average failure temperature for all heated tests.

The wide variation of the average through-thickness temperatures with normalized applied stress has significant implications in regards to construction involving FRP laminates. For a typical FRP laminate, such as the E-glass vinyl ester considered in this research, the glass transition temperature is approximately 120°C. Guidelines for marine structures state that the FRP laminates must be maintained below the glass transition temperature to protect the structural integrity of the design [63]. As previously stated, using the exposed or unexposed surface temperatures is not sufficient to define the failure of the laminate. The average temperature at failure varies widely around the glass transition temperature with higher stress levels failing at lower temperatures and lower stress levels failing at higher temperatures. If the failure criterion is defined as the glass transition temperature, it is evident that it is possible for the panel to fail prior to reaching this temperature at higher stress levels. Also, it is possible for the laminate to fail at temperatures much higher than the glass transition temperature for lower stress levels. Therefore, it is not advisable to use the average through-thickness laminate temperature, or any single laminate temperature, as the failure criterion for a compressively loaded laminate.

The relationship between the applied stress and average through-thickness temperature was also analyzed with respect to the slenderness ratio of the laminate. This relationship is plotted for both the applied stress and applied stress normalized to the room-temperature critical stress in Figure 41. The data corresponding to the 28 and 38.5 slenderness ratios was attained from the Royal Melbourne Institute of Technology (RMIT) [48] and Virginia Tech [27], respectively. These two series of tests were performed on similar E-glass vinyl ester laminates.

The experimental setups used for the small-scale tests performed at Virginia Tech and RMIT are shown in Figure 40. The small-scale tests performed at Virginia Tech used laminates comprised of St. Gobain/Vetrotex E-glass woven roving with a quasi-isotropic layup and Derakane 510A vinyl ester resin. This is the same material system used in the thermal model

validation. The laminates had a nominal thickness of 6mm and width of 25mm. The heated bending length of the laminates was 50mm. The laminates were placed between clamps in the loading mechanism and their scale inherently lends to compressive behavior governing laminate failure. The small-scale tests performed at RMIT used the same material system as the intermediate-scale tests performed in this research. The laminates had a nominal thickness of 9mm and width of 50mm. The bending length of the tests was 560mm; however, only the center 100mm of the laminate was heated with the regions above and below the heated section protected with high temperature insulation. The ends of the laminate were clamped at the grips. The laminate is treated in this research as though the bending length is the same as the heated length because the heating effects are of primary concern. Also, the end conditions are treated as pinned-pinned to more accurately represent the behavior at the ends of the heated section. Failure of the laminates used by RMIT was governed by axial compression with thermally induced bending due to the overall length of the laminates. The data for the Virginia Tech and RMIT small-scale tests were normalized with the ultimate stress and pinned-pinned Euler buckling stress, respectively, in accordance with the governing behavior for each set of tests.

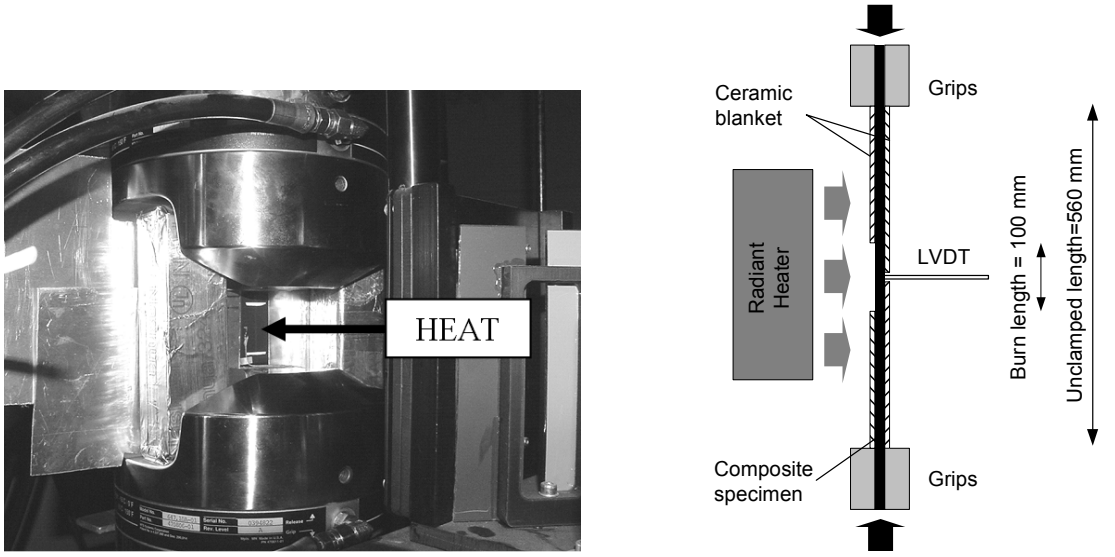

(a) (b)

Figure 40. Experimental setups for small-scale testing at (a) Virginia Tech [27] and (b) RMIT [48].

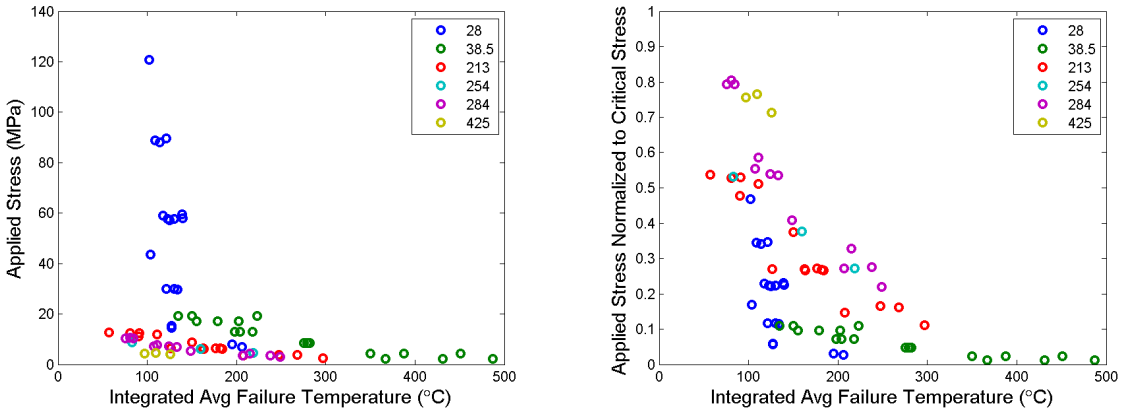

(a) (b)

Figure 41. The integrated average through-thickness temperature against (a) applied stress and (b) applied stress normalized with the room-temperature critical stress respective to scale.

The plot showing the applied stress demonstrates the effect different scales have on the average temperature at failure. This is most evident in the small-scale tests at a slenderness ratio of 28. These tests were performed with high applied stresses and low heat fluxes; however, normalization of the stress with the appropriate critical stress, the ultimate stress, results in a trend similar to that seen for the intermediate-scale tests performed in this research. The same result is achieved for the RMIT data when the applied stress is normalized with the appropriate critical stress, the Euler buckling stress. This demonstrates that a relationship exists between the normalized applied stress and the through-thickness temperature of the laminate at failure with a slight dependence on the slenderness ratio.

Compressive Stress-Strain Relationship

Compressive stress-strain curves for E-glass vinyl ester were obtained using constant temperature tests performed in a furnace environment. The compressive stress-strain curves were analyzed to determine the behavior of the laminate as it is compressed. The stress-strain curves are shown for several temperatures in Figure 42. The stress-strain relationship below 105°C exhibits linear elastic behavior until failure is reached. The stress-strain curve at 120°C shows a slight deviation from linear elastic behavior, however, this behavior remains a good approximation up to failure. The stress-strain curve at 135°C, which is above the glass transition temperature, shows two distinct regions of linear elastic and plastic behavior. The behavior remains linear elastic until the elastic limit is reached, at which point the material begins to behave plastically. The E-glass vinyl ester exhibits linear elastic behavior below the glass transition temperature; however, at temperatures above this, the behavior transitions to bilinear elastic-plastic. Due to this, it is assumed that the E-glass vinyl ester follows a bilinear elastic-plastic stress-strain relationship with no non-linear behavior.

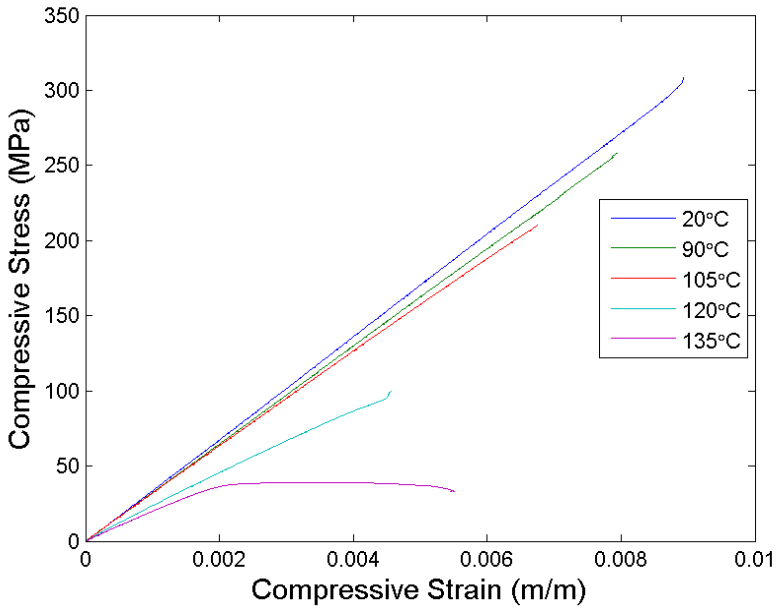

Figure 42. Stress-strain curves for E-glass vinyl ester at several temperatures.

Non-dimensionalized Stress and Slenderness Ratio Relationship

The relationship between the applied stress, slenderness ratio, and laminate temperature at failure was further analyzed to determine if it could be reduced to a simple relationship. In the analysis of steel and aluminum structures, buckling curves for compressed members can be generated in a dimensionless relationship [64]. These non-dimensionalized parameters are

$$\bar{\sigma} = \frac{\sigma_{cr}}{f_{0.2}} \qquad \text{Equation 109}$$

$$\bar{\lambda} = \frac{\lambda}{\lambda_0} = \frac{\lambda}{\pi\sqrt{E/f_{0.2}}} \qquad \text{Equation 110}$$

where σ_{cr} is the failure stress and $f_{0.2}$ is the proof stress and defines the elastic region of material with a non-linear stress-strain relationship. The equation for λ_0 is derived from the Euler buckling stress equation where the proof stress is substituted for the critical buckling stress. This set of non-dimensionalized equations is adapted for use with the thermally exposed, compressively loaded FRP laminates by adjusting the parameters resulting in

$$\bar{\sigma} = \frac{\sigma_{app}}{\sigma_c(T)} \qquad \text{Equation 111}$$

$$\bar{\lambda} = \frac{\lambda}{\lambda_0} = \frac{\lambda}{\pi\sqrt{E(T)/\sigma_c(T)}} \qquad \text{Equation 112}$$

Using this, the family of curves representing the properties at each temperature collapses into a single curve shown in Figure 43. The applied stress, σ_{app}, was substituted for the critical stress because the stress remains constant during testing of the thermally exposed laminate. The proof stress was replaced with the compressive strength as the critical stress for non-dimensionalization. The elastic modulus and compressive strength were made functions of temperature. Single values for the elastic modulus and compressive strength were calculated using the temperature measurements through the laminate thickness at failure. This completes the objective of creating a simple relationship to represent the relationship between the applied stress, slenderness ratio, and laminate temperature at failure.

The non-dimensionalized parameters developed in Equation 111 and Equation 112 are plotted in Figure 43. The data included in the plot includes the intermediate-scale tests performed in this research denoted by the three thicknesses, 6, 9, and 12mm, the small-scale tests performed by Virginia Tech [27], RMIT [48], and a single large-scale test performed at a research facility in Switzerland (EMPA) [54]. The solid line in the plot is considered the design line and data is compared to this line to determine how well it fits the associated failure mode. The failure modes selected to generate the design line are compressive and buckling failure. The selection of these failure modes assumes bilinear material behavior in the stress-strain relationship. The design line was created by setting the applied stress to the critical stress for the failure criteria associated with the current slenderness ratio. The flat portion corresponds to setting the applied stress to the compressive strength and the remainder sets the applied stress to the Euler buckling stress. This is plotted over a range of temperatures; however, the dependence on temperature is removed from the relationship by non-dimensionalizing the applied stress and slenderness ratio. This causes all of the lines generated for different temperatures to fall on the same line in the plot. The temperature dependence is represented in the non-dimensionalization of the applied stress and slenderness ratio.

The intermediate-scale test data was used to directly determine the compressive strength and elastic modulus at laminate failure. The through-thickness thermocouple measurements at failure were used to calculate the compressive strength and elastic modulus at each thermocouple location. A trapezoidal integration scheme was then used to determine the average compressive strength and elastic modulus values to use in non-dimensionalizing the applied stress and slenderness ratio. The four thermocouple measurements used to calculate the average mechanical properties provide sufficient accuracy, refer to Appendix B. The small-scale RMIT and Virginia Tech test data and the large-scale EMPA test data do not include enough thermocouple measurements through the thickness to accurately calculate either average mechanical property. In order to accurately calculate the mechanical properties at failure, the thermal model was used to predict the temperatures with time. The model was adjusted so as to accurately predict the measured temperatures in the test. The temperature profile from the model was used as the temperature profile of the laminate at failure. The average compressive strength and elastic modulus were calculated using the trapezoidal integration scheme over the full temperature profile. These values were then used to non-dimensionalize the applied stress and slenderness ratio for the small-scale and large scale tests.

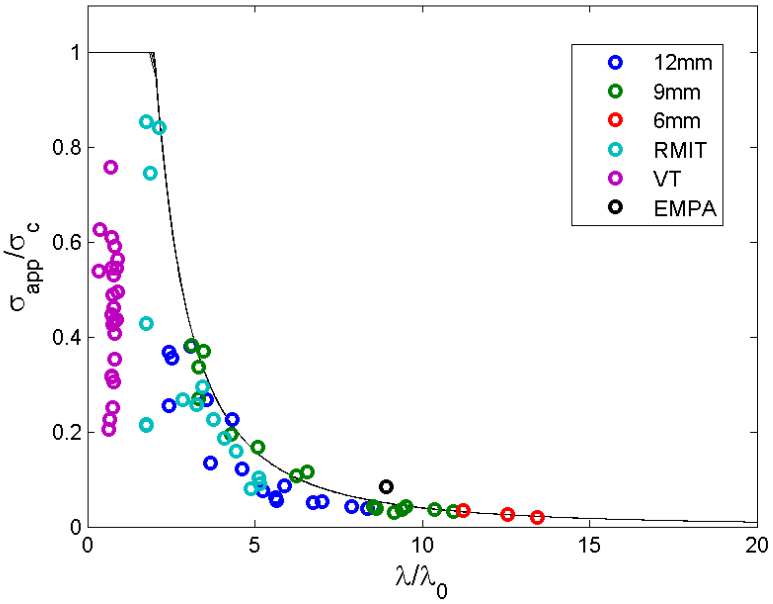

Figure 43. Non-dimensionalized applied stress against non-dimensionalized slenderness as a function of temperature.

The intermediate-scale data from tests performed in this research match well with the design line over the range of non-dimensionalized slenderness ratios. The data deviates from the line slightly at a non-dimensionalized slenderness ratio of approximately four. This may be attributed to some non-linear material behavior that is not represented with the assumption of two failure modes. The large-scale EMPA test deviates slightly but agrees well with the design line. The small-scale tests from RMIT show good agreement with the design line with two outliers at a non-dimensionalized slenderness ratio of approximately two. The small-scale tests from Virginia Tech, however, do not agree well with the design line. Reviewing the small-scale data in Figure 41 shows that significantly higher stresses were applied to the laminates in this set of tests than in the other test sets. Also, these tests were performed at lower heat fluxes of 5 to 20kW/m^2 and failed at average through-thickness temperatures that were approximately the glass transition temperature of E-glass vinyl ester. The inclusion of viscoelastic behavior in the compressive strength calculations would reduce the strength of the material and would adjust the data to more closely agree with the design line [42].

The non-dimensionalized plot of applied stress and slenderness ratio captures the relationship between the applied stress, slenderness ratio, and laminate temperature at failure. The non-dimensionalization simplifies the relationship between these parameters by reducing the family of curves for temperature to a single design line. The use of the non-dimensionalized slenderness ratio simplifies the analysis of the cross-section, potentially lending this as a simple form of analysis for more complicated cross-sections. The design line was generated using two assumed failure modes, compressive and buckling failure, as a function of temperature. The agreement of the intermediate-scale tests performed in this research and the large-scale EMPA test to the design line demonstrates the validity of the assumption that temperature-dependent buckling is the dominant failure mode for this scale of laminate. The small-scale RMIT data shows good agreement with the design line with some deviation which could be due to non-

linear material behavior. The small-scale Virginia Tech data does not agree well with the design line generated solely based on the compressive strength of the laminate. For better agreement, the compressive strength in these tests must be reduced by the inclusion of viscoelastic effects.

The non-dimensionalized plot for applied stress and slenderness ratio may be used in the design of compressively loaded FRP laminates subjected to fire conditions. The primary use of the plot is to relate the applied stress, slenderness ratio, and laminate temperature to the failure of the laminate. The plot may be used to determine an unknown parameter if the other two are known. This is achieved by determining the value of the third parameter that will cause the non-dimensionalized parameters to intersect at the design line. For example, in designing a load-bearing FRP laminate, the slenderness ratio and a pre-determined maximum laminate temperature are known. Using these two parameters, the applied stress that causes failure is determined by determining the applied stress that causes the non-dimensionalized parameters to intersect at the design line. In the same manner, if the applied stress and slenderness ratio of the load-bearing FRP laminate is known, the laminate temperature that causes failure may be determined. The non-dimensionalized parameters are calculated by varying the laminate temperature until the parameters intersect at the design line. The temperature that causes the intersection of the non-dimensionalized parameters at the design line is the laminate temperature causing failure.

The deviation of the test data from the design line needs to be taken into account when using the non-dimensionalized plot in Figure 43 for design purposes. The relative deviation appears to be separated into distinct regions associated with the two failure mechanisms considered, compressive strength and Euler buckling. To account for this deviation, a factor of safety for the non-dimensionalized applied stress was defined for both regions to ensure a conservative approximation based on the given test data. The compressive strength region, containing non-dimensionalized slenderness ratios less than approximately two, should be assigned a factor of safety of five. The region governed by Euler buckling, containing non-dimensionalized slenderness ratios greater than two, should be assigned a factor of safety of two. This factor of safety for the Euler buckling region covers all data points except two outliers. Inclusion of these outliers will cause the factor of safety to increase to three. Applying these factors of safety to the non-dimensionalized applied stress will account for the deviation between test data and the design line, ensuring a conservative design approximation using the design line. In summary, the non-dimensionalized plot for applied stress and slenderness ratio proves to be a useful tool in design by aiding in the determination of laminate failure based on its applied stress, slenderness ratio, and the temperature of the laminate.

CHAPTER 5 - Thermo-Structural Model Validation

Introduction

The thermo-structural model was validated using the results of the tests performed on the intermediate-scale E-glass vinyl ester laminates under compressive loads and subjected to one-sided heating. The thermo-structural modeling of the intermediate-scale tests performed in this research used the thermal and mechanical properties of E-glass Derakane 411-350 vinyl ester listed in Appendix A. The thermo-structural model was investigated to determine the sensitivity of the out-of-plane deflections and the predicted direction of failure to applied loads and heat fluxes. The model was then validated against the intermediate-scale test results. The model was only provided the parameters that were known prior to testing with no adjustments made based on the test results. The thermo-structural model results and intermediate-scale test results were then analyzed to determine the predictive capabilities of the model.

Model Sensitivity to Applied Load

The sensitivity of the thermo-structural model predictions to the applied loads and heat fluxes was investigated. A series of loads was applied to a 9mm thick laminate at each heat flux used in testing. The model predictions for the mid-height out-of-plane deflections are shown in Figure 44. The applied loads were varied from 5 to 25% of the Euler buckling load. The equation used to calculate the out-of-plane deflection in the model, Equation 97, has two major competing terms. These terms are the thermal moment, M_x^T, and the eccentric loading, Pe. The testing performed in this research considers one-sided heating of the composite. In the case of one-sided heating, the thermal moment, calculated using Equation 101, was calculated as negative and the eccentricity was calculated as positive using Equation 100. The relative scale of the two terms will therefore determine the direction and magnitude of the predicted deflections.

The thermal moment and eccentric loading terms interact to cause the laminate to deflect either toward or away from the heat source at failure. The individual effects of the thermal moment and eccentric load are to drive the laminate towards and away from the heat source, respectively. At the beginning of the simulations, a slight deflection occurs at all heat fluxes towards the heat source. This is caused by the large thermal gradient that is initially present in the laminate. The thermal moment is at a maximum negative value at this point and causes the deflection. The magnitude of the initial deflection is largest for the 38kW/m^2 heat flux due to the steep thermal gradient at this heat flux. As the simulation continues, the higher load levels have a tendency to fail towards the heat source. The laminate fails towards the heat source in these cases because the mechanical properties have been sufficiently reduced such that the laminate can no longer support the applied load. Since the laminate was initially deflected towards the heat source, the laminate will continue to deflect in this direction at failure.

The lower load levels, particularly at the highest heat flux, will experience failure of the laminate away from the heat source as the simulation continues. This is due to a combination of

both the thermal moment and the eccentric load. While the eccentric load drives the laminate to deflect away from the heat source, the thermal moment becomes positive for a short period of time. This is due to the effect of decomposition of the laminate on thermal expansion. As shown in Figure 45, the material decomposition greatly reduces the in-plane thermal expansion at the exposed surface while the remainder of the laminate continues in-plane thermal expansion. This, in combination with the reduction of the elastic modulus, will cause a reduction of the thermal moment from its maximum negative value and it may transition to positive, driving the laminate away from the heat source. When this occurs, the thermal moment and the eccentric load will jointly drive the laminate away from the heat source, causing the laminate to fail in this direction. The heat fluxes other than 38kW/m^2 do not cause high enough temperatures to cause the decomposition required to sufficiently affect the thermal moment; therefore, the laminate deflections will not change direction.

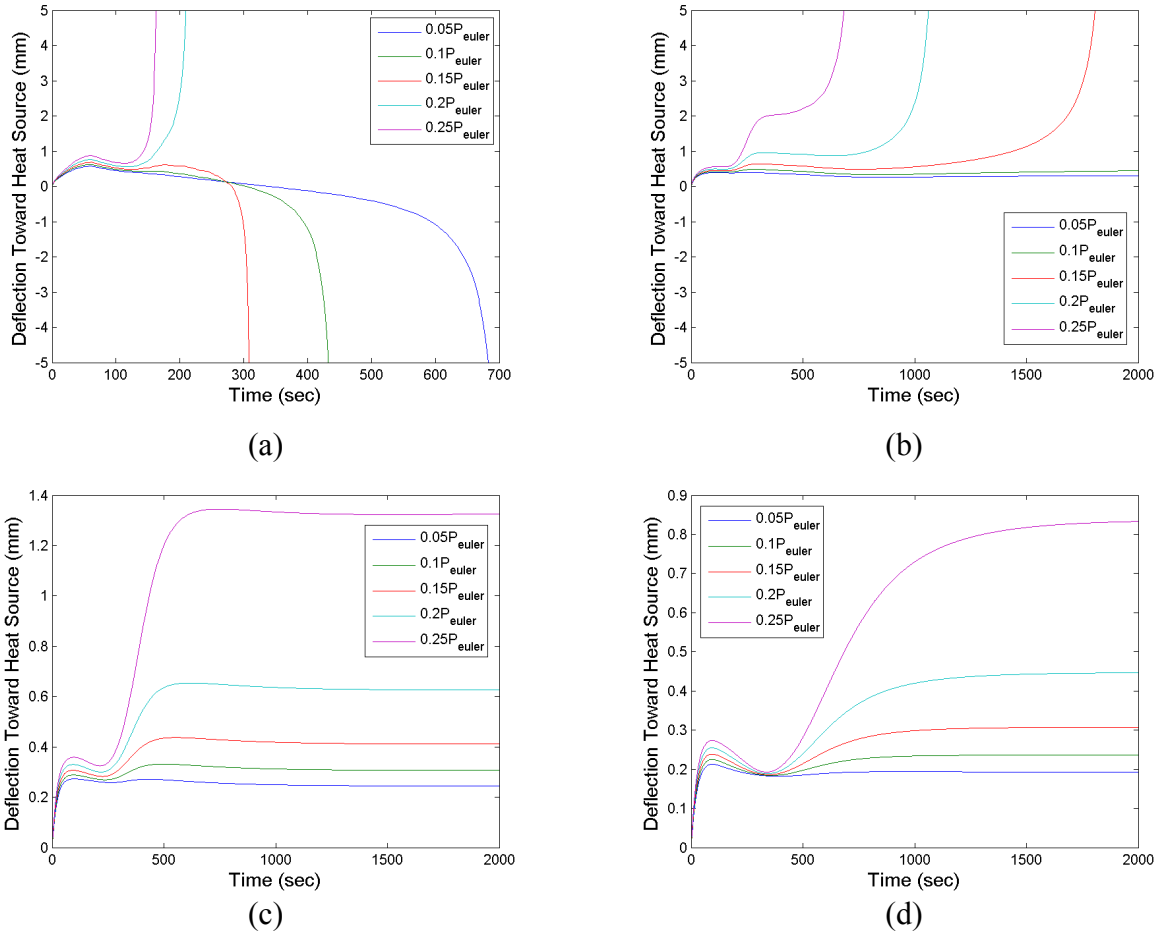

Figure 44. Sensitivity of thermo-structural model predictions to applied load for a 9mm thick laminate at (a) 38kW/m^2 (b) 19.3kW/m^2 (c) 11.8kW/m^2 and (d) 8kW/m^2.

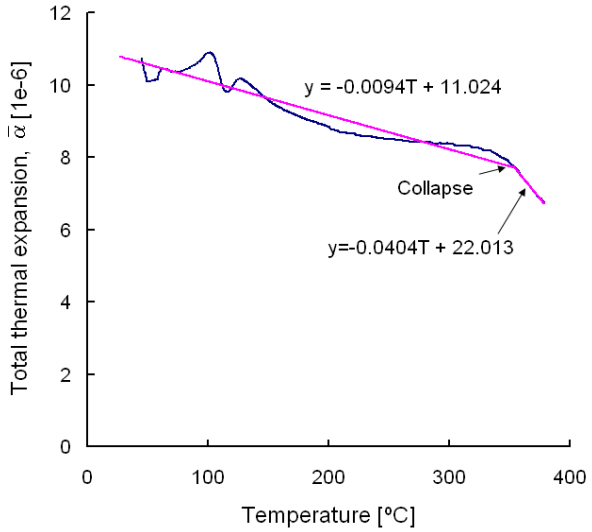

Figure 45. In-plane thermal expansion coefficient for E-glass vinyl ester [65].

Comparison of Model Predictions to Intermediate-Scale Test Results

The thermo-structural model was used as a tool to predict the results of the intermediate-scale tests performed in this research. The inputs to the model were considered as only those which were known prior to performing the tests. Additional changes were not made to the model parameters from post-test inspection or after analysis of the test results. In this sense, the model was used a purely predictive tool. Three tests were selected to demonstrate the predictive capabilities of the thermo-structural model. These tests were performed on laminates with a 12mm thickness and a 38kW/m^2 heat flux and applied loads of 15, 25, and 50% of the Euler buckling load. Plots of the comparison are shown in Figure 46, Figure 47, and Figure 48, respectively. Three plots are shown for each test prediction. The upper-left figure plots the mid-height out-of-plane deflections with time with a positive deflection being defined as towards the heater panels. The upper-right right plot depicts the local failure criterion with time. The maximum combined compressive stress non-dimensionalized by the local compressive strength is plotted with time. The solid black line at unity corresponds to the local compressive strength with time. Laminate failure is predicted to occur when the normalized maximum compressive stress is greater than this line, or unity. The discontinuity that occurs at approximately 400 seconds in the 15% buckling load test corresponds to the laminate changing directions of bending and is caused by the location of the maximum combined stress changing within the laminate. The bottom plot shows the mid-height through-thickness temperature profile predicted by the model against the corresponding temperature measurements with time. The solid and dashed lines represent the model predictions and test measurements, respectively, in the deflection and temperature plots.

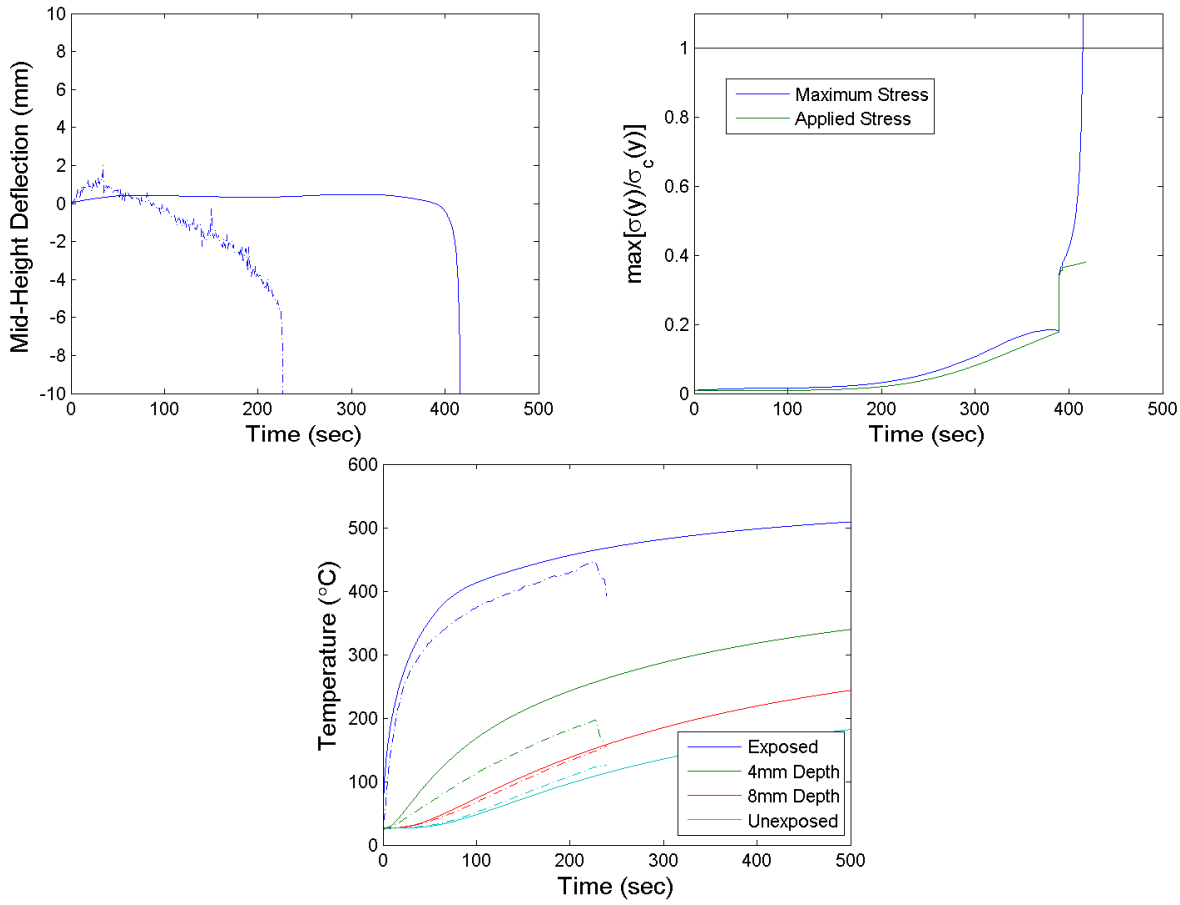

Figure 46. Comparison of the thermo-structural model predictions to the intermediate-scale test results for 12mm, 38kW/m^2, 15% buckling load test. Predicted time-to-failure was 415 seconds and experimental time-to-failure was 215 seconds.

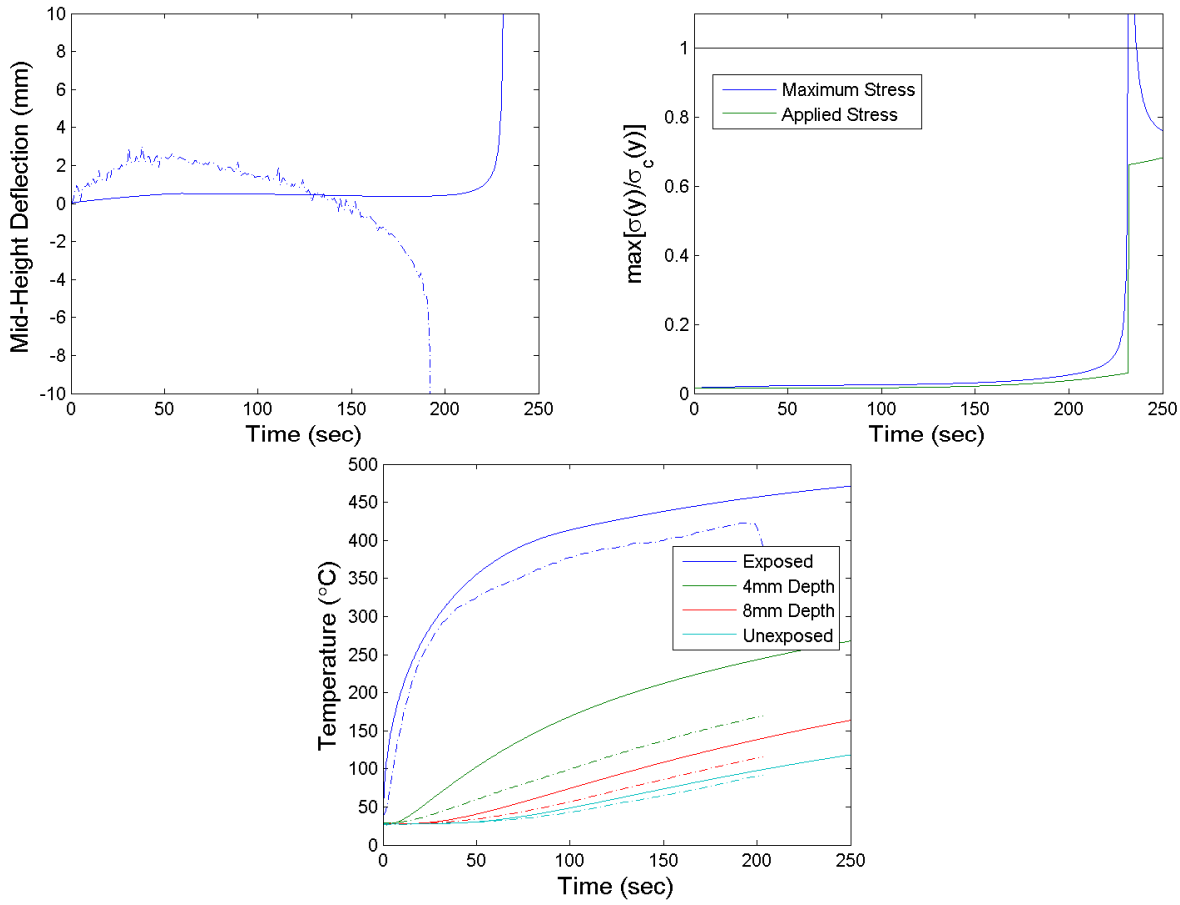

Figure 47. Comparison of the thermo-structural model predictions to the intermediate-scale test results for 12mm, 38kW/m^2, 25% buckling load test. Predicted time-to-failure was 232 seconds and experimental time-to-failure was 193 seconds.

The thermo-structural model predictions for these tests demonstrate the sensitivity of the out-of-plane deflections to the applied load. The predictions for the 15% buckling load case predict the laminate will fail away from the heaters, which agrees with what was seen experimentally. However, the predictions for the 25% buckling load case predict the laminate will fail towards the heater while the experiment shows it failing away from the heater again. The model predictions for these test cases agree with the previously performed sensitivity analysis; however, the directions of failure in the intermediate-scale test do not agree with the model.

The test results for the next load level for the 12mm thick laminate at 38kW/m^2 is shown in Figure 48. The thermocouple at the exposed surface in this test detached from the surface of the laminate causing the difference between the predicted and observed exposed surface temperature. The laminate was subjected to a compressive load of 50% of the Euler buckling load in this test. At this applied load, the laminate fails towards the heaters in both the intermediate-scale test results and thermo-structural model prediction. The intermediate-scale tests behave similarly to the model; however, the load level required to overcome the thermal

effects appears to be higher than predicted in the model. This behavior is generally followed at all thicknesses and heat fluxes.

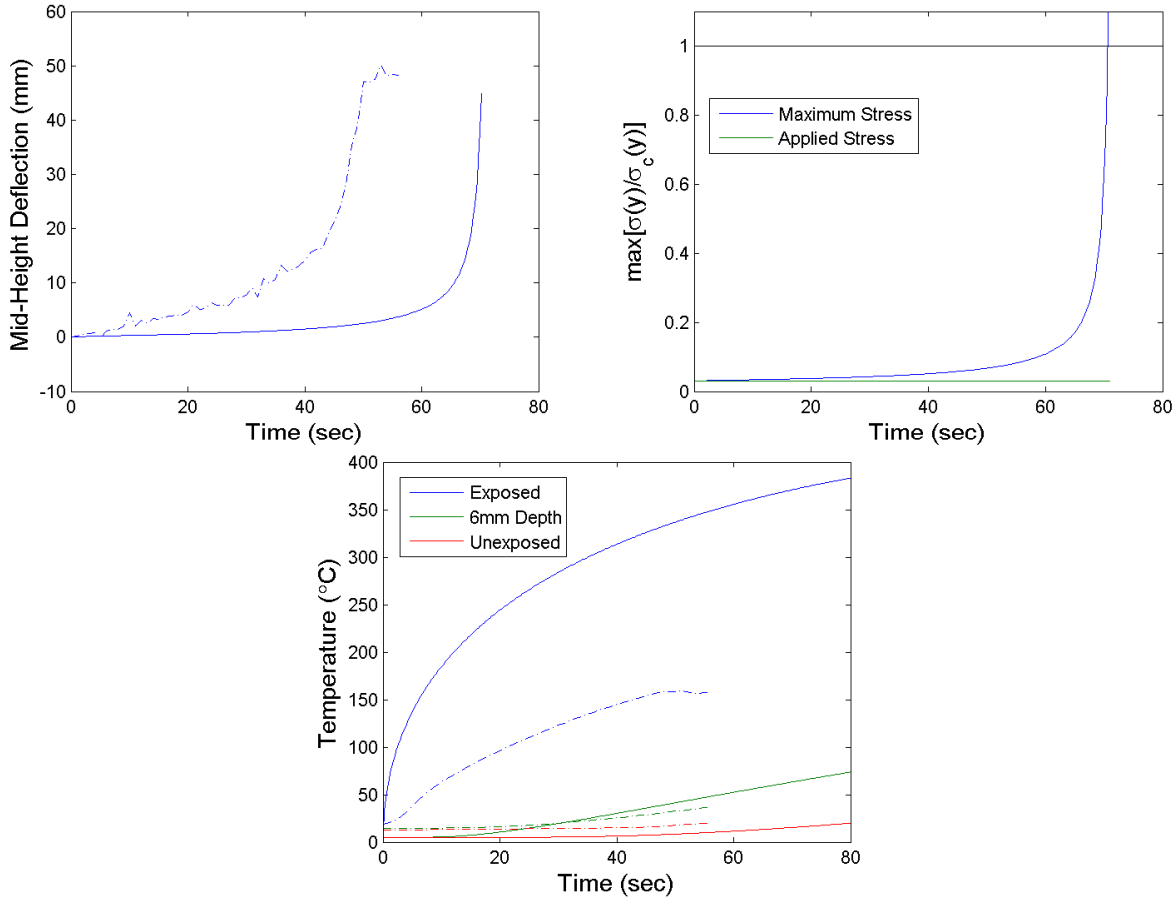

Figure 48. Comparison of the thermo-structural model predictions to the intermediate-scale test results for 12mm, 38kW/m^2, 50% buckling load test. Predicted time-to-failure was 71 seconds and experimental time-to-failure was 46 seconds.

The predicted through-thickness temperatures compare well with those measured experimentally except for those measured within the thickness of the composite. This is especially apparent in the shown tests at the 4mm depth. This deviation between the predicted and observed temperature within the thickness may be caused by the thermocouple mounting technique at these locations. The 3mm diameter hole for thermocouple mounting was made using a drill press with a depth stop with an accuracy of approximately 0.8mm. The thermocouple bead itself has a diameter of approximately 0.8mm. Given the conical shape of the hole caused by the drill bit, the accuracy of the drill press, and the size of the thermocouple bead, it is possible that the temperature measurement was actually up to a maximum of 1.6mm from the desired location.

The steep temperature gradients through the thickness of the composite could cause the temperature measurement to vary greatly with a variation of 1.6mm. Plots were created in Figure 49 to analyze the effect of the thermocouple location changing 1.6mm in a 12mm thick

laminate. The predicted temperatures due to the location change are shown as dashed lines while the solid lines represent the temperature for a perfect mounting depth. The relative scale of the change in temperature is constant at all of the heat fluxes. The difference in the predicted and measured temperatures in Figure 46, Figure 47, and Figure 48 falls within the bounds of the change in predicted temperatures due to a change in location. Therefore, the difference between the predicted and observed temperatures in the thickness of the laminate may be explained by the uncertainty in the measurement location.

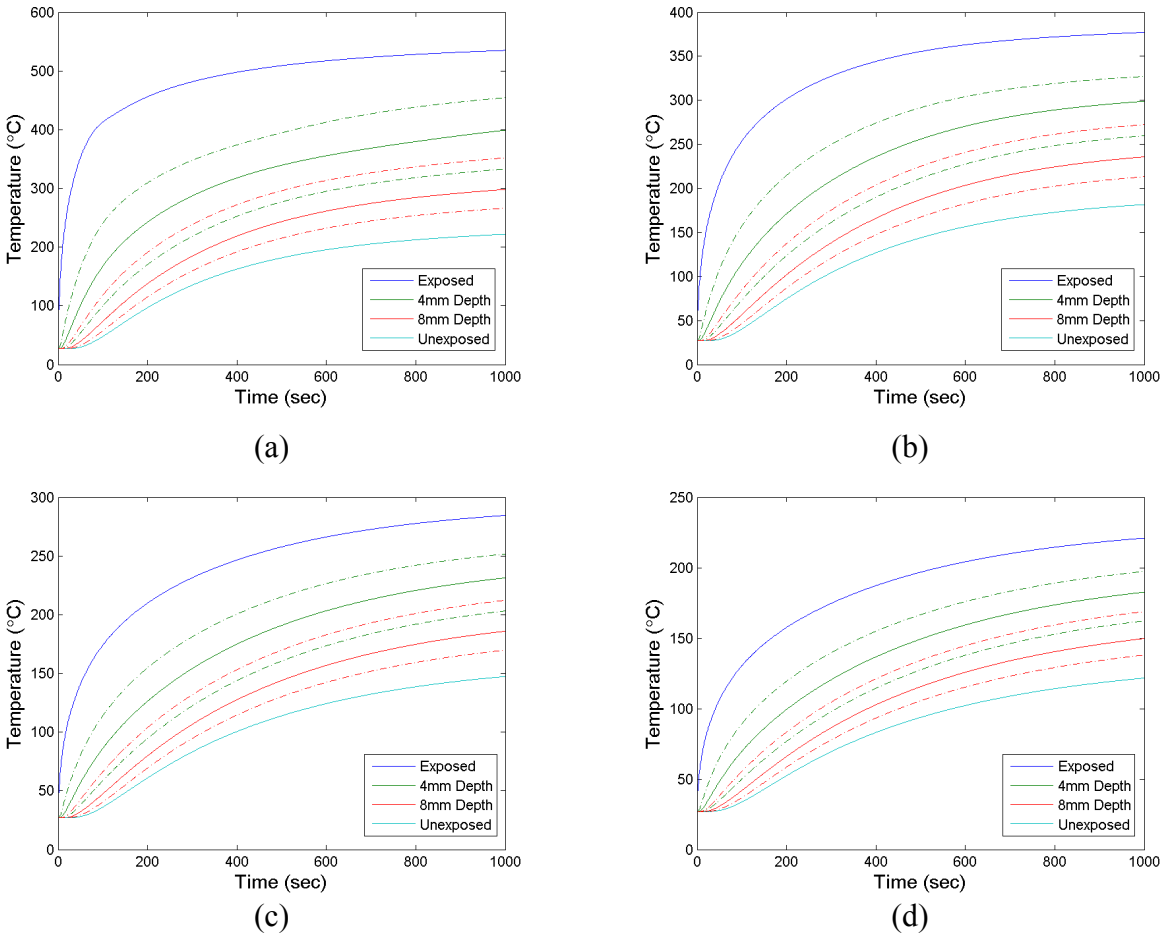

Figure 49. Through-thickness temperature profiles for 12mm laminate at (a) 38kW/m^2 (b) 19.3kW/m^2 (c) 11.8kW/m^2 and (d) 8kW/m^2 showing temperature bands for 1.6mm change in measurement location.

Comparison of Time-to-Failure Predictions

The thermo-structural model predictions for the time-to-failure of the laminate were compared against the observed times-to-failure from the intermediate-scale tests. A comparison of the times-to-failure is shown in Figure 50. The linear scale gives a good basis for comparison of the actual times-to-failure while the log-log plot compares the relative scale of the difference

between the predicted and observed times-to-failure. The solid line in both plots represents perfect agreement between predicted and observed times-to-failure.

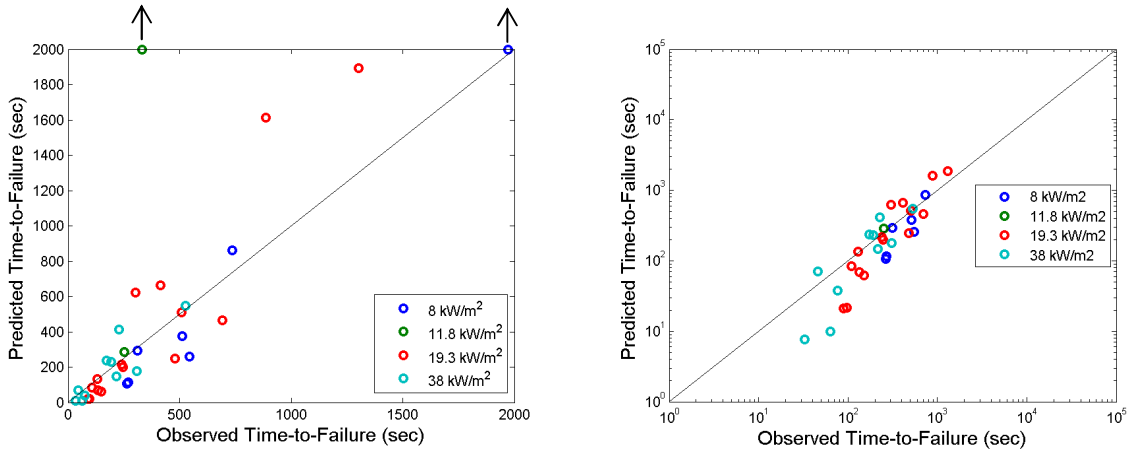

Figure 50. Predicted times-to-failure against observed times-to-failure plotted in (a) linear and (b) log-log scales.

The plot with the linear scale shows good agreement for a majority of the tests. Two tests were not predicted to fail and are shown at the top of the plot as run-out times in the model predictions. These tests are the 25% Euler buckling load tests at 8kW/m^2 and 11.8kW/m^2 for the 12mm thick laminate. In these tests, the laminate was subjected to the lowest applied loads that failed each test article at its respective heat flux for this thickness. Additionally, two predictions noticeably over-predict the time-to-failure at 19.3kW/m^2. These tests were both performed for the 12mm thick laminate with applied load levels of 15% of the Euler buckling load, again close to the lowest levels required to cause failure at the applied heat flux level.

The log-log plot also shows good agreement between the predicted and observed times-to-failure. The over-prediction of the two 19.3kW/m^2 tests in the linear plot is not noticeable in the log-log plot because this plot compares the relative scale of the difference in time-to-failure. For example, the linear plot will show the difference between a 1000 second failure prediction and a 2000 second observed time-to-failure as much greater than that for a 50 second failure prediction and 100 second observed time-to-failure. The log-log plot takes the magnitude of the times-to-failure into account and will plot these two example cases as equidistant from the line of agreement. This effect causes the log-log plot to show that good agreement between the predicted and observed times-to-failure exists; however, several outliers exist at the lower bound of the plotted data. These data points correspond to tests performed at loading levels exceeding 50% of the Euler buckling load for 9mm and 6mm thick laminates.

Overall, the thermo-structural model predicts the times-to-failure well when compared to the heated compression tests performed on intermediate-scale laminates in this research. The repeatability tests performed determined the uncertainty in the times-to-failure of the laminates to be approximately 24%. A majority of the data points fall within an error bound of 50% for the line of agreement for predicted and observed times-to-failure in Figure 50. Therefore, given the

error associated with the observed times-to-failure, the thermo-structural model predicts the time-to-failure of the compressively loaded, intermediate-scale FRP laminate accurately.

Comparison of Average Laminate Temperate at Failure

The thermo-structural model was further analyzed by comparing the measured average through-thickness laminate temperature at mid-height with that predicted by the model. The average through-thicknesses temperatures were calculated using a trapezoidal integration technique at the respective time-to-failure for the model predictions and testing. The comparison is shown in Figure 51. The average temperature at predicted model failure agrees well with the average temperature from test measurements at the observed laminate failure in testing. At higher temperatures, the model tends to predict the temperatures at failure as slightly higher than those observed in testing. This may be caused by one of several factors. As explained previously, there is error associated with the depth of the thermocouple position within the laminate. This could cause the measured laminate temperatures to be lower due to the thermocouple being placed further towards the unexposed surface than intended. There could also be non-linear mechanical behaviors, such as viscoelastic behavior, which the model does not take into account when predicting laminate failure. These effects include time-based material behavior and would cause the laminate to fail in a shorter period of time. This would be consistent with the over-prediction at higher temperatures, as higher temperatures generally infer longer times-to-failure. In summary, the thermo-structural model predicts an average through-thickness temperature at the predicted time-to-failure that is in good agreement with that measured at the observed time-to-failure during testing.

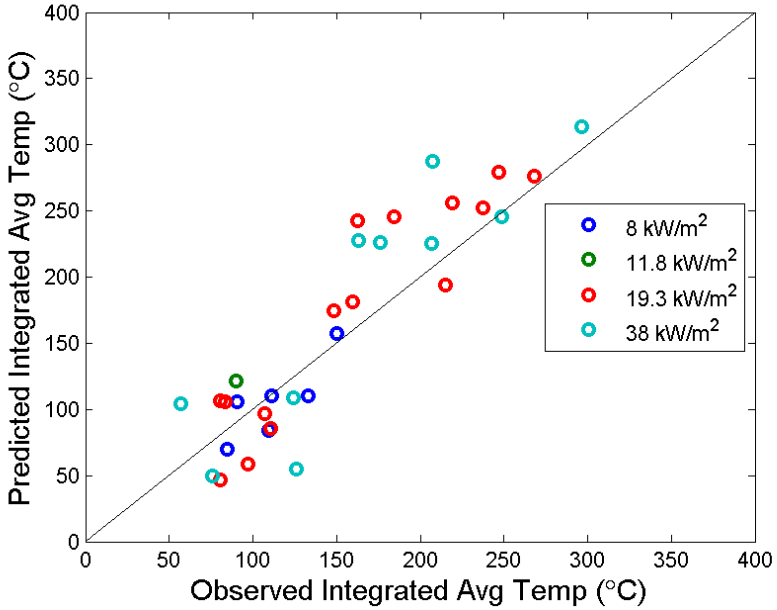

Figure 51. Predicted average through-thickness temperature at predicted laminate failure against the observed average through-thickness temperature of the laminate at observed failure in testing.

CHAPTER 6 - Summary & Conclusions

Summary

A thermo-structural model was developed to predict the thermal and structural response of a compressively loaded FRP laminate in fire conditions. The temperatures and decomposition state through the laminate thickness were calculated using a one-dimensional pyrolysis model developed in this research. The thermal model was developed based on that previously developed by Henderson, *et al.* [4]. The model calculates the thermal response using a set of three simultaneous equations: the energy equation, the mass conservation equation, and an equation for solid material decomposition. The thermal properties were defined as functions of both temperature and decomposition state of the material. The boundary conditions were defined such that Dirchlet (defined temperature), Neumann (defined heat flux), and Robin (convection, radiation, and heat flux) boundary conditions may be defined. The thermal model was implemented in MATLAB using the Galerkin method of weighted residuals, a form of the finite element method. The thermal model was verified using HEATING 7.3 [60] with excellent agreement and validated using tests performed by Lattimer, *et al.* [55] with good agreement.

The one-dimensional thermal model was implemented in a thermo-structural model to predict the through-thickness temperature gradient and material decomposition at the mid-height of a compressively loaded FRP laminate in fire conditions. The predicted temperature gradient was assumed to scale vertically according to an assumed parabolic shape due to centered heating. The mechanical properties were calculated as functions of temperature and material decomposition state. The structural portion of the model was developed to predict the structural response of the laminate considering thermally induced effects due to one-sided heating. The non-uniform temperature gradient through the laminate thickness causes a non-uniform mechanical property gradient, causing a shift in the neutral axis and a thermal moment due to non-uniform in-plane thermal expansion. The out-of-plane deflection and maximum combined compressive stress due to bending and axial compression were calculated by the thermo-structural model. The model used a local failure criterion to predict failure of the laminate when, at any point through the laminate thickness, the maximum combined compressive stress exceeded the compressive strength.

A series of intermediate-scale thermo-structural tests were performed on E-glass vinyl ester laminates to validate the thermo-structural model and develop design correlations. An intermediate-scale load frame capable of applying loads up to 200kN with fixed-fixed end conditions was constructed to perform these tests. An array of quartz-faced heater panels was used to apply one-sided heating to the test articles. The thermo-structural response was characterized with measurement of in-plane and out-of-plane deflections, temperatures, heat flux, and applied load during testing. A parametric study was performed on the E-glass vinyl ester laminates for varying thicknesses of 6, 9, and 12mm with a nominal height of 737mm and width of 203mm. The laminates were loaded from 10% to 75% of the laminate's Euler buckling load and heat fluxes were varied from 8 to 38kW/m^2.

The intermediate-scale tests performed generally exhibited one of three failure modes: kinking, localized kinking, and forced-response deflection. The test results were analyzed to develop correlations between the various parameters for use in design. An inverse relationship was observed between the observed time-to-failure and the normalized applied stress and heat flux. To further evaluate this relationship, the normalized applied stress was compared to temperatures in the laminate at failure. No relationship was evident between the applied stress and the surface temperatures at failure; however, a relationship was observed between the normalized applied stress and the average temperature through the laminate thickness at failure. In the aforementioned analyses, no relationship was observed in slightly varying the effective length or width of the laminate. The relationship relating normalized stress to average temperature was further analyzed on the basis of the laminate's slenderness ratio, introducing three additional test sets performed at RMIT [48], Virginia Tech [27], and EMPA [54]. A relationship was shown to exist between the normalized applied stress, average temperature at failure, and slenderness ratio of the laminate. The applied stress and slenderness ratios were non-dimensionalized using the method employed by Mazzolani [64] modified to be a function of temperature. A plot was created for the non-dimensionalized parameters with a design line plotted to show idealized bilinear behavior based on the non-dimensionalized buckling stress and compressive strength. The intermediate and large-scale tests, which were within the region governed by buckling, showed good agreement with the design line. The small-scale tests from RMIT were at the boundary between the two regions and showed noticeable deviations from the design line at points close to the compressive region. The small-scale tests from Virginia Tech fell within the compressive strength region and showed significant deviation from the design line. This demonstrates the scales of the laminate may change the dominant mechanics. This may be caused by additional behaviors, such as viscoelasticity, which are not included in the idealized material behavior. The non-dimensionalized plot for applied stress and slenderness ratio proves to be a useful tool to determine laminate failure by relating applied stress, slenderness ratio, and the laminate temperature at failure.

The intermediate-scale tests performed in this research were also used to validate the thermo-structural model for compressively loaded FRP laminates in fire conditions. The parametric nature of the tests lent itself to evaluating the model in various loading and heating conditions. The model was first used to demonstrate the sensitivity of laminate failure direction on the relative applied load and heat flux. At all loading and heating levels, the laminate initially deflected towards the heat source due to the thermal gradient through the laminate thickness. As the simulation continued the failure direction largely depended on the relative loading and heating levels with the combination of low loads and high heat fluxes causing the laminate to fail away from the heat source. This is the only combination of load and heat flux levels which caused failure away from the heat source in the analysis and is attributed to material decomposition which occurs at this level of heating. The thermo-structural model was run as a predictive model for all of the intermediate-scale tests performed in this research. The inputs to the model were used as only those values which were known prior to performing the tests. The predicted times-to-failure from the model showed good agreement with the observed times-to-failure. The predicted average temperature at failure was also compared to the average temperature at failure observed in testing with good agreement.

Conclusions

Many conclusions were made based on this research. The conclusions can be separated into those made in intermediate-scale testing and those in the thermo-structural modeling of FRP laminates. The lists below give the conclusions that were made.

Intermediate-Scale Testing

- Compressive loading of heated FRP laminates using a hydraulic system requires the implementation of a device to account for additional loading due to thermal expansion and maintain a constant load throughout a test.
- Three failure modes were observed in intermediate-scale compressive testing: kinking, localized kinking, and forced-response deflection. The failure modes were observed to be dependent on the stress level and independent of applied heat flux and laminate thickness.
- An inverse relationship exists between the applied stress normalized with the Euler buckling stress and the time-to-failure and applied heat flux.
- No apparent relationship exists between the normalized applied stress and the surface temperatures of the laminate at failure.
- A relationship was observed between normalized applied stress and the average temperature through the thickness of the laminate at failure.
- The plot of the normalized applied stress against the average temperature at failure showed some separation with slenderness ratio, showing a dependency on the slenderness ratio.
- No dependencies were observed between the various parameters (normalized applied stress, time-to-failure, surface temperatures at failure, and average temperature at failure) when the length and width of the laminate were varied.
- A non-dimensionalized plot was created based on the relationships used by Mazzolani [64] as a function of temperature with a design line plotted assuming bilinear elastic-plastic material behavior of E-glass vinyl ester. Intermediate-scale and large-scale tests show good agreement with the design line; however, small-scale tests show some deviation.
- The non-dimensionalized plot can be used in design to determine the value of one of the three parameters (applied stress, slenderness ratio, average laminate temperature at failure) which will cause laminate failure in fire conditions.

Thermo-structural Modeling of FRP Laminates

- A pyrolysis model can be used to accurately predict the thermal response of FRP laminates.
- Accurate thermal predictions require defining the thermal properties as functions of temperature and material decomposition state.
- The kinetic parameters in the solid material decomposition equation must be calculated properly using specifications defined by Goodrich [7] and Chodak [8] to obtain accurate thermal predictions.

- The finite element method in the form of the Galerkin method of weighted residuals is a satisfactory method in solving the set of simultaneous governing equations for the thermal response of decomposing material.
- Accurate predictions of the structural response require defining the mechanical properties as functions of temperature and material decomposition state.
- Structural modeling of slender FRP laminates in fire conditions must consider the thermally induced effects due to non-uniform heating of the exposed surface and the temperature gradient through the laminate thickness.
- The structural response of slender FRP laminates is adequately modeled using a thermally exposed beam approximation which takes into account the thermally induced moment and a shift in the neutral bending axis due to degradation of mechanical properties.
- The model was validated with good agreement using intermediate-scale tests performed with E-glass vinyl ester FRP laminates of 6, 9, and 12mm thickness with varying applied stresses and heat fluxes.
- The model predicts the initial deflection towards the heat source observed in testing.
- The times-to-failure predicted by the thermo-structural model show good agreement with the times-to-failure observed in intermediate-scale testing of FRP laminates.
- The predicted average temperatures through the laminate thickness at failure show good agreement with the average temperatures at failure measured in intermediate-scale testing of FRP laminates.

CHAPTER 7 - Recommendations

While this research has made substantial progress over what was known before it was undertaken, a great deal of work remains. The following list outlines some potential research objectives for future consideration.

- The pyrolysis model should be expanded from one-dimension to multiple dimensions to more accurately capture the temperature distribution of the compressively loaded FRP laminates.
- The thermo-structural model should be expanded to include out-of-plane thermal expansion and pore effects due to permeability and porosity.
- Time-dependency should be introduced to the model capture viscoelastic behavior.
- An adaptive mesh and time-step should be added to the thermo-structural model to improve model efficiency and reduce run-time.
- The effective bending rigidity should be changed to also follow the parabolic distribution of temperatures with height in development of the structural model.
- The compressive strength failure criterion should be changed to include the time-dependent behavior of the compressive strength due to the viscoelastic behavior of FRP laminates.
- More extensive tests should be performed on intermediate-scale FRP laminates to investigate the structural response at higher heat fluxes.
- More extensive tests should be performed on FRP laminates by more widely varying the width and height at the intermediate-scale.
- Tests should be performed to determine the effect of insulation on the structural response.
- Tests should be performed to evaluate the structural response of FRP laminates to non-uniform heating with height.
- Tests should be performed on FRP laminates at 6mm in thickness at load levels below 50% of the Euler buckling load to ensure the behavior follows that of the thicker laminates.
- Additional thermo-structural tests should be performed for different material systems within the family of fiber-reinforced polymers to verify the results of E-glass vinyl ester used in this research.
- The failure modes of the compressively loaded FRP laminates should be investigated for the incipient failure mechanisms.
- The non-dimensionalized design plot should be expanded to include viscoelastic behavior in the region governed by compressive failure.
- The analytical thermo-structural model should be verified using a three-dimensional finite element model, specifically investigating the predicted direction of failure and the effects of possible experimental errors, such as misalignment, on the failure direction.

References

1. Kung, H.C., *Mathematical model of wood pyrolysis.* Combustion and Flame, 1972. **18**(Compendex): p. 185-195.

2. Kansa, E.J., H.E. Perlee, and R.F. Chaiken, *Mathematical model of wood pyrolysis including internal forced-convection.* Combustion and Flame, 1977. **29**(3): p. 311-324.

3. Fredlund, B., *Modelling of heat and mass transfer in wood structures during fire.* Fire Safety Journal, 1993. **20**(1): p. 39-69.

4. Henderson, J.B., J.A. Wiebelt, and M.R. Tant, *A model for the thermal response of polymer composite-materials with experimental-verification.* Journal of Composite Materials, 1985. **19**(6): p. 579-595.

5. Henderson, J.B. and T.E. Wiecek, *A mathematical-model to predict the thermal response of decomposing, expanding polymer composites.* Journal of Composite Materials, 1987. **21**(4): p. 373-393.

6. Henderson, J.B., et al., *Characterization of the high-temperature behavior of a glass-filled polymer composite.* Composites, 1987. **18**(3): p. 205-215.

7. Goodrich, T.W., *Thermophysical Properties and Microstructural Changes of Composite Material at Elevated Temperatures*, in *Mechanical Engineering*. 2009, Virginia Polytechnic Institute & State University: Blacksburg, VA.

8. Chodak, J., *Pyrolysis and Hydrodanimcs of Fluidized Bed Media*, in *Mechanical Engineering*. 2010, Virginia Polytechnic Institute & State University: Blacksburg, VA.

9. Florio, J., et al., *A study of the effects of the assumption of local-thermal equilibrium on the overall thermally-induced response of a decomposing, glass-filled polymer composite.* International Journal of Heat and Mass Transfer, 1991. **34**(1): p. 135-147.

10. McManus, H.L.N. and G.S. Springer, *High-temperature thermomechanical behavior of carbon-phenolic and carbon-carbon composites-1. Analysis.* Journal of Composite Materials, 1992. **26**(2): p. 206-229.

11. McManus, H.L.N. and G.S. Springer, *High-temperature thermomechanical behavior of carbon-phenolic and carbon-carbon composites-2. Results.* Journal of Composite Materials, 1992. **26**(2): p. 230-255.

12. Dimitrienko, Y.I., *Thermomechanical behaviour of composite materials and structures under high temperatures .1. Materials.* Composites Part a-Applied Science and Manufacturing, 1997. **28**(5): p. 453-461.

13. Dimitrienko, Y.I., *Thermal stresses and heat-mass transfer in ablating composite materials.* International Journal of Heat and Mass Transfer, 1995. **38**(1): p. 139-146.

14. Gibson, A.G., et al. *A model for the thermal performance of thick composite laminates in hydrocarbon fires*. in *International Conference on Composite Materials in the Petroleum Industry*. 1994. Rueil-Malmaison, France: Editions Technip.

15. Looyeh, M.R.E., P. Bettess, and A.G. Gibson, *A one-dimensional finite element simulation for the fire-performance of GRP panels for offshore structures.* International Journal of Numerical Methods for Heat & Fluid Flow, 1997. **7**(5-6): p. 609-&.

16. Yu, B., V. Till, and K. Thomas, *Modeling of thermo-physical properties for FRP composites under elevated and high temperature.* Composites Science and Technology, 2007. **67**(15-16): p. 3098-3109.

17. Bai, Y., T. Vallee, and T. Keller, *Modeling of thermal responses for FRP composites under elevated and high temperatures.* Composites Science and Technology, 2008. **68**(1): p. 47-56.

18. Krysl, P., et al., *Finite element modelling of fibre reinforced polymer sandwich panels exposed to heat.* International Journal for Numerical Methods in Engineering, 2004. **61**(1): p. 49-68.

19. Sullivan, R.M. and N.J. Salamon, *A finite-element method for the thermochemical decomposition of polymeric materials-1. Theory.* International Journal of Engineering Science, 1992. **30**(4): p. 431-441.

20. Sullivan, R.M. and N.J. Salamon, *A finite-element method for the thermo-chemical decomposition of polymeric materials-2. Carbon phenolic composites.* International Journal of Engineering Science, 1992. **30**(7): p. 939-951.

21. Milke, J.A. and A.J. Vizzini, *Thermal response of fire-exposed composites.* Journal of Composites Technology & Research, 1991. **13**(3): p. 145-151.

22. Wu, Y.N. and N. Katsube, *A constitutive model for thermomechanical response of decomposing composites under high heating rates.* Mechanics of Materials, 1996. **22**(3): p. 189-201.

23. Wu, Y. and N. Katsube, *A thermomechanical model for chemically decomposing composites .1. Theory.* International Journal of Engineering Science, 1997. **35**(2): p. 113-128.

24. Wu, Y. and N. Katsube, *A thermomechanical model for chemically decomposing composites .2. Application.* International Journal of Engineering Science, 1997. **35**(2): p. 129-139.

25. Lua, J., et al., *A temperature and mass dependent thermal model for fire response prediction of marine composites.* Composites Part a-Applied Science and Manufacturing, 2006. **37**(7): p. 1024-1039.

26. Bausano, J.V., J.J. Lesko, and S.W. Case, *Composite life under sustained compression and one sided simulated fire exposure: Characterization and prediction.* Composites Part a-Applied Science and Manufacturing, 2006. **37**(7): p. 1092-1100.

27. Boyd, S., et al., *Mechanistic Approach to Structural Fire Modeling of Composites.* Fire Technology, 2010.

28. Kulcarni, A.P. and R.F. Gibson, *Non-destructive characterisation of effects of temperature and moisture on elastic moduli of vinyl ester resin and Eglass/vinyl ester resin composite*, in *American Society of Composites, 18th annual technical conference*. 2003: Florida.

29. Liu, L., et al., *Thermal buckling of a heat-exposed, axially restrained composite column.* Composites Part a-Applied Science and Manufacturing, 2006. **37**(7): p. 972-980.

30. Gibson, A.G., et al., *Laminate theory analysis of composites under load in fire.* Journal of Composite Materials, 2006. **40**(7): p. 639-658.

31. Feih, S., et al. *Modelling the compression strength of polymer laminates in fire*. in *3rd International Conference on Composites Testing and Model Identification*. 2006. Oporto, PORTUGAL.

32. Feih, S., et al., *Modelling the tension and compression strengths of polymer laminates in fire.* Composites Science and Technology, 2007. **67**(3-4): p. 551-564.

33. Dao, M. and R.J. Asaro. *A study on failure prediction and design criteria for fiber composites under fire degradation*. in *Symposium M on Advances in Polymer Matrix Composites - Microscopic to Macroscopic, at the Fall 1997 Materials-Research-Society Meeting*. 1999. Boston, Massachusetts.

34. Gu, P. and R.J. Asaro, *Structural buckling of polymer matrix composites due to reduced stiffness from fire damage.* Composite Structures, 2005. **69**: p. 65-75.

35. Gu, P. and R.J. Asaro. *Distortion of polymer matrix composite panels under transverse thermal gradients*. in *Joint Conference of the ASME Pressure Vessels and Piping Division/8th International Conference on Creep and Fatigue at Elevated Temperatures*. 2007. San Antonio, TX: Amer Soc Mechanical Engineers.

36. Gu, P. and R.J. Asaro, *Designing polymer matrix composite panels for structural integrity in fire.* Composite Structures, 2008. **84**(4): p. 300-309.

37. Gu, P., M. Dao, and R.J. Asaro, *Structural stability of polymer matrix composite panels in fire.* Marine Structures, 2009. **22**(3): p. 354-372.

38. Asaro, R.J., B. Lattimer, and W. Ramroth, *Structural response of FRP composites during fire.* Composite Structures, 2009. **87**(4): p. 382-393.

39. Kardomateas, G.A., G.J. Simitses, and V. Birman, *Structural Integrity of Composite Columns Subject to Fire.* Journal of Composite Materials, 2009. **43**(9): p. 1015-1033.

40. Liu, L., et al., *Compressive Response of Composites Under Combined Fire and Compression Loading.* Fire Technology, 2010.

41. Budiansky, B. and N.A. Fleck, *Compressive failure of fibre composites.* Journal of the Mechanics and Physics of Solids, 1993. **41**(1): p. 183-211.

42. Boyd, S.E., S.W. Case, and J.J. Lesko, *Compression creep rupture behavior of a glass/vinyl ester composite subject to isothermal and one-sided heat flux conditions.* Composites Part a-Applied Science and Manufacturing, 2007. **38**(6): p. 1462-1472.

43. Boyd, S.E., J.J. Lesko, and S.W. Case, *Compression creep rupture behavior of a glass/vinyl ester composite laminate subject to fire loading conditions.* Composites Science and Technology, 2007. **67**(15-16): p. 3187-3195.

44. Zhang, Z., S.W. Case, and J. Lua, *A model and finite element implementation for the thermo-mechanical analysis of polymer composites exposed to fire*, in *17th International Conference on Composite Materials*. 2009: Edinburgh, UK.

45. Key, C.T. and J. Lua, *Constituent based analysis of composite materials subjected to fire conditions.* Composites Part a-Applied Science and Manufacturing, 2006. **37**(7): p. 1005-1014.

46. Lua, J., *Thermal-mechanical cell model for unbalanced plain weave woven fabric composites.* Composites Part a-Applied Science and Manufacturing, 2007. **38**(3): p. 1019-1037.

47. Lua, J., *Hybrid Progressive Damage Prediction Model for Loaded Marine Sandwich Composite Structures Subjected to a Fire.* Fire Technology, 2010.

48. Mouritz, A., et al., *Mechanical Property Degradation of Naval Composite Materials.* Fire Technology, 2010.

49. Lattimer, B.Y., et al., *Structural Response of Fiber Reinforced Plastic Composites During Fires*. 2007.

50. IMO_Resolution_A.754(18), *Recommendation on Fire Resistance Tests for "A", "B", and "F" Class Division*, in *FTP Code - International Code for Application of Fire Test Procedures*. 1998, International Maritime Organization.

51. UL1709, *Rapid rise fire tests of protection materials for structural steel*. 1991, Underwriters Laboratories, Inc.: Northbrook, IL.

52. Greene, E., *Marine Composites*. Second ed: Online (http://www.marinecomposites.com).

53. *ASTM Standard E119, 2009c, "Standard Test Methods for Fire Tests of Building Construction and Materials," ASTM International, West Conshohocken, PA, 2009, DOI: 10.1520/E0119-09C, www.astm.org.*

54. Hugi, E., *Personal Communication*. 2010.

55. Lattimer, B., J. Ouellette, and J. Trelles, *Thermal Response of Composite Materials to Elevated Temperatures.* Fire Technology, 2010.

56. Dollimore, D., *The application of thermal-analysis in studying the thermal-decomposition of solids.* Thermochimica Acta, 1992. **203**: p. 7-23.

57. Flynn and Wall, *A quick, direct method for the determination of activation energy from thermogravimetric data.* Polymer Letters, 1966. **4**: p. 323-328.

58. Cunningham and Mcmanus, *Experimental investigation and modeling of high temperature degradation mechanisms*, NASA/CR-97-206190, Editor. 1996: NASA Lewis Research Center. p. March.

59. Pepper, D.W. and J.C. Heinrich, *The Finite Element Method: Basic Concepts and Applications*. 2nd ed. Computational and Physical Processes in Mechanics and Thermal Sciences. 2005: Taylor & Francis.

60. Childs, K.W., *HEATING 7 multidimensional, finite-difference heat conduction analysis code system*, in *Version 7.3*. 1999, Oak Ridge National Laboratory: RSICC Report PSR-199.

61. UNIFRAX, *Technical Data*. 2002.

62. Feih, S., *Temperature dependent bending and tensile stiffness*. 2010: Newcastle, U.K.

63. Beeston, A., *Reducing the weight of structural fire protection in composite ships.* BrandPosten, 2006. **34**.

64. Mazzolani, F.M., *Aluminum Alloy Structures*. 2nd ed. 1995, London, UK: E & FN Spon imprint of Chapman & Hall.

65. Feih, S., et al., *Modelling approaches for thermal-mechanical loading of composites during fire*. 2005, CRC-ACS.

Appendix A - Material Properties

Thermal Properties of Selected Materials

E-glass Derakane 510A Brominated Vinyl Ester Laminate

Material properties for the E-glass Derakane 510A brominated vinyl ester laminate were gathered from Lattimer, *et al.* [55]. The laminate used Saint-Gobain/Vetrotex 0.81kg/m^2 E-glass woven roving. The laminate was manufactured using the SCRIMP process with a quasi-isotropic layup. The thermal properties of this material are given as functions of temperature.

Thermal Conductivity

$$k_v = \left(4.405 \times 10^{-5}\right)T + 0.312 \qquad \text{Equation 113}$$

$$k_d = \left(2.830 \times 10^{-4}\right)T + 0.0949 \qquad \text{Equation 114}$$

Specific Heat Capacity

$$C_v = 0.0452T + 1080 \qquad \text{Equation 115}$$

$$C_d = 0.259T + 1041 \qquad \text{Equation 116}$$

$$C_g = \left(-1.7297 \times 10^{-2}\right)T^2 + 4.4007T - 91.151 \qquad \text{Equation 117}$$

Density

$$\rho_v = 1683 \qquad \text{Equation 118}$$

$$\rho_d = 1235 \qquad \text{Equation 119}$$

Solid Material Decomposition Model Parameters

$$A = 8.00 \times 10^{-39} \qquad \text{Equation 120}$$

$$E_a = 5.15 \times 10^5 \qquad \text{Equation 121}$$

$$n = 2.00 \qquad \text{Equation 122}$$

$$Q = -103.0 \qquad \text{Equation 123}$$

E-glass Derakane 411-350 Vinyl Ester Laminate

Material properties for the E-glass Derakane 411-350 vinyl ester laminate were gathered from various sources. The laminate used Colan AR105 0.83kg/m^2 Woven Roving plain weave E-glass fibers. The laminate was manufactured using the VARTM process with a warp-aligned layup. The thermal properties of this material are given as functions of temperature.

Thermal Conductivity

$$k_v = \left(-2.592\times10^{-4}\right)T + 0.3889 \qquad \text{Equation 124}$$

$$k_d = \left(2.830\times10^{-4}\right)T + 0.0949 \qquad \text{Equation 125}$$

Specific Heat Capacity

$$C_v = \left(-4.666\times10^{-3}\right)T^2 + 5.911T - 524 \qquad \text{Equation 126}$$

$$C_d = \left(3.850\times10^{-2}\right)T^2 - 64.68T + 28065 \qquad \text{Equation 127}$$

$$C_g = \left(-1.7297\times10^{-2}\right)T^2 + 4.4007T - 91.151 \qquad \text{Equation 128}$$

In-Plane Thermal Expansion

$$\alpha = \begin{cases} \left(-9.400\times10^{-9}\right)T + \left(1.359\times10^{-5}\right) & 273K < T \le 623K \\ \left(-4.040\times10^{-8}\right)T + \left(3.304\times10^{-5}\right) & 623K < T \le 648K \\ 0 & T > 648K \end{cases} \qquad \text{Equation 129}$$

Density

$$\rho_v = 1683 \qquad \text{Equation 130}$$

$$\rho_d = 1235 \qquad \text{Equation 131}$$

Solid Material Decomposition Model Parameters

$$A = 1.00\times10^{14} \qquad \text{Equation 132}$$

$$E_a = 216.5\times10^3 \qquad \text{Equation 133}$$

$$n = 0.90 \qquad \text{Equation 134}$$

$$Q = -870 \qquad \text{Equation 135}$$

Mechanical Properties of Selected Materials

E-glass Derakane 411-350 Vinyl Ester Laminate

The mechanical properties for the E-glass Derakane 411-350 vinyl ester laminate were gathered from [31, 62]. The elastic modulus and compressive strength properties were calculated using the semi-empirical relationship from Equation 99. This equation is referenced for clarification of parameter definitions.

$$P(T) = \left(\frac{P_{(0)} + P_{(R)}}{2} - \frac{P_{(0)} + P_{(R)}}{2} \tanh\left(\Phi\left(T - T_k\right)\right) \right) R_{rc}(T)^{\beta} \qquad \text{Equation 99}$$

Elastic Modulus Empirical Relationship Parameters

$$E_{(0)} = 25.3 \times 10^9 \qquad \text{Equation 136}$$

$$E_{(R)} = 7.9 \times 10^9 \qquad \text{Equation 137}$$

$$\Phi = 0.054 \qquad \text{Equation 138}$$

$$T_k = 385.0 \qquad \text{Equation 139}$$

$$\beta = 3.0 \qquad \text{Equation 140}$$

Compressive Strength Empirical Relationship Parameters

$$\sigma_{c,(0)} = 433.3 \times 10^6 \qquad \text{Equation 141}$$

$$\sigma_{c,(R)} = 10.0 \times 10^6 \qquad \text{Equation 142}$$

$$\Phi = 0.0264 \qquad \text{Equation 143}$$

$$T_k = 361.3 \qquad \text{Equation 144}$$

$$\beta = 3.0 \qquad \text{Equation 145}$$

Appendix B - Error Analysis

Measurement Error

The experimental error is listed for each measurement taken during testing in Table B-1. The error associated with measurement and measurement device are used to analyze the error associated with calculations performed in this research.

Table B-1. Measurement devices and associated error.

Measurement	Measurement Device	Accuracy	Range	Error
Load	Omega LCCA-15K	0.037%	66.7 kN	± 24.7N
In-plane deflection	Celesco 254mm string potentiometer	0.05%	0 – 254mm	± 0.127mm
Out-of-plane deflection	Celesco 381mm string potentiometer	0.05%	0 – 381mm	± 0.191mm
Heat flux	Medtherm #64-20SB-19	3%	0 – 200kW/m^2	± 6kW/m^2
Temperature	Omega K-type thermocouple	--	-200°C – 1350°C	± 2.2°C
Laminate Thickness	Dial calipers	--	254mm	± 12.7μm
Laminate Height/Width	Graduated ruler	--	1.22m	± 0.79mm

Repeatability Error

The error associated with the repeatability of a single test was determined. The error associated with the repeatability is characterized by the times-to-failure of the four sets of repeatability tests. The four sets of repeatability tests and their associated times-to-failure are shown in Table B-2 and Figure B-1 to Figure B-4. The mean time-to-failure was calculated for each repeatability test set. The percent difference of the individual tests from the mean time-to-failure was then calculated. The cumulative error of the mean difference in time-to-failure and the standard deviation of the differences between test sets was calculated to be 24.12%.

Table B-2. Description of repeatability test sets.

Repeatability Set	Thickness (mm)	Heat Flux (kW/m^2)	$\%P_{euler}$	Test Number	TTF (sec)	Mean TTF (sec)	Error (%)
1	12	8.0	50	11 14	311 513	412 ± 101	24.5
2	12	38.0	25	2 15	887 1303	1095 ± 208	19.0
3	12	19.3	25	6 16	303 414	358.5 ± 55.5	15.5
4	12	19.3	15	7 17	193 173	183 ± 10	5.5

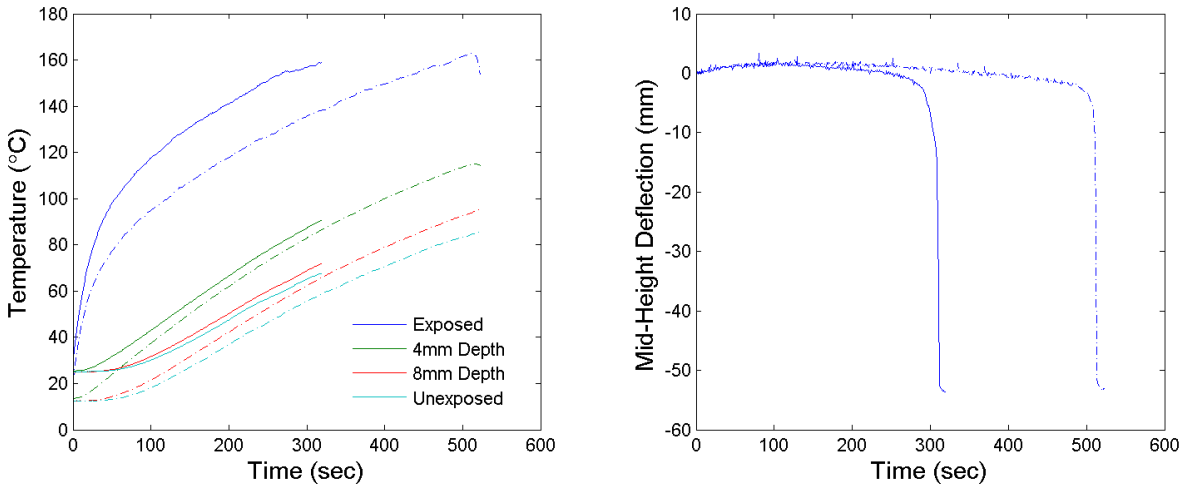

Figure B-1. Comparison of repeatability test set for 12mm thick laminate with 8kW/m^2 applied heat flux and applied load of 50% of the Euler buckling load.

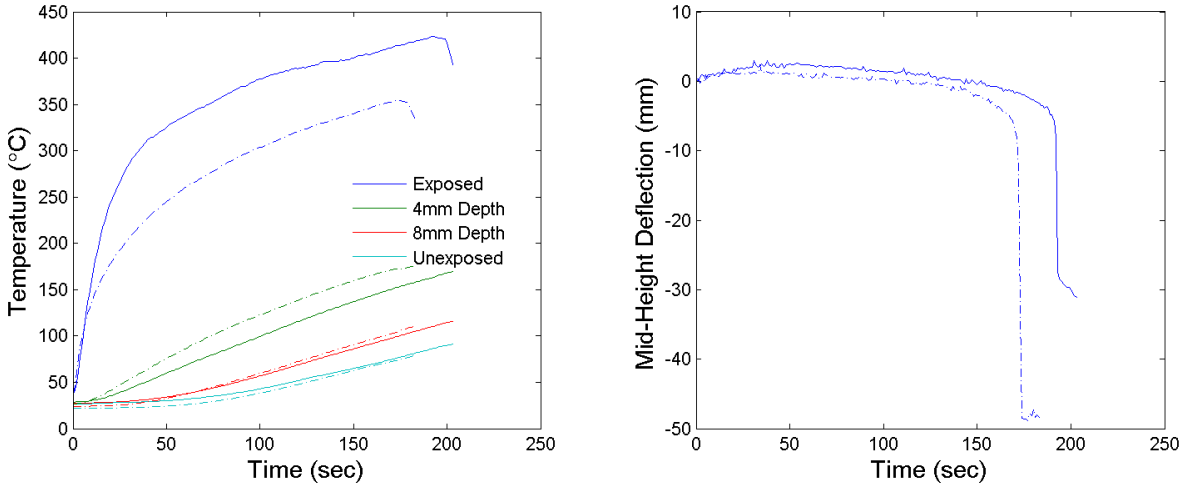

Figure B-2. Comparison of repeatability test set for 12mm thick laminate with 38kW/m^2 applied heat flux and applied load of 25% of the Euler buckling load.

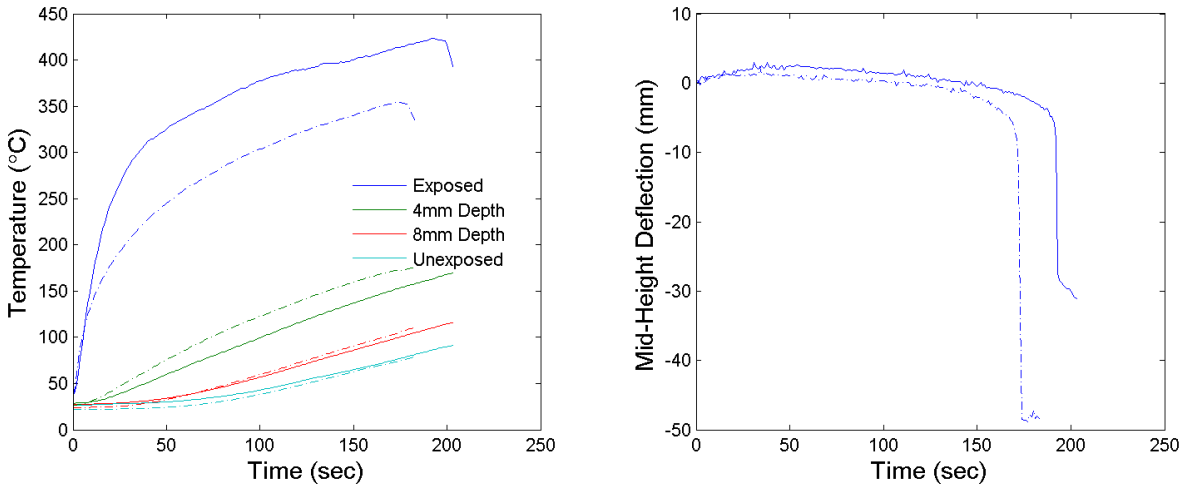

Figure B-3. Comparison of repeatability test set for 12mm thick laminate with 19.3kW/m^2 applied heat flux and applied load of 25% of the Euler buckling load.

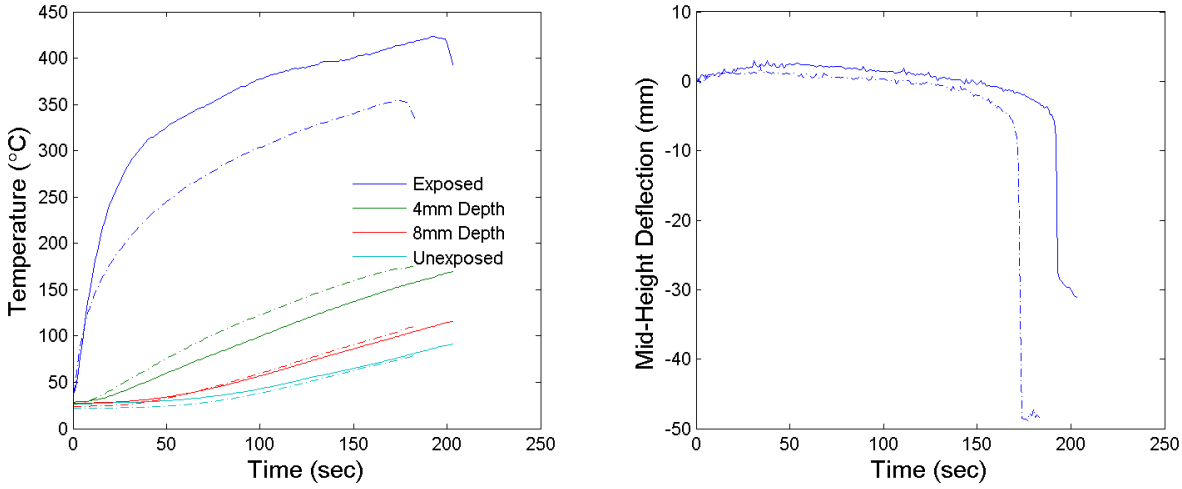

Figure B-4. Comparison of repeatability test set for 12mm thick laminate with 19.3kW/m^2 applied heat flux and applied load of 15% of the Euler buckling load.

Mechanical Property Error

The error associated for the mechanical properties was determined from the data sets provided in Feih, *et al.* [31, 62]. The error associated with these properties calculated as the average percent error from the tabulated data provided in these sources. The average error values for the elastic modulus and compressive strength are provided in Table B-3.

Table B-3. Mechanical property error.

Mechanical Property	Error (%)
Elastic modulus	4.0
Compressive strength	4.0

Error Analysis for Parameter Calculation

The error associated with the calculation of parameters was calculated using the following general relationship for calculating error

$$\psi_y = \left[\left(\frac{\partial y}{\partial x_1} \psi_{x_1} \right)^2 + \left(\frac{\partial y}{\partial x_2} \psi_{x_2} \right)^2 + \left(\frac{\partial y}{\partial x_3} \psi_{x_3} \right)^2 + \cdots \right]^{1/2} \quad \text{Equation 146}$$

where w is the variation in a particular variable, y is the parameter being calculated, and the x values are the variables in the expression.

Applied Stress Error

The error in the applied stress calculation is determined using Equation 146. The errors associated with the load, thickness, and width measurements are combined with the appropriate derivatives of the applied stress equation to calculate the applied stress error

$$\sigma_{app} = \frac{P}{A_{cs}} = \frac{P}{l \cdot w} \quad \text{Equation 147}$$

$$\psi_{\sigma_{app}} = \left[\left(\frac{1}{l \cdot w} \psi_P \right)^2 + \left(-\frac{P}{l^2 w} \psi_l \right)^2 + \left(-\frac{P}{l w^2} \psi_w \right)^2 \right]^{1/2} \quad \text{Equation 148}$$

Critical Euler Buckling Load Error

The error in the critical Euler buckling load is calculated in multiple steps. First, the error in the moment of inertia is calculated

$$I = \frac{1}{12} w l^3 \quad \text{Equation 149}$$

$$\psi_I = \left[\left(\frac{w l^2}{4} \psi_l \right)^2 + \left(\frac{l^3}{12} \psi_w \right)^2 \right]^{1/2} \quad \text{Equation 150}$$

Then, the error for the critical Euler buckling load for fixed-fixed end conditions is calculated

$$P_{euler} = \frac{4\pi^2 EI}{L^2}$$ Equation 151

$$\psi_{P_{euler}} = \left[\left(\frac{4\pi^2 I}{L^2} \psi_E \right)^2 + \left(\frac{4\pi^2 E}{L^2} \psi_I \right)^2 + \left(-\frac{8\pi^2 EI}{L^3} \psi_L \right)^2 \right]^{1/2}$$ Equation 152

The error associated with the measurement of the elastic modulus, Ψ_E, is not known. The percent error of the elastic modulus is known; however, and this form may be substituted into the equation using

$$\psi_E = E\xi_E$$ Equation 153

where ξ_E is the percent error associated with the elastic modulus. Substituting this into the equation for the critical Euler buckling load error

$$\psi_{P_{euler}} = \left[\left(\frac{4\pi^2 EI}{L^2} \xi_E \right)^2 + \left(\frac{4\pi^2 E}{L^2} \psi_I \right)^2 + \left(-\frac{8\pi^2 EI}{L^3} \psi_L \right)^2 \right]^{1/2}$$ Equation 154

Slenderness Ratio Error

The error in the slenderness ratio calculation is calculated using the measurement error for the thickness and bending length.

$$\lambda = \sqrt{12}\frac{L}{l}$$ Equation 155

$$\psi_\lambda = \left[\left(\sqrt{12}\frac{1}{l} \psi_L \right)^2 + \left(-\sqrt{12}\frac{L}{l^2} \psi_l \right)^2 \right]^{1/2}$$ Equation 156

Applied Load Normalized with Critical Euler Buckling Load Error

The normalized applied load error was calculated using the previously calculated error in the critical Euler buckling load and the measurement error for load.

$$\psi_{P/P_{euler}} = \left[\left(\frac{1}{P_{euler}} \psi_P \right)^2 + \left(-\frac{P}{P_{euler}^2} \psi_{P_{euler}} \right)^2 \right]^{1/2}$$ Equation 157

Non-dimensionalized Applied Stress Error

The applied stress is non-dimensionalized with the compressive strength. The error was calculated using the previously calculated applied stress error. The compressive strength must be

dealt with in the same manner as the elastic modulus in calculating the error for the critical Euler buckling load in Equation 154. The known percent error for the compressive strength is substituted into the equation using

$$\psi_{\sigma_c} = \sigma_c \xi_{\sigma_c} \qquad \text{Equation 158}$$

$$\psi_{\sigma_{app}/\sigma_c} = \left[\left(\frac{1}{\sigma_c} \psi_{\sigma_{app}} \right)^2 + \left(-\frac{\sigma_{app}}{\sigma_c} \xi_{\sigma_c} \right)^2 \right]^{1/2} \qquad \text{Equation 159}$$

Non-dimensionalized Slenderness Ratio

The non-dimensionalized slenderness ratio was calculated using the previously calculated slenderness ratio error. First, the error for the non-dimensionalization term was calculated

$$\lambda_0 = \pi \left(\frac{E}{\sigma_c} \right) \qquad \text{Equation 160}$$

where the elastic modulus, E, and compressive strength, σ_c, are represented in terms of percent error as in previous calculations. The non-dimensionalization term error was then calculated

$$\psi_{\lambda_0} = \left[\left(\pi \left(\frac{E}{\sigma_c} \right)^{1/2} \xi_E \right)^2 + \left(\pi \left(\frac{E}{\sigma_c} \right)^{1/2} \xi_{\sigma_c} \right)^2 \right]^{1/2} \qquad \text{Equation 161}$$

This expression is then used with the slenderness ratio error to determine the non-dimensionalized slenderness ratio error

$$\psi_{\lambda/\lambda_0} = \left[\left(\frac{1}{\lambda_0} \psi_{\lambda_0} \right)^2 + \left(-\frac{\lambda}{\lambda_0^2} \psi_{\lambda_0} \right)^2 \right]^{1/2} \qquad \text{Equation 162}$$

Average Through-Thickness Temperature Calculation Error

The analysis of the intermediate-scale testing results include the use of an integrated average temperature calculation for the through-thickness temperature profile. In this calculation, the thermocouples that measure the mid-height through-thickness temperature profile are averaged using a trapezoidal integration scheme. The error in representing the average through-thickness temperature using this integration scheme was determined using the thermal model.

The thermal model was used to determine the error associated with using the though-thickness thermocouple measurements to calculate the average laminate temperature. The model was used to simulate heating of a 12mm thick laminate at three heat fluxes, 8, 19.3, and 38kW/m^2. The temperatures were calculated at 121 nodes through the thickness of the laminate. The resulting temperatures were averaged in two ways. First, an accurate estimation of the average through-thickness temperature with time was calculated using a trapezoidal integration scheme for the temperature at all nodes. This was compared with the method used to calculate the average temperature from the test data. The test data was analyzed using a trapezoidal integration scheme for the four thermocouple measurements through the thickness of laminate at mid-height. The temperatures from the model at the locations coinciding with the measurement locations in testing were selected and then the average was calculated with time.

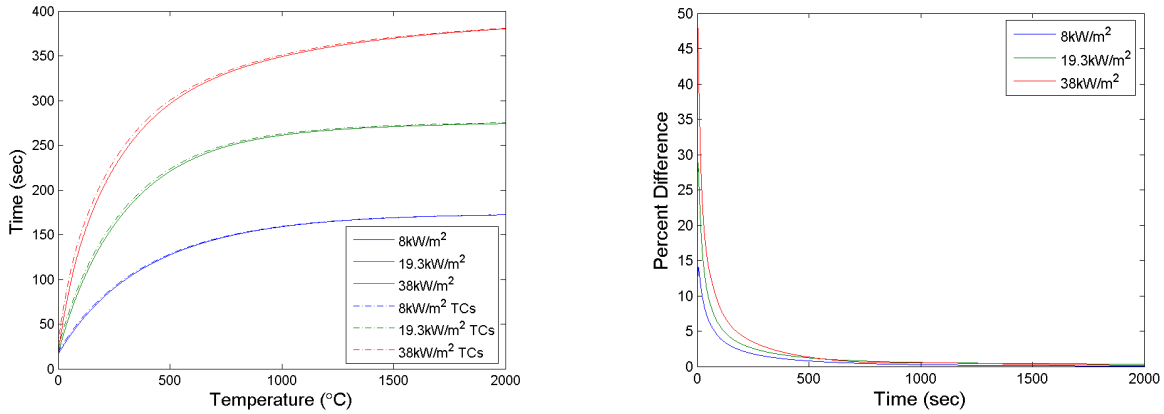

(a) (b)

Figure B-5. Comparison of (a) average through-thickness temperature for three heat fluxes for a 12mm laminate calculated using 120 points (solid line) and 4 points (dashed line) and (b) percent difference between average temperature calculation methods.

The figure shows that a direct visual comparison of the average calculated temperatures shows no distinguishable difference between the two calculation methods. The plot of the percent difference of the average temperatures shows a noticeable spike near the beginning of the simulation. This spike is as high as 48% for the 38kW/m^2 case; however, the spike reduces to approximately a 5% difference by approximately 150 seconds. After this point, the percent difference reduces towards zero, validating the use of this method calculating the average temperature using the measurements from the through-thickness thermocouples.

Appendix C - Intermediate-Scale Testing Results

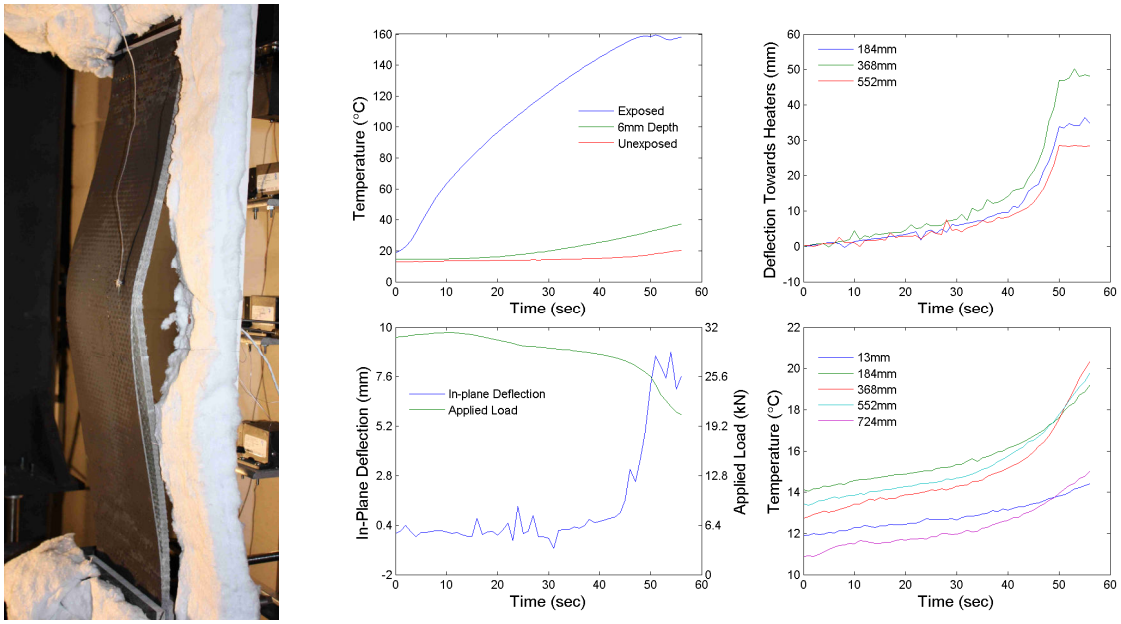

(a) (b)

Figure C-1. Test results for 12mm thick, 203mm width, 737mm height, 38kW/m^2, 50% Euler buckling load test showing (a) the laminate after failure and (b) plots of mid-height through-thickness temperature profile, out-of-plane deflections, in-plane deflection and applied load, and unexposed surface temperatures. Failure occurred at 46 seconds.

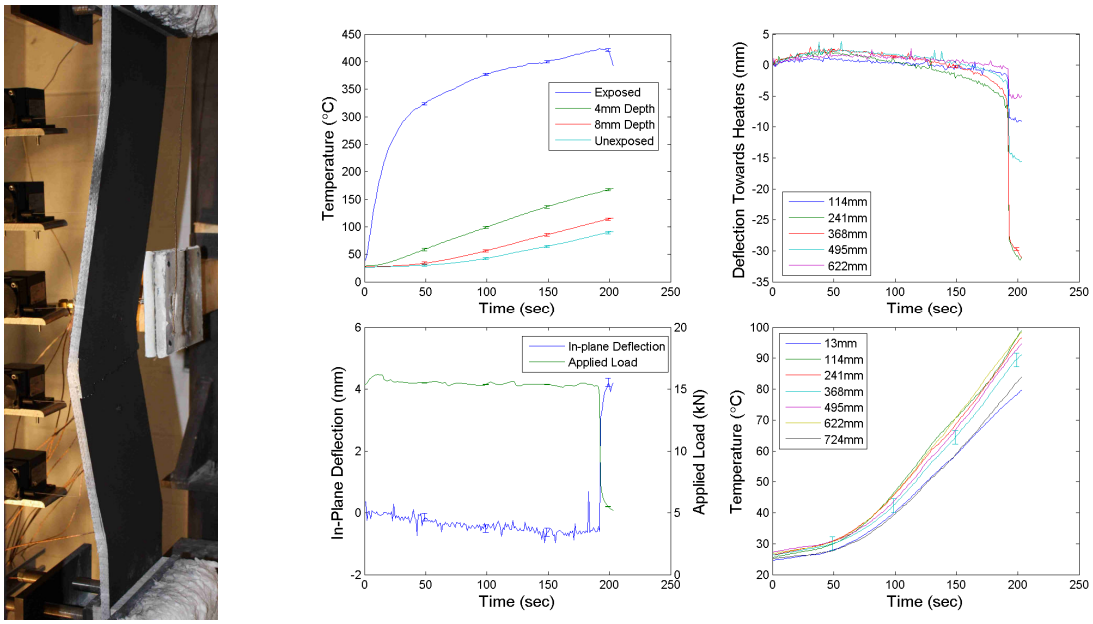

(a) (b)

Figure C-2. Test results for 12mm thick, 203mm width, 737mm height, 38kW/m^2, 25% Euler buckling load test with (a) the laminate after failure and (b) plots of mid-height through-thickness temperature profile, out-of-plane deflections, in-plane deflection and applied load, and unexposed surface temperatures. Failure occurred at 193 seconds.

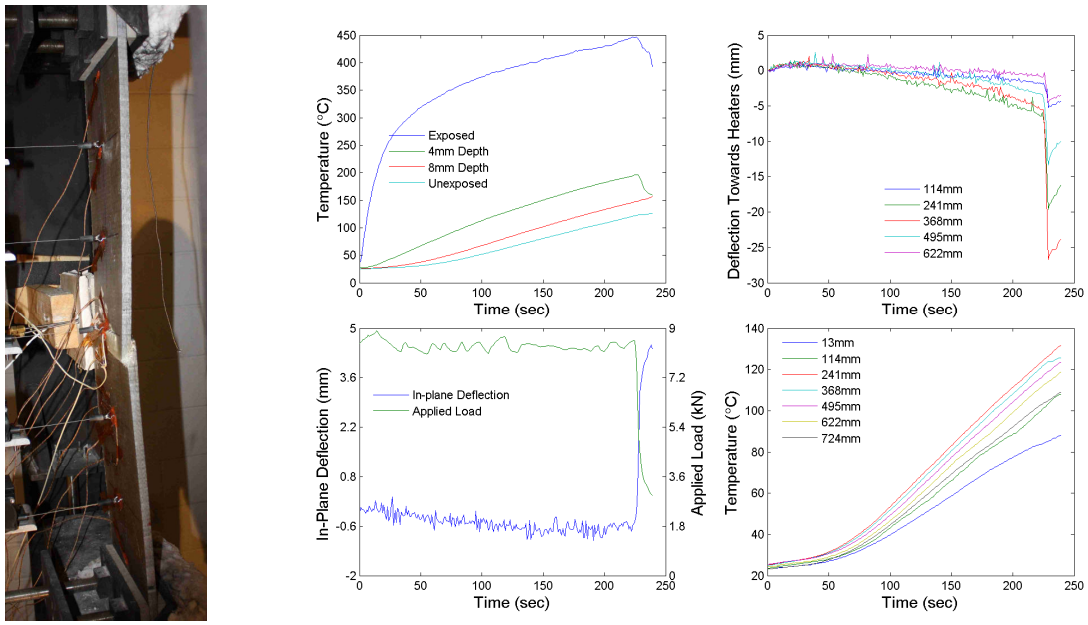

(a) (b)

Figure C-3. Test results for 12mm thick, 203mm width, 737mm height, 38kW/m^2, 15% Euler buckling load test with (a) the laminate after failure and (b) plots of mid-height through-thickness temperature profile, out-of-plane deflections, in-plane deflection and applied load, and unexposed surface temperatures. Failure occurred at 229 seconds.

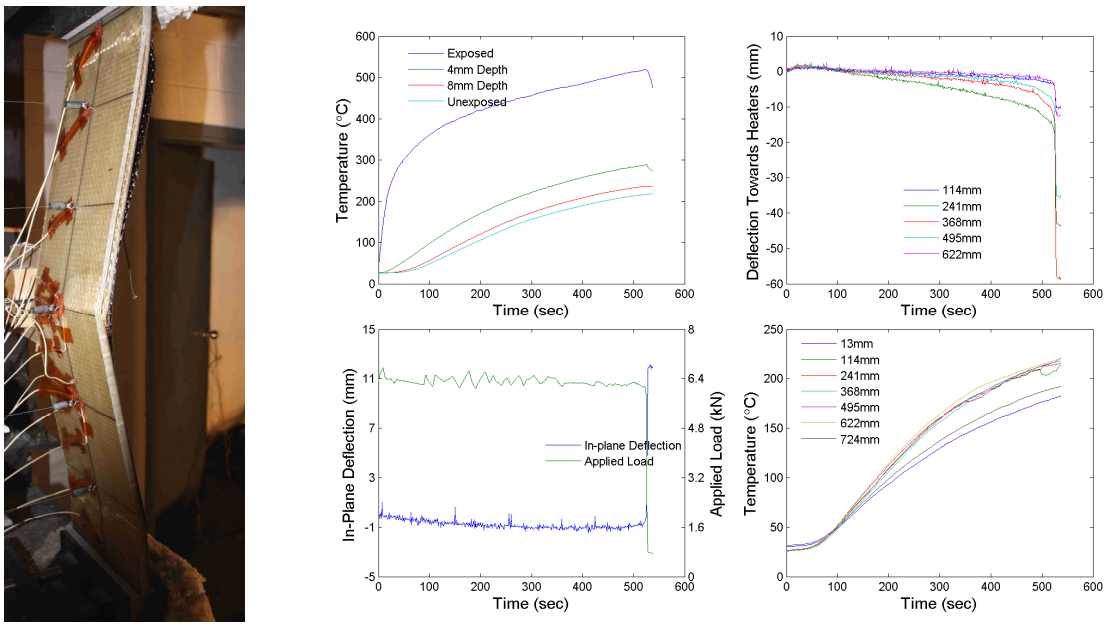

(a) (b)

Figure C-4. Test results for 12mm thick, 203mm width, 737mm height, 38kW/m^2, 10% Euler buckling load test with (a) the laminate after failure and (b) plots of mid-height through-thickness temperature profile, out-of-plane deflections, in-plane deflection and applied load, and unexposed surface temperatures. Failure occurred at 527 seconds.

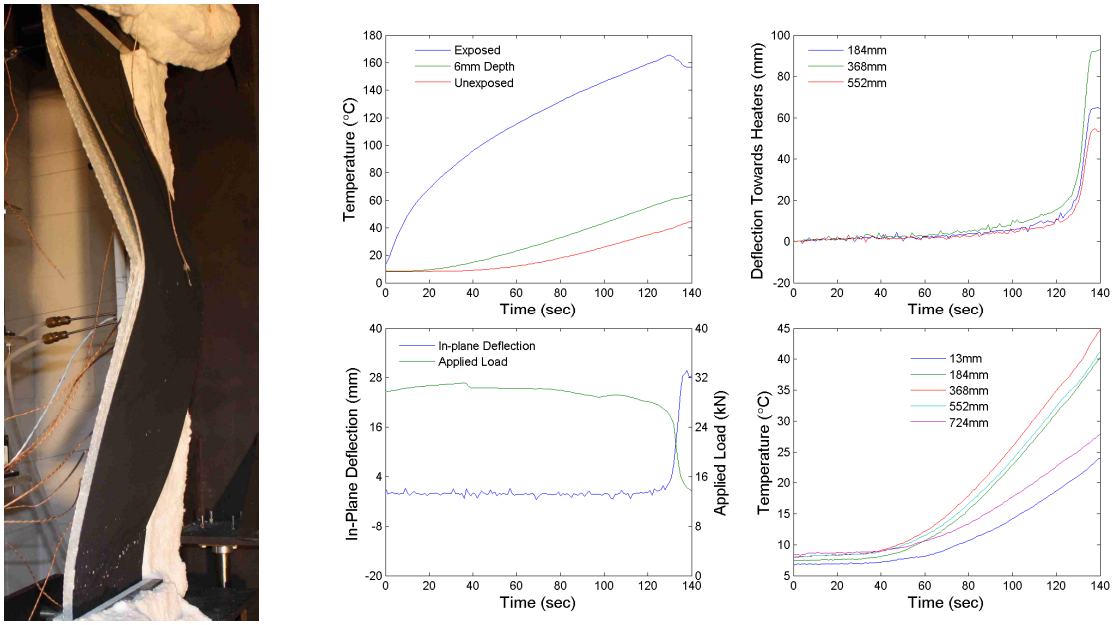

(a) (b)

Figure C-5. Test results for 12mm thick, 203mm width, 737mm height, 19.3kW/m^2, 50% Euler buckling load test with (a) the laminate after failure and (b) plots of mid-height through-thickness temperature profile, out-of-plane deflections, in-plane deflection and applied load, and unexposed surface temperatures. Failure occurred at 130 seconds.

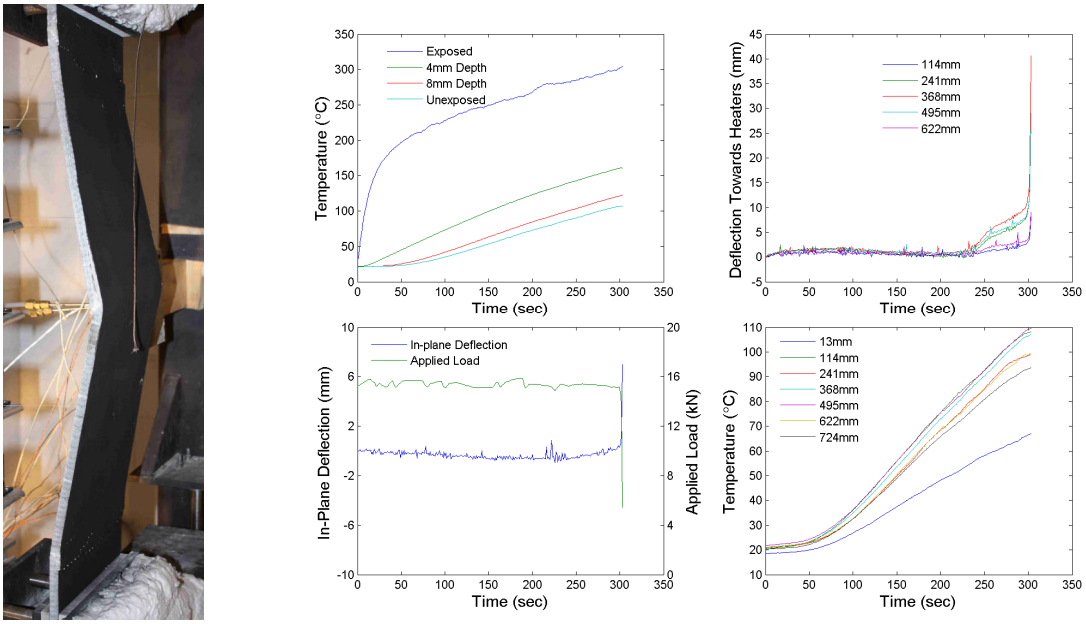

(a) (b)

Figure C-6. Test results for 12mm thick, 203mm width, 737mm height, 19.3kW/m^2, 25% Euler buckling load test with (a) the laminate after failure and (b) plots of mid-height through-thickness temperature profile, out-of-plane deflections, in-plane deflection and applied load, and unexposed surface temperatures. Failure occurred at 303 seconds.

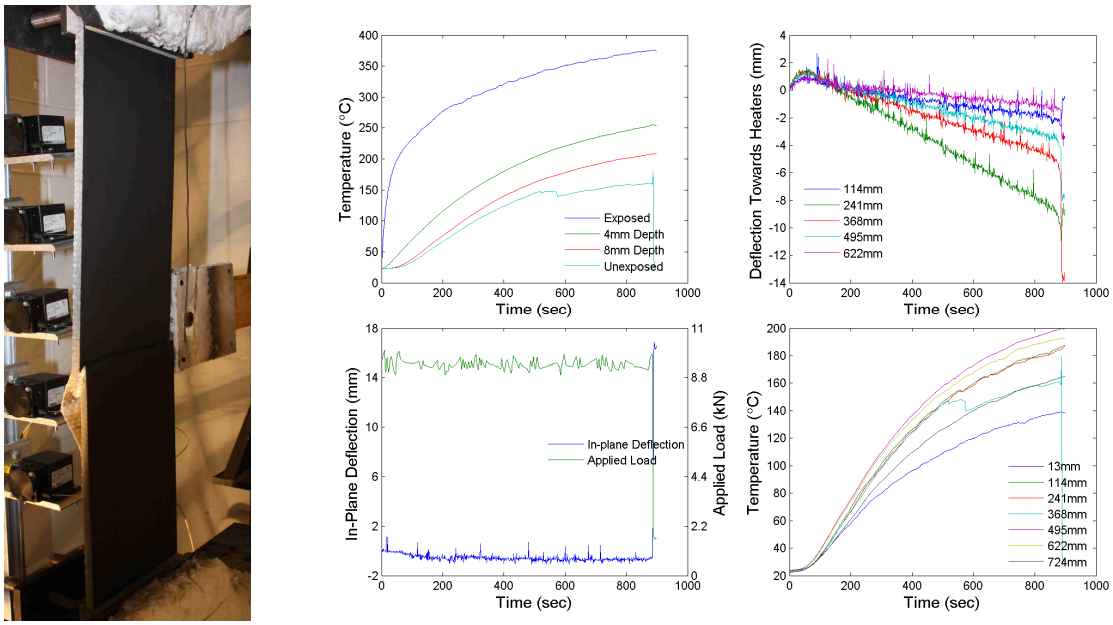

(a) (b)

Figure C-7. Test results for 12mm thick, 203mm width, 737mm height, 19.3kW/m^2, 15% Euler buckling load test with (a) the laminate after failure and (b) plots of mid-height through-thickness temperature profile, out-of-plane deflections, in-plane deflection and applied load, and unexposed surface temperatures. Failure occurred at 887 seconds.

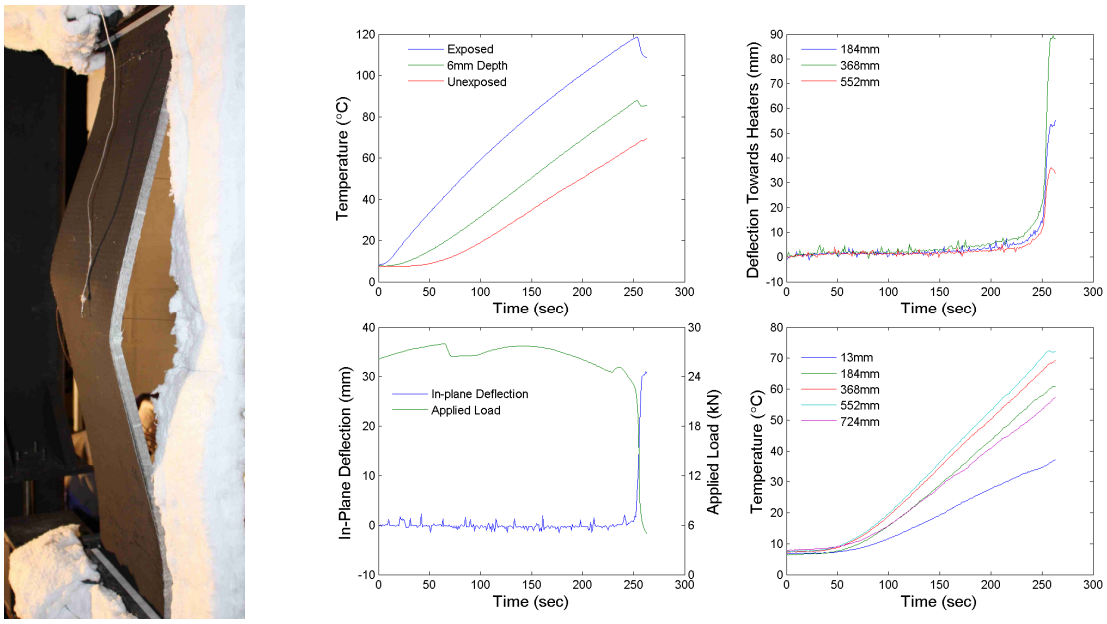

(a) (b)

Figure C-8. Test results for 12mm thick, 203mm width, 737mm height, 11.8kW/m^2, 50% Euler buckling load test with (a) the laminate after failure and (b) plots of mid-height through-thickness temperature profile, out-of-plane deflections, in-plane deflection and applied load, and unexposed surface temperatures. Failure occurred at 253 seconds.

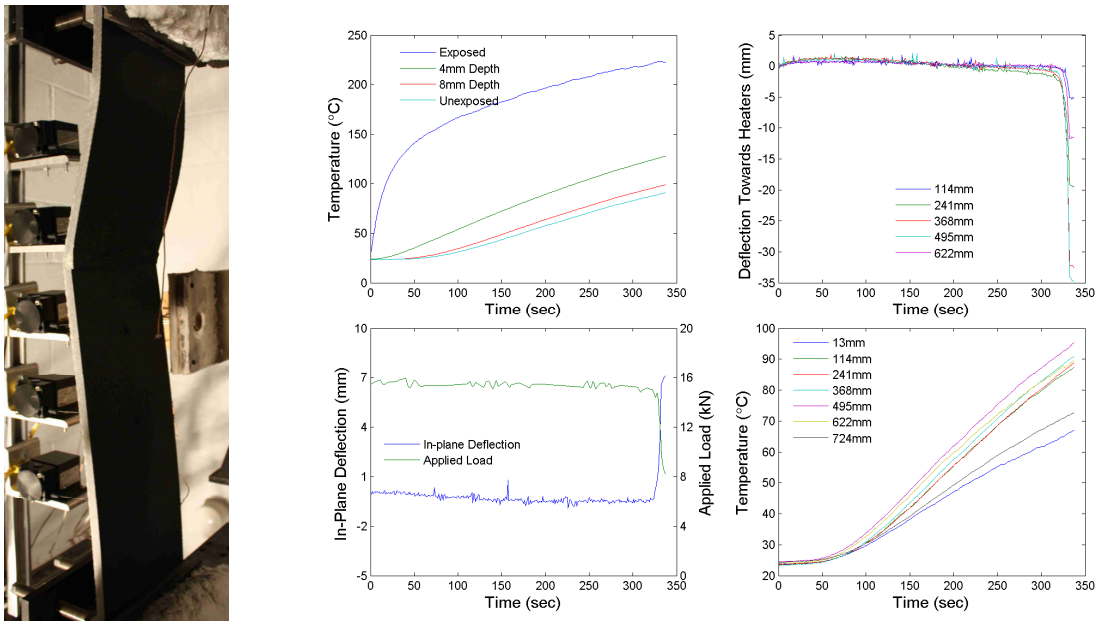

(a) (b)

Figure C-9. Test results for 12mm thick, 203mm width, 737mm height, 11.8kW/m^2, 25% Euler buckling load test with (a) the laminate after failure and (b) plots of mid-height through-thickness temperature profile, out-of-plane deflections, in-plane deflection and applied load, and unexposed surface temperatures. Failure occurred at 331 seconds.

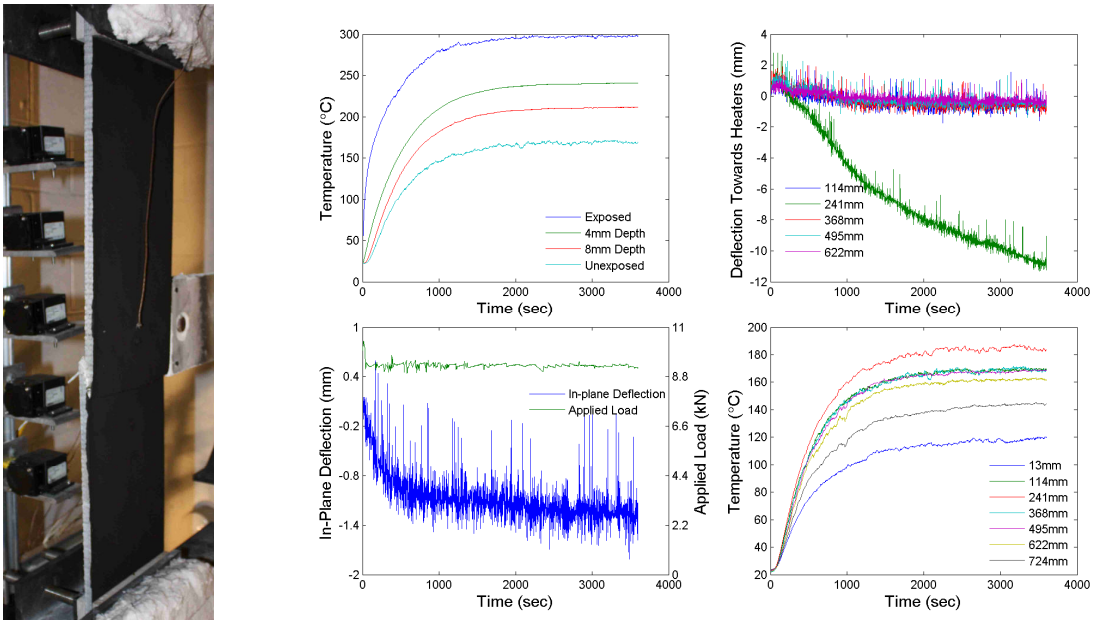

(a) (b)

Figure C-10. Test results for 12mm thick, 203mm width, 737mm height, 11.8kW/m^2, 15% Euler buckling load test with (a) the laminate after failure and (b) plots of mid-height through-thickness temperature profile, out-of-plane deflections, in-plane deflection and applied load, and unexposed surface temperatures. The test is a run-out and did not fail within an hour.

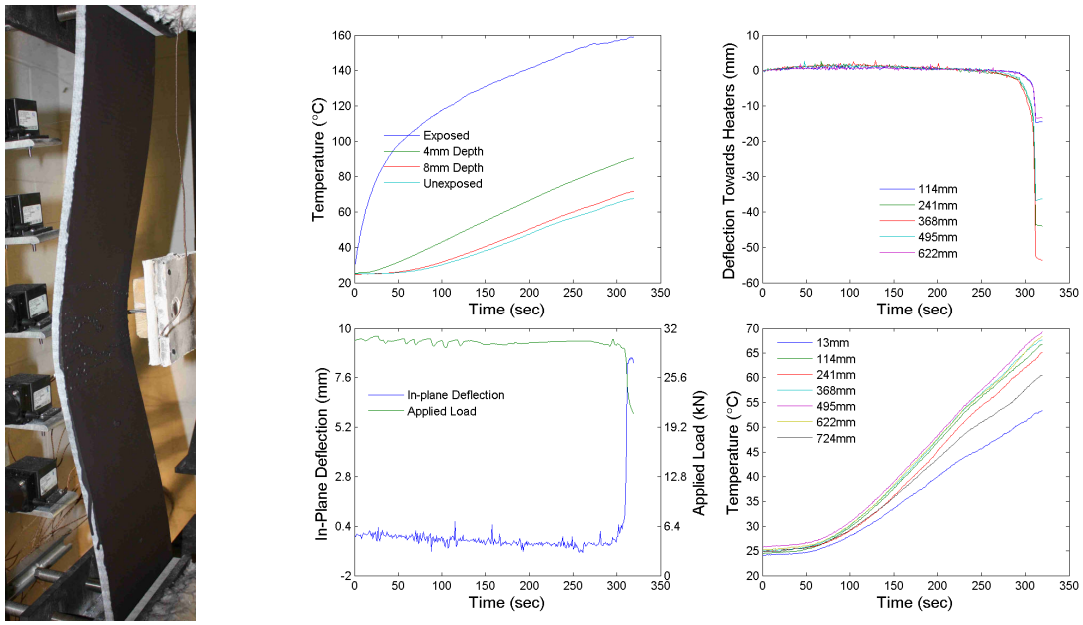

(a) (b)

Figure C-11. Test results for 12mm thick, 203mm width, 737mm height, 8kW/m^2, 50% Euler buckling load test with (a) the laminate after failure and (b) plots of mid-height through-thickness temperature profile, out-of-plane deflections, in-plane deflection and applied load, and unexposed surface temperatures. Failure occurred at 311 seconds.

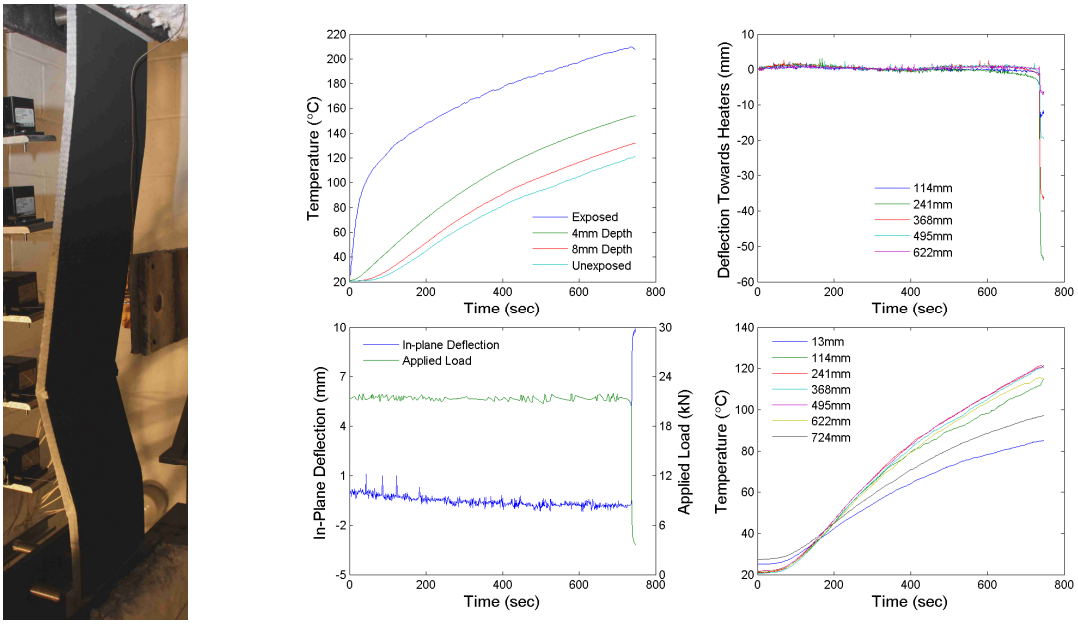

(a) (b)

Figure C-12. Test results for 12mm thick, 203mm width, 737mm height, 8kW/m^2, 35% Euler buckling load test with (a) the laminate after failure and (b) plots of mid-height through-thickness temperature profile, out-of-plane deflections, in-plane deflection and applied load, and unexposed surface temperatures. Failure occurred at 737 seconds.

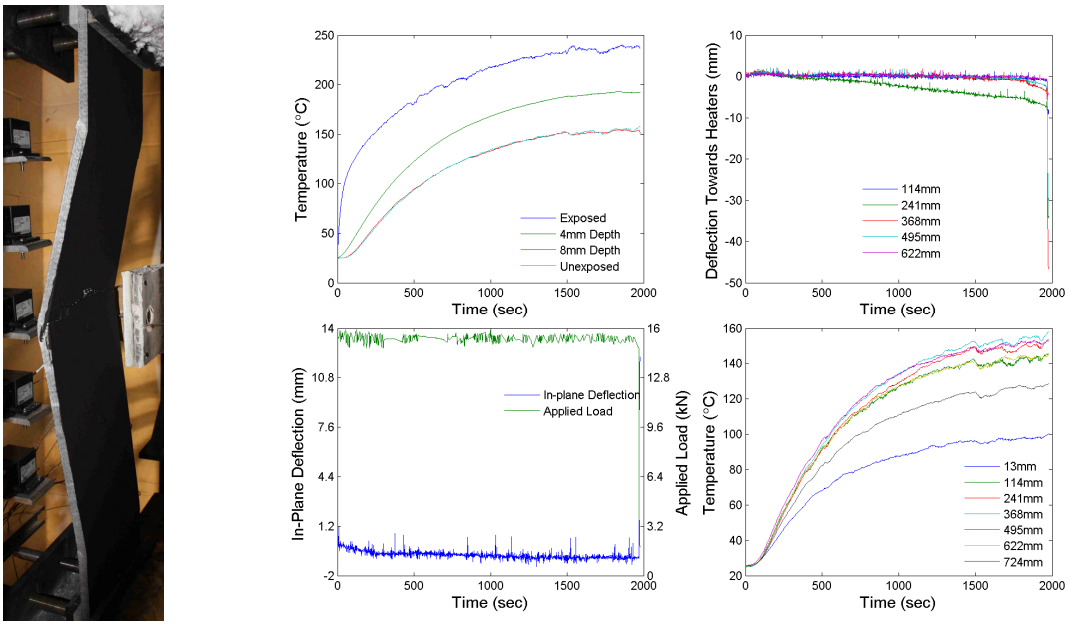

(a) (b)

Figure C-13. Test results for 12mm thick, 203mm width, 737mm height, 8kW/m^2, 25% Euler buckling load test with (a) the laminate after failure and (b) plots of mid-height through-thickness temperature profile, out-of-plane deflections, in-plane deflection and applied load, and unexposed surface temperatures. Failure occurred at 1971 seconds.

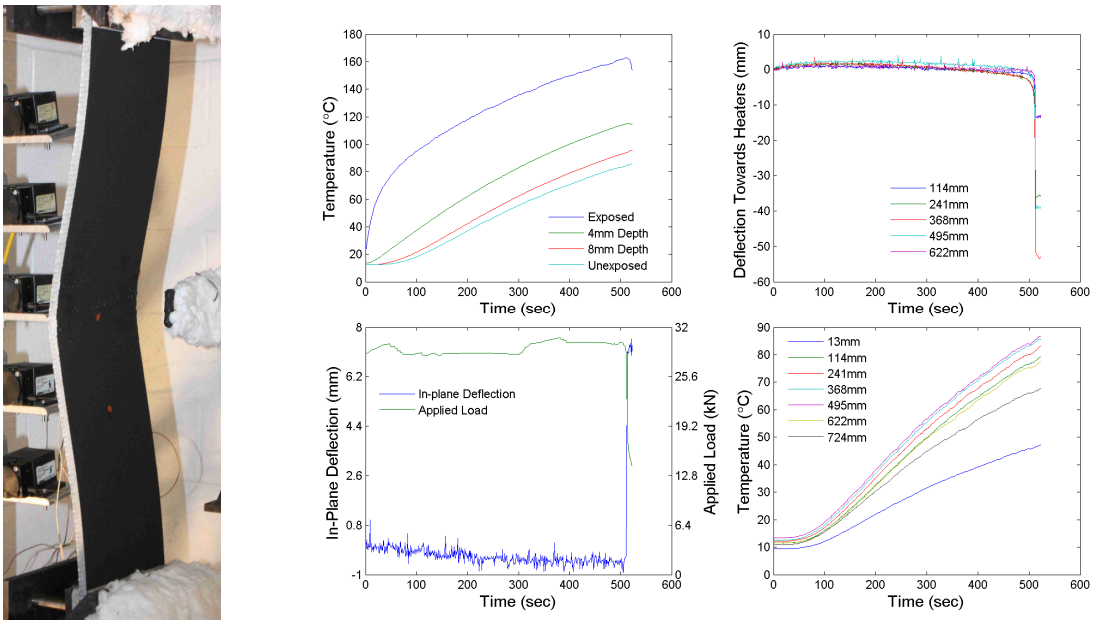

(a) (b)

Figure C-14. Repeatability test results for 12mm thick, 203mm width, 737mm height, 8kW/m^2, 50% Euler buckling load test with (a) the laminate after failure and (b) plots of mid-height through-thickness temperature profile, out-of-plane deflections, in-plane deflection and applied load, and unexposed surface temperatures. Failure occurred at 513 seconds.

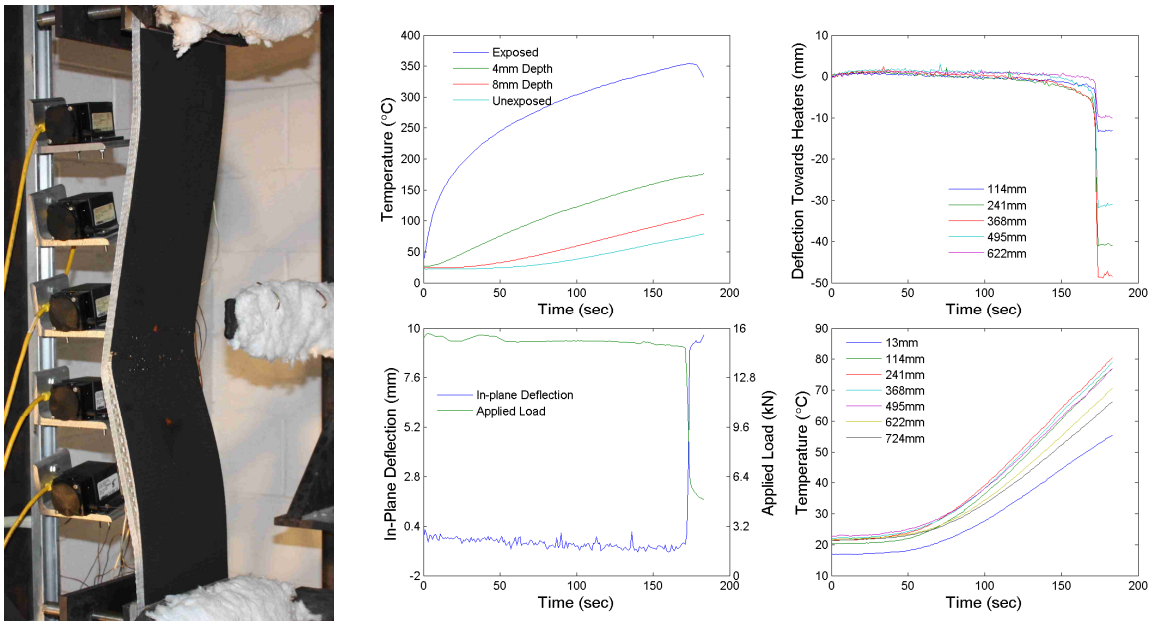

(a) (b)

Figure C-15. Repeatability test results for 12mm thick, 203mm width, 737mm height, 38kW/m^2, 25% Euler buckling load test with (a) the laminate after failure and (b) plots of mid-height through-thickness temperature profile, out-of-plane deflections, in-plane deflection and applied load, and unexposed surface temperatures. Failure occurred at 173 seconds.

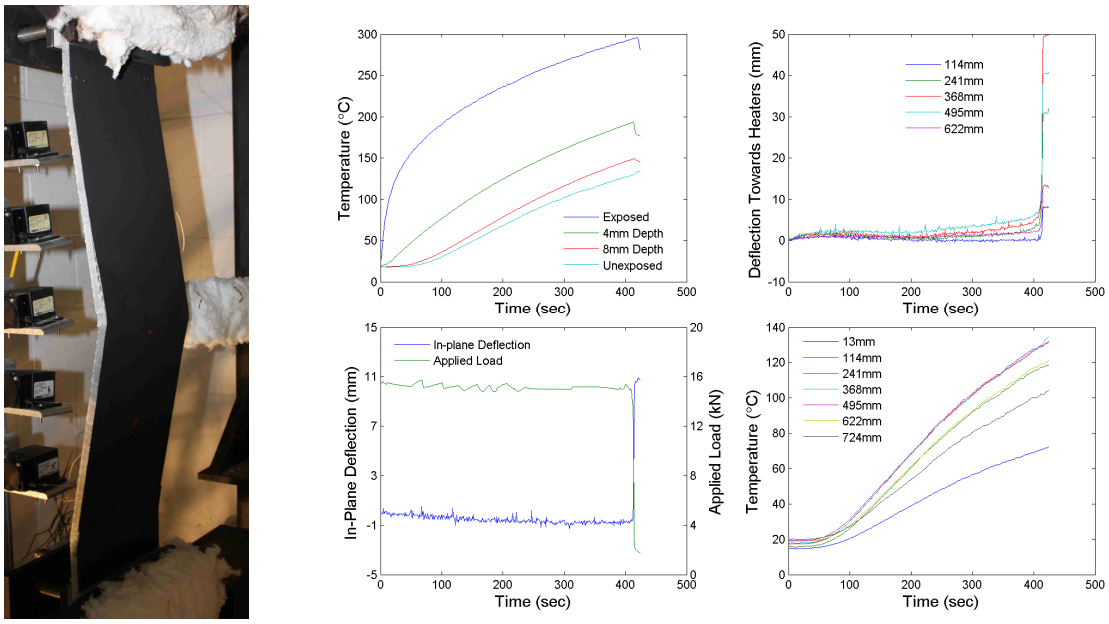

(a) (b)

Figure C-16. Repeatability test results for 12mm thick, 203mm width, 737mm height, 19.3kW/m^2, 25% Euler buckling load test with (a) the laminate after failure and (b) plots of mid-height through-thickness temperature profile, out-of-plane deflections, in-plane deflection and applied load, and unexposed surface temperatures. Failure occurred at 414 seconds.

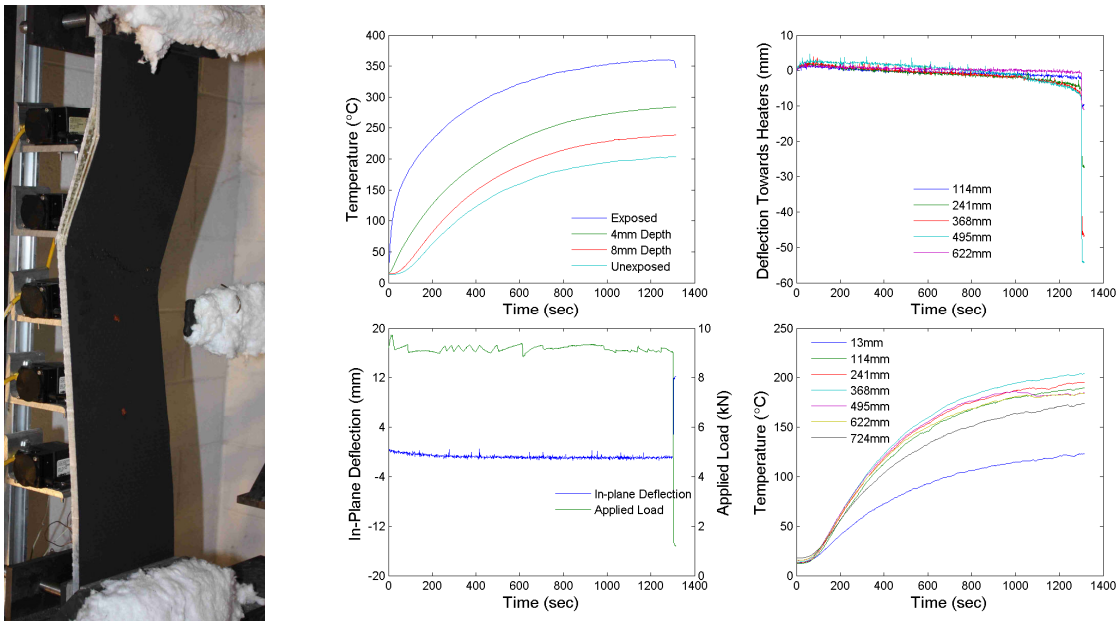

(a) (b)

Figure C-17. Repeatability test results for 12mm thick, 203mm width, 737mm height, 19.3kW/m^2, 15% Euler buckling load test with (a) the laminate after failure and (b) plots of mid-height through-thickness temperature profile, out-of-plane deflections, in-plane deflection and applied load, and unexposed surface temperatures. Failure occurred at 1303 seconds.

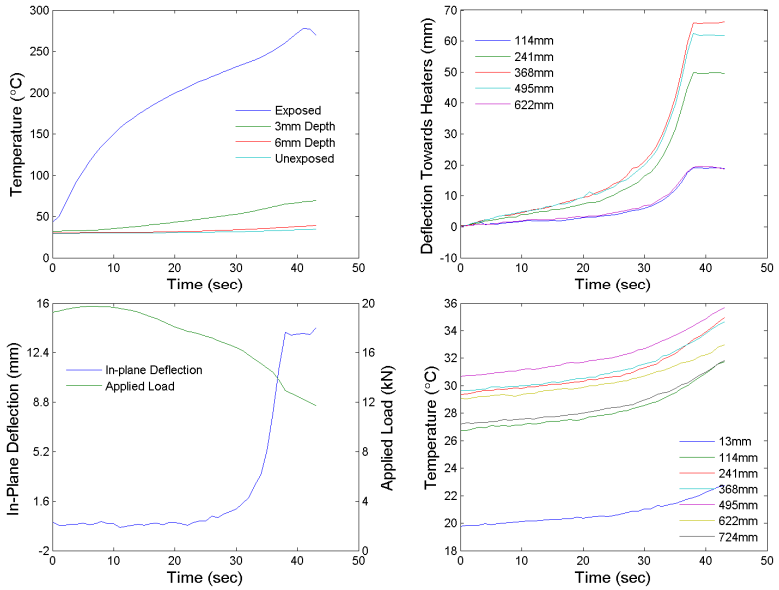

(a) (b)

Figure C-18. Test results for 9mm thick, 203mm width, 737mm height, 38kW/m^2, 75% Euler buckling load test with (a) the laminate after failure and (b) plots of mid-height through-thickness temperature profile, out-of-plane deflections, in-plane deflection and applied load, and unexposed surface temperatures. Failure occurred at 33 seconds.

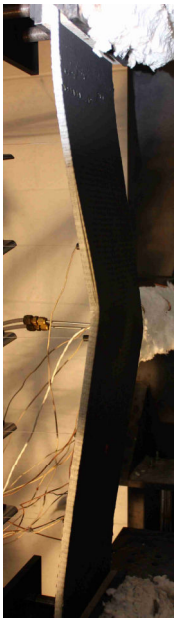

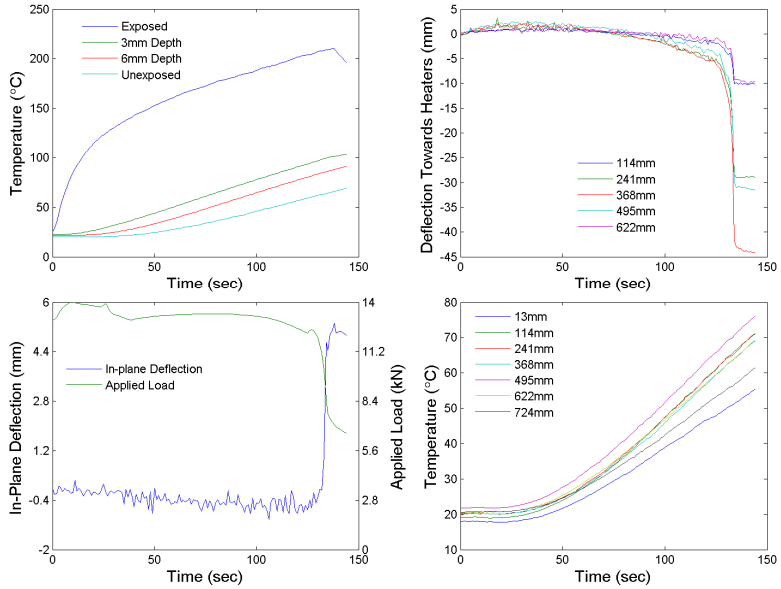

(a) (b)

Figure C-19. Test results for 9mm thick, 203mm width, 737mm height, 38kW/m^2, 50% Euler buckling load test with (a) the laminate after failure and (b) plots of mid-height through-thickness temperature profile, out-of-plane deflections, in-plane deflection and applied load, and unexposed surface temperatures. Failure occurred at 76 seconds.

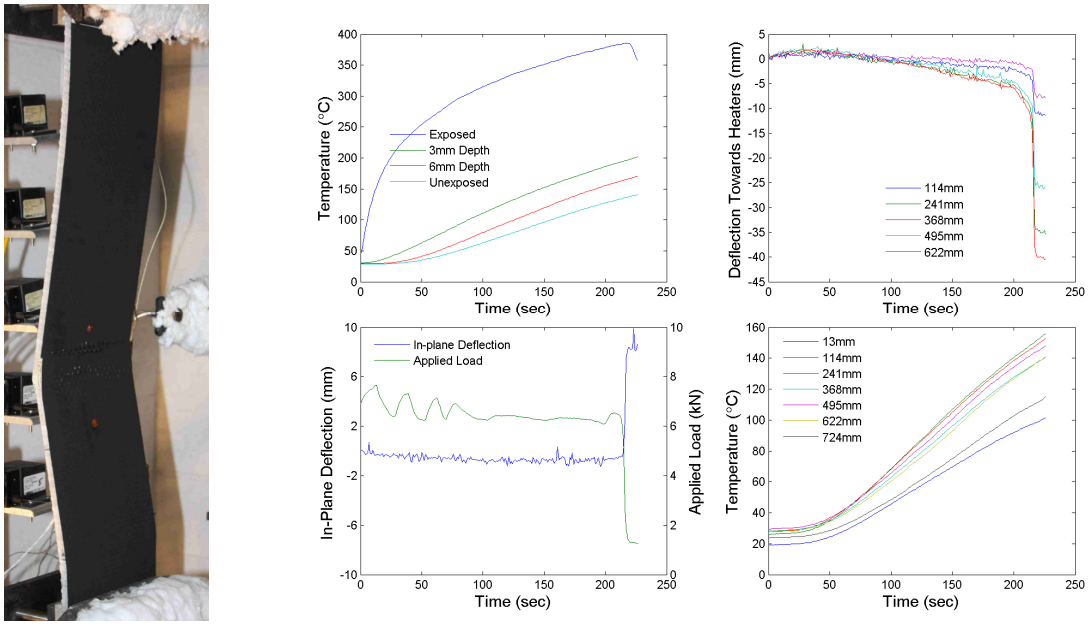

(a) (b)

Figure C-20. Test results for 9mm thick, 203mm width, 737mm height, 38kW/m^2, 25% Euler buckling load test with (a) the laminate after failure and (b) plots of mid-height through-thickness temperature profile, out-of-plane deflections, in-plane deflection and applied load, and unexposed surface temperatures. Failure occurred at 216 seconds.

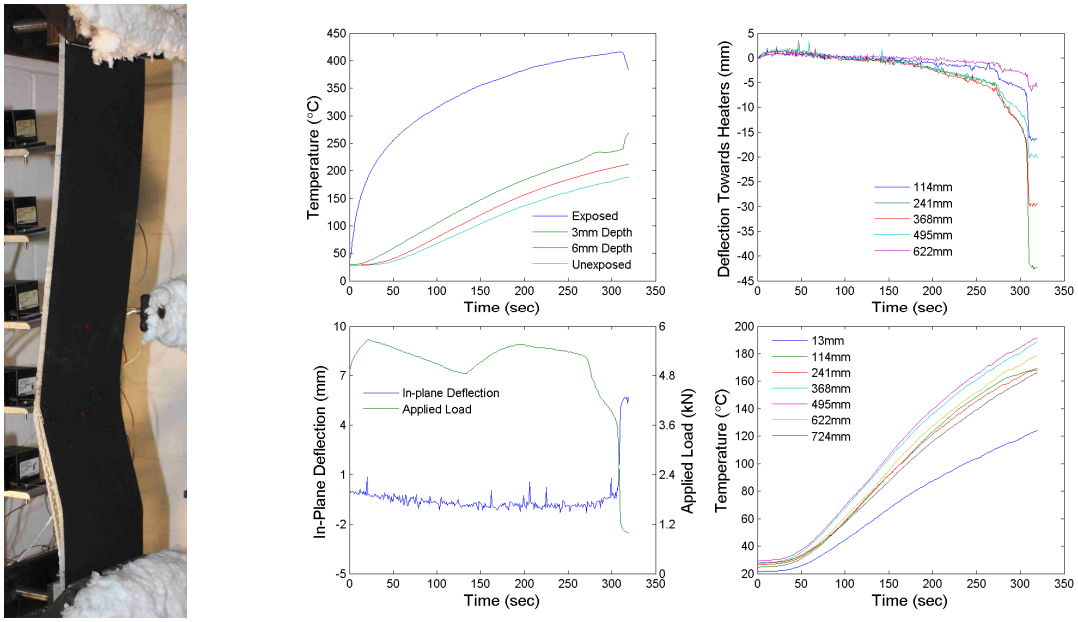

(a) (b)

Figure C-21. Test results for 9mm thick, 203mm width, 737mm height, 38kW/m^2, 15% Euler buckling load test with (a) the laminate after failure and (b) plots of mid-height through-thickness temperature profile, out-of-plane deflections, in-plane deflection and applied load, and unexposed surface temperatures. Failure occurred at 309 seconds.

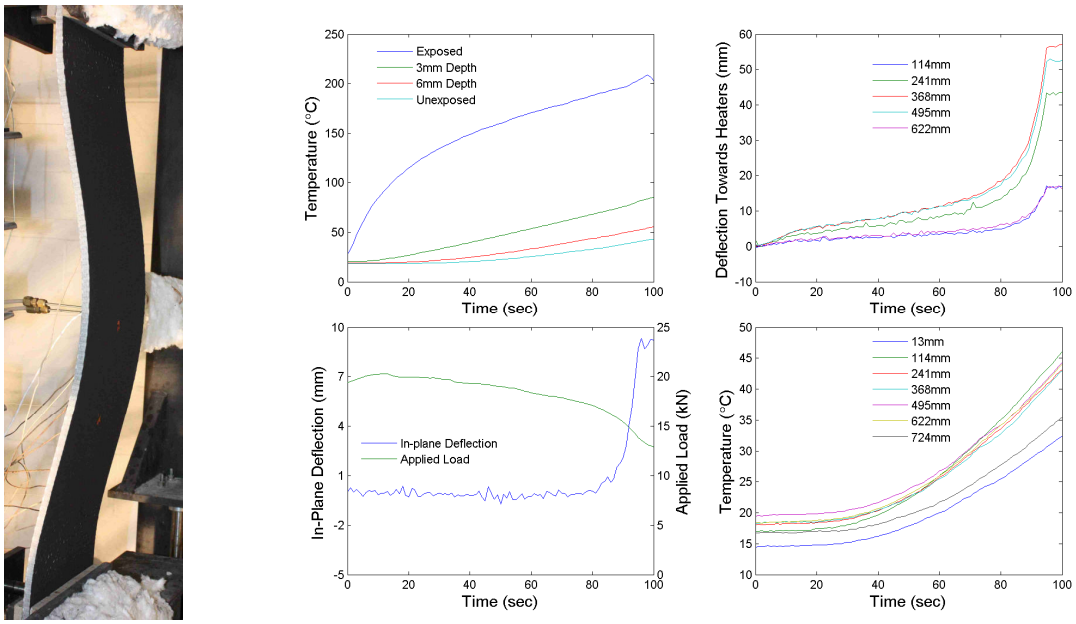

(a) (b)

Figure C-22. Test results for 9mm thick, 203mm width, 737mm height, 19.3kW/m^2, 75% Euler buckling load test with (a) the laminate after failure and (b) plots of mid-height through-thickness temperature profile, out-of-plane deflections, in-plane deflection and applied load, and unexposed surface temperatures. Failure occurred at 90 seconds.

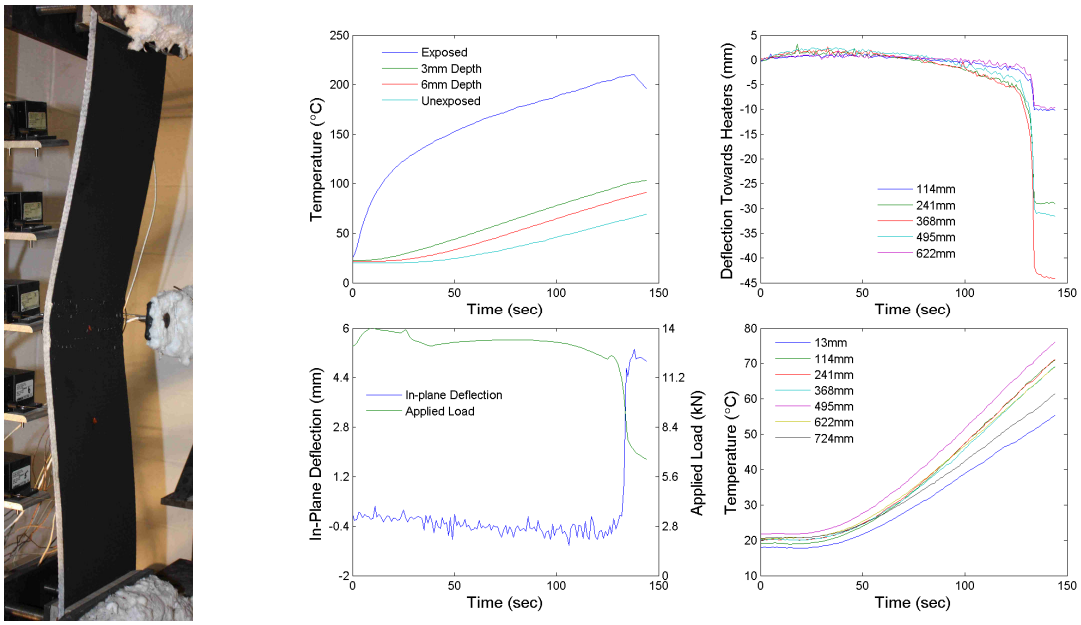

(a) (b)

Figure C-23. Test results for 9mm thick, 203mm width, 737mm height, 19.3kW/m^2, 50% Euler buckling load test with (a) the laminate after failure and (b) plots of mid-height through-thickness temperature profile, out-of-plane deflections, in-plane deflection and applied load, and unexposed surface temperatures. Failure occurred at 134 seconds.

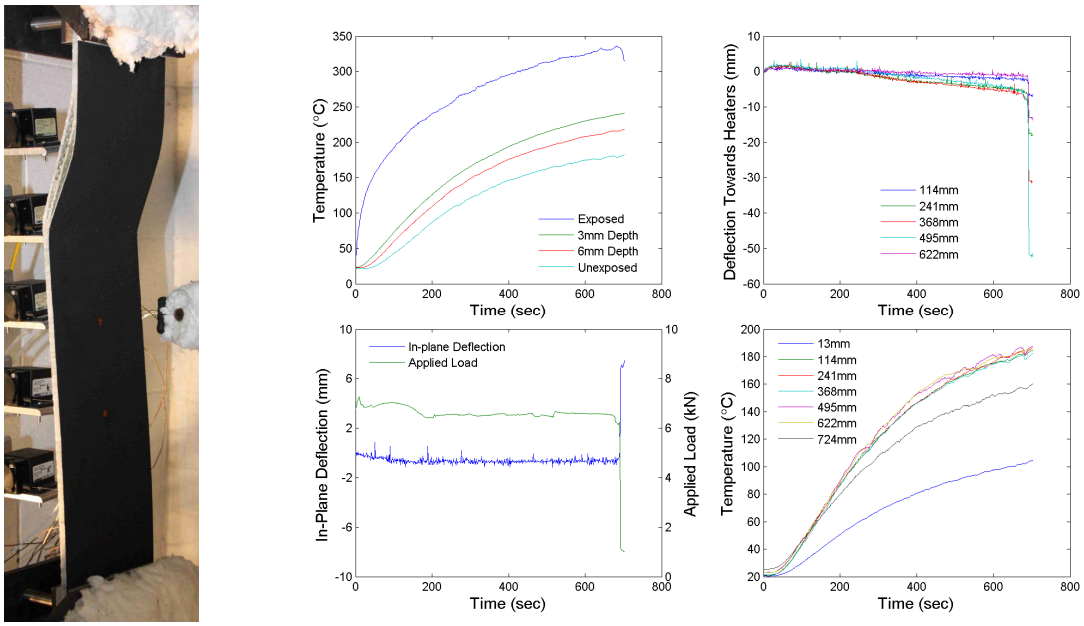

(a) (b)

Figure C-24. Test results for 9mm thick, 203mm width, 737mm height, 19.3kW/m^2, 25% Euler buckling load test with (a) the laminate after failure and (b) plots of mid-height through-thickness temperature profile, out-of-plane deflections, in-plane deflection and applied load, and unexposed surface temperatures. Failure occurred at 692 seconds.

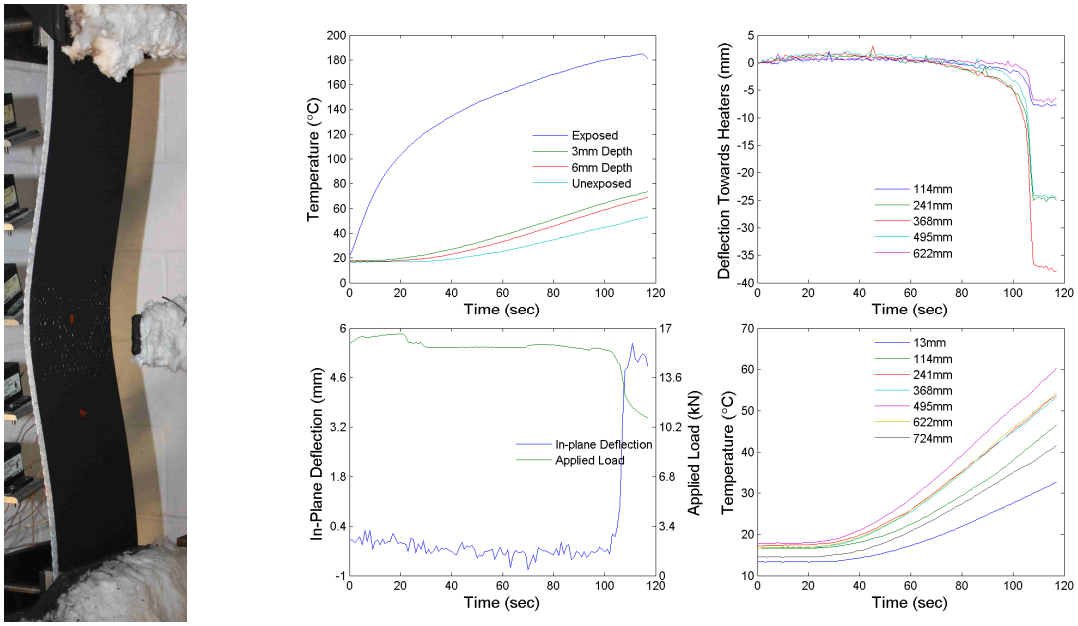

(a) (b)

Figure C-25. Test results for 9mm thick, 203mm width, 660mm height, 19.3kW/m^2, 50% Euler buckling load test with (a) the laminate after failure and (b) plots of mid-height through-thickness temperature profile, out-of-plane deflections, in-plane deflection and applied load, and unexposed surface temperatures. Failure occurred at 109 seconds.

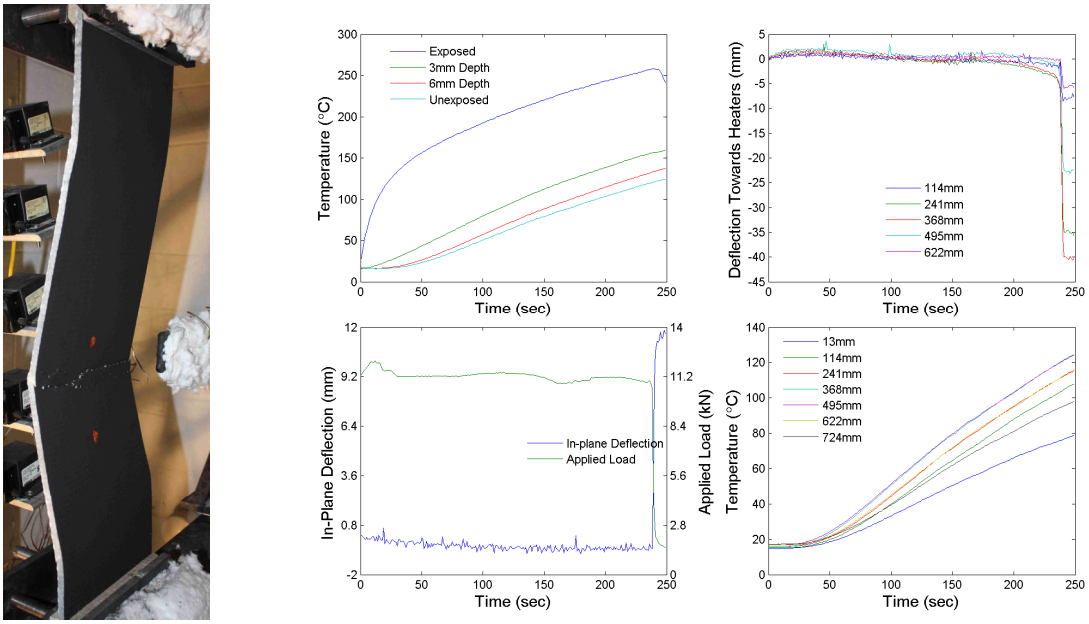

(a) (b)

Figure C-26. Test results for 9mm thick, 203mm width, 660mm height, 19.3kW/m^2, 35% Euler buckling load test with (a) the laminate after failure and (b) plots of mid-height through-thickness temperature profile, out-of-plane deflections, in-plane deflection and applied load, and unexposed surface temperatures. Failure occurred at 239 seconds.

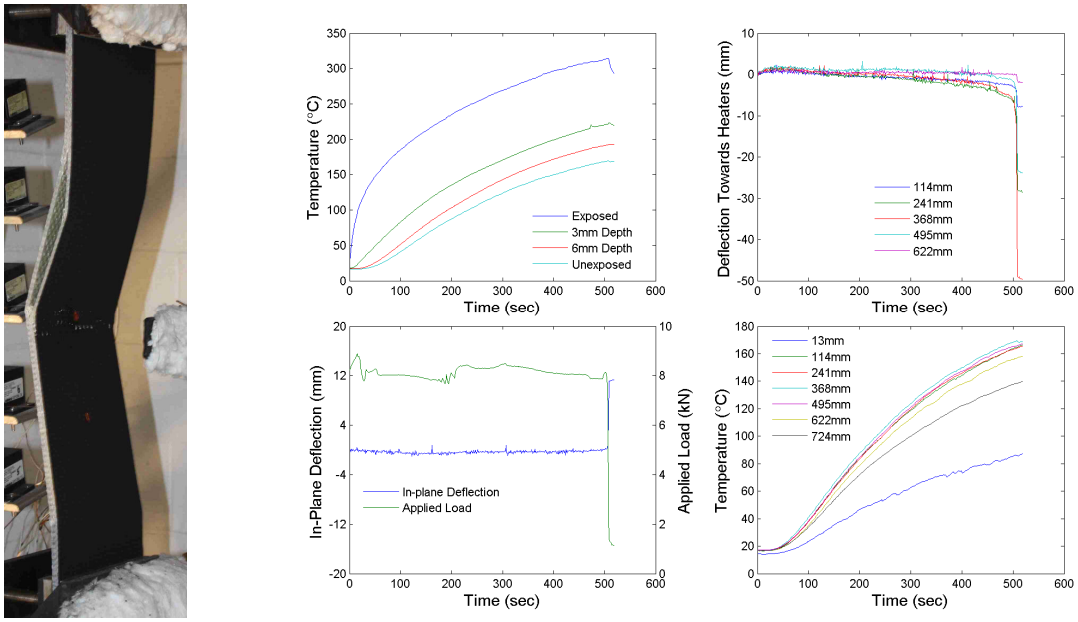

(a) (b)

Figure C-27. Test results for 9mm thick, 203mm width, 660mm height, 19.3kW/m^2, 25% Euler buckling load test with (a) the laminate after failure and (b) plots of mid-height through-thickness temperature profile, out-of-plane deflections, in-plane deflection and applied load, and unexposed surface temperatures. Failure occurred at 508 seconds.

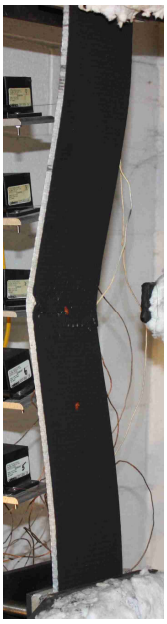

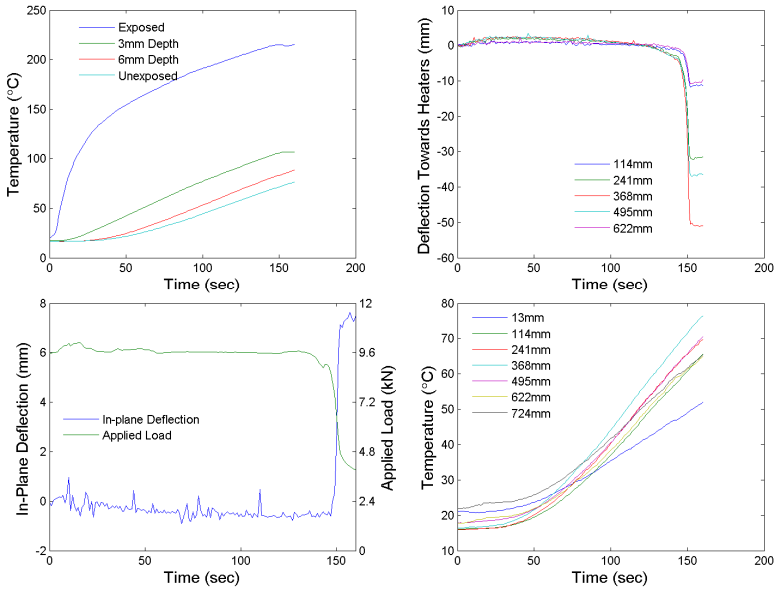

(a) (b)

Figure C-28. Test results for 9mm thick, 140mm width, 737mm height, 19.3kW/m^2, 50% Euler buckling load test with (a) the laminate after failure and (b) plots of mid-height through-thickness temperature profile, out-of-plane deflections, in-plane deflection and applied load, and unexposed surface temperatures. Failure occurred at 150 seconds.

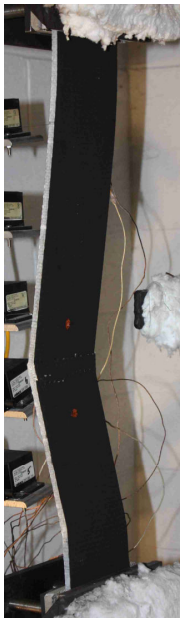

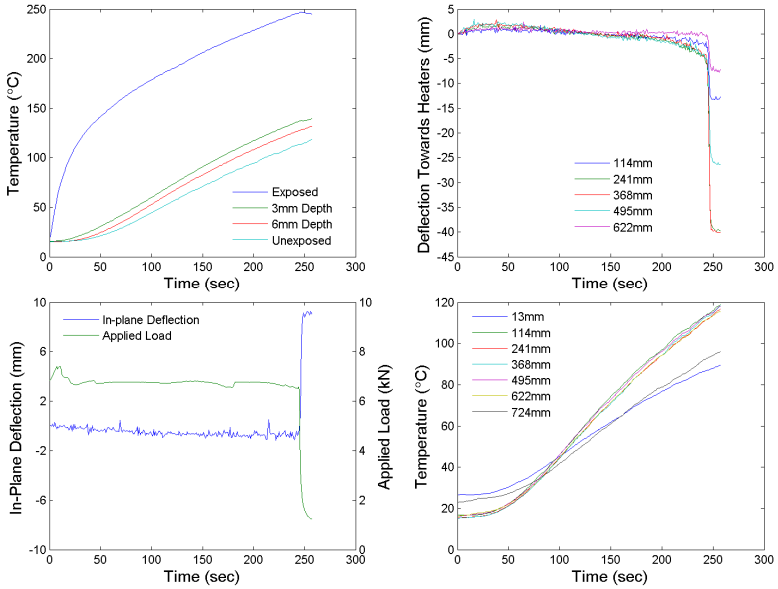

(a) (b)

Figure C-29. Test results for 9mm thick, 140mm width, 737mm height, 19.3kW/m^2, 35% Euler buckling load test with (a) the laminate after failure and (b) plots of mid-height through-thickness temperature profile, out-of-plane deflections, in-plane deflection and applied load, and unexposed surface temperatures. Failure occurred at 247 seconds.

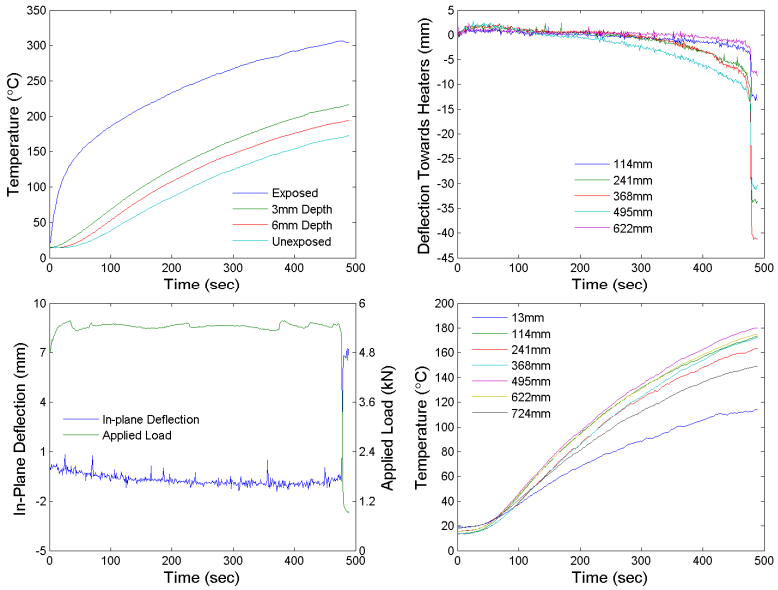

(a) (b)

Figure C-30. Test results for 9mm thick, 140mm width, 737mm height, 19.3kW/m^2, 25% Euler buckling load test with (a) the laminate after failure and (b) plots of mid-height through-thickness temperature profile, out-of-plane deflections, in-plane deflection and applied load, and unexposed surface temperatures. Failure occurred at 479 seconds.

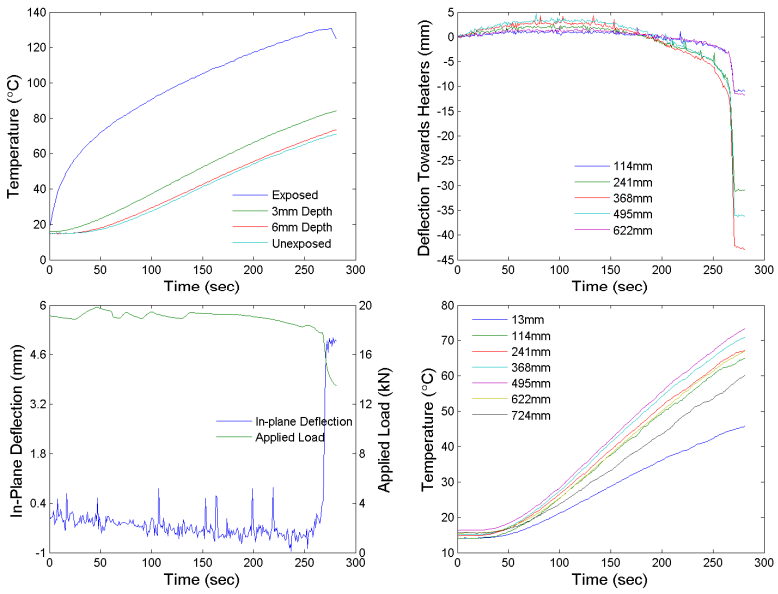

(a) (b)

Figure C-31. Test results for 9mm thick, 203mm width, 737mm height, 8kW/m^2, 75% Euler buckling load test with (a) the laminate after failure and (b) plots of mid-height through-thickness temperature profile, out-of-plane deflections, in-plane deflection and applied load, and unexposed surface temperatures. Failure occurred at 271 seconds.

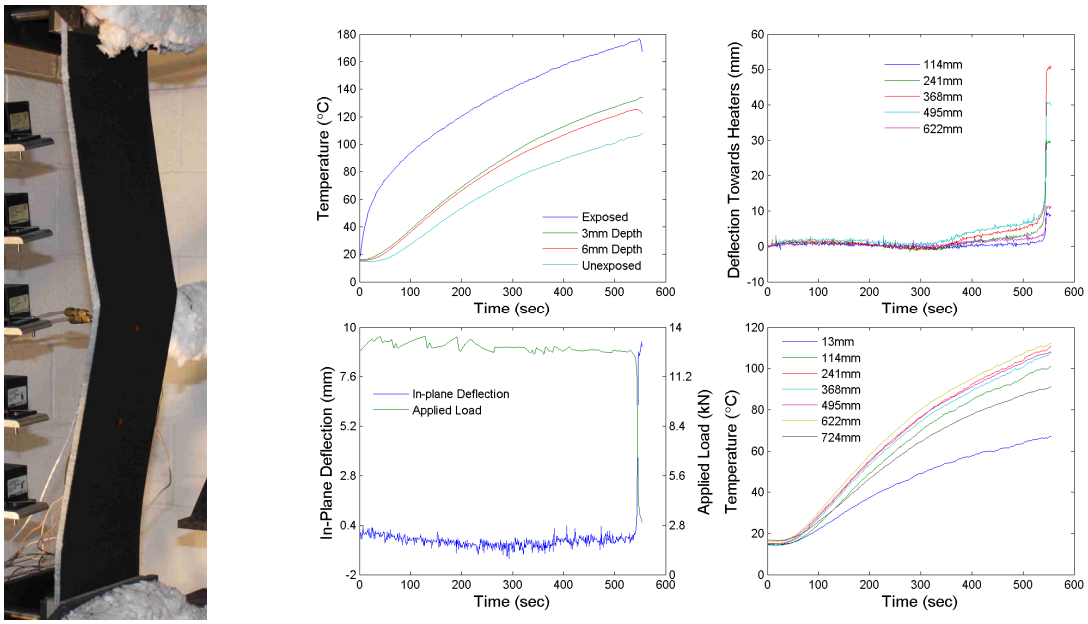

(a) (b)

Figure C-32. Test results for 9mm thick, 203mm width, 737mm height, 8kW/m^2, 50% Euler buckling load test with (a) the laminate after failure and (b) plots of mid-height through-thickness temperature profile, out-of-plane deflections, in-plane deflection and applied load, and unexposed surface temperatures. Failure occurred at 545 seconds.

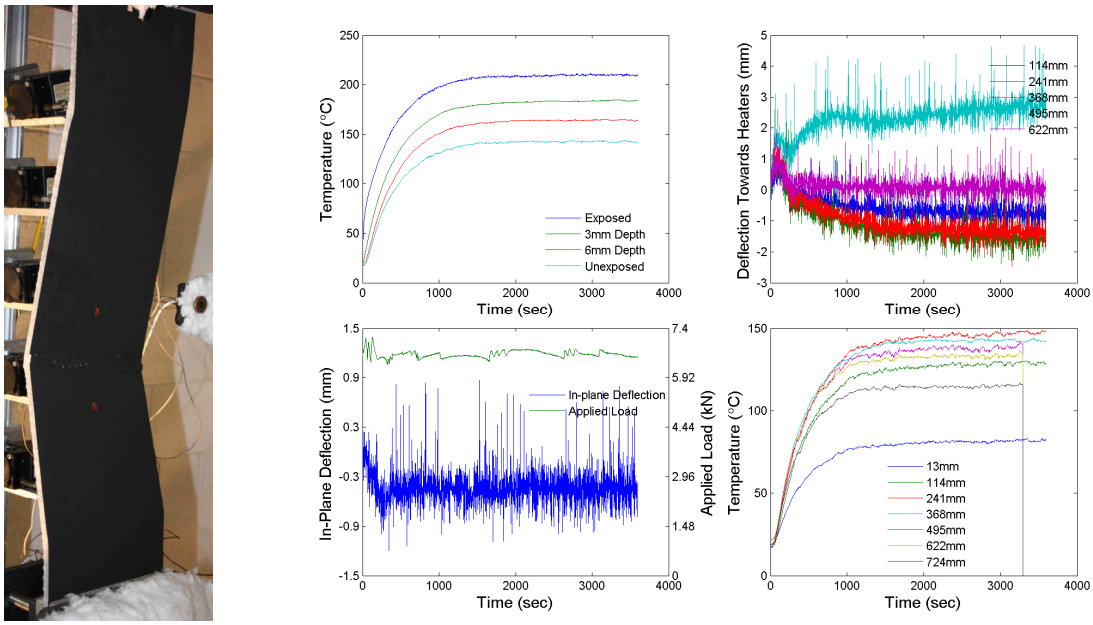

(a) (b)

Figure C-33. Test results for 9mm thick, 203mm width, 737mm height, 8kW/m^2, 25% Euler buckling load test with (a) the laminate after failure and (b) plots of mid-height through-thickness temperature profile, out-of-plane deflections, in-plane deflection and applied load, and unexposed surface temperatures. The test is a run-out and did not fail within an hour.

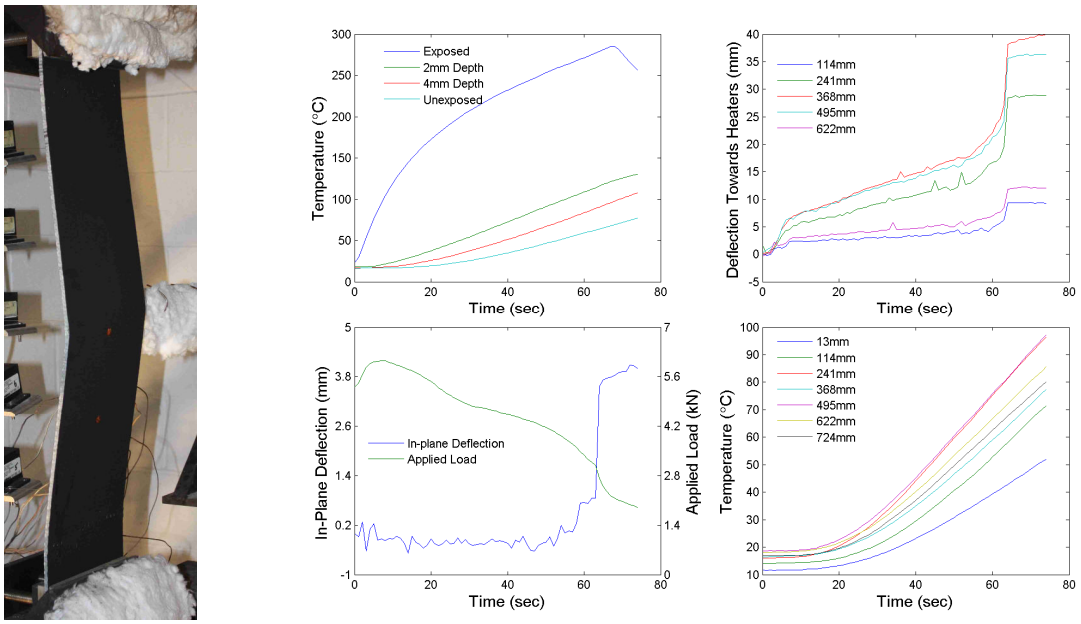

(a) (b)

Figure C-34. Test results for 6mm thick, 203mm width, 737mm height, 38kW/m^2, 50% Euler buckling load test with (a) the laminate after failure and (b) plots of mid-height through-thickness temperature profile, out-of-plane deflections, in-plane deflection and applied load, and unexposed surface temperatures. Failure occurred at 64 seconds.

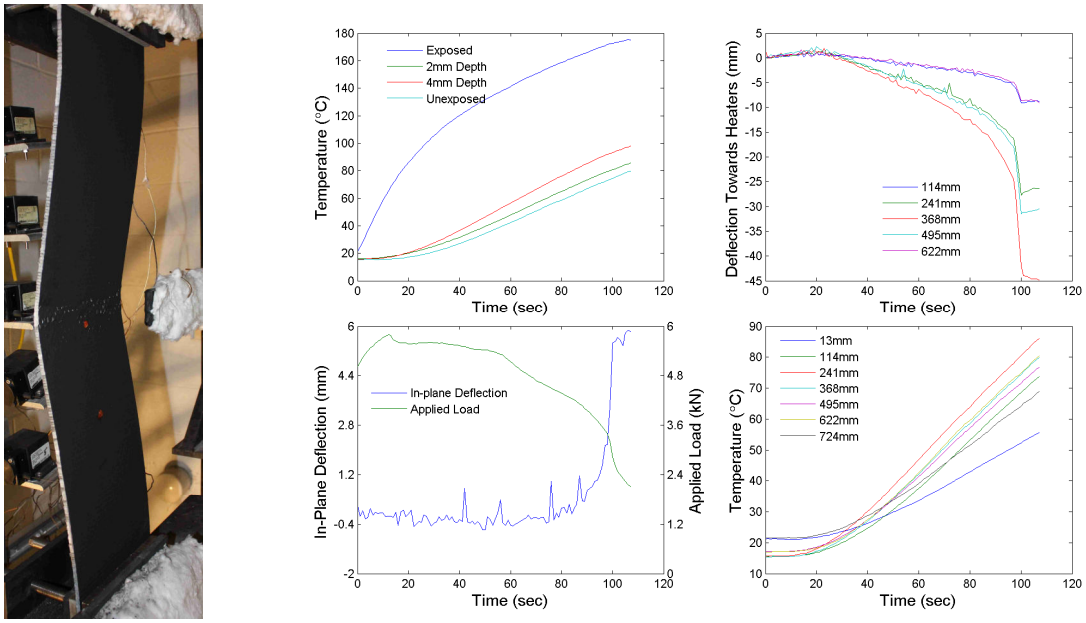

(a) (b)

Figure C-35. Test results for 6mm thick, 203mm width, 737mm height, 19.3kW/m^2, 50% Euler buckling load test with (a) the laminate after failure and (b) plots of mid-height through-thickness temperature profile, out-of-plane deflections, in-plane deflection and applied load, and unexposed surface temperatures. Failure occurred at 97 seconds.

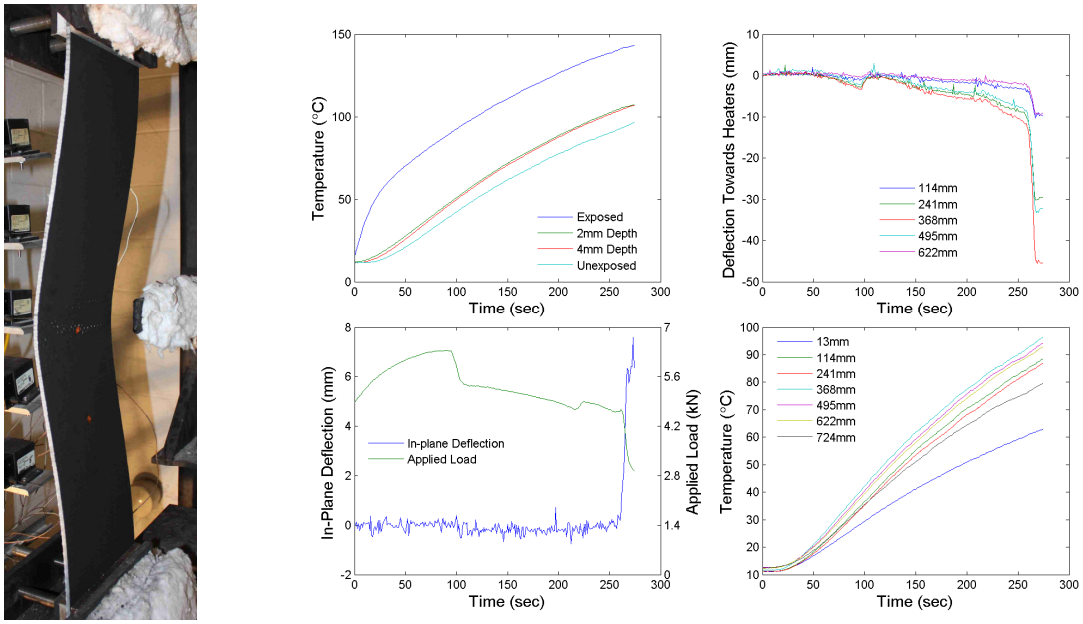

(a) (b)

Figure C-36. Test results for 6mm thick, 203mm width, 737mm height, 8kW/m^2, 50% Euler buckling load test with (a) the laminate after failure and (b) plots of mid-height through-thickness temperature profile, out-of-plane deflections, in-plane deflection and applied load, and unexposed surface temperatures. Failure occurred at 264 seconds.

Appendix D - Thermo-Structural Model Validation

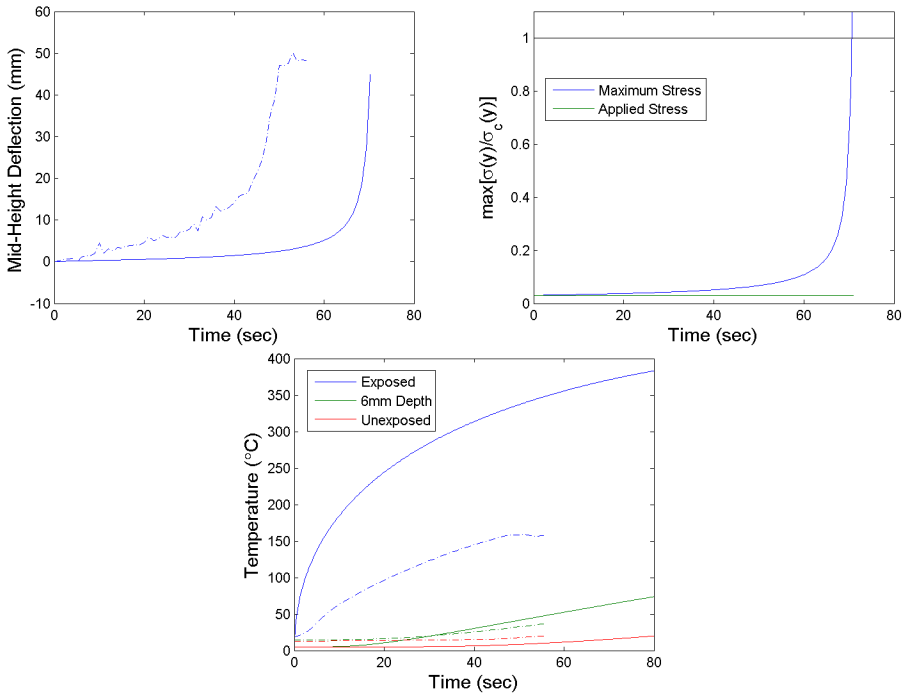

Figure D-1. Comparison of the thermo-structural model predictions to the intermediate-scale test results for 12mm, 38kW/m^2, 50% buckling load test. Predicted time-to-failure was 71 seconds and experimental time-to-failure was 193 seconds.

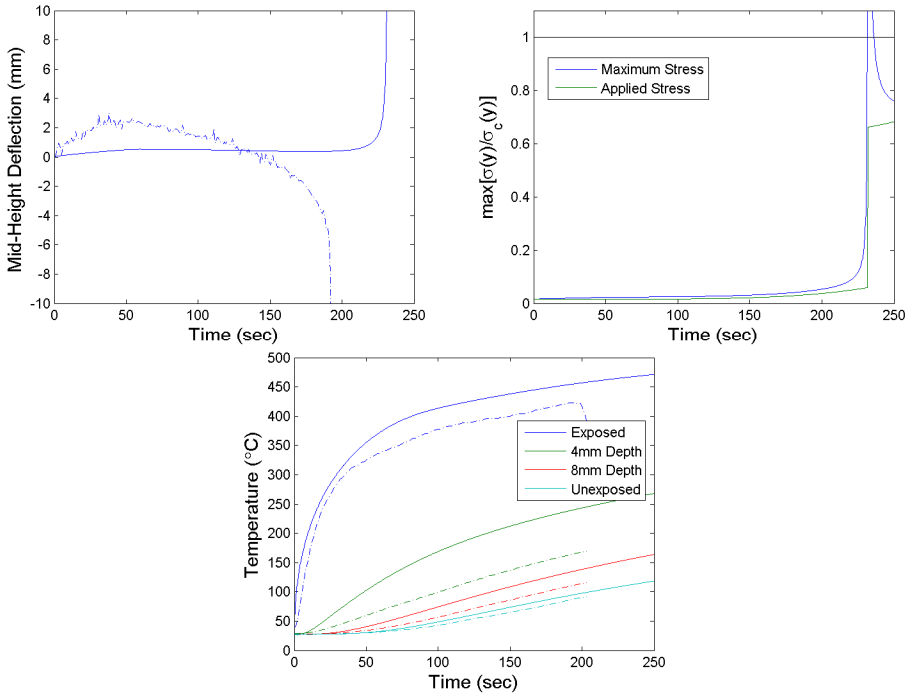

Figure D-2. Comparison of the thermo-structural model predictions to the intermediate-scale test results for 12mm, 38kW/m^2, 25% buckling load test. Predicted time-to-failure was 232 seconds and experimental time-to-failure was 193 seconds.

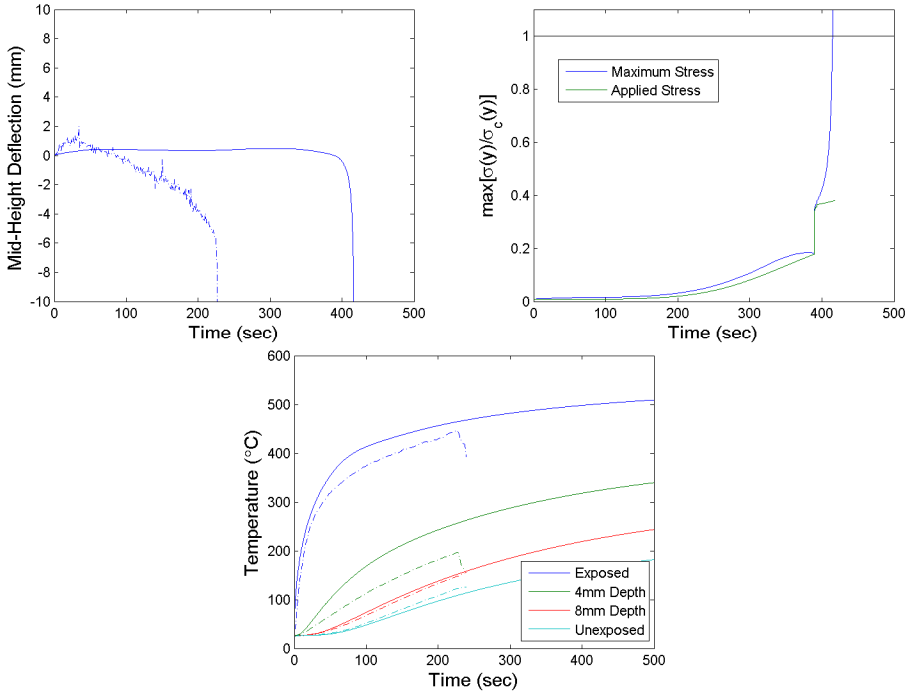

Figure D-3. Comparison of the thermo-structural model predictions to the intermediate-scale test results for 12mm, 38kW/m^2, 15% buckling load test. Predicted time-to-failure was 415 seconds and experimental time-to-failure was 229 seconds.

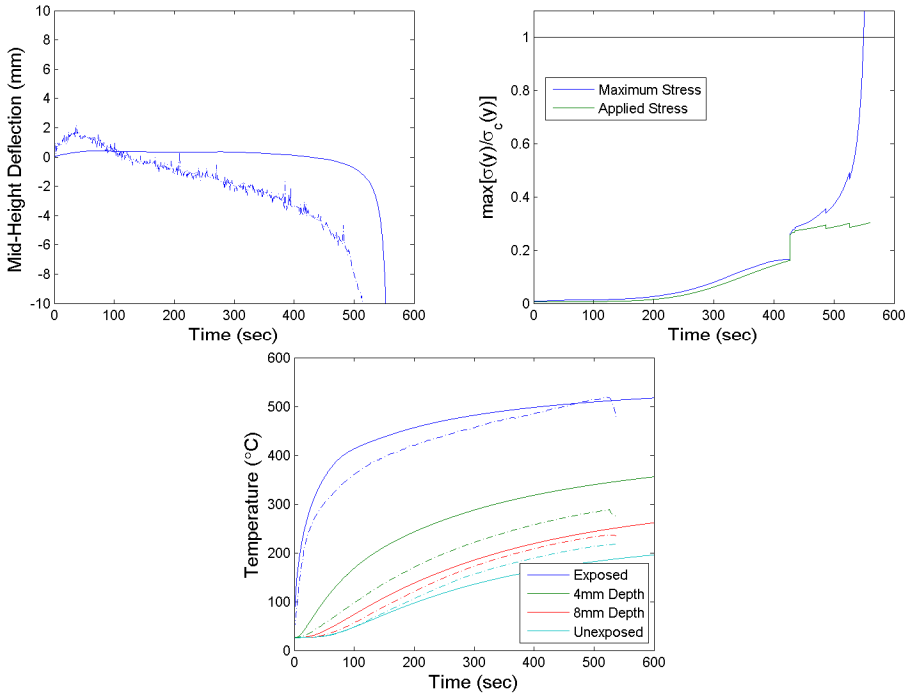

Figure D-4. Comparison of the thermo-structural model predictions to the intermediate-scale test results for 12mm, 38kW/m^2, 10% buckling load test. Predicted time-to-failure was 550 seconds and experimental time-to-failure was 527 seconds.

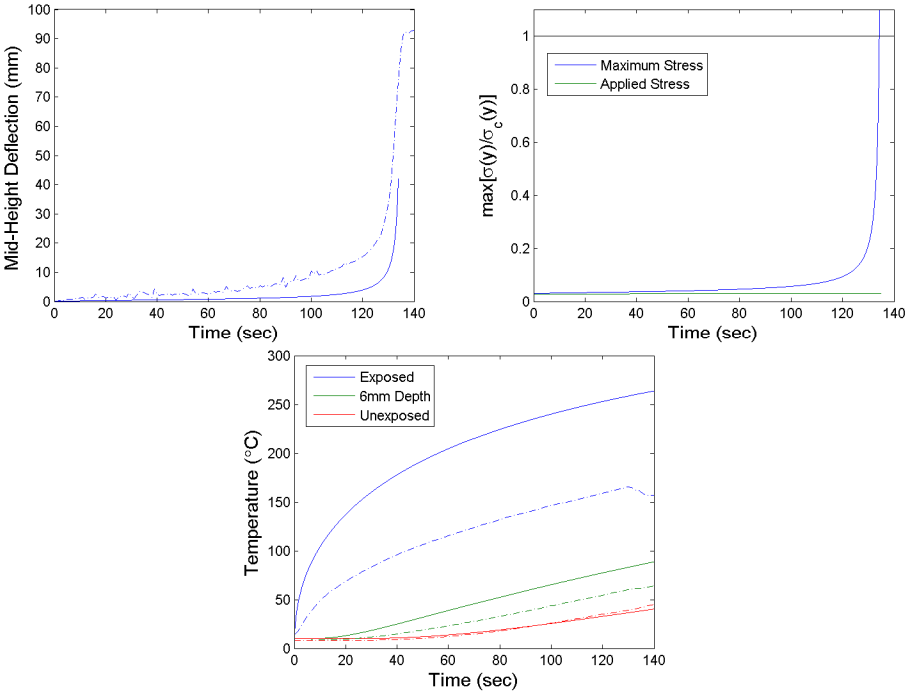

Figure D-5. Comparison of the thermo-structural model predictions to the intermediate-scale test results for 12mm, 19.3kW/m^2, 50% buckling load test. Predicted time-to-failure was 135 seconds and experimental time-to-failure was 130 seconds.

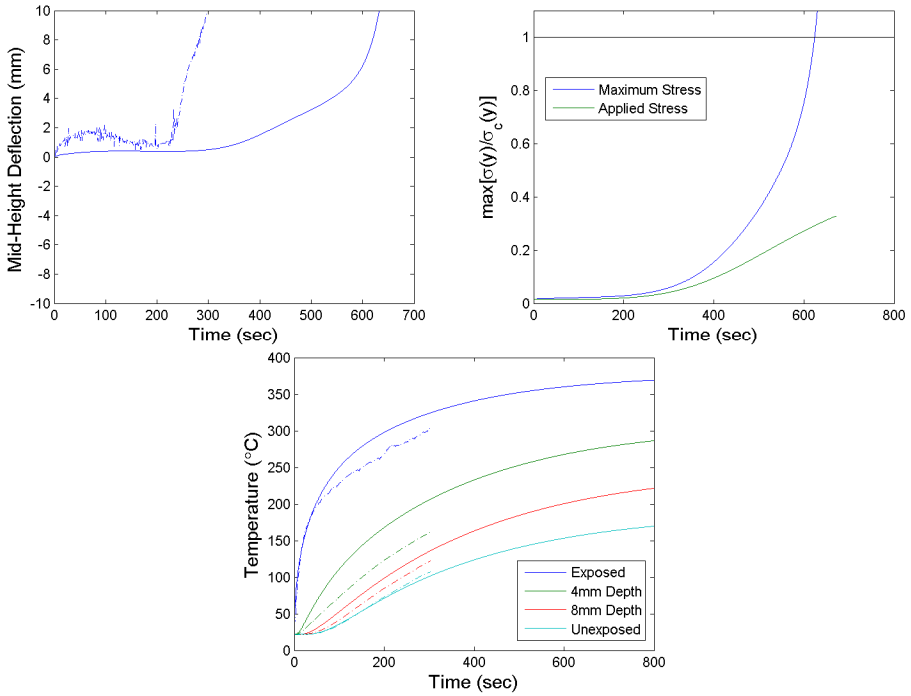

Figure D-6. Comparison of the thermo-structural model predictions to the intermediate-scale test results for 12mm, 19.3kW/m^2, 25% buckling load test. Predicted time-to-failure was 624 seconds and experimental time-to-failure was 303 seconds.

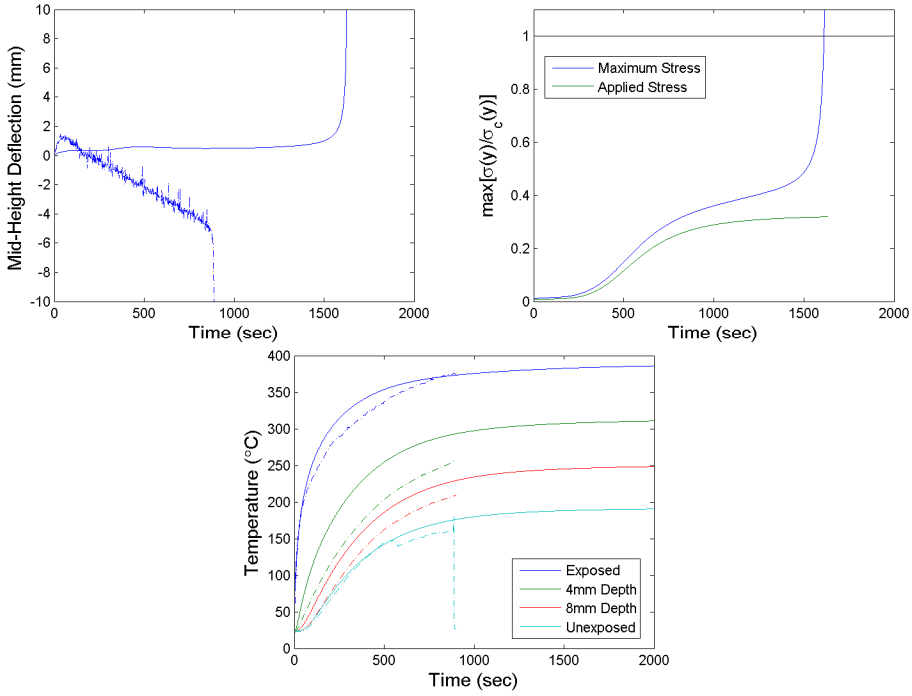

Figure D-7. Comparison of the thermo-structural model predictions to the intermediate-scale test results for 12mm, 19.3kW/m^2, 15% buckling load test. Predicted time-to-failure was 1612 seconds and experimental time-to-failure was 887 seconds.

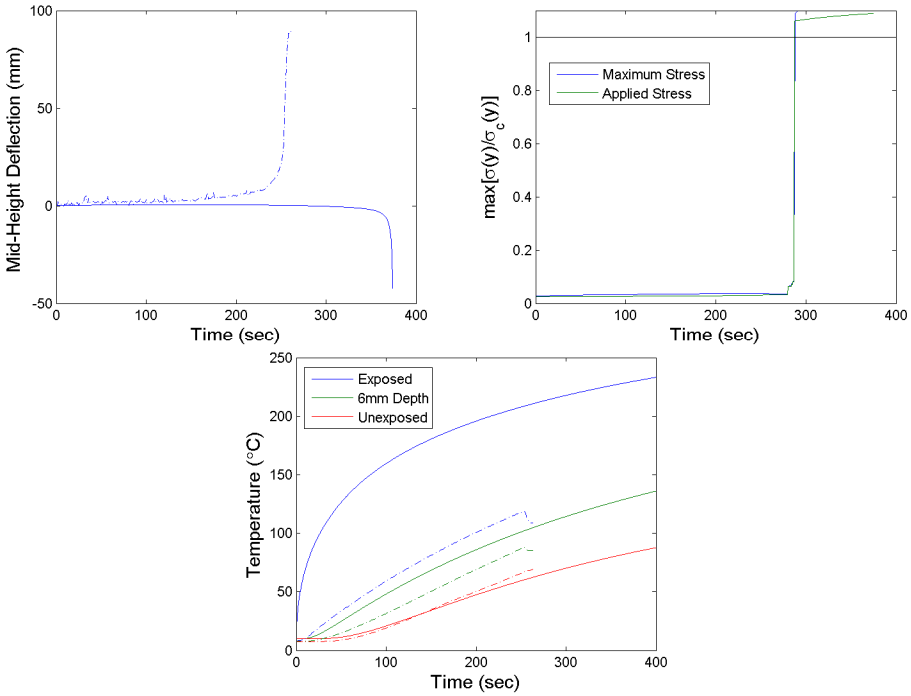

Figure D-8. Comparison of the thermo-structural model predictions to the intermediate-scale test results for 12mm, 11.8kW/m^2, 50% buckling load test. Predicted time-to-failure was 287 seconds and experimental time-to-failure was 253 seconds.

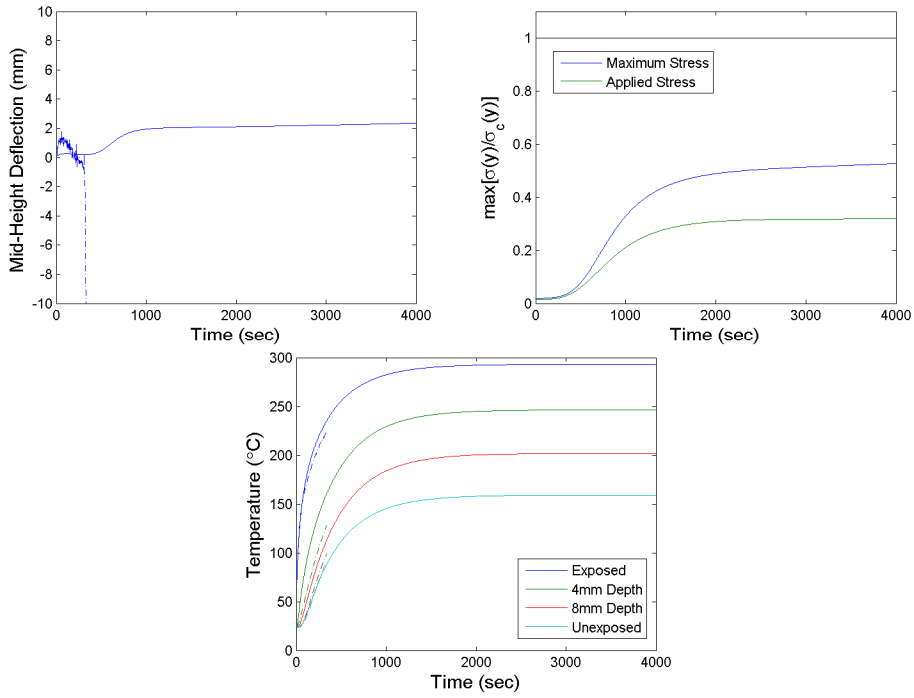

Figure D-9. Comparison of the thermo-structural model predictions to the intermediate-scale test results for 12mm, 11.8kW/m^2, 25% buckling load test. Failure of the laminate was not predicted; however, experimental time-to-failure was 331 seconds.

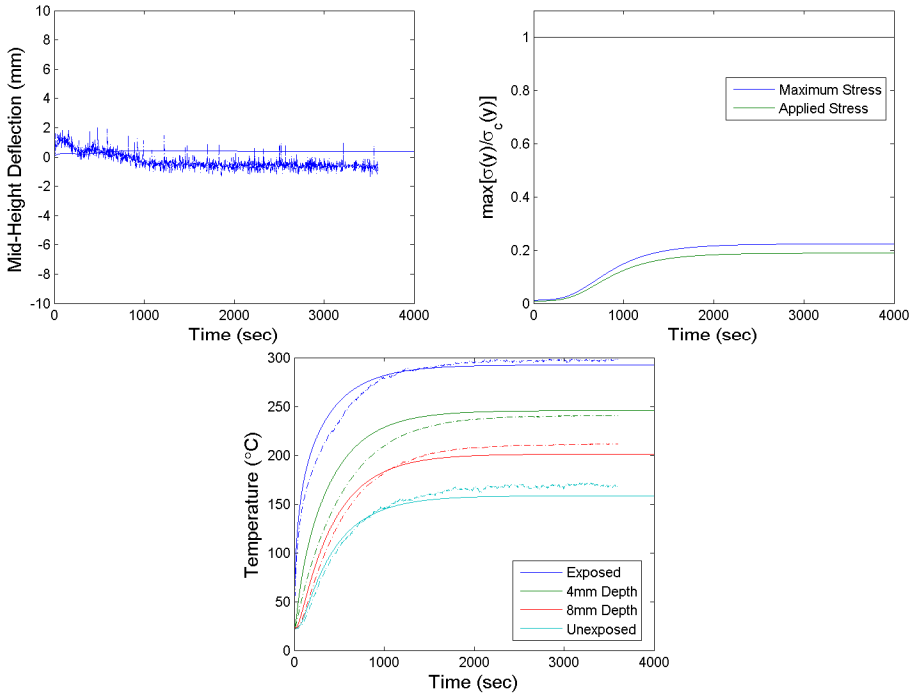

Figure D-10. Comparison of the thermo-structural model predictions to the intermediate-scale test results for 12mm, 11.8kW/m^2, 15% buckling load test. Failure of the laminate was not predicted or observed in testing.

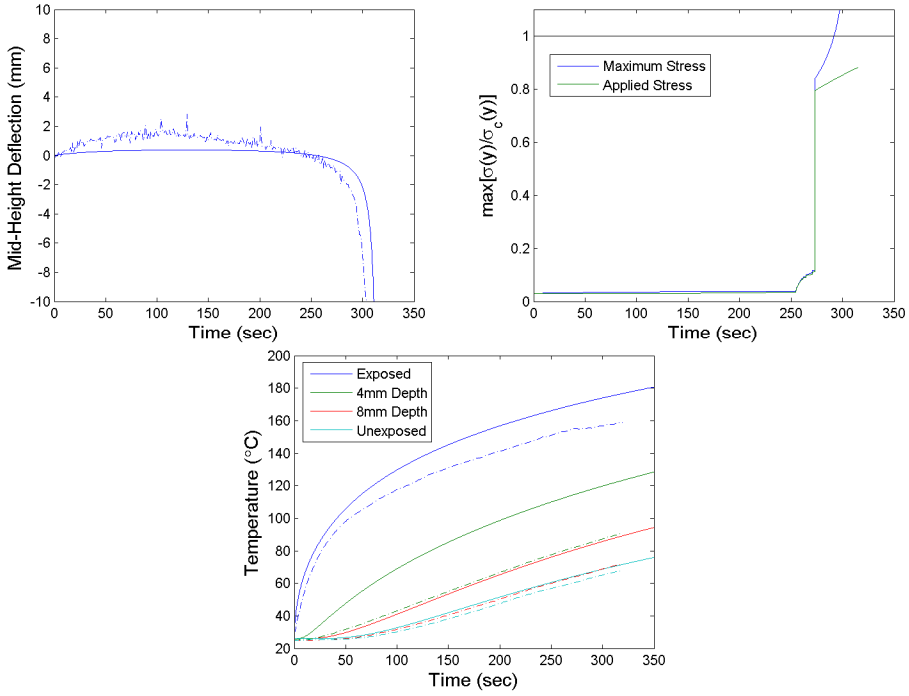

Figure D-11. Comparison of the thermo-structural model predictions to the intermediate-scale test results for 12mm, 8kW/m^2, 50% buckling load test. Predicted time-to-failure was 292 seconds and experimental time-to-failure was 311 seconds.

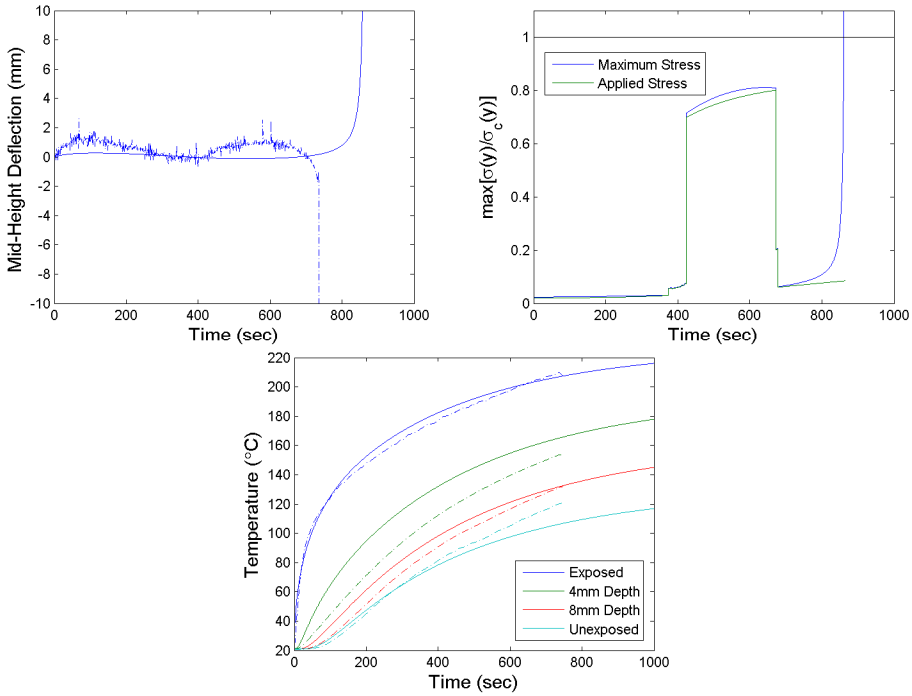

Figure D-12. Comparison of the thermo-structural model predictions to the intermediate-scale test results for 12mm, 8kW/m^2, 35% buckling load test. Predicted time-to-failure was 861 seconds and experimental time-to-failure was 737 seconds.

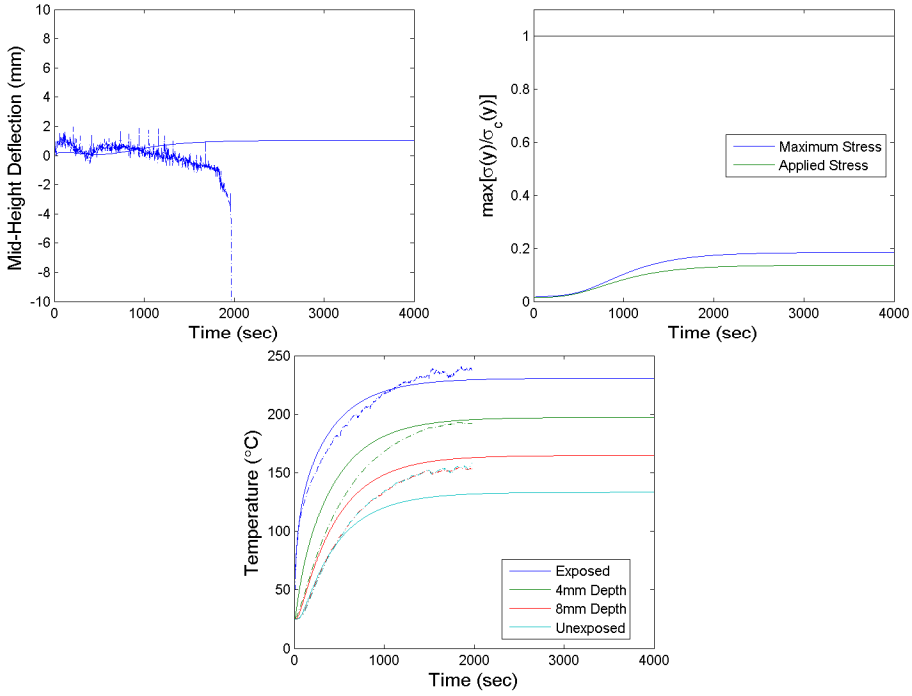

Figure D-13. Comparison of the thermo-structural model predictions to the intermediate-scale test results for 12mm, 8kW/m^2, 25% buckling load test. Failure of the laminate was not predicted; however, experimental time-to-failure was 1971 seconds.

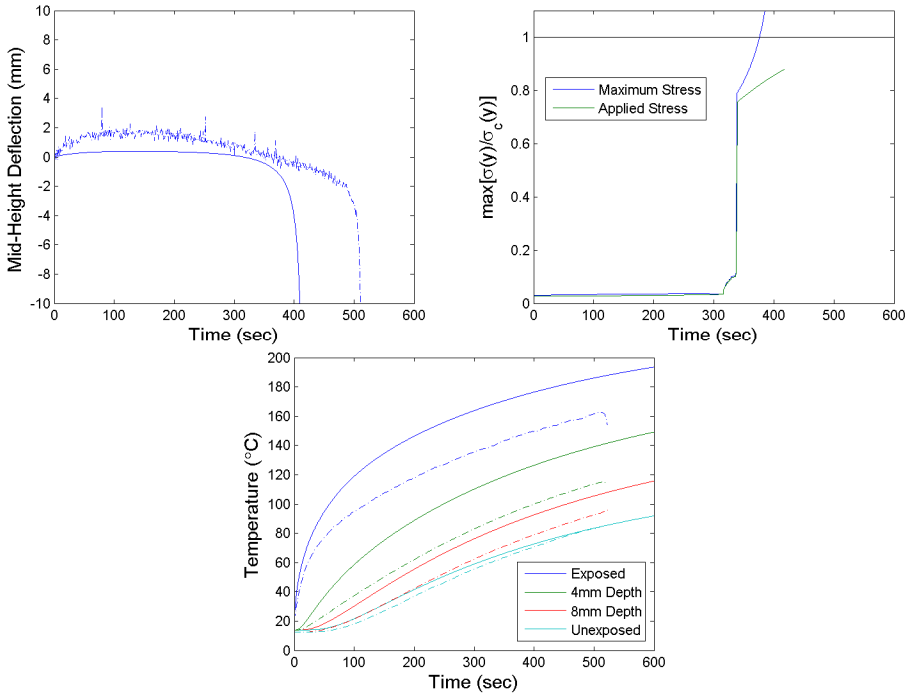

Figure D-14. Comparison of the thermo-structural model predictions to the intermediate-scale repeatability test results for 12mm, 8kW/m^2, 50% buckling load test. Predicted time-to-failure was 376 seconds and experimental time-to-failure was 513 seconds.

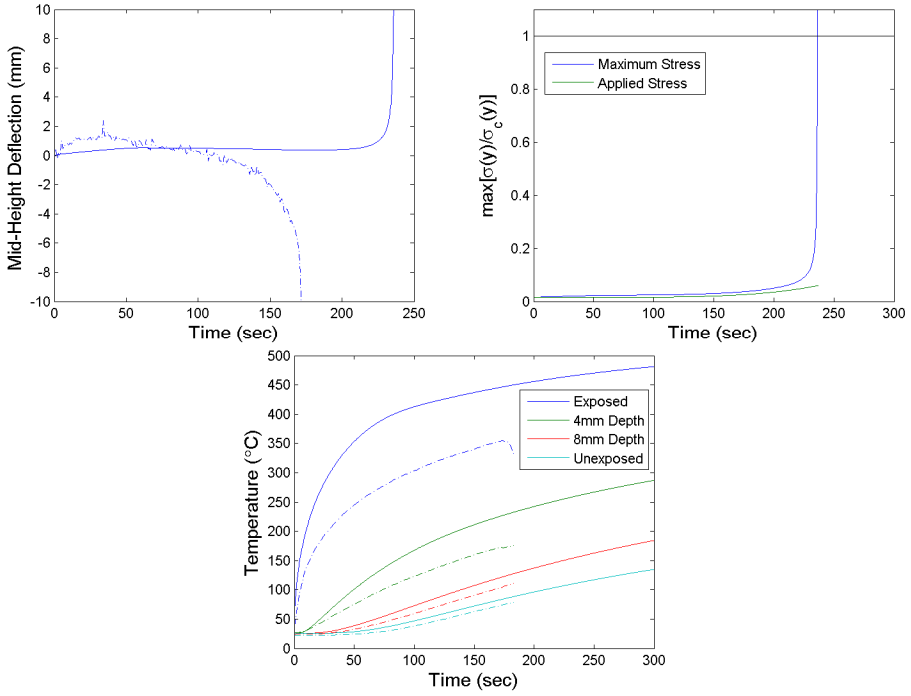

Figure D-15. Comparison of the thermo-structural model predictions to the intermediate-scale repeatability test results for 12mm, 38kW/m^2, 25% buckling load test. Predicted time-to-failure was 237 seconds and experimental time-to-failure was 173 seconds.

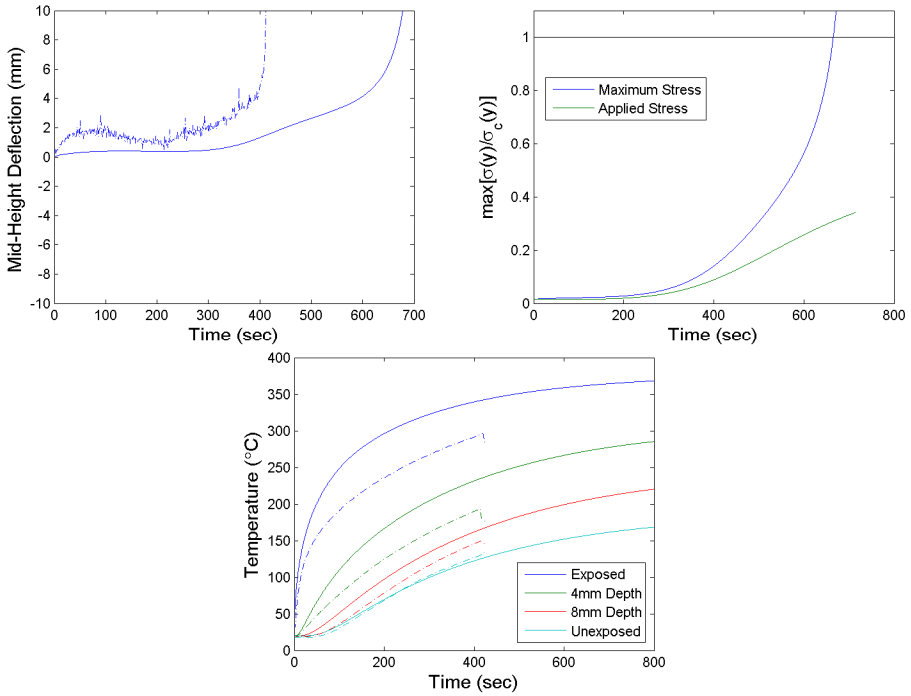

Figure D-16. Comparison of the thermo-structural model predictions to the intermediate-scale repeatability test results for 12mm, 19.3kW/m^2, 25% buckling load test. Predicted time-to-failure was 665 seconds and experimental time-to-failure was 414 seconds.

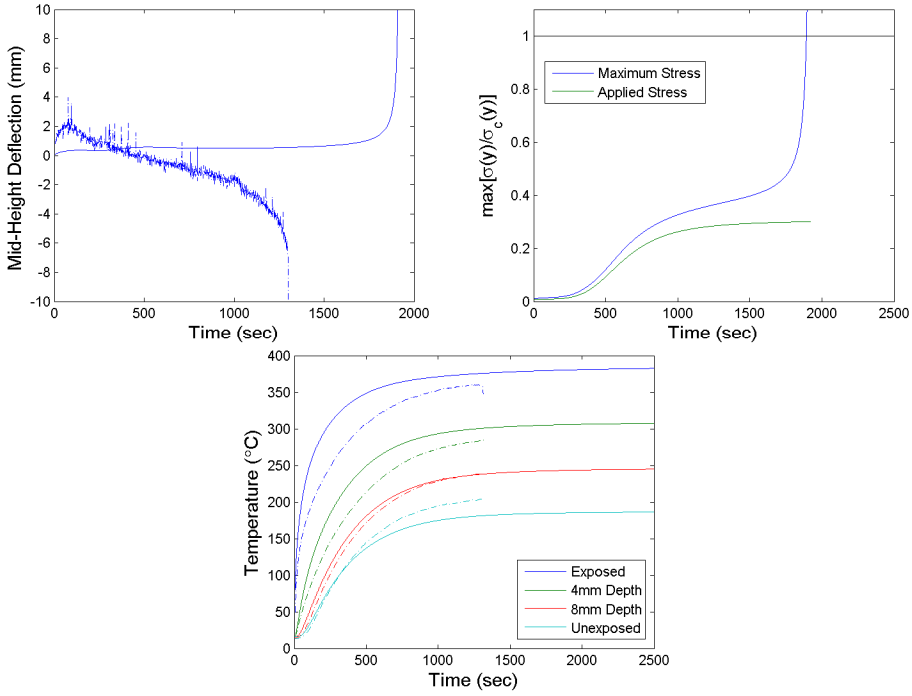

Figure D-17. Comparison of the thermo-structural model predictions to the intermediate-scale repeatability test results for 12mm, 19.3kW/m^2, 15% buckling load test. Predicted time-to-failure was 1893 seconds and experimental time-to-failure was 1303 seconds.

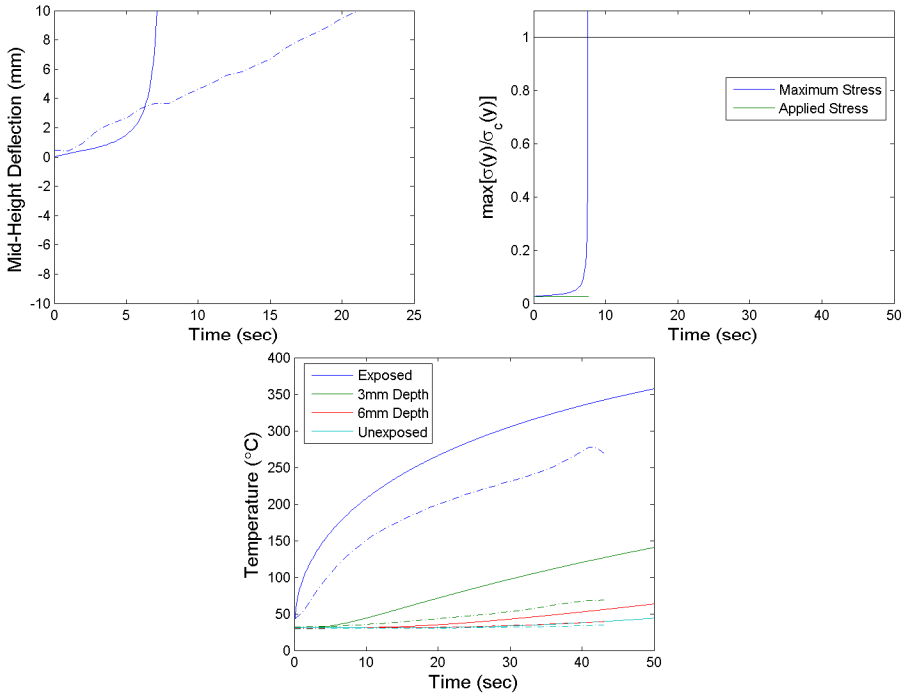

Figure D-18. Comparison of the thermo-structural model predictions to the intermediate-scale test results for 9mm, 38kW/m^2, 75% buckling load test. Predicted time-to-failure was 8 seconds and experimental time-to-failure was 33 seconds.

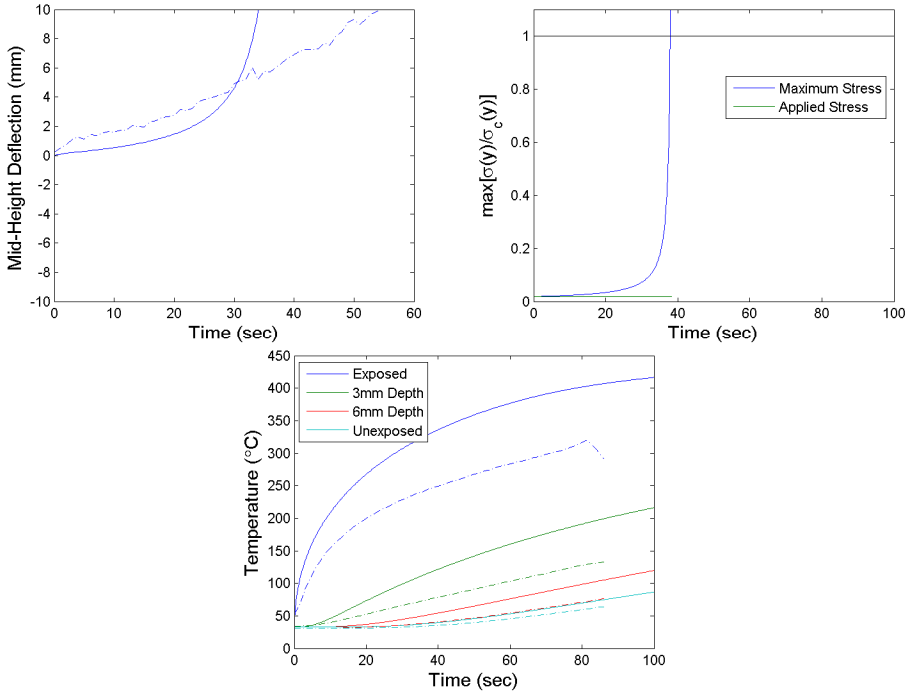

Figure D-19. Comparison of the thermo-structural model predictions to the intermediate-scale test results for 9mm, 38kW/m^2, 50% buckling load test. Predicted time-to-failure was 38 seconds and experimental time-to-failure was 76 seconds.

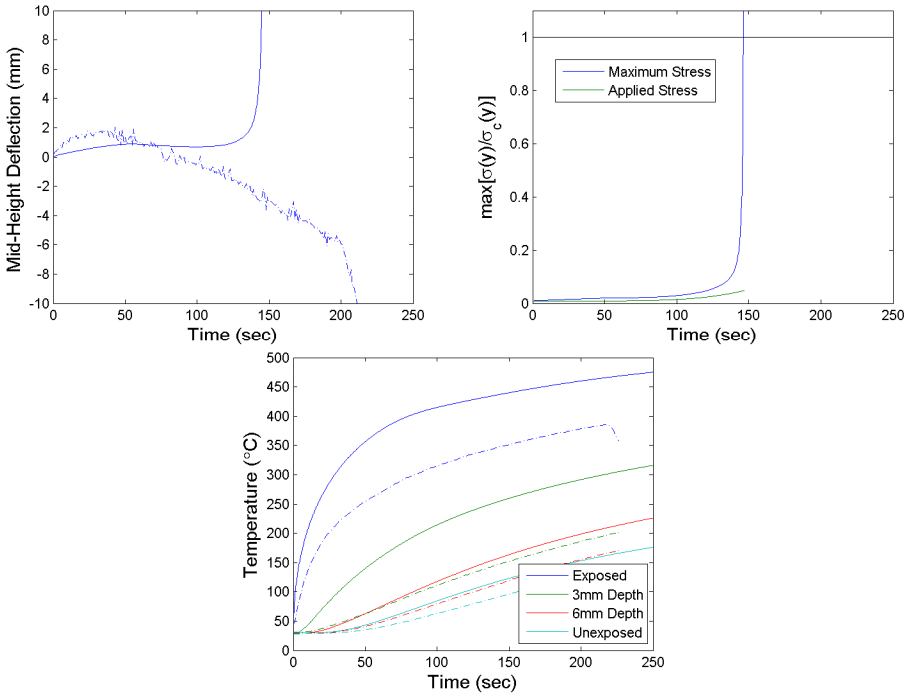

Figure D-20. Comparison of the thermo-structural model predictions to the intermediate-scale test results for 9mm, 38kW/m^2, 25% buckling load test. Predicted time-to-failure was 146 seconds and experimental time-to-failure was 216 seconds.

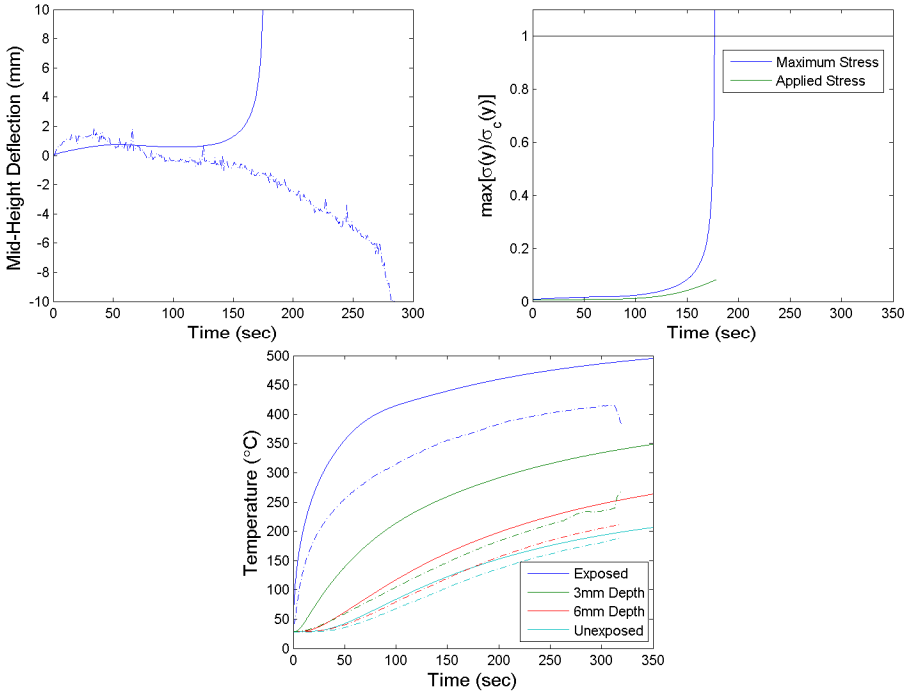

Figure D-21. Comparison of the thermo-structural model predictions to the intermediate-scale test results for 9mm, 38kW/m^2, 15% buckling load test. Predicted time-to-failure was 177 seconds and experimental time-to-failure was 309 seconds.

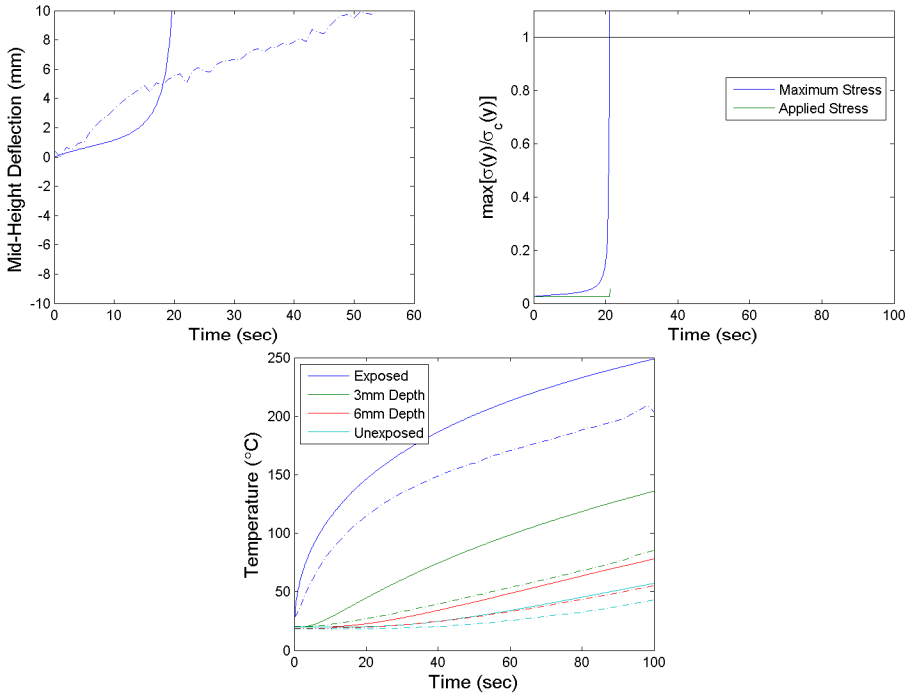

Figure D-22. Comparison of the thermo-structural model predictions to the intermediate-scale test results for 9mm, 19.3kW/m^2, 75% buckling load test. Predicted time-to-failure was 21 seconds and experimental time-to-failure was 90 seconds.

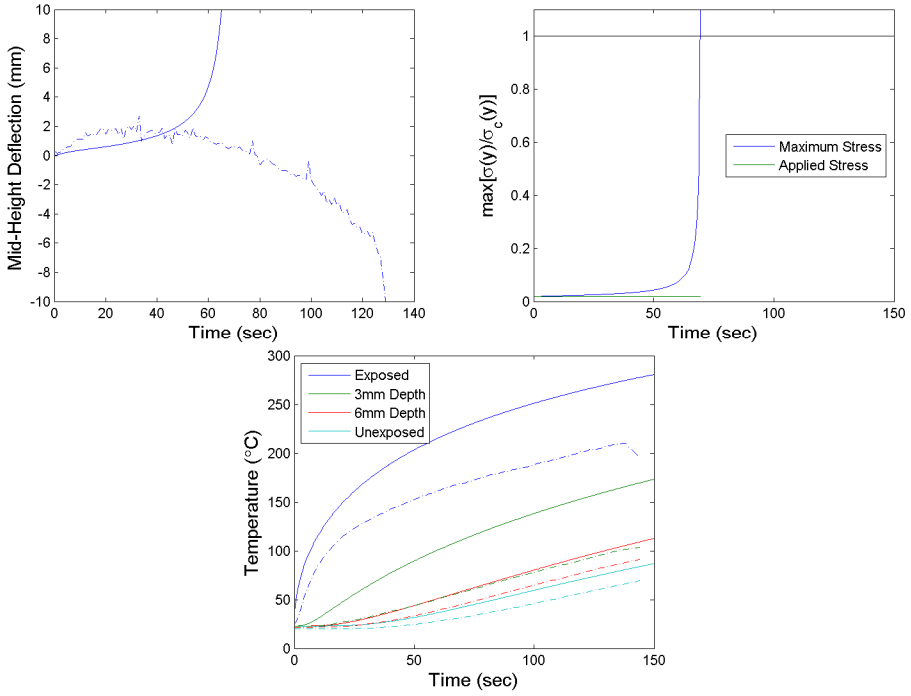

Figure D-23. Comparison of the thermo-structural model predictions to the intermediate-scale test results for 9mm, 19.3kW/m^2, 50% buckling load test. Predicted time-to-failure was 70 seconds and experimental time-to-failure was 134 seconds.

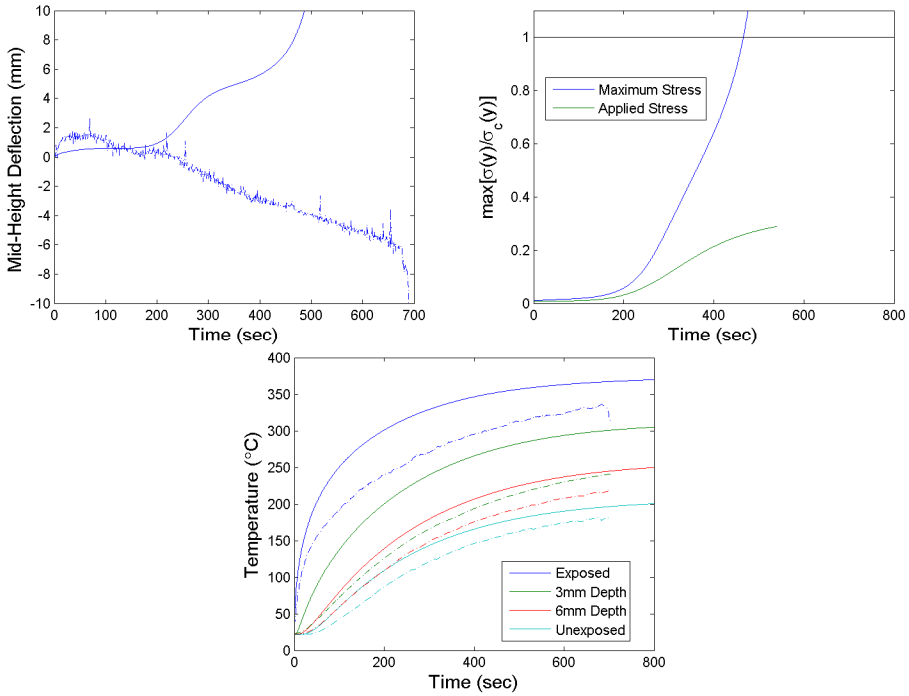

Figure D-24. Comparison of the thermo-structural model predictions to the intermediate-scale test results for 9mm, 19.3kW/m^2, 25% buckling load test. Predicted time-to-failure was 466 seconds and experimental time-to-failure was 692 seconds.

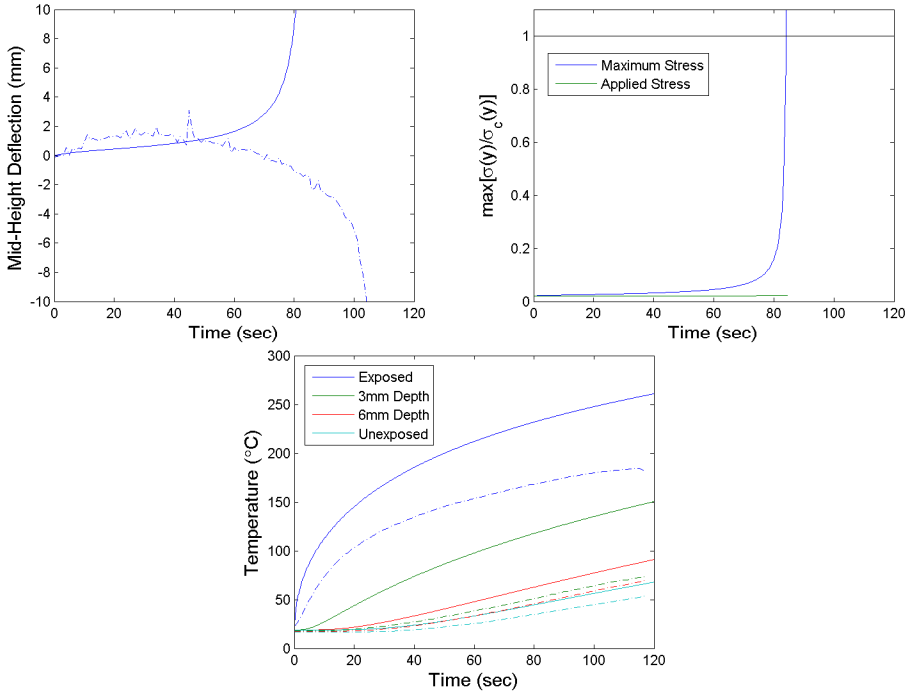

Figure D-25. Comparison of the thermo-structural model predictions to the intermediate-scale test results for 9mm, 660mm height, 19.3kW/m^2, 50% buckling load test. Predicted time-to-failure was 84 seconds and experimental time-to-failure was 109 seconds.

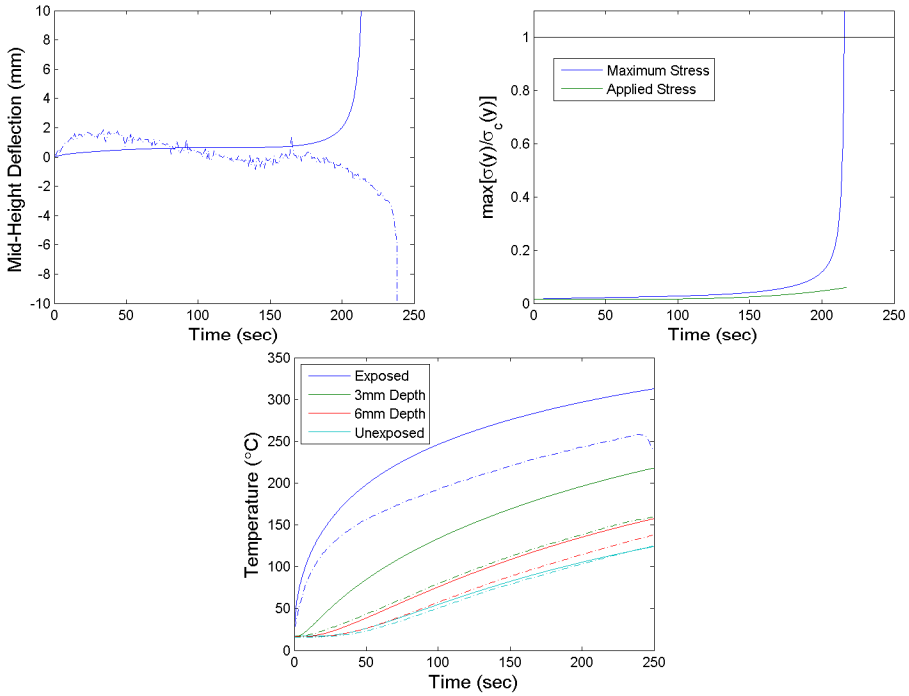

Figure D-26. Comparison of the thermo-structural model predictions to the intermediate-scale test results for 9mm, 660mm height, 19.3kW/m^2, 35% buckling load test. Predicted time-to-failure was 216 seconds and experimental time-to-failure was 239 seconds.

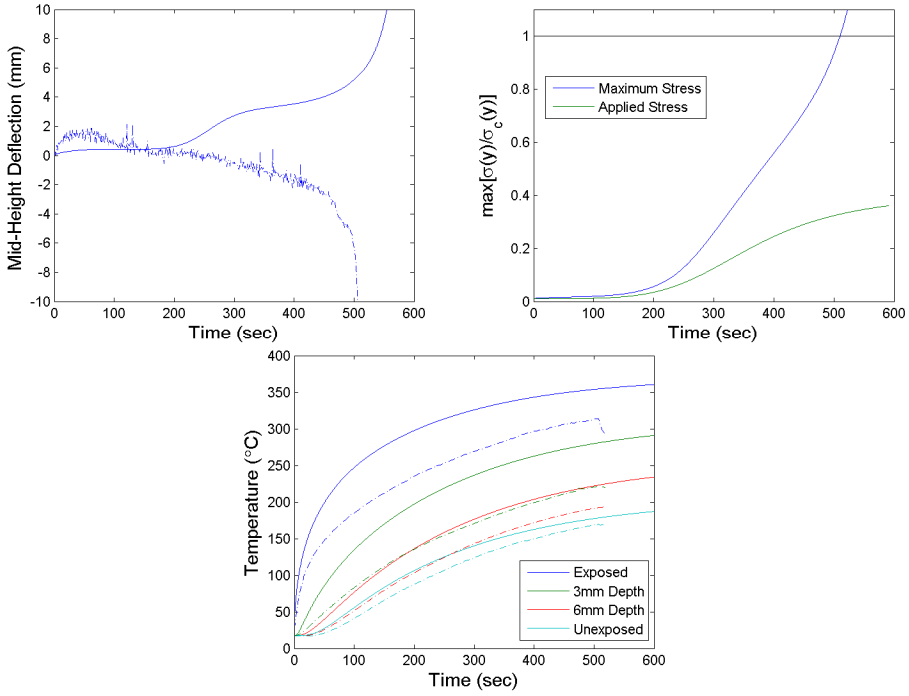

Figure D-27. Comparison of the thermo-structural model predictions to the intermediate-scale test results for 9mm, 660mm height, 19.3kW/m^2, 25% buckling load test. Predicted time-to-failure was 510 seconds and experimental time-to-failure was 508 seconds.

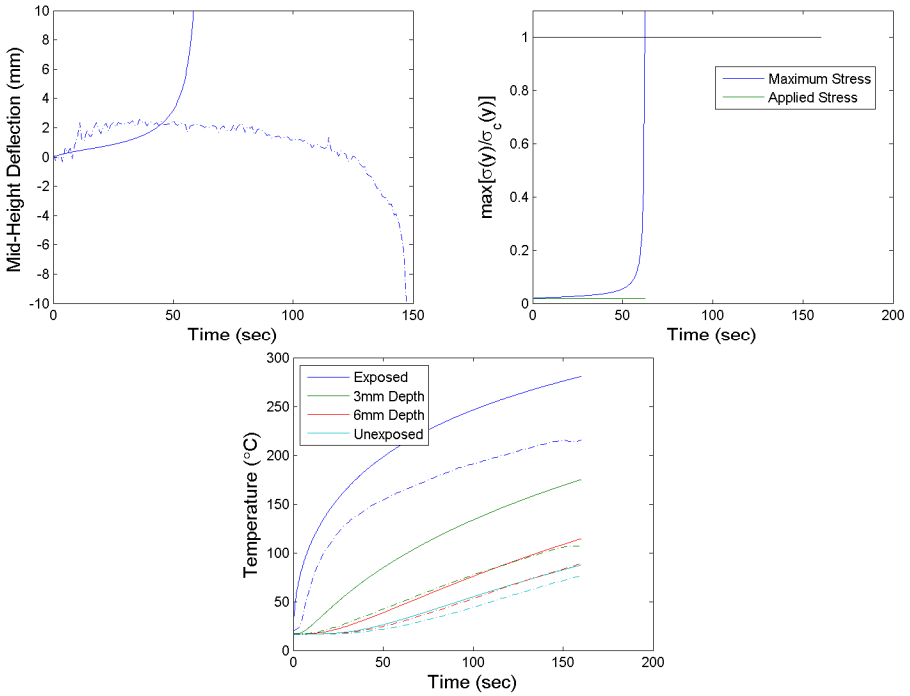

Figure D-28. Comparison of the thermo-structural model predictions to the intermediate-scale test results for 9mm, 140mm width, 19.3kW/m^2, 50% buckling load test. Predicted time-to-failure was 62 seconds and experimental time-to-failure was 150 seconds.

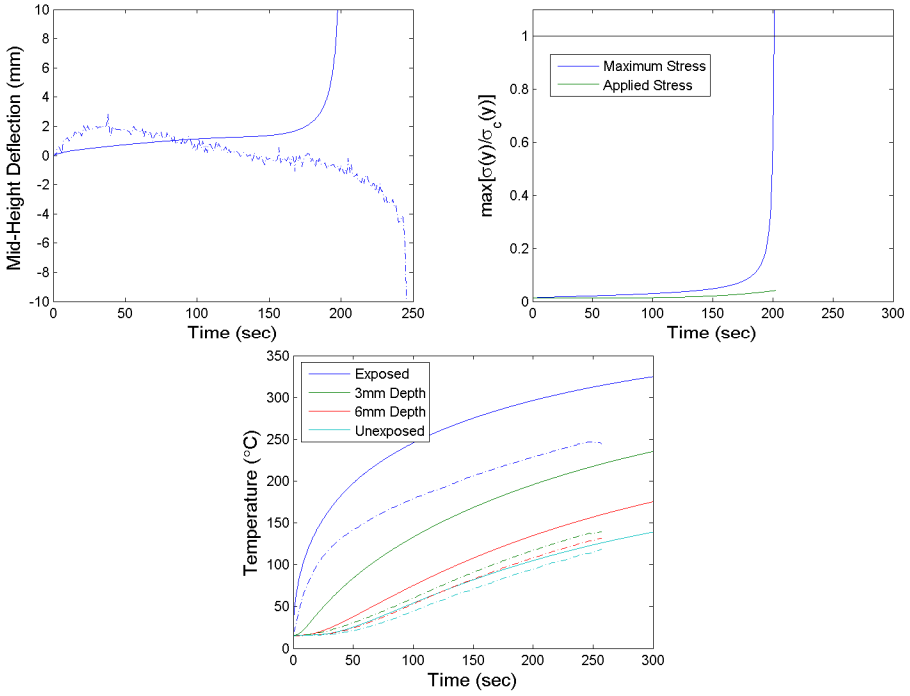

Figure D-29. Comparison of the thermo-structural model predictions to the intermediate-scale test results for 9mm, 140mm width, 19.3kW/m^2, 35% buckling load test. Predicted time-to-failure was 201 seconds and experimental time-to-failure was 247 seconds.

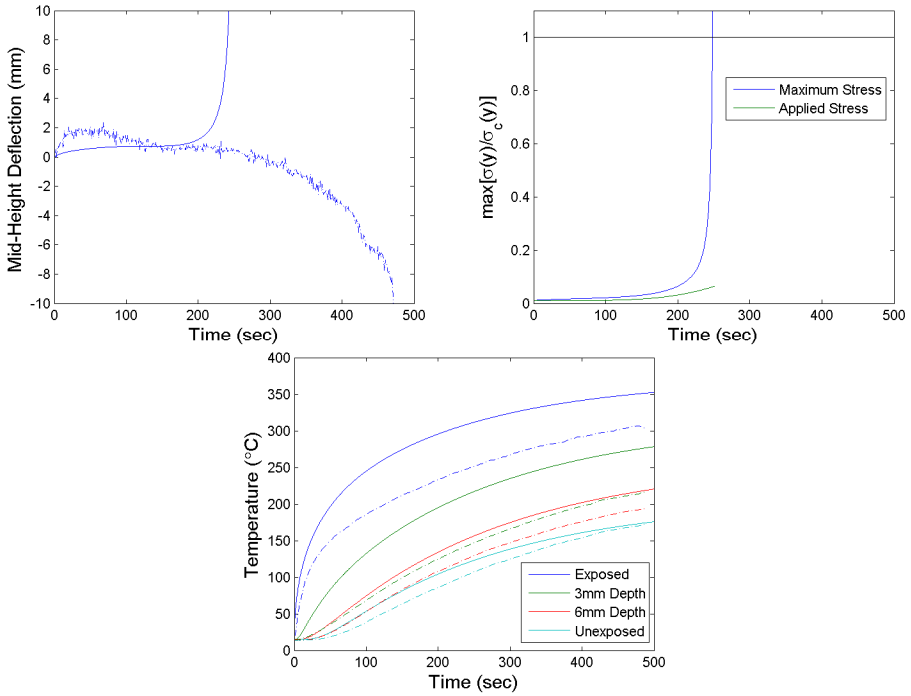

Figure D-30. Comparison of the thermo-structural model predictions to the intermediate-scale test results for 9mm, 140mm width, 19.3kW/m^2, 25% buckling load test. Predicted time-to-failure was 249 seconds and experimental time-to-failure was 479 seconds.

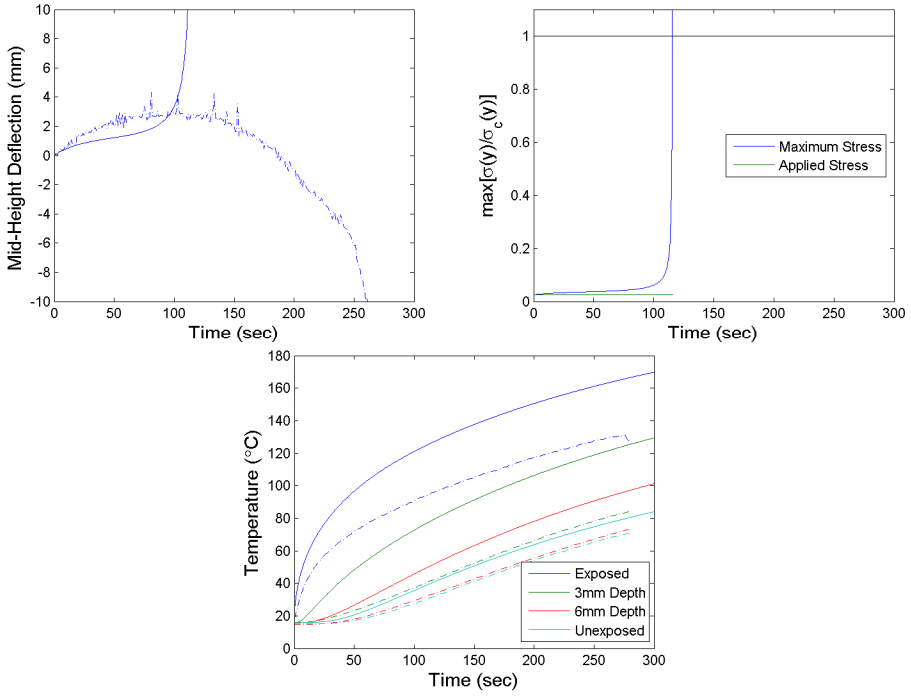

Figure D-31. Comparison of the thermo-structural model predictions to the intermediate-scale test results for 9mm, 8kW/m^2, 75% buckling load test. Predicted time-to-failure was 116 seconds and experimental time-to-failure was 271 seconds.

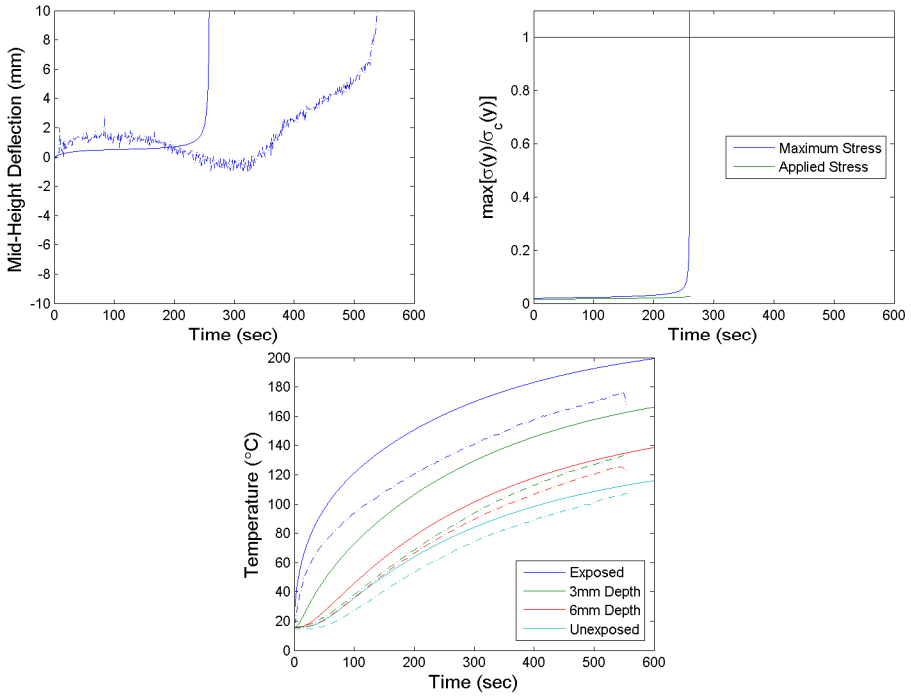

Figure D-32. Comparison of the thermo-structural model predictions to the intermediate-scale test results for 9mm, 8kW/m^2, 50% buckling load test. Predicted time-to-failure was 260 seconds and experimental time-to-failure was 545 seconds.

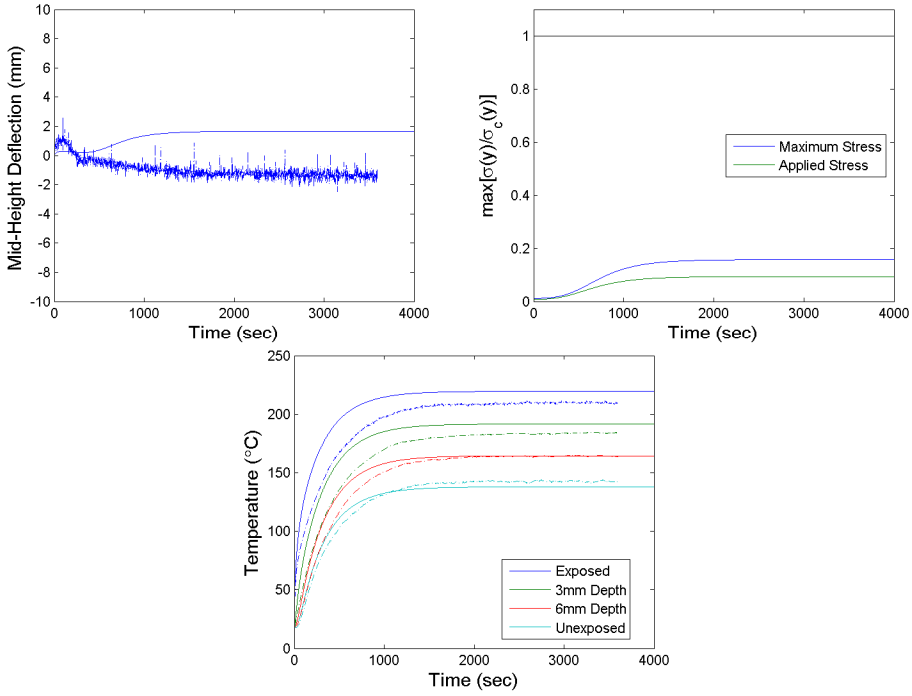

Figure D-33. Comparison of the thermo-structural model predictions to the intermediate-scale test results for 9mm, 8kW/m^2, 25% buckling load test. Failure of the laminate was not predicted or observed in testing.

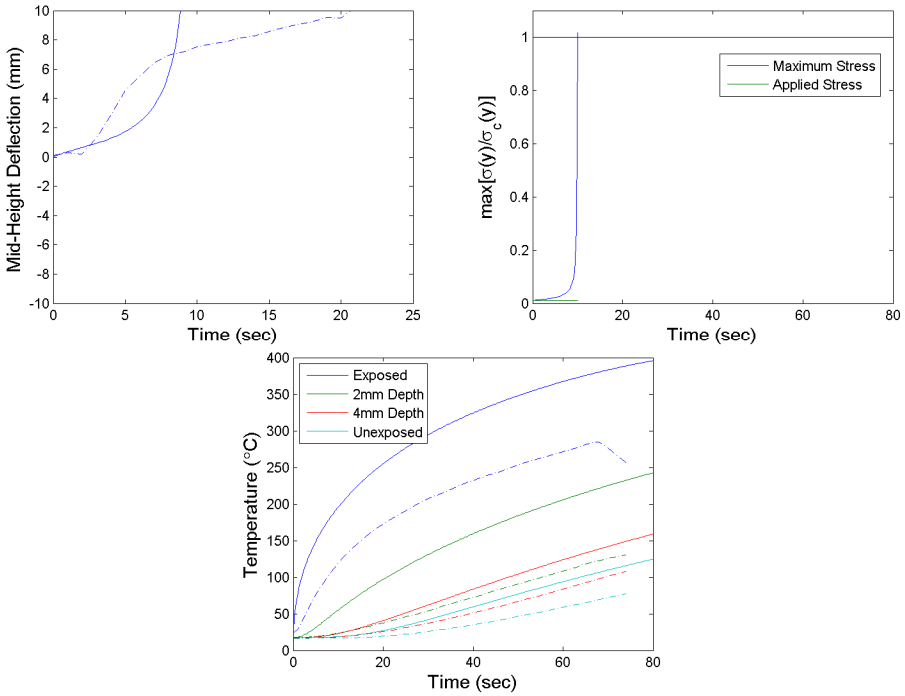

Figure D-34. Comparison of the thermo-structural model predictions to the intermediate-scale test results for 6mm, 38kW/m^2, 50% buckling load test. Predicted time-to-failure was 10 seconds and experimental time-to-failure was 64 seconds.

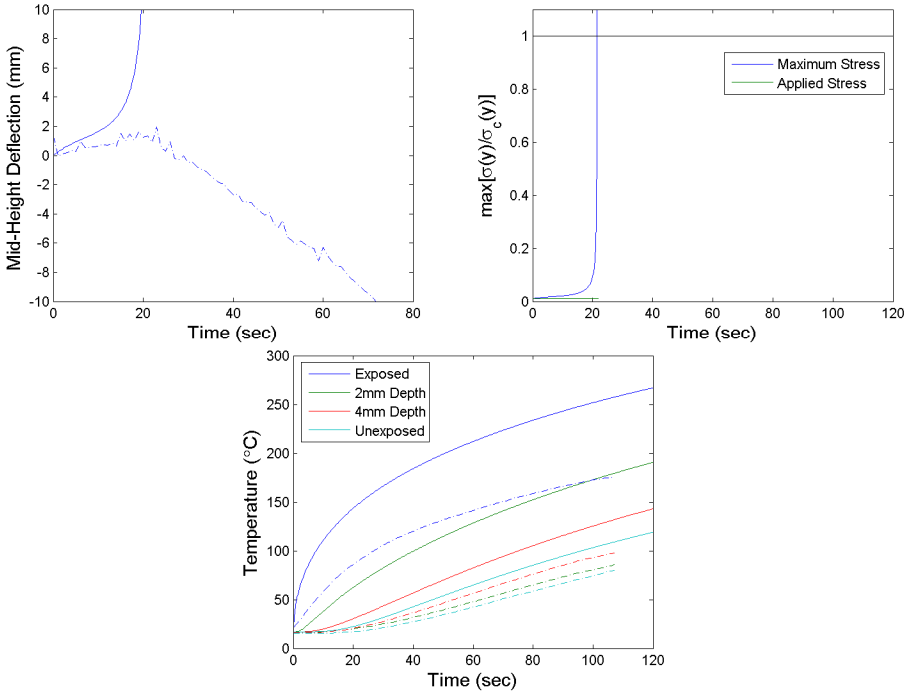

Figure D-35. Comparison of the thermo-structural model predictions to the intermediate-scale test results for 6mm, 19.3kW/m^2, 50% buckling load test. Predicted time-to-failure was 22 seconds and experimental time-to-failure was 97 seconds.

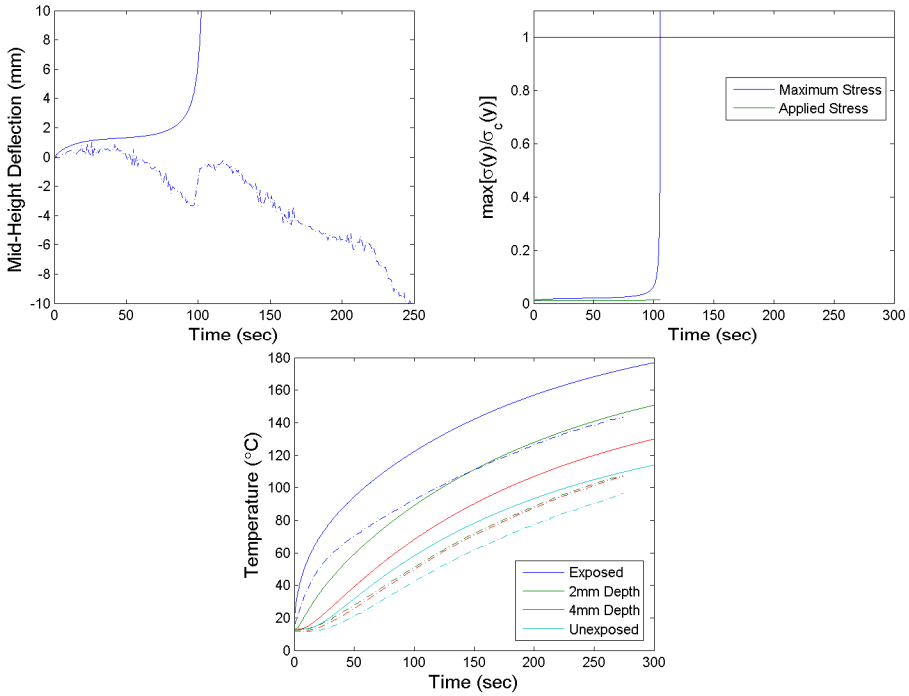

Figure D-36. Comparison of the thermo-structural model predictions to the intermediate-scale test results for 6mm, 8kW/m^2, 50% buckling load test. Predicted time-to-failure was 106 seconds and experimental time-to-failure was 264 seconds.